

# **Seismic Spectral Ratio Analysis Considering Rupture Directivity Effect and Source Heterogeneity**

Shota Shimmoto





# TABLE OF CONTENTS

Chapter 1	INTRODUCTION.....	1
1.1.	BACKGROUND.....	1
1.2.	OBJECTIVE AND OVERVIEW .....	6
1.3.	ORGANIZATION.....	9
	REFERENCES.....	11
Chapter 2	SOURCE SPECTRUM MODEL CONSIDERING RUPTURE DIRECTIVITY EFFECT .....	15
2.1.	OVERVIEW .....	15
2.2.	KINEMATIC SOURCE MODEL.....	16
2.3.	MODEL OF SEISMIC SOURCE SPECTRAL ENVELOPE.....	19
2.4.	CONCLUSIONS.....	27
	REFERENCES.....	27
Chapter 3	SPECTRAL RATIO METHOD .....	29
3.1.	OVERVIEW .....	29
3.2.	DATA .....	30
3.3.	METHOD.....	31
3.3.1.	Spectral Ratio Stacks Using Multiple Empirical Green’s Functions.....	31
3.3.2.	Spectral Ratio Model.....	35
3.3.3.	Comparison of Model Spectral Ratio with Observed Data .....	37
3.4.	RESULTS .....	41
3.5.	DISCUSSION .....	46
3.6.	CONCLUSIONS.....	48
	REFERENCES.....	49
Chapter 4	SEISMIC SPECTRA AND SOURCE HETEROGENEITY .....	53
4.1.	BACKGROUND AND OVERVIEW .....	53
4.2.	WHAT IS THE ESTIMATED RUPTURE AREA? .....	54

4.3.	REVISE OF STRESS DROP CALCULATION METHOD .....	57
4.4.	STRESS DROP RESULTS .....	59
4.4.1.	Seismic Moment Dependence .....	59
4.4.2.	Faulting Type Dependence .....	61
4.4.3.	Rupture Speed Dependence .....	62
4.4.4.	Stress Drop and Corner Frequency .....	63
4.4.5.	Depth Dependence .....	66
4.5.	STRESS DROP UNCERTAINTY .....	68
4.6.	DISCUSSION .....	72
4.6.1.	Stress Drops .....	72
4.6.2.	Seismic Spectra and Localized Area with Large Slip .....	74
4.6.3.	Corner-Frequency-Based Stress Drop .....	75
4.7.	CONCLUSIONS.....	76
	REFERENCES.....	78
Chapter 5	EARTHQUAKE ENERGY BUDGET AND SOURCE PARAMETER SCALING RELATIONS .....	81
5.1.	OVERVIEW .....	81
5.2.	EARTHQUAKE ENERGY BUDGET AND STRESS DROP .....	82
5.3.	METHOD OF RADIATED ENERGY ESTIMATION.....	85
5.4.	RESULTS.....	87
5.4.1.	Radiated Energy and Stress Drop.....	87
5.4.2.	Radiation Efficiency.....	90
5.4.3.	Corner-Frequency-Based Stress Drop.....	94
5.4.4.	Comparison with Other Crustal Earthquakes.....	96
5.4.5.	Comparison with Subduction Zone Interplate Earthquakes.....	103
5.5.	DISCUSSION .....	105
5.5.1.	Radiation Efficiency and Earthquake Rupture Dynamics.....	105
5.5.2.	Source Parameter Scaling Relations.....	107
5.6.	CONCLUSIONS.....	110
	REFERENCES.....	111
Chapter 6	CONCLUSIONS AND FUTURE STUDIES .....	118
6.1.	CONCLUSIONS.....	118
6.2.	FUTURE STUDIES.....	122
	REFERENCES.....	122
	ACKNOWLEDGMENT.....	124

APPENDICES .....	125
A1. CALCULATION NOTES FOR CHAPTER 2 .....	125
A1.1. Derivation of $K$ .....	125
A1.2. Solution of the Source Spectrum.....	126
A1.3. Envelope Approximation of the Source Spectrum .....	128
A2. SPECTRAL RATIO FITTING RESULTS.....	131

# LIST OF SYMBOLS

The symbols frequently used in this dissertation are listed below. Please note that the meaning of some symbols sometimes differs from that in the list, depending on the context.

Symbol	Description
$AR, AR'$	Aspect ratio, $AR = L/W$ and $AR' = \max(L/W, W/L)$
$C_{VS}$	The ratio of rupture speed to S-wave velocity ( $V_{rmax}/V_S$ or $V_r/V_S$ ).
$D$	Slip
$\dot{D}$	Slip velocity (the time derivative of slip)
$E_R$	Radiated energy
$E_G$	Fracture energy
$E_P$	Total potential energy
$E_F$	Frictional energy ( $E_F = E_P - E_R - E_G$ )
$f$	Circular frequency (Hz)
$f_c$	Corner frequency
$F_{res}, F_{res\omega^2}$	The residual between observed and model spectral ratio (misfit value).
$G, G^E$	Fracture energy per unit area
$H(\cdot)$	Heaviside step function
$I_{pq}$	L1 distance (norm) from a center of the rectangular source $I_{pq} =  p - 0.5  +  q - 0.5 $
$k_c$	A constant used to calculate $\Delta\sigma_{fc}$ from corner frequency. The subscript $c$ is replaced by $S$ or $P$ depending on the wave type used to obtain corner frequency.
$K$	Amount of instantaneous dislocation, recommendation $K = 3$
$L$	Rupture length
$LW, S$	Rupture area
$M_0$	Seismic moment
$M_w$	Moment magnitude
$p, q$	Location of rupture starting point
$r_h$	Hypocenter distance
$SR_{obs}$	Observed spectral ratio
$SR_{\omega^2}, SR_E$	Model spectral ratio
$V_c$	Velocity of wave type P or S. Subscript designates a wave type.
$V_r$	Rupture speed
$V_r/\sin\theta$	Rupture speed along length direction, $0 \leq \theta \leq \pi/2$

$V_r/\cos\theta$	Rupture speed along width direction, $0 \leq \theta \leq \pi/2$
$V_{rmax}$	Maximum rupture speed of the rectangular source model, $\max(V_r/\sin\theta, V_r/\cos\theta)$
$VR_{egf}, VR_{env}$	Variance reduction
$W$	Rupture width
$\gamma$	The parameter to describe the sharpness of a spectral corner
$\delta$	Dip angle
$\delta(\cdot)$	Dirac's delta function
$\overline{\Delta\sigma}$	Average static stress drop
$\Delta\sigma_R$	A parameter whose unit is the same as the stress drop
$\Delta\sigma_s$	Average static stress drop calculated with the seismic moment and the overall rupture area (the moment-based stress drop)
$\Delta\sigma_E$	The energy-related stress drop
$\Delta\sigma_{la}$	The stress drop on the localized area with large slip (the largest-asperity area)
$\Delta\sigma_{fc}$	The stress drop calculated from corner frequency
$\Delta W_0$	The available energy
$\eta_R$	The radiation efficiency defined as $\eta_R = E_R/(E_R + E_G)$
$\eta_R'$	The radiation efficiency defined as $\eta_R' = 2\sigma_a/\Delta\sigma_s$
$\eta_R^E$	The radiation efficiency defined as $\eta_R^E = 2\sigma_a/\Delta\sigma_E$
$\theta, \phi$	Angles in polar coordinate
$\Lambda$	The rupture orientation angle
$\mu$	Shear rigidity
$\sigma_a$	The apparent stress, $\sigma_a = \mu E_R/M_0$
$\sigma_d$	Dynamic stress level
$\sigma_f$	Frictional stress during an earthquake
$\sigma_0$	Average initial shear stress before an earthquake
$\sigma_1$	Average final shear stress after an earthquake
$\tau_{L1}, \tau_{L2}, \tau_{W1}, \tau_{W2}$	Apparent rupture time
$\tau_r$	Rise time
$\varphi_s$	Strike angle
$\omega$	Angular frequency, $\omega = 2\pi f$ (rad/s)
$\Omega$	Source time function or source spectral amplitude
$\Omega_E$	The envelope spectrum (the proposed source spectrum model)
$\Omega_{EN}$	The normalized envelope spectrum

---

# Chapter 1

## INTRODUCTION

### 1.1. BACKGROUND

Mitigating social loss due to earthquake disasters is a fundamental objective in earthquake engineering. Rapid recovery of earthquake-damaged urban functions immediately after a severe earthquake disaster is a key to minimizing the loss of society due to earthquake disasters. It is expected to be beneficial to prepare a post-earthquake recovery strategy that contributes to the early recovery of the earthquake-damaged urban functions, considering not only damage to buildings and infrastructure from the mainshock but also the cumulative damage from aftershocks. For this purpose, the earthquake damage estimation for potential severe earthquakes and their aftershocks in a target region is necessary. Predicting ground motions for potentially expected earthquakes is one of the most important subjects in the damage evaluation of buildings and infrastructures. Since a precise model of an earthquake source is necessary for reliable ground motion prediction, accumulating our knowledge of earthquake source properties leads to improve earthquake-damage evaluation.

Understanding the source properties of small-to-moderate earthquakes, not only large earthquakes, is important in earthquake engineering. For example, aftershocks with moderate magnitudes may cause additional damage to a structure suffering the mainshock shaking. Besides, small-to-moderate earthquakes are advantageous for investigating the statistical properties of source parameters, e.g., the joint probability distribution of source parameters, since the number of small-to-moderate earthquakes

is much greater than that of large earthquakes. For example, we can predict the ground motions of a target earthquake by prescribing the source parameters randomly from their joint distribution. Evaluating possible strong ground motions that can cause severe earthquake damage for a target urban area helps evaluate potential earthquake damage and helps plan a post-earthquake recovery strategy for mitigating social loss due to expected earthquake disasters.

Investigating the relationships between the seismic moment or magnitude and source parameters (source parameter scaling laws) is one of the most fundamental subjects in seismology. A precise understanding of the scaling law of source parameters over small to large earthquakes may be helpful for predicting the strong ground motions of a target region where seismic records of a past large earthquake are absent. For example, the scaling law of the average static stress drop (or simply stress drop in this dissertation) has been studied widely. The stress drop is one of the source parameters associated with the strength of earthquake ground motion and is also a fundamental parameter for a deeper understanding of the physics of earthquakes. The independence of stress drop on the magnitude indicates the self-similar scaling under the assumption of a constant rupture speed (Aki, 1967). The stress drops of large earthquakes (e.g.,  $M_w > 6.0$ ) are independent of the magnitude and are 1 to 10 MPa approximately for typical crustal or subduction zone earthquakes (Aki, 1972; Kanamori & Anderson, 1975; Kanamori & Brodsky, 2004; Venkataraman & Kanamori, 2004). In contrast, for small-to-moderate earthquakes, the scaling relation of the stress drops is still controversial, i.e., some studies suggest a magnitude-independent scaling of the stress drop, but some other studies show the increasing stress drop with the magnitude (e.g., Abercrombie, 2021 and references therein). Thus, investigating the source properties of small-to-moderate earthquakes is still an ongoing subject, and accumulating reliable data on the source parameters of small-to-moderate earthquakes is necessary.

Extracting a source effect from seismic records is fundamental for investigating earthquake source properties but is often difficult for small-to-moderate earthquakes. We can interpret a recorded ground motion as a convolution of the source, the path-site effect (e.g., geometrical spreading, scattering attenuation, and site amplification), and the response of the recording instrument. In the frequency domain, a recorded seismic spectrum  $u(f)$  is represented as

$$u(f) = s(f) \cdot g(f) \cdot i(f) \tag{1.1}$$

where  $s(f)$ ,  $g(f)$  and  $i(f)$  represent the source effect, the path-site effect, and the instrumental response, respectively. The instrumental response is a known property. Thus, removing the path-site effect  $g(f)$  from seismic records is a fundamental issue in extracting the source effect  $s(f)$ . The rupture process of large earthquakes is usually investigated by finite-fault inversion using long-period waveforms (e.g., Hartzell & Heaton, 1983). The path-site effect  $g(f)$ , can be obtained using the relatively simple earth model because long-period waveforms do not suffer from small-scale heterogeneity in the earth's interior. However, a simple earth model is usually inadequate for investigating the source properties of small earthquakes. Since short-period waveforms carry information on the source properties of small earthquakes, the wave propagation and site amplification effects need to be evaluated for short-period (or high-frequency) components when analyzing the source properties of small earthquakes. A detailed earth model is required to remove the path-site effects in high-frequency ranges from ground motion records. However, there should be limitations in the resolution of an earth's interior structure model due to our limited observation networks and thus limitations in the approach to analyzing small earthquakes by removing the path-site effect using a detailed earth model considering small-scale heterogeneity.

Taking the ratio of seismic spectral amplitudes (spectral ratio) is a widely used approach to extract the source of small-to-moderate earthquakes (e.g., Abercrombie, 2021). If two earthquakes are in proximity and have similar focal mechanisms, the path-site effects, e.g., attenuation in propagating the earth's interior and site amplification, in the seismic spectra can be similar. In this case, the spectral ratio cancels the path-site effects. Suppose the path-site effects and instrument responses are the same for two earthquakes. Then, the spectral ratio is

$$\frac{u_1(f)}{u_2(f)} = \frac{s_1(f)}{s_2(f)} \cdot \frac{g(f)}{g(f)} \cdot \frac{i(f)}{i(f)} = \frac{s_1(f)}{s_2(f)} \quad (1.2)$$

where subscripts 1 and 2 identify the two earthquakes. An advantage of taking spectral ratio is that is not necessary to model path-site effect. Since it is usually hard to evaluate path-site effect adequately at a high-frequency range, taking spectral ratio is one of the most reliable approaches for extracting the source of small-to-moderate earthquakes (e.g., Abercrombie, 2021; Ide et al., 2003).

The spectral ratio analysis estimates source parameters by fitting model spectral ratios predicted from a source spectrum model to observed spectral ratios. The corner frequency of a source spectral



amplitude is usually estimated by the spectral ratio analysis to calculate the stress drop by assuming a simple source model. The corner-frequency-based stress drop  $\Delta\sigma_{f_c}$  is calculated from the following equation using the corner frequency  $f_c$  (Brune, 1970):

$$\Delta\sigma_{f_c} = \frac{7M_0}{16} \left( \frac{f_c}{k_c V_S} \right)^3 \quad (1.3)$$

where  $M_0$  is the seismic moment, and  $V_S$  is the S-wave velocity. The stress drop is commonly calculated from the corner frequency by assuming a simple source model, a circular source with symmetric rupture propagation. The coefficient  $k_c$  relates the corner frequency to the source radius of a circular crack (Brune, 1970; Dong & Papageorgiou, 2003; Kaneko & Shearer, 2015; Madariaga, 1976; Sato & Hirasawa, 1973). Usually, a constant  $k_c$  is used for all earthquakes of interest to calculate the stress drops. Using the same value of  $k_c$  implies all earthquakes are assumed to have the same source geometry, rupture speed, and location of rupture start point on a rupture plane. The rupture start point on a rupture plane is associated with the directionality of rupture propagation (called rupture directivity in this study). For example, Madariaga (1976) derived the  $k_c$  value from the dynamic simulation of a circular source rupturing symmetrically from the center with a rupture speed of  $0.9V_S$ . The problem is that the source model assumption (i.e., the choice of the  $k_c$  value) considerably affects the stress drop values. For example, the stress drop estimates using the circular source models by Brune (1970) and Madariaga (1976) have a factor of 5.6 difference. Using other source models (the  $k_c$  values) is also possible since there is no exact relationship between the corner frequency and the source radius and no consensus on which source models we should use (Atkinson & Beresnev, 1997; Beresnev, 2001).

The previous studies support that the stress drop needs to be estimated by considering rupture speed, geometry, and directivity. Kaneko & Shearer (2015) performed numerical analysis for circular and elliptical sources assuming various rupture speeds and rupture propagation patterns. Their results show that the  $k_c$  value is significantly affected by the rupture geometry, speed, and directivity. For example, many studies have observed small earthquakes with prominent rupture directivity effects (Abercrombie et al., 2017; Bakun et al., 1978; Boatwright, 2007; Courboux et al., 2013; Fletcher & Boatwright, 2019; Kane et al., 2013; Lengliné & Got, 2011; Yoshida, 2019). This observation implies that the symmetric rupture assumption does not necessarily valid. Wu et al. (2019) observed a complex event with  $M_w = 4.0$  and pointed out the insufficiency of using a simple source model. Variations in rupture

geometry, speed, and directivity may cause significant errors in the stress drop estimation if a constant  $k_c$  is used.

The average static stress drop plays a fundamental role in studying the earthquake energy budget (e.g., Kanamori & Rivera, 2006; Noda et al., 2013). For example, under the assumption of a simple slip-weakening model (i.e., no stress overshoot and undershoot), the stress drop  $\overline{\Delta\sigma}$  involves the sum of radiated energy  $E_R$  and fracture energy  $E_G$  as  $E_R + E_G = 1/2\overline{\Delta\sigma}DS$  ( $D$ : average slip,  $S$ : rupture area) (e.g., Kanamori & Rivera, 2006). The radiated energy is the energy released as seismic waves and is thus seismologically measurable. The fracture energy is the energy involved with the resistance to rupture propagation, e.g., cracking, off-fault plastic deformation, and latent heat due to thermal pressurization or melting. The twice the ratio of the apparent stress  $\sigma_a = \mu E_R/M_0$  ( $E_R$ : radiated energy,  $\mu$ : shear rigidity) to the stress drop  $\overline{\Delta\sigma}$  characterizes the ratio of the radiated energy  $E_R$  and the fracture energy  $E_G$ ,  $E_R/(E_R + E_G) = 2\sigma_a/\overline{\Delta\sigma}$  (e.g., Kanamori & Brodsky, 2004; Kanamori & Rivera, 2006). The ratio  $2\sigma_a/\overline{\Delta\sigma}$  is called the radiation efficiency (e.g., Kanamori & Brodsky, 2004; Venkataraman & Kanamori, 2004). For example, radiation efficiency helps investigate the difference in the rupture characteristics between earthquakes classified into different categories (e.g., small versus large earthquakes or crustal versus subduction zone interplate earthquakes).

The average static stress drop is often calculated from the rupture area  $S$  and the seismic moment  $M_0$ , (Eshelby, 1957; Kanamori & Anderson, 1975).

$$\Delta\sigma_s = \frac{7M_0}{16(S/\pi)^{3/2}} \quad (1.4)$$

The corner-frequency-based stress drop is also calculated from the seismic moment and source area. However, Noda et al. (2013) suggested that the average static stress drop calculated with the seismic moment and the source area is inadequate for investigating the earthquake energy budget. The stress drop calculated with equation (1.4) corresponds to the spatial average of the stress drop weighted by the slip distribution calculated for the circular crack model with a uniform stress drop distribution (Madariaga, 1979; Noda, 2013). We need the stress drop averaged by weighting local stress drops with corresponding local slips for the study of the earthquake energy budget. The average static stress drop weighted by local slips is called the energy-related stress drop  $\Delta\sigma_E$  (Noda et al., 2013):



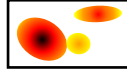
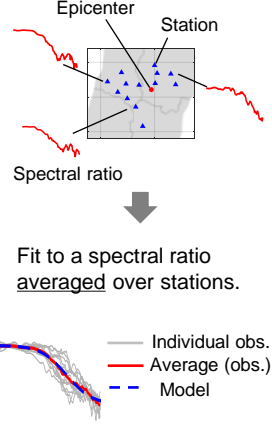
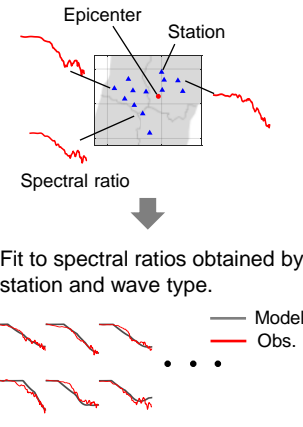
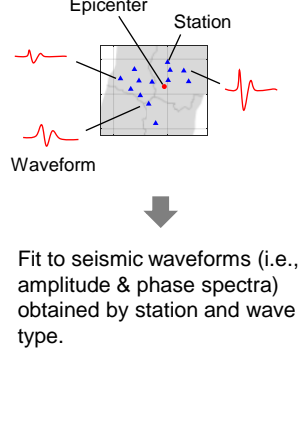
$$\Delta\sigma_E = \frac{\int_{\Sigma} \Delta\sigma_1 \Delta u_1 dS}{\int_{\Sigma} \Delta u_1 dS} \quad (1.5)$$

where  $\Delta\sigma_1$  and  $\Delta u_1$  are local stress drop and slip at each point of the studied fault, and  $\Sigma$  indicates that the integral is taken over the entire fault plane. We usually obtain slip and stress drop distributions by finite fault inversion. Equation (1.5) is a simplified formulation derived by assuming that the components of stress drop and slip in the overall slip direction are dominant (see Noda et al., 2013 for the detail). Noda et al. (2013) showed that the energy-related stress drop  $\Delta\sigma_E$  is always greater than or equal to the moment-based stress drop,  $\Delta\sigma_s = CM_0/S^{3/2}$  ( $C$  is a constant). If a target earthquake has a nearly uniform stress drop,  $\Delta\sigma_s$  can be comparable to  $\Delta\sigma_E$ . Hence, if the stress drop distribution of a target earthquake is relatively uniform, the stress drop calculated with equation (1.4) can be adequate for studying the earthquake energy budget. However, some previous observational studies demonstrate that small-to-moderate earthquakes have heterogeneous distributions of slip and stress drop (e.g., Dreger et al., 2007; Kim et al., 2016).

## 1.2. OBJECTIVE AND OVERVIEW

Developing an earthquake source analysis method for small-to-moderate earthquakes that goes further than the standard corner-frequency-based approach is fruitful. Performing a finite fault inversion for a target earthquake is ideal, but the data are not usually adequate, especially for small-to-moderate earthquakes. The finite fault inversion needs much detailed information about the fault geometry. Also, calculating accurate high-frequency Green's functions for inversion of small earthquakes needs detailed (possibly 3D) local velocity structures. Since extracting a source effect is one of the most critical difficulties in investigating the source properties of small-to-moderate earthquakes, extending the spectral ratio approach would be one appropriate research direction. Specifically, more detailed source properties than the corner frequency need to be obtained from the source term extracted as observed spectral ratios. This study aims to develop a new spectral ratio approach of investigating the source properties of small-to-moderate earthquakes, which does not rely on a simple circular source assumption but is not so complex as finite fault inversion. Besides, this dissertation studies the source parameter scaling relations based on the developed spectral ratio approach.

Simple → Detailed

	Previous spectral ratio approach	This study	Finite fault inversion
Source model	 Uniform stress drop	 Concentrated (uniform) stress drop Heterogeneous stress drop (The single asperity model) Zero stress drops (slips are not zero)	 Heterogeneous stress drop
From seismic records, obtaining	Corner frequency	Rupture size, shape, speed, & rupture start point (of the large-slip asperity area)	Slip distribution (If necessary, rupture speed, size, & shape)
Fitting to	 Epicenter Station Spectral ratio Fit to a spectral ratio <u>averaged</u> over stations. — Individual obs. — Average (obs.) - - - Model	 Epicenter Station Spectral ratio Fit to spectral ratios obtained by station and wave type. — Model — Obs.	 Epicenter Station Waveform Fit to seismic waveforms (i.e., amplitude & phase spectra) obtained by station and wave type.

**Figure 1.1** Descriptions of the differences between this study and previous studies.

This study develops a spectral ratio approach to estimate the stress drop of small-to-moderate earthquakes considering rupture geometry, speed, and directivity firstly (consideration of rupture directivity effect). Then, by applying the developed spectral ratio approach to shallow crustal earthquakes ( $3.2 \leq M_w \leq 6.0$ ) in Japan, it is revealed that the rupture area estimated by the spectral ratio analysis is a localized rupture area with large slip and is not the overall rupture area. When we calculate the stress drop from the seismic moment and source area using equation (1.4), we need to use the total rupture area. Hence, the stress drops calculated from the rupture area estimated by the spectral ratio analysis suffer systematic overestimation. This study proposes a procedure to calculate the stress drop  $\Delta\sigma_s$  by modifying the estimated rupture area to the expected overall rupture area (consideration of source heterogeneity). Then, the revised stress drop estimates,  $\Delta\sigma_s$ , are confirmed to be within a plausible range. The result of this study implies that a source of small-to-moderate earthquakes can be described well as a heterogeneous source model with a localized rupture area with a high average stress

drop. Therefore, a single asperity model, whose stress drop is concentrated on a small area located in the overall rupture area and is zero outside of this area, is assumed to calculate the energy-related stress drop  $\Delta\sigma_E$  (consideration of source heterogeneity).

Figure 1.1 summarizes the difference between the method proposed in this study and other methods (the corner-frequency-based method and finite fault inversion). The single asperity model, introduced in this study, is one of the simplest heterogeneous earthquake source models but is more detailed than a typical circular source with a uniform stress drop. The spectral ratio analysis developed in this study provides the rupture area with large slip of a target earthquake as a rectangular source model, which is interpreted as the localized area of concentrated stress drop in the single asperity model. As a source model becomes complicated, more detailed observational information is expected to be required. Spectral ratios observed by stations are necessary to estimate the rectangular source parameters in the proposed approach, although the corner-frequency-based method requires spectral ratio averaged over stations. Finite fault inversion needs seismic waveforms (i.e., both amplitude and phase spectra) obtained for each station.

There are several expected advantages by developing a new spectral ratio approach. The following are the examples of the benefits or improvements from the accomplishment of this research.

### ***Source Parameter Scaling Relations***

The rupture speed  $V_r$  is a key parameter for understanding the earthquake source scaling law in addition to the average static stress drop  $\overline{\Delta\sigma}$  ( $\Delta\sigma_s$  or  $\Delta\sigma_E$  in this study). The relationship between the seismic moment  $M_0$  and corner frequency  $f_c$  is widely used to study the similarity of earthquakes. For example, a self-similar scaling implies that the seismic moment is inversely proportional to the cube of the corner frequency,  $M_0 \propto f_c^{-3}$  (e.g., Aki, 1967). Some studies observed non-self-similar scalings (e.g., Walter et al., 2006 and references therein). Suppose a non-self-similar scaling relation  $M_0 \propto f_c^{-(3+\varepsilon)}$  holds with  $\varepsilon > 0$ . Kanamori & Rivera (2004) derived the relation:

$$\overline{\Delta\sigma} V_r^3 \propto M_0^{\varepsilon/(\varepsilon+3)} \quad (1.6)$$

An observed relationship between  $M_0$  and  $f_c$  determines the exponent  $\varepsilon$ . Since  $\overline{\Delta\sigma}$  and  $V_r$  must satisfy equation (14) for a prescribed  $\varepsilon$ , they cannot vary independently. Therefore, when we have a non-self-similar scaling relation  $M_0 \propto f_c^{-(3+\varepsilon)}$ , we cannot distinguish at least the following two cases: (1)  $\overline{\Delta\sigma}$  is scale-independent, and  $V_r$  is scale-dependent; (2)  $\overline{\Delta\sigma}$  is scale-dependent, and  $V_r$  is scale-

independent. According to Kanamori & Rivera (2004), the first case indicates that the rupture dynamics between small and large earthquakes are different. On the other hand, the second case indicates that small and large earthquakes are dynamically similar but statically not. To distinguish these two scaling relations, we need to estimate both  $\overline{\Delta\sigma}$  and  $V_r$ .

### ***Earthquake Energy Budget***

The rupture speed is also important for studying the earthquake energy budget. The radiation efficiency derived by the analysis of a simple crack depends on the rupture speed explicitly (e.g., Kanamori & Brodsky, 2004). Thus, rupture speed is essential for evaluating radiation efficiency. Furthermore, the energy-related stress drop  $\Delta\sigma_E$  is necessary for calculating the radiation efficiency and fracture energy. The calculation of  $\Delta\sigma_E$  assuming the single asperity model is simple but beneficial. The proposed stress drop calculation with the single asperity model does not require conducting finite fault inversion. It is usually hard to perform finite fault inversion for small-to-moderate earthquakes.

### ***Earthquake Engineering***

Improving the analysis method of small-to-moderate earthquakes can help develop the physics-based probabilistic seismic hazard assessment (physics-based PSHA). The physics-based PSHA mentioned here predicts the ground motions of a target earthquake by prescribing the source parameters randomly from their joint distribution (Hutchings et al., 2007). The evaluation of the joint distribution is important. For example, Causse & Song (2015) suggested that the rupture speed can be correlated inversely to the stress drop. Since both the stress drop and rupture speed are influential to the strength of high-frequency radiated energy, the joint distribution of the stress drop and rupture speed (and other parameters) is necessary. Small-to-moderate earthquakes are suitable for accumulating data on the source parameters since their number is greater than that of large earthquakes.

## **1.3. ORGANIZATION**

The dissertation comprises six chapters. Chapter 1 introduces the background and aims of this research. Chapters 2 to 5 contain the main contents of the dissertation described above. Chapter 6 summarizes the main findings of the dissertation and future perspectives.

The main topics studied in this dissertation are summarized as follows.

- (1) Developing a new source spectrum model incorporating the effect of the rupture size, shape, speed, and directivity (Chapter 2).
- (2) Incorporating the proposed source spectrum model into a spectral ratio approach and confirming that model spectral ratios fit observed spectral ratios well (Chapter 3).
- (3) Revealing that the estimated rupture area corresponds to a localized area with large slip rather than the total rupture area (Chapter 4).
- (4) Proposing the procedure to calculate the stress drop  $\Delta\sigma_s$  by modifying the estimated rupture area to the expected total rupture area and investigating the stress drop results (e.g., the scaling relation, rupture speed dependence, comparison of  $\Delta\sigma_s$  to  $\Delta\sigma_{fc}$ , and uncertainty assessment) (Chapters 4).
- (5) Introducing the energy-related stress drop  $\Delta\sigma_E$  assuming the single asperity model (Chapter 5).
- (6) Investigating the stress drop, apparent stress, and radiation efficiency (e.g., the scaling relations) (Chapter 5).

Chapter 2 develops a new source spectrum model enabling us to estimate the rupture area, shape (aspect ratio), speed, and directivity (rupture start point) with spectral ratio fitting. Source spectrum model incorporating the effect of the rupture size, shape, speed, and directivity as the source parameters is needed to develop a new spectral ratio approach as this study seeks. Hence, this study derives the mathematical representation of a new source spectrum model from a rectangular kinematic source model with uniform slip distribution. Then, the mathematical representation of the envelope of this source spectrum is proposed. This study calls the source spectrum model the envelope spectrum.

Chapter 3 develops a spectral ratio approach using the envelope spectrum and confirms that model spectral ratios using the envelope spectrum can fit observed spectral ratios well. The effects of rupture geometry, speed, and directivity appear in the difference in spectral ratios for each station or wave type. Hence, the model spectra ratio using the developed source spectrum model is needed to fit observed spectral ratios obtained by station and wave type in order to estimate the source parameters. It is unknown whether the developed spectrum model (the envelope spectra) works well to explain observed spectra. Thus, it is necessary to confirm the effectiveness of the envelope spectra through the application to observed earthquakes. The spectral ratio approach is applied to 409 shallow crustal earthquakes in Japan. The new spectral ratio approach enables us to estimate the rupture length, width, speed, and rupture start point. Then, we can calculate the stress drop directly from the estimated rupture area and the seismic moment. However, this chapter submits an issue that the stress drops calculated from the

estimated rupture area and the seismic moment are more than ten times systematically higher than the typical range suggested by the previous studies of large earthquakes.

Chapter 4 solves the high-stress drop issue submitted in Chapter 3 and revises the stress drop calculation procedure from the estimated rupture area and the seismic moment. This chapter shows the evidence that the estimated rupture area corresponds to a localized area with large slip rather than the total rupture area. This result suggests that a compact rupture area compared to the overall rupture area mainly controls the shape of the seismic spectrum in a broadband frequency range. The cause of this result is the heterogeneous stress drop distribution of natural earthquakes. This chapter proposes a way to calculate the static stress drop  $\Delta\sigma_s$  by modifying the estimated rupture area to the expected total rupture area. Then, the validity of the revised stress drop is confirmed, and the relationships between the stress drop  $\Delta\sigma_s$  and other parameters (e.g., the seismic moment, depth, and rupture speed) are investigated.

Chapter 5 shows the way to relate the stress drop  $\Delta\sigma_s$  obtained in Chapter 4 to the energy-related stress drop  $\Delta\sigma_E$  by assuming the single asperity model. Then, this chapter estimates the radiated energy, radiation efficiency, and fracture energy for the shallow crustal earthquakes studied in Chapters 3 and 4 and reveals the scaling relation of the source parameters (e.g.,  $\sigma_a$ ,  $\Delta\sigma_s$ , and  $\eta_R^E$ ).

## REFERENCES

- Abercrombie, R. E. (2021). Resolution and uncertainties in estimates of earthquake stress drop and energy release. *Philosophical Transactions of the Royal Society A*, **379**, 20200131.
- Abercrombie, R. E., Poli, P., & Bannister, S. (2017). Earthquake directivity, orientation, and stress drop within the subducting plate at the Hikurangi Margin, New Zealand. *Journal of Geophysical Research: Solid Earth*, **122**(12), 10,176–10,188.
- Aki, K. (1967). Scaling Law of Seismic Spectrum. *Journal of Geophysical Research*, **72**(4), 1217-1231.
- Aki, K. (1972). Earthquake mechanism. *Tectonophysics*, **13**, 423–446.
- Atkinson, G. M., & Beresnev, I. (1997). Don't call it stress drop. *Seismological Research Letters*, **68**(1), 3–4.
- Bakun, W. H., Stewart, R. M., & Bufe, C., G. (1978). Directivity in the high-frequency radiation of



- small earthquakes. *Bulletin of the Seismological Society of America*, **68**(5), 1253–1263.
- Beresnev, I. A. (2001). What we can and cannot learn about earthquake sources from the spectra of seismic waves. *Bulletin of the Seismological Society of America*, **91** (2), 397–400.
- Boatwright, J. (2007). The persistence of directivity in small earthquakes, *Bulletin of the Seismological Society of America*, **97**(6), 1850–1861.
- Brune, J. N. (1970). Tectonic stress and the spectra of seismic shear waves from earthquakes, *Journal of Geophysical Research*, **75**(26), 4997–5009.
- Causse, M., & Song, S. G. (2015). Are stress drop and rupture speed of earthquakes independent? Insight from observed ground motion variability. *Geophysical Research Letters*, **42**(18), 7383–7389.
- Courboulex, F., Dujardin, A., Vallee, M., Delouis, B., Sira, C., Deschamps, A., Honore, L., & Thouvenot, F. (2013). High-frequency directivity effect for an  $M_w$  4.1 earthquake, widely felt by the population in southeastern France. *Bulletin of the Seismological Society of America*, **103**(6), 3347–3353.
- Dong, G., & Papageorgiou, A. S. (2003). On a new class of kinematic models: symmetrical and asymmetrical circular and elliptical cracks, *Physics of the Earth and Planetary Interior*, **137**, 129–151.
- Dreger, D., Nadeau, R. M., & Chung, A. (2007). Repeating earthquake finite source models: Strong asperities revealed on the San Andreas Fault. *Geophysical Research Letters*, **34**, L23302.
- Eshelby, J. D. (1957). The determination of the elastic field of an ellipsoidal inclusion, and related problems. *Proceedings of the Royal Society of London*, **241**(1226), 376-396.
- Fletcher, J. B., & Boatwright, J. (2019). Directivity of M 3.1 earthquake near Anza, California and the effect on peak ground motion, *Bulletin of the Seismological Society of America*, **110**(1), 312-318.
- Hartzell, S. H., & Heaton, T. H. (1983). Inversion of strong ground motion and teleseismic waveform data for the fault rupture history of the 1979 Imperial Valley, California, earthquake. *Bulletin of the Seismological Society of America*, **73**(6A), 1553–1583.
- Hutchings, L., Ioannidou, E., Foxall, W., Voulgaris, N., Savy, J., Kalogeras, I., Scognamiglio, L., & Stavrakakis, G. (2007). A physically based strong ground-motion prediction methodology; application to PSHA and the 1999  $M_w = 6.0$  Athens earthquake. *Geophysical Journal International*, **168**(2), 659–680.
- Ide, S., Beroza, G. C., Prejean, S. G., & Ellsworth, W. L. (2003). Apparent break in earthquake scaling

- due to path and site effects on deep borehole recordings. *Journal of Geophysical Research*, **108**(B5), 2271.
- Kanamori, H., & Anderson, D. L. (1975). Theoretical basis of some empirical relations in seismology. *Bulletin of the Seismological Society of America*, **65**(5), 1073–1095.
- Kanamori, H., & Brodsky, E. E. (2004). The physics of earthquakes. Reports on Progress in Physics, **67**(8), 1429–1496.
- Kanamori, H., & Rivera, L. (2004). Static and dynamic scaling relations for earthquakes and their implications for rupture speed and stress drop. *Bulletin of the Seismological Society of America*, **94**(1), 314–319.
- Kanamori, H. & Rivera, L. (2006). Energy partitioning during an earthquake. *Earthquakes: Radiated Energy and the Physics of Faulting* (pp. 3–13), eds Abercrombie, R. McGarr, A. Di Toro, G. & Kanamori, H., American Geophysical Union.
- Kane, D. L., Shearer, P. M., Goertz-Allmann, B. P., & Vernon, F. L. (2013). Rupture directivity of small earthquakes at Parkfield. *Journal of Geophysical Research: Solid Earth*, **118**(1), 212–221.
- Kaneko, Y., & Shearer, P. M. (2015). Variability of source spectra, estimated stress drop, and radiated energy, derived from cohesive-zone models of symmetrical and asymmetrical circular and elliptical ruptures. *Journal of Geophysical Research: Solid Earth*, **120**(2): 1053–1079.
- Kim, A., Dreger, D. S., Taira, T., & Nadeau, R. M. (2016). Changes in repeating earthquake slip behavior following the 2004 Parkfield main shock from waveform empirical Green's functions finite-source inversion. *Journal of Geophysical Research: Solid Earth*, **121**, 1910–1926.
- Lengliné, O., & Got, J. L. (2011). Rupture directivity of microearthquake sequences near Parkfield, California. *Geophysical Research Letters*, **38**, L08310.
- Madariaga, R. (1976). Dynamics of an expanding circular fault. *Bulletin of the Seismological Society of America*, **66**(3), 639–666.
- Madariaga, R. (1979). On the relation between seismic moment and stress drop in the presence of stress and strength heterogeneity. *Journal of Geophysical Research: Solid Earth*, **84**(B5), 2243–2250.
- Noda, H. Lapusta, N. & Kanamori, H. (2013). Comparison of average stress drop measures for ruptures with heterogeneous stress change and implications for earthquake physics. *Geophysical Journal International*, **193**(3). 1691–1712.
- Sato, T., & Hirasawa, T. (1973). Body wave spectra from propagating shear cracks. *Journal of Physics*

*of the Earth*, **21**(4), 415–431.

- Venkataraman, A., & Kanamori, H. (2004). Observational constraints on the fracture energy of subduction zone earthquakes. *Journal of Geophysical Research*, **109**, B05302.
- Walter, W. R., Mayeda, K., Gok, R., & Hofstetter, A. (2006). The scaling of seismic energy with moment: Simple models compared with observations. *Earthquakes: Radiated energy and the physics of faulting* (pp. 25–41), eds. R. E. Abercrombie, A. McGarr, G. D. Toro, & H. Kanamori, American Geophysical Union.
- Wu, Q., Chen, X., & Abercrombie, R. E. (2019). Source complexity of the 2015 Mw 4.0 Guthrie, Oklahoma earthquake. *Geophysical Research Letters*, **46**, 4674–4684.
- Yoshida, K. (2019). Prevalence of asymmetrical rupture in small earthquakes and its effect on the estimation of stress drop: a systematic investigation in inland Japan. *Geoscience Letters*, **6**, 16.

## **Chapter 2**

### **SOURCE SPECTRUM MODEL**

### **CONSIDERING RUPTURE DIRECTIVITY EFFECT**

#### **2.1. OVERVIEW**

This chapter develops a source spectrum model that incorporates rupture size, geometry, speed, and rupture start point. A spectral ratio analysis with this source spectrum model enables us to estimate the rupture size, geometry, speed, and rupture start point (Chapters 3 and 4). Since observed spectral ratios are often smoothed by applying a tapering or stacking technique, a source spectrum model with a smooth spectral shape (i.e., without spectral holes) is useful (e.g., Shimmoto, 2020 and 2022). Besides, the deconvolution by seismic source spectra is generally unstable if there are some spectral holes in its amplitude spectrum (Mueller, 1985). A source spectral amplitude model without spectral holes is needed to make the deconvolution operation stable. One of the most commonly used source spectrum models with a simple smooth spectral shape is the omega-square model by Brune (1970). The omega-square model has succeeded in describing observed earthquake source spectra (e.g., Aki, 1967). However, Brune's spectrum model does not consider the rupture directivity effect. Thus, this chapter proposes a source spectrum model to satisfy the following conditions (Shimmoto et al., 2020): (1) the rupture directivity effect is considered; (2) the shape of the source spectral amplitude is smooth (i.e., without spectral holes); (3) the high-frequency spectral falloff rate is inversely proportional to the square of the frequency as similar to the omega-square model.

## 2.2. KINEMATIC SOURCE MODEL

The kinematic source model with rectangular fault for an isotropic homogeneous whole space was used to model rupture propagation. Haskell (1964) proposed a source model with unilateral rupture propagation. The rupture speed for the width component is seen as infinite in this model. Hirasawa & Stauder (1965) and Mikumo (1971) used the bidirectional rupture propagation model. In this model, the rupture speed can be finite for both fault length and width direction. However, the location of the rupture starting point on the fault plane in the bidirectional model is limited to the edge of the fault plane. The location of the rupture starting point is one of the important parameters for rupture modeling (Miyake et al., 2003; Mai et al. 2005).

Two conditions are considered for the rupture modeling in this study: (1) the rupture speed along both fault length and width directions can be finite, (2) the location of the rupture starting point can be set freely on the fault plane. The bilateral-bidirectional rupture model satisfies both these conditions (Figure 2.1). This type of model has been used by Khattri (1969). In the bilateral-bidirectional rupture model, the fault plane is expressed by fault length  $L$  and width  $W$ . The location of the rupture starting point is set as origin, and the fault plane is constructed by introducing the parameters  $p$  and  $q$  (Figure

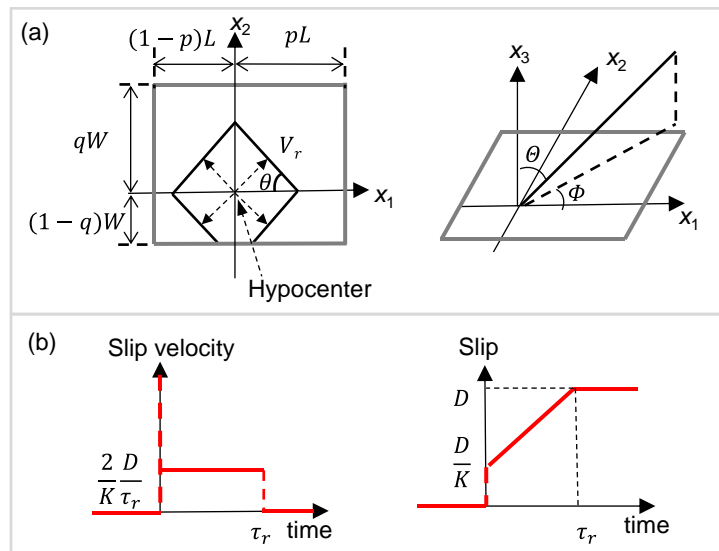


**Figure 2.1** The bilateral–bidirectional fault model and coordinate systems. (a) The bilateral–bidirectional fault model and the coordinate systems used to calculate the source spectrum. A gray solid line shows the fault plane and black solid straight lines show the rupture fronts. The  $x_1$  axis and  $x_2$  axis are set to be parallel to the direction along the strike and up-dip, respectively. The direction of the  $x_3$  axis is set as normal to the fault plane. (b) The slip velocity function and slip function.

2.1a). The uniform velocity of the rupture fronts  $V_r$  and the angle  $\theta$  are introduced to express the rupture propagation (Figure 2.1a).

A boxcar-type slip velocity function characterized by rise time  $\tau_r$  and final dislocation  $D$  is often used. However, when boxcar-type slip velocity is used for a rectangular fault, the source spectral amplitude decays as  $\omega^{-3}$  at high frequency (e.g., Geller, 1976). Thus, the boxcar function combined with the Dirac's delta function  $\delta_D(t)$  is used as the slip function (Figure 2.1b).

$$\dot{D}_1(t) = \frac{D}{K} \delta_D(t) + \frac{K-1}{K} \frac{D}{\tau_r} \{H(t) - H(t - \tau_r)\} \quad (2.1)$$

$H(t)$  is Heaviside's unit step function and  $K$  is related to the amount of slip that is displaced instantaneously. The first term with the delta function is interpreted to be related to the radiation of the high frequency component during the initial phases of the rupture (Heaton & Hartzell, 1989). The slip function is derived as an integration of equation (2.1) (Figure 2.1b).

$$D_1(t) = \begin{cases} 0, & t \leq 0 \\ \frac{D}{K} H(t) + \frac{K-1}{K} \frac{D}{\tau_r} t, & 0 < t \leq \tau_r \\ D, & \tau_r < t \end{cases} \quad (2.2)$$

I considered that it would be useful to determine the value of  $K$  by referring to the specific slip function. In this study, the slip velocity function derived from the dynamic simulation of fault rupture by Day (1982) is used as the reference model with modification. The reference slip velocity is given as

$$\dot{D}_r(t) = \frac{D}{2\sqrt{\tau_r t}} \{H(t) - H(t - \tau_r)\} \quad (2.3)$$

The reference slip function is derived by integration of equation (2-3).

$$D_r(t) = \begin{cases} 0, & t \leq 0 \\ \frac{D}{\sqrt{\tau_r}} \sqrt{t}, & 0 < t \leq \tau_r \\ D, & \tau_r < t \end{cases} \quad (2.4)$$

The value of  $K$  is determined so as to make the values of integration of the two slip functions in equations (2.2) and (2.4) from  $t = 0$  to  $t = \tau_r$  equal. The result is  $K = 3$  (see Appendix A1 for the derivation).

The source spectrum is obtained from the Fourier transform of the source time function.

The source time function is formulated as

$$\Omega(\mathbf{x}, t) = \mu \int_{-(1-q)W}^{qW} \int_{-(1-p)L}^{pL} \dot{D}_1[t - T_v - T_r] d\xi_1 d\xi_2 \quad (2.5)$$

where  $\mu$  is a shear rigidity.  $T_r$  is the time delay due to wave propagation from the rupture point to the

observation station. In the far-field approximation (Aki & Richards, 2002),  $T_r$  is expressed as

$$T_r = \frac{r_h - \xi_1 \sin\theta \cos\Phi - \xi_2 \sin\theta \sin\Phi}{V_c} \quad (2.6)$$

where  $V_c$  is the velocity of wave-type, P or S. The hypocenter distance  $r_h$ , and the angles  $\theta$  and  $\Phi$  are components of the polar coordinates shown in Figure 2.1a.  $T_v$  is the time delay due to rupture propagation from the hypocenter to rupture point.

$$T_v = \frac{|\xi_1| \sin\theta + |\xi_2| \cos\theta}{V_r} \quad (2.7)$$

As a result, the source spectrum  $\Omega(\mathbf{x}, \omega)$  is formulated as equations (2.8) and (2.9).

$$\Omega(\mathbf{x}, \omega) = \exp\left(\frac{i\omega r_h}{c}\right) \cdot M_0 \cdot F_\tau \cdot F_L \cdot F_W \quad (2.8)$$

$$F_\tau = \frac{1}{K} + \frac{K-1}{K} \exp\left(-i\omega \frac{\tau_r}{2}\right) \frac{\sin\left(\frac{\omega\tau_r}{2}\right)}{\frac{\omega\tau_r}{2}} \quad (2.9a)$$

$$F_L = p \exp\left(-i\omega \frac{\tau_{L1}}{2}\right) \frac{\sin\left(\frac{\omega\tau_{L1}}{2}\right)}{\frac{\omega\tau_{L1}}{2}} + (1-p) \exp\left(-i\omega \frac{\tau_{L2}}{2}\right) \frac{\sin\left(\frac{\omega\tau_{L2}}{2}\right)}{\frac{\omega\tau_{L2}}{2}} \quad (2.9b)$$

$$F_W = q \exp\left(-i\omega \frac{\tau_{W1}}{2}\right) \frac{\sin\left(\frac{\omega\tau_{W1}}{2}\right)}{\frac{\omega\tau_{W1}}{2}} + (1-q) \exp\left(-i\omega \frac{\tau_{W2}}{2}\right) \frac{\sin\left(\frac{\omega\tau_{W2}}{2}\right)}{\frac{\omega\tau_{W2}}{2}} \quad (2.9c)$$

$$\tau_{L1} = pL \left( \frac{\sin\theta}{V_r} - \frac{\sin\theta \cos\Phi}{V_c} \right) \quad (2.9d)$$

$$\tau_{L2} = (1-p)L \left( \frac{\sin\theta}{V_r} + \frac{\sin\theta \cos\Phi}{V_c} \right) \quad (2.9e)$$

$$\tau_{W1} = qW \left( \frac{\cos\theta}{V_r} - \frac{\sin\theta \sin\Phi}{V_c} \right) \quad (2.9f)$$

$$\tau_{W2} = (1-q)W \left( \frac{\cos\theta}{V_r} + \frac{\sin\theta \sin\Phi}{V_c} \right) \quad (2.9g)$$

$M_0$  is the seismic moment, which is defined as  $M_0 = \mu LWD$ ,  $\mathbf{x}$  stands for the location of the observation station, and  $i = \sqrt{-1}$ .  $F_\tau$  is the Fourier transformation of the slip velocity.  $F_L$  is interpreted as the frequency domain representation of the one-dimensional bilateral rupture propagation along the fault length with rupture speed of  $V_r/\sin\theta$ .  $\tau_{L1}$  and  $\tau_{L2}$  are the apparent rupture times of the two one-dimensional faults with unilateral rupture propagation in opposite directions to each other, whose fault lengths are  $pL$  and  $(1-p)L$ , respectively. The symbols used for the representation of the source spectrum model are summarized in Table 2.1. The detailed derivation of equation (2.9) can

be found in Appendix A1.

The source spectral amplitude of the proposed spectrum model is required to decay as  $\omega^{-2}$  at high frequency.  $|F_\tau|$  goes to the constant  $1/K$  as  $\omega \rightarrow \infty$ . On the other hand,  $|F_L|$  and  $|F_W|$  are dependent on  $\omega^{-1}$  as  $\omega \rightarrow \infty$ , respectively. Thus, the source spectral amplitude decays proportionally to  $\omega^{-2}$  in the high frequency range in most cases. Note that the source spectral amplitude decays proportionally to  $\omega^{-1}$  in the high frequency range when  $\tau_{L1} = \tau_{L2} = 0$  or  $\tau_{W1} = \tau_{W2} = 0$ .

**Table 2.1.** Description of symbols used in the source spectrum model

Symbol	Description
$\omega$	Angular frequency (rad/s)
$L, W$	Fault length and width
$K$	Amount of instantaneous dislocation, recommendation $K = 3$
$\tau_r$	Rise time of dislocation
$M_0$	Seismic moment, $M_0 = \mu L W D_0$
$V_c$	Velocity of wave type P or S
$V_r/\sin\theta$	Rupture speed along strike direction $0 \leq \theta \leq \pi/2$
$V_r/\cos\theta$	Rupture speed along dip direction
$p, q$	Location of rupture starting point $0 \leq p, q \leq 1$
$r_h$	Hypocenter distance
$\theta, \phi$	The angles in polar coordinate (Figure 1-1)

### 2.3. MODEL OF SEISMIC SOURCE SPECTRAL ENVELOPE

The purpose of approximating the source spectral amplitude by its envelope is to make the deconvolution by the source spectrum stable. Approximating the amplitude spectrum by its envelope is a suitable simplification to extract the features of spectral shape and spectral level. In this chapter, the source spectral amplitude approximated by its envelope is called the envelope spectrum. The envelope spectrum was assumed to have the form of

$$\Omega_E(\mathbf{x}, \omega) = M_0 \cdot F_{E\tau} \cdot F_{EL} \cdot F_{EW} \quad (2.10)$$

where  $F_{E\tau}$ ,  $F_{EL}$ , and  $F_{EW}$  correspond to the envelopes for  $|F_\tau|$ ,  $|F_L|$ , and  $|F_W|$ , respectively. I



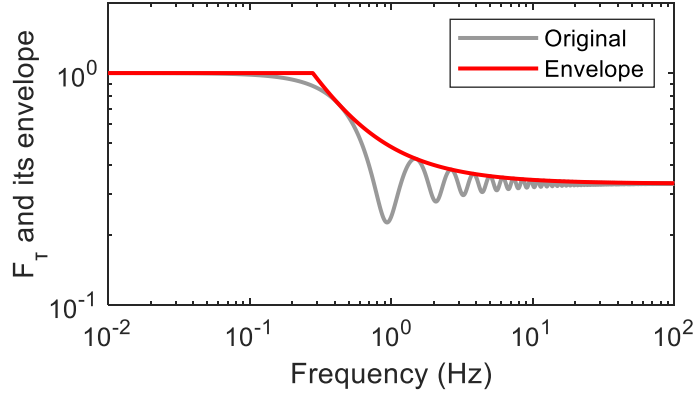


**Figure 2.2** The envelope  $F_{E\tau}$ , and the original spectral amplitude for slip velocity  $|F_\tau|$ .

derived the  $F_{E\tau}$  by referring to the mathematical form of equations (2.9a).

$$F_{E\tau} = \begin{cases} 1, & \omega < \frac{2K}{\tau_r(K+1)} \\ \frac{1}{K} \sqrt{1 + \sqrt{\left(\frac{K-1}{\frac{\omega\tau_r}{2}}\right)^2 + \left(\frac{(K-1)^2}{2\left(\frac{\omega\tau_r}{2}\right)^2}\right)^2} + \frac{(K-1)^2}{2\left(\frac{\omega\tau_r}{2}\right)^2}}, & \frac{2K}{\tau_r(K+1)} \leq \omega \end{cases} \quad (2.11)$$

The detailed derivation of equation (2.11) can be found in Appendix A1.3. I derived the mathematical representation of  $F_{EL}$  by trial and error by referring to the mathematical form of  $|F_L|$ . Specifically, some functions describing the envelope were assumed based on the theoretical solution in equation (2.9) and tested by comparing the envelope predicted from an assumed function to the original spectrum  $|F_L|$  predicted from the theoretical solution. Appendix A1.3 shows the derivation of the mathematical representation of the envelope  $F_{EL}$  for the case that  $\tau_{L1}$  and  $\tau_{L2}$  have positive values. When  $\tau_{L1}$  or  $\tau_{L2}$  has a negative value, it becomes hard to infer the mathematical representation of the envelope  $F_{EL}$ . The mathematical representation of  $F_{EL}$  is shown in equations (2.12). That for  $F_{EW}$  is obtained by replacing  $\tau_{L1}$ ,  $\tau_{L2}$ , and  $p$  with  $\tau_{W1}$ ,  $\tau_{W2}$ , and  $q$ , respectively, in equation (2.12). The derivation was similar to equation (2.11) for equations (2.12a) to (2.12c). Equations (2.12d) to (2.12g), the case that the apparent rupture time becomes minus, were derived by testing some functions.

(i)  $1 \leq \tau_{L1}/\tau_{L2}$

$$F_{EL} = \begin{cases} 1.0, & \omega < \frac{2}{\tau_{L1}} \\ 1 - p + \frac{p}{\omega\tau_{L1}/2}, & \frac{2}{\tau_{L1}} \leq \omega < \frac{2}{\tau_{L2}} \\ \frac{p}{\omega\tau_{L1}/2} + \frac{1-p}{\omega\tau_{L2}/2}, & \frac{2}{\tau_{L2}} \leq \omega \end{cases} \quad (2.12a)$$

(ii)  $0 \leq \tau_{L1}/\tau_{L2} < 1$

$$F_{EL} = \begin{cases} 1.0, & \omega < \frac{2}{\tau_{L2}} \\ p + \frac{1-p}{\omega\tau_{L2}/2}, & \frac{2}{\tau_{L2}} \leq \omega < \frac{2}{\tau_{L1}} \\ \frac{p}{\omega\tau_{L1}/2} + \frac{1-p}{\omega\tau_{L2}/2}, & \frac{2}{\tau_{L1}} \leq \omega \end{cases} \quad (2.12b)$$

(iii)  $\tau_{L1} = \tau_{L2} = 0$

$$F_{EL} = 1.0 \quad (2.12c)$$

(iv)  $-1 \leq \tau_{L1}/\tau_{L2} < 0, \tau_{L1} < 0$

$$F_{EL} = \begin{cases} a_{L1}\omega + 1.0, & \omega < \frac{2}{\tau_{L2}} \\ (1-p)\frac{\exp(\omega\tau_{L1})}{\omega\tau_{L2}/2} + p\frac{\sin(\omega\tau_{L1}/2)}{\omega\tau_{L1}/2}, & \frac{2}{\tau_{L2}} \leq \omega < \frac{-2\sin^{-1}(1)}{\tau_{L1}} \\ -\frac{p}{\omega\tau_{L1}/2} + \frac{1-p}{\omega\tau_{L2}/2}\exp(-2\sin^{-1}(1)), & \frac{-2\sin^{-1}(1)}{\tau_{L1}} \leq \omega \end{cases} \quad (2.12d)$$

$$a_{L1} = \frac{p(\tau_{L2})^2}{2\tau_{L1}} \sin\left(\frac{\tau_{L1}}{\tau_{L2}}\right) + \frac{1-p}{2}\tau_{L2} \exp\left(2\frac{\tau_{L1}}{\tau_{L2}}\right) - \frac{\tau_{L2}}{2}$$

(v)  $\tau_{L1}/\tau_{L2} < -1, \tau_{L1} < 0$

$$F_{EL} = \begin{cases} a_{L2}\omega + 1.0, & \omega < \frac{-2}{\tau_{L1}} \\ (1-p)\frac{\exp(\omega\tau_{L1})}{\omega\tau_{L2}/2} + p\frac{\sin(\omega\tau_{L1}/2)}{\omega\tau_{L1}/2}, & \frac{-2}{\tau_{L1}} \leq \omega < \frac{-2\sin^{-1}(1)}{\tau_{L1}} \\ -\frac{p}{\omega\tau_{L1}/2} + \frac{1-p}{\omega\tau_{L2}/2}\exp(-2\sin^{-1}(1)), & \frac{-2\sin^{-1}(1)}{\tau_{L1}} \leq \omega \end{cases} \quad (2.12e)$$

$$a_{L2} = (1-p)\frac{(\tau_{L1})^2}{2\tau_{L2}}\exp(-2) + \frac{\tau_{L1}}{2}(1-p\sin(1))$$

(vi)  $-1 \leq \tau_{L1}/\tau_{L2} < 0, \tau_{L2} < 0$

$$F_{EL} = \begin{cases} a_{L3}\omega + 1.0, & \omega < \frac{-2}{\tau_{L2}} \\ p\frac{\exp(\omega\tau_{L2})}{\omega\tau_{L1}/2} + (1-p)\frac{\sin(\omega\tau_{L2}/2)}{\omega\tau_{L2}/2}, & \frac{-2}{\tau_{L2}} \leq \omega < \frac{-2\sin^{-1}(1)}{\tau_{L2}} \\ -\frac{1-p}{\omega\tau_{L2}/2} + \frac{p}{\omega\tau_{L1}/2}\exp(-2\sin^{-1}(1)), & \frac{-2\sin^{-1}(1)}{\tau_{L2}} \leq \omega \end{cases} \quad (2.12f)$$

$$a_{L3} = \frac{p(\tau_{L2})^2}{2\tau_{L1}}\exp(-2) + \frac{\tau_{L2}}{2}\{1 - (1-p)\sin(1)\}$$

(vii)  $\tau_{L1}/\tau_{L2} < -1, \tau_{L2} < 0$

$$F_{EL} = \begin{cases} a_{L4}\omega + 1.0, & \omega < \frac{2}{\tau_{L1}} \\ p\frac{\exp(\omega\tau_{L2})}{\omega\tau_{L1}/2} + (1-p)\frac{\sin(\omega\tau_{L2}/2)}{\omega\tau_{L2}/2}, & \frac{2}{\tau_{L1}} \leq \omega < \frac{-2\sin^{-1}(1)}{\tau_{L2}} \\ -\frac{1-p}{\omega\tau_{L2}/2} + \frac{p}{\omega\tau_{L1}/2}\exp(-2\sin^{-1}(1)), & \frac{-2\sin^{-1}(1)}{\tau_{L2}} \leq \omega \end{cases} \quad (2.12g)$$

$$a_{L4} = (1-p)\frac{(\tau_{L1})^2}{2\tau_{L2}}\sin\left(\frac{\tau_{L2}}{\tau_{L1}}\right) + \frac{p}{2}\tau_{L1}\exp\left(2\frac{\tau_{L2}}{\tau_{L1}}\right) - \frac{\tau_{L1}}{2}$$

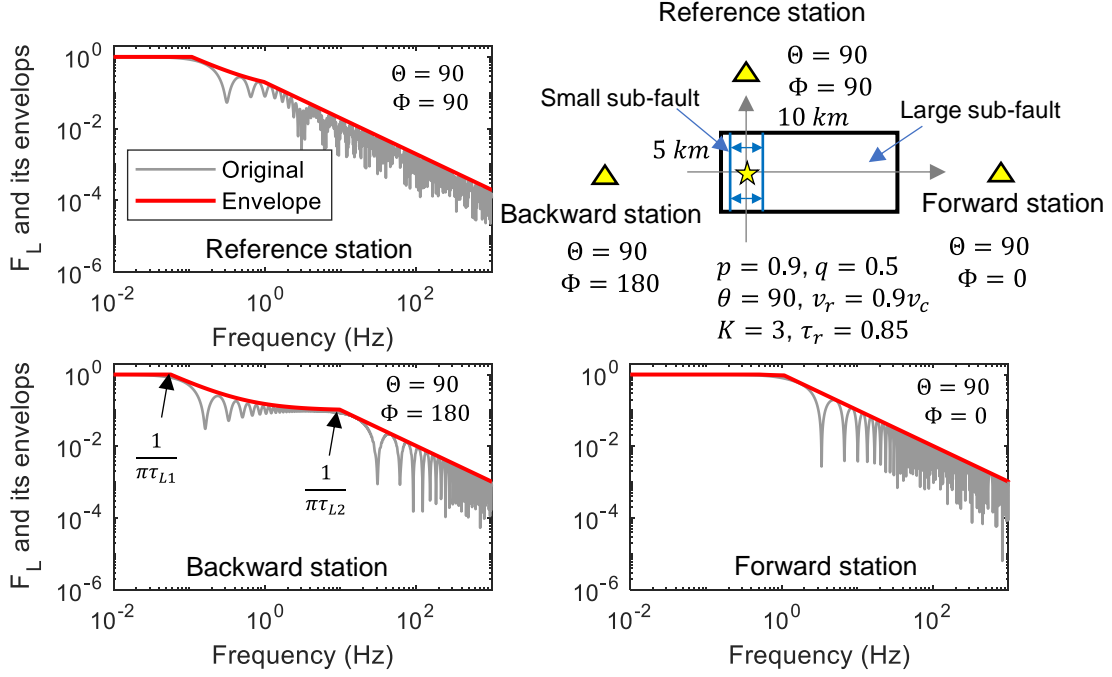
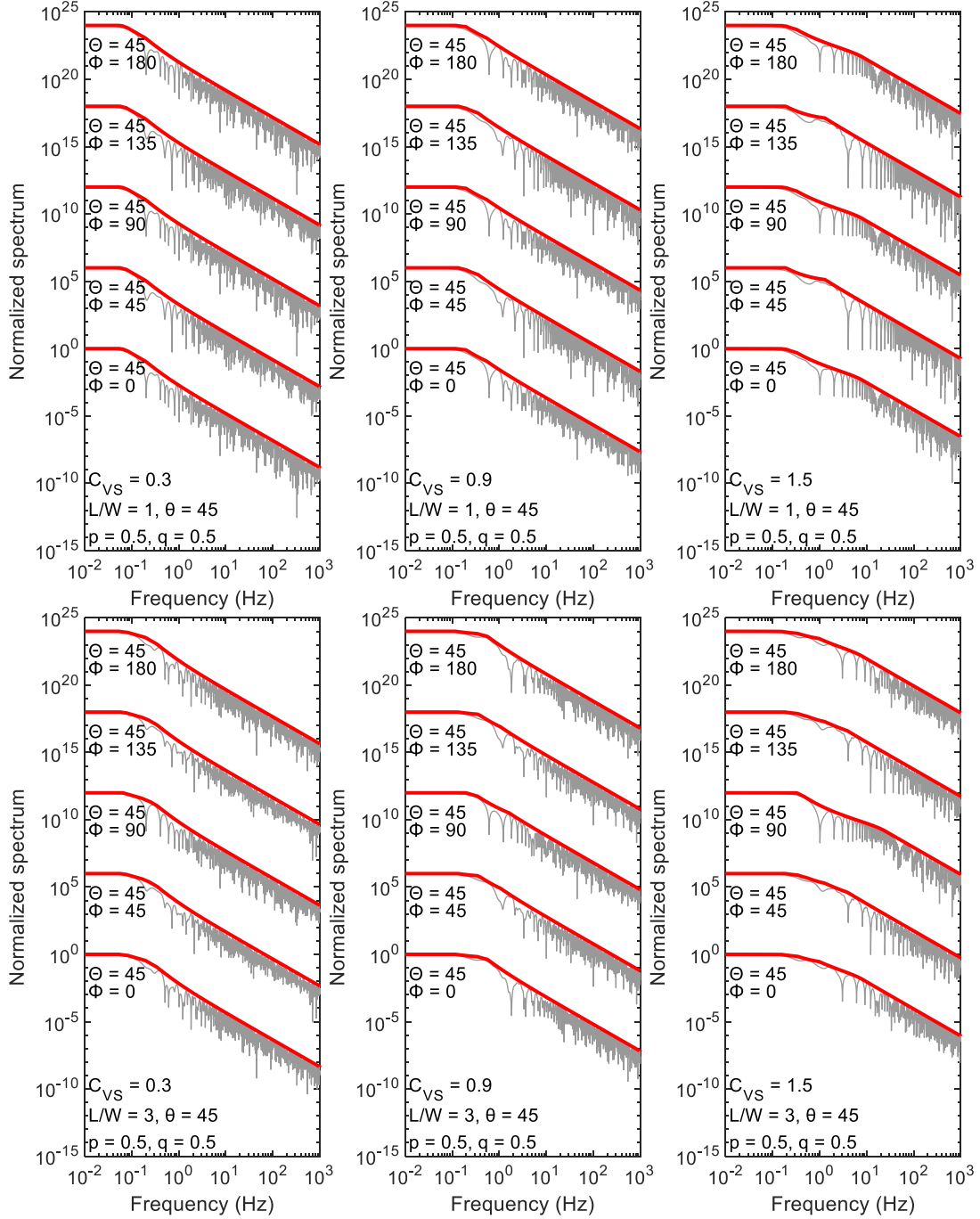


**Figure 2.3** The envelope  $F_{EL}$  (red) and the original spectral amplitude  $|F_L|$  (gray). These spectra were calculated using the source model in the right-top for the three stations (forward, backward, and reference stations). The yellow triangles stand for these stations.

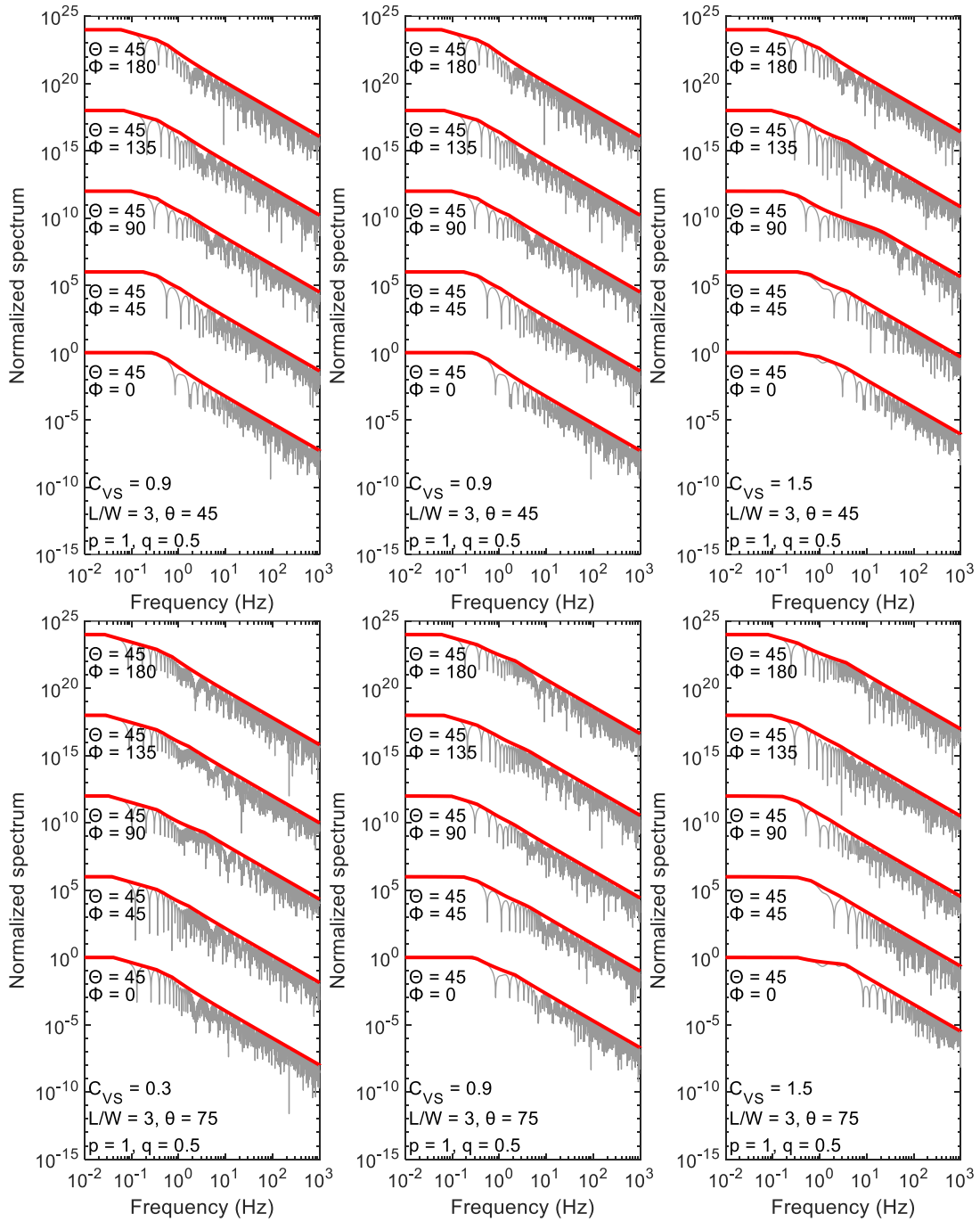
Figure 2.3 compares the original spectrum  $|F_L|$  to its envelope  $F_{EL}$  predicted from equation (2.12). The envelope model  $F_{EL}$  (red) describes the envelope of the original spectrum  $|F_L|$  (gray) adequately. The source spectra were calculated from the source model with bilateral-unidirectional rupture propagation. The bilateral-unidirectional source model consists of two sub-faults (right-top). The source areas of these sub-faults are different (identified as large and small). The spectra  $F_{EL}$  have two corner frequencies defined as  $1/\pi\tau_{L1}$  for the large sub-fault and  $1/\pi\tau_{L2}$  for the small one (Figure 2.3). Three representative stations (forward, backward, and reference) are selected to show the differences in spectral properties due to the rupture directivity effect. Figure 2.3 illustrates the shifts of the two corner frequencies in the three stations due to the rupture directivity effect. In the forward station, the apparent rupture time of the large sub-fault,  $\tau_{L1}$ , becomes shorter, and that of the small sub-fault,  $\tau_{L2}$ , becomes longer. On the other hand, in the backward station, the apparent rupture time of the large sub-fault,  $\tau_{L1}$ , becomes longer, and that of the small sub-fault,  $\tau_{L2}$ , becomes shorter.

Figure 2.4 shows the comparison between the envelope spectra  $\Omega_E(\mathbf{x}, f)$  and the original spectra  $|\Omega(\mathbf{x}, f)|$  calculated from the theoretical solution in equation (2.9). The envelope spectrum is a good

approximation of the envelope of the original source spectral amplitude according to the examples shown in Figure 2.4.



**Figure 2.4a** Comparison of the envelope spectra (red) and the original source spectral amplitudes (gray) for representative cases. The model earthquake has length of 10 km. The rupture speed is  $V_r = \sin\theta C_{VS} V_S$ , where  $V_S$  is the S-wave velocity. P- and S-wave velocities are 5.8 and 3.4 km/s, respectively.  $K = 3$  is used, and  $M_0$  is normalized. The other parameters are described in each panel.



**Figure 2.4b** Description is the same as Figure 2.4a.

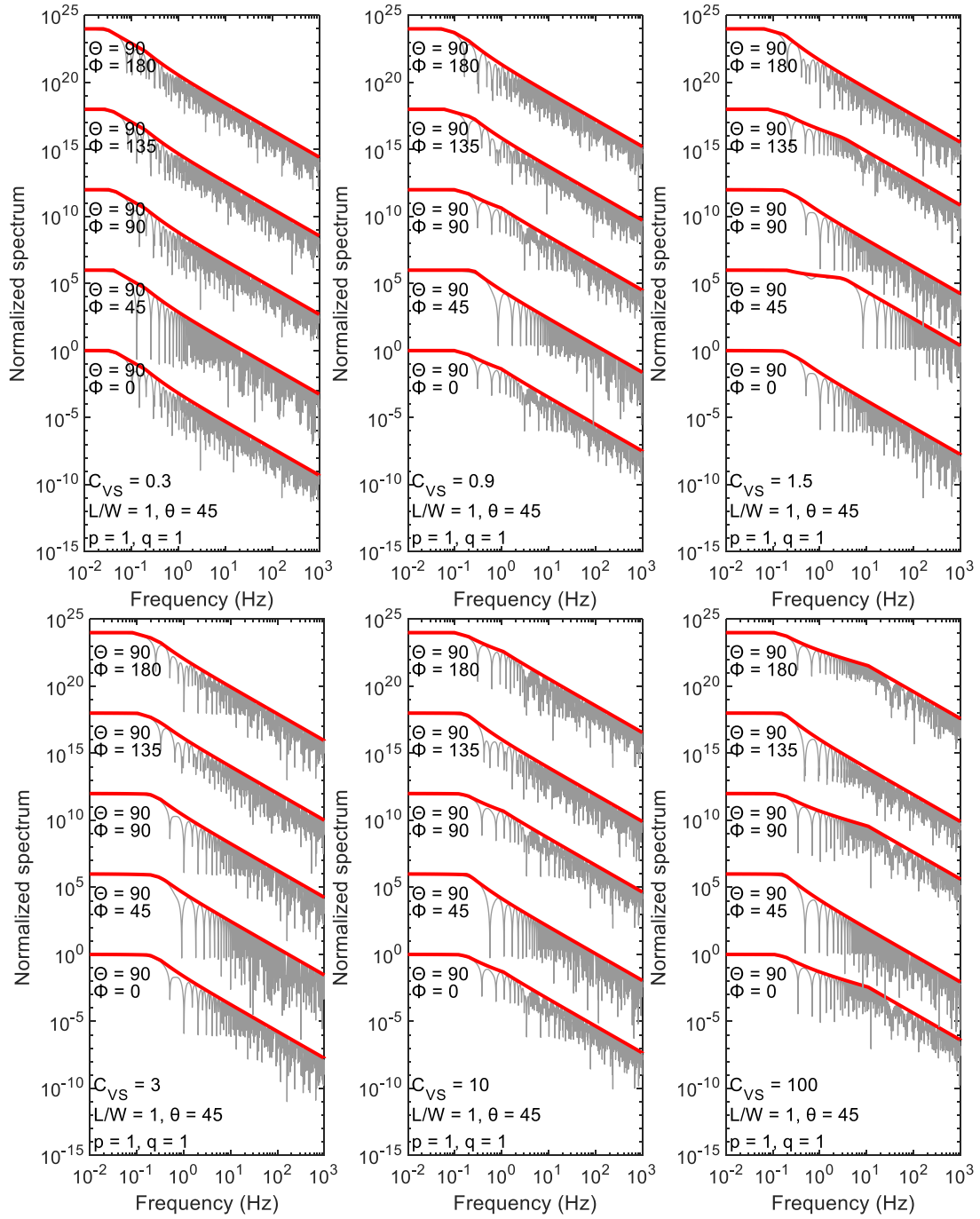


Figure 2.4c Description is the same as Figure 2.4a.

## 2.4. CONCLUSIONS

This chapter developed a source spectrum model (the envelope spectrum) considering the rupture directivity effect. Firstly, the mathematical representation of the source spectrum of the rectangular kinematic source model with bilateral–bidirectional rupture propagation was derived. Then, the equations to approximate the theoretical solution of the source spectral amplitude by its envelope were proposed. This approximation removes the spectral holes from the source spectral amplitude. Finally, it was demonstrated that the envelope spectrum is an adequate approximation of the envelope of the original source spectrum (Figure 2.4). The purpose of developing the envelope spectrum is to enable us to estimate rupture size, geometry, speed, and directivity from the spectral ratio analysis. The previous standard spectral ratio approach estimates corner frequency from observed spectral ratios. Then, the corner frequency is related to the source radius by assuming rupture speed, geometry, and directivity to estimate the stress drop. In contrast, the envelope spectrum enables us to infer the finite source properties of the rectangular source model, i.e., rupture size, shape, speed, and rupture start point, from observed spectral ratios.

## REFERENCES

- Aki, K. (1967). Scaling Law of Seismic Spectrum. *Journal of Geophysical Research*, **72**(4), 1217–1231.
- Aki, K. & Richards, P. G. (2002). *Quantitative Seismology*. Second Ed., University Science Books, Sausalito, California, pages 700.
- Brune, J. N. (1970). Tectonic stress and the spectra of seismic shear waves from earthquakes. *Journal of Geophysical Research*, **75**, 4997–5009.
- Day, S. M. (1982). Three-dimensional finite difference simulation of fault dynamics: rectangular faults with fixed rupture speed. *Bulletin of the Seismological Society of America*, **72**, 705–727.
- Geller, R. J. (1976). Scaling relations for earthquake source parameters and magnitudes. *Bulletin of the Seismological Society of America*, **66**(5), 1501–1523.
- Haskell, N. A. (1964). Total energy and energy spectral density of elastic wave radiation from propagating faults. *Bulletin of the Seismological Society of America*, **54**(6), 1811–1841.



- Heaton, T. H. & Hartzell, S. H. (1989). Estimation of strong ground motions from hypothetical earthquakes on the Cascadia subduction zone, Pacific Northwest. *Pure and Applied Geophysics*, **129**(1-2), 131–201.
- Hirasawa, T. & Stauder, W. (1965). On the seismic body waves from a finite moving source. *Bulletin of the Seismological Society of America*, **55**(2), 237–262.
- Khattri, K. (1969). Determination of earthquake fault plane, fault area, and rupture speed from the spectra of long period P waves and the amplitude of SH waves. *Bulletin of the Seismological Society of America*, **59**(2), 615–630.
- Mai, P. M., Spudich, P. & Boatwright, J. (2005). Hypocenter locations in finite-source rupture models. *Bulletin of the Seismological Society of America*, **95**(3), 965–980.
- Mikumo, T. (1971). Source process of deep and intermediate earthquakes as inferred from long-period P and S waveforms 1. intermediate-depth earthquakes in the southwest Pacific region. *Journal of Physics of the Earth*, **19**, 1–20.
- Miyake, H., Iwata, T., & Irikura, K. (2003). Source characterization for broadband ground-motion simulation: kinematic heterogeneous source model and strong motion generation area. *Bulletin of the Seismological Society of America*, **93**(6), 2531–2545.
- Mueller, C. S. (1985). Source pulse enhancement by deconvolution of an empirical Green's function. *Geophysical Research Letters*, **12**(1), 33–36.
- Shimmoto, S. (2020). An earthquake source spectrum model considering rupture directivity and its application for obtaining Green's functions. *Bulletin of the Seismological Society of America*, **110**(6), 2711–2727.
- Shimmoto, S. (2022). Stress drop estimates for small to moderate earthquakes in Tohoku, Japan considering rupture geometry, speed, and directivity. *Journal of Geophysical Research: Solid Earth*, **127**, e2022JB025157.

## **Chapter 3**

# **SPECTRAL RATIO METHOD**

### **3.1. OVERVIEW**

This chapter develops a spectral ratio approach incorporating the envelope spectrum to estimate the stress drop of small-to-moderate earthquakes considering rupture geometry, speed, and directivity. Spectral ratios are stacked by station and wave type for multiple empirical Green's functions (EGFs), and then, the spectral ratio stacks from all stations are fitted simultaneously to the model spectra to estimate the source parameters (Shimmoto, 2022). We can calculate the stress drop directly from the estimated rupture area. The spectral ratio method is applied to small-to-moderate earthquakes in Japan. It is not obvious whether or not the envelope spectrum (or the rectangular source model) is appropriate to explain observed seismic spectra. Thus, it is confirmed that the model spectral ratio using the envelope spectrum fits observed spectral ratios well. Next, the stress drops are calculated from the estimated rupture areas and the seismic moment. However, despite the success in the spectral ratio fitting, it is shown that the stress drop estimates are systematically more than one order higher than typical stress drop ranges implied from previous studies of large earthquakes (Shimmoto, 2022).

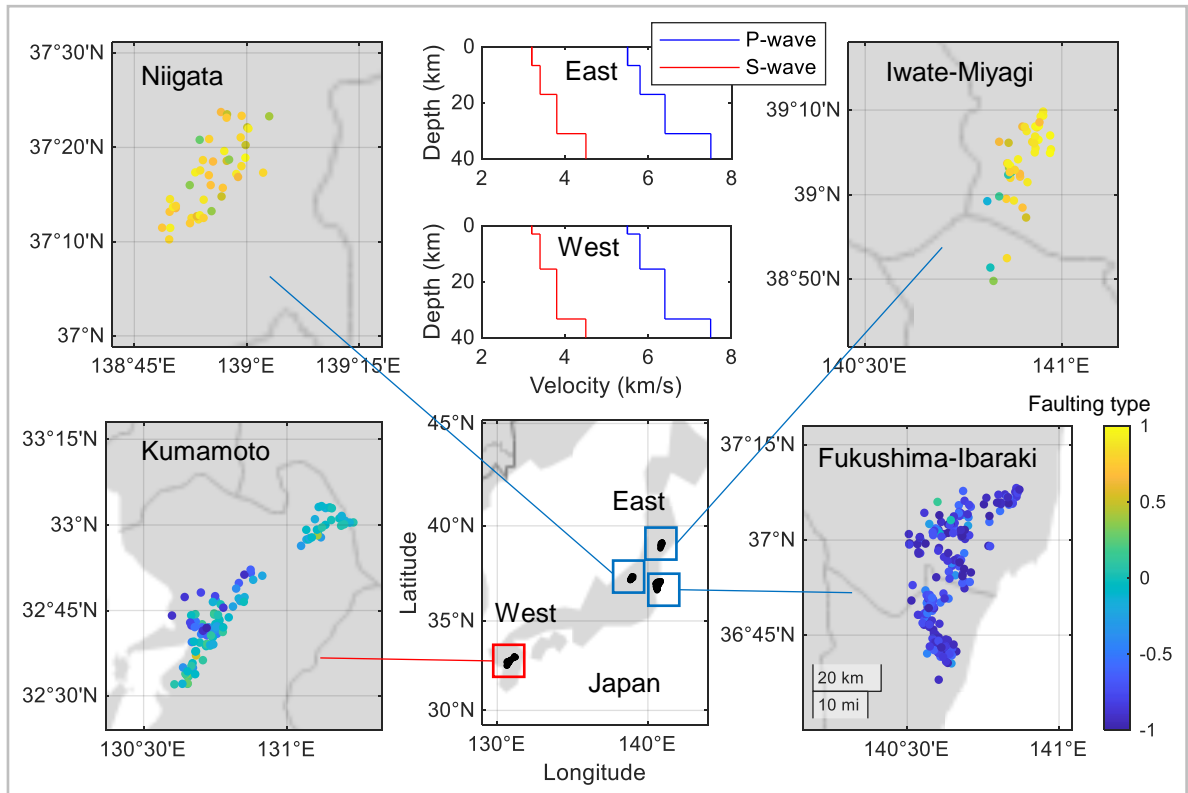


**Figure 3.1.** Epicenters and focal mechanisms of the target earthquakes in the four regions, and 1-D velocity structure models (top-middle) used in this study. The color maps indicate the type of focal mechanism. The value in the color bar ranges from -1.0 for a normal fault (blue) to 1.0 for a reverse fault (yellow) (Shearer et al., 2006).

## 3.2. DATA

This study estimates the stress drops and radiated energies of  $M_w$  3.2 to 6.0 shallow crustal earthquakes in the four regions shown in Figure 3.1 (Niigata, Iwate-Miyagi, Fukushima-Ibaraki, and Kumamoto) in Japan. These earthquakes are recorded by typically 15 to 25 Hi-net stations (NIED 2019a; Okada et al., 2004) at distances of 10 to 100 km. The sampling rate of the Hi-net data is 100 Hz, and three components were used. The seismic moments, fault plane solutions, and hypocenters of these earthquakes are provided by F-net (NIED 2019b) and JMA. The depths of the target earthquakes are less than 20 km. Hi-net stations are deployed in boreholes so data have low noise levels and minimal

site effects which facilitates the spectral analyses in this study. The focal mechanisms of the earthquakes in the four regions cover all faulting types: strike-slip (Kumamoto), normal fault (Fukushima-Ibaraki), and reverse fault (Niigata and Iwate-Miyagi) (Figure 3.1). The seismic phase data provided by JMA was used to extract the P- and S-waves. The 1-D velocity structure model obtained based on Koketsu et al. (2012) was used to calculate take-off angles (Figure 3.1). The spectral ratio analysis results of the earthquakes in the Fukushima-Ibaraki region are from Shimmoto (2022).

### 3.3. METHOD

#### 3.3.1. Spectral Ratio Stacks Using Multiple Empirical Green's Functions

The spectrum of a target event divided by the spectrum of an EGF cancels the path, site, and instrument effect in the resultant spectral ratio, enabling the extraction of the source effect from seismic records. This study stacked spectral ratios for multiple EGFs by station and wave type to improve the stability of the spectral ratios (Abercrombie et al., 2017). The stack represents the geometric mean. The spectral ratio models using the source spectrum model developed in the Chapter 2 (the envelope spectrum) were fit to the observed spectral ratios obtained by station and wave type to estimate the source parameters of a target earthquake.

Both P- and S-waves were used to calculate amplitude spectra. The time window length was determined from

$$t_w = 1.8 \times (10^{-14} \times M_0)^{\frac{1}{3}} \quad (3.1)$$

where  $M_0$  is the seismic moment of a target event. The time window length by equation (3.1) is approximately eight times the source duration (Kanamori & Brodsky, 2004). If an extracted P-wave contains the S-wave, I did not use the P-wave. Pre-event noise spectra were obtained with the same time window length to calculate signal-to-noise ratio (SNR). The amplitude spectra were smoothed using a multi-taper method (Thomson, 1982; Park et al., 1987).

Small earthquakes were selected from the vicinity of target earthquakes to search for suitable EGFs. The JMA magnitudes of small earthquakes were 0.7 to 2.0 units smaller than the target events. The

unified earthquake catalog by JMA provides the hypocenter location and JMA magnitude of small earthquakes. The differences in the epicentral distance between the target earthquakes and EGF events were within 4 km for earthquakes with  $M_w$  less than 4.0, within 6 km for earthquakes with  $M_w$  4.0 to 5.0, and within 12 km for earthquakes with  $M_w$  larger than 5.0. The depth differences between the target earthquakes and EGF events were within 2 km for earthquakes with  $M_w$  less than 4.0, within 3 km for earthquakes with  $M_w$  4.0 to 5.0, and within 6 km for earthquakes with  $M_w$  larger than 5.0. I did not set strict distance criteria since this spectral ratio analysis only uses amplitude spectra (e.g., Ross & Ben-Zion, 2016).

After selecting small earthquakes based on the location criteria, I calculated spectral ratios and selected suitable ones for stacking. I applied three criteria: (1) signal-to-noise ratio (SNR), (2) variance reduction (e.g., Uchide & Imanishi, 2016), and (3) low- and high-frequency amplitude ratio (Abercrombie, 2014; Abercrombie et al., 2017). These criteria contribute to removing spectral ratios with irregular shapes or bumps. The SNRs were calculated for every frequency point within the target frequency range. Their minimum was required to be at least 3.0 (e.g., Abercrombie et al., 2017; Ross & Ben-Zion, 2016; Viegas et al., 2010). I fitted spectral ratio calculated from the omega-square model (Aki, 1967; Brune, 1970; Boatwright, 1980) to an observed spectral ratio to evaluate the variance reduction and the amplitude ratio at low- and high-frequency in the best-fit spectral ratio model. The spectral ratio using the omega-square model is

$$SR_{\omega 2} = C \left\{ \frac{1 + \left(\frac{f}{f_{c2}}\right)^{n\gamma}}{1 + \left(\frac{f}{f_{c1}}\right)^{n\gamma}} \right\}^{\frac{1}{\gamma}} \quad (3.2)$$

where  $n$  describes the high-frequency falloff rate and was assumed as,  $n = 2$  (e.g., Abercrombie et al., 2017). When  $n = 2$ ,  $\gamma = 1$  corresponds to the model by Brune (1970), and  $\gamma = 2$  corresponds to the model by Boatwright (1980). The omega-square model with a higher  $\gamma$  value has a sharper spectral corner. The range of  $\gamma$  was assumed as,  $1 \leq \gamma \leq 2$ . The constant  $C$  is the ratio of the seismic moments of a target and small earthquake. The variance reduction is defined as

$$VR_{egf} = \left( 1 - \frac{F_{res\omega 2}}{\sum_{i=1}^{N_f} (\log_{10} SR_{obs}(f_i) - E[\log_{10} SR_{obs}(f)])^2} \right) \times 100 \quad (3.3)$$

$$F_{res\omega_2} = \sum_{i=1}^{N_f} \left( \log_{10} SR_{obs}(f_i) - \log_{10} SR_{\omega_2}(f_i) \right)^2 \quad (3.4)$$

where  $N_f$  is the number of frequency components,  $SR_{obs}(f_i)$  is the observed spectral ratio, and  $E[\log_{10} SR_{obs}(f)]$  is the expected value of  $\log_{10} SR_{obs}(f)$ . The spectral ratios with a variance reduction of more than 90% were only stacked. Additionally, I removed spectral ratios with the ratio of the spectral levels at low- and high-frequency in the fit of the omega-square model being smaller than 2 (Abercrombie, 2014). I applied the three criteria in the previous paragraph to a spectral ratio for a target and EGF pair and stacked it if all the three criteria were satisfied. These criteria were examined for each of the three components (NS, EW, and UD) for each EGF event by station and wave type, and only the components that satisfy the three criteria were used for stacking. After selecting spectral ratios satisfying the three criteria, the spectral ratios were stacked by station and wave type. Then, the stacked spectral ratios were normalized so that their low-frequency spectral level equals 1.0. A stacked spectral ratio for P- or S-wave at a station is only used in the spectral ratio fitting if the number of spectral ratios in the stack is 8 or more. Figure 3.2 illustrates the example of the spectral ratio stacking.

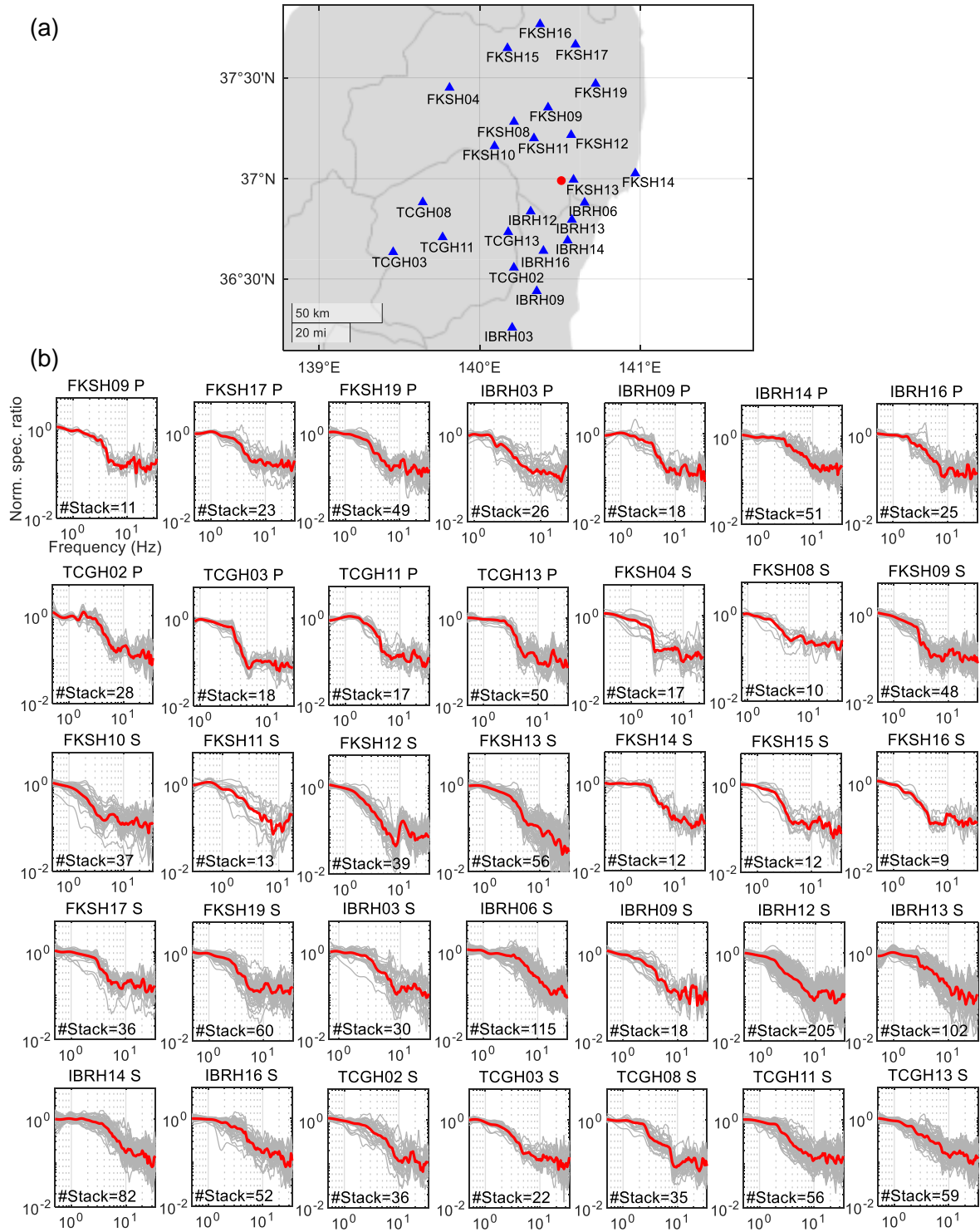


**Figure 3.2.** An example of the stacked spectral ratio for the  $M_w$  3.8 event that occurred on July 4th, 2011, in the Fukushima-Ibaraki region. (a) The stations (blue triangles) and the epicenter (red dot). (b) The normalized stacked spectral ratios (red curves) and the individual spectral ratios used for the stacking (gray curves) with the number of stacks. The title on each panel shows the station name and wave type.

### 3.3.2. Spectral Ratio Model

The model spectra were simultaneously fit to all the normalized stacked spectral ratios  $SR_{obs}^c(\mathbf{x}_j, f_i)$  to estimate the source parameters by minimizing the following residual:

$$F_{res} = \sum_{i,j,c} \left( \log_{10} SR_{obs}^c(\mathbf{x}_j, f_i) - \log_{10} SR_E^c(\mathbf{x}_j, f_i) \right)^2 \quad (3.5)$$

where the indices  $c$ ,  $j$ , and  $i$  represent the wave type, station, and frequency components, respectively.  $SR_E^c(\mathbf{x}_j, f_i)$  is

$$SR_E^c(\mathbf{x}, f) = \frac{\Omega_{EN}(\mathbf{x}, f)}{\Omega_{\omega^2}(\mathbf{x}, f)} \quad (3.6)$$

where  $\Omega_{EN}(\mathbf{x}, f)$  is the (normalized) envelope spectrum, and  $\Omega_{\omega^2}(\mathbf{x}, f)$  is the omega-square spectrum.

$$\Omega_{\omega^2}(\mathbf{x}, f) = \frac{1}{\left\{ 1 + \left( \frac{f}{f_{c2}} \right)^{2\gamma} \right\}^{\frac{1}{\gamma}}} \quad (3.7)$$

The rectangular source model developed in the Chapter 2 enables us to estimate source spectra at all stations for both P- and S-waves (Shimmoto, 2020). The envelope of the source spectrum model is described as  $\Omega_E(\mathbf{x}, f)$ , equation (2.10):

$$\Omega_E(\mathbf{x}, f) = M_0 F_E(\mathbf{x}, f | L, W, p, q, V_r, \theta, \Theta, \Phi, V_c, \tau_r) \quad (3.8)$$

where  $f$  is the frequency, and  $\mathbf{x}$  is the vector to indicate the location of an observation station, and  $M_0$  is the seismic moment. The details of the parameters can be found in Figure 3.3. The polar coordinates,  $\Theta$  and  $\Phi$ , can be obtained from dip  $\delta$ , strike  $\varphi_s$ , azimuth  $\psi_{az}$ , take-off angle  $\psi_{tf}$ , and the rupture orientation angle  $\Lambda$  (Figures 3.3a and 3.3b). The relationships between the polar coordinates and these angles are summarized in the following equations.

$$\begin{bmatrix} \sin\theta \cos\Phi' \\ \sin\theta \sin\Phi' \\ \cos\theta \end{bmatrix} = \begin{bmatrix} \cos\varphi_s & \sin\varphi_s & 0 \\ \cos\delta \sin\varphi_s & -\cos\delta \cos\varphi_s & -\sin\delta \\ -\sin\delta \sin\varphi_s & \sin\delta \cos\varphi_s & -\cos\delta \end{bmatrix} \begin{bmatrix} \sin\psi_{tf} \cos\psi_{az} \\ \sin\psi_{tf} \sin\psi_{az} \\ \cos\psi_{tf} \end{bmatrix} \quad (3.9)$$

$$\Phi = \Phi' - \Lambda \quad (3.10)$$



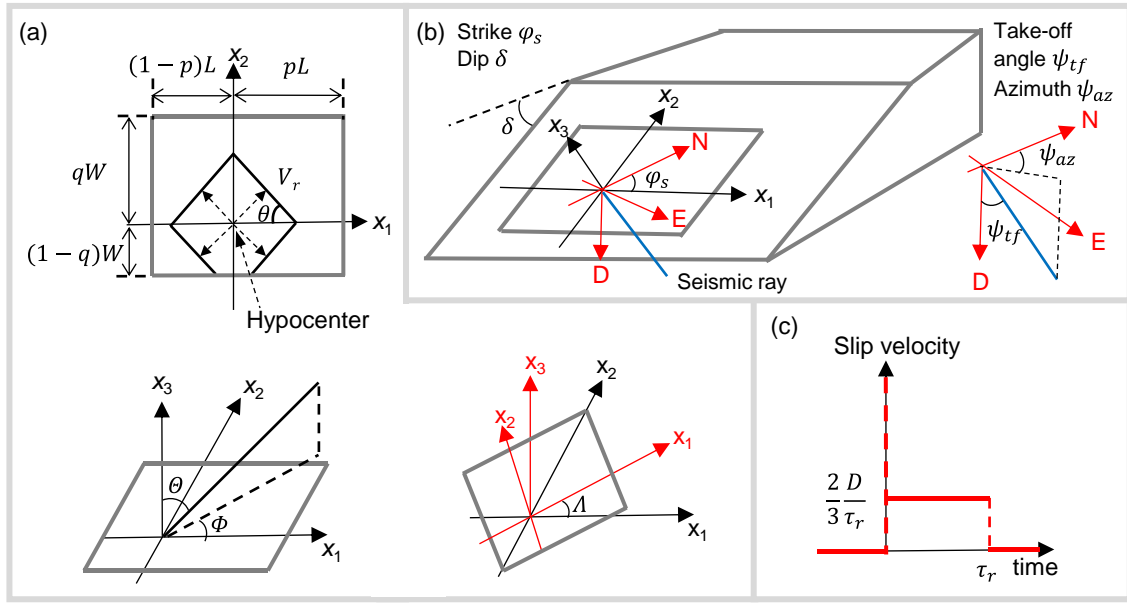


**Figure 3.3.** Description of the source and source spectrum model. (a) Rectangular fault with bilateral–bidirectional rupture propagation. The axes  $x_1$  and  $x_2$  (black arrows) are parallel to the strike and dip direction, respectively. The positive direction of axis  $x_2$  is the up-dip direction. The axis  $x_3$  is normal to the fault plane. The angle  $\Lambda$  designates the orientation of the rectangular source on the fault plane. The coordinate system is rotated  $\Lambda$  degree counter-clockwise around  $x_3$  (coordinate system colored with red). (b) Geometrical configuration of the fault plane (dip and strike), the fault coordinate system, the take-off angle, and azimuth. (c) Slip velocity function.

The take-off angle was obtained using the 1-D velocity structure model. The envelope is normalized so that its low-frequency asymptote would equal one.

$$\Omega_{EN}(\mathbf{x}, f) = \frac{\Omega_E(\mathbf{x}, f)}{M_0} = F_E \quad (3.11)$$

This normalized envelope,  $\Omega_{EN}(\mathbf{x}, f)$ , is called the envelope spectrum in the following studies. The value of  $\theta$  in the bilateral–bidirectional source model (Figure 3.3a) was assumed as 45 degrees, which indicates that the rupture propagates with a square rupture front. The square rupture front was selected because it is analogous to the circular rupture front used in finite fault inversion frequently. The rise time was calculated using the following equation (Geller, 1976):

$$\tau_r = \frac{16\sqrt{LW}}{7\pi^{3/2}V_s} \quad (3.12)$$

where  $V_S$  is the S-wave velocity at a depth of the hypocenter. The rupture speed was controlled by the ratio of the maximum rupture speed  $V_{rmax} = \sqrt{2}V_r$  to the S-wave velocity  $V_S$ , which is  $C_{VS} = V_{rmax}/V_S$ .

### 3.3.3. Comparison of Model Spectral Ratio with Observed Data

We need to determine the corner frequency  $f_{c2}$  and the sharpness of spectral corner  $\gamma$  of the spectral model given in equation (3.7) for each station and wave type. The estimate of the source parameters of the target earthquake becomes unstable unless we restrict the parameters  $\gamma$  and  $f_{c2}$ . Therefore, I limited the range of  $f_{c2}$  and  $\gamma$  values using the spectral ratio model of equation (3.2) before searching for the minimum residual of equation (3.5). The observed spectral ratios were normalized (Figure 3.4a), and hence, I set  $C = 1.0$  in equation (3.2). To constrain the range, I first determine  $\gamma$  values by fitting the spectral ratio (Figure 3.4b) to equation (3.2). I used these determined  $\gamma$  values as the fixed values when searching the minimum residual of equation (3.5). Then, the constrained range for  $f_{c2}$  was determined using the criterion of Viegas et al. (2010), where the values of  $f_{c2}$  with normalized residuals less than 1.05 were used (Figure 3.4c). The residuals were obtained for each prescribed  $f_{c2}$  and normalized by the minimum residual.

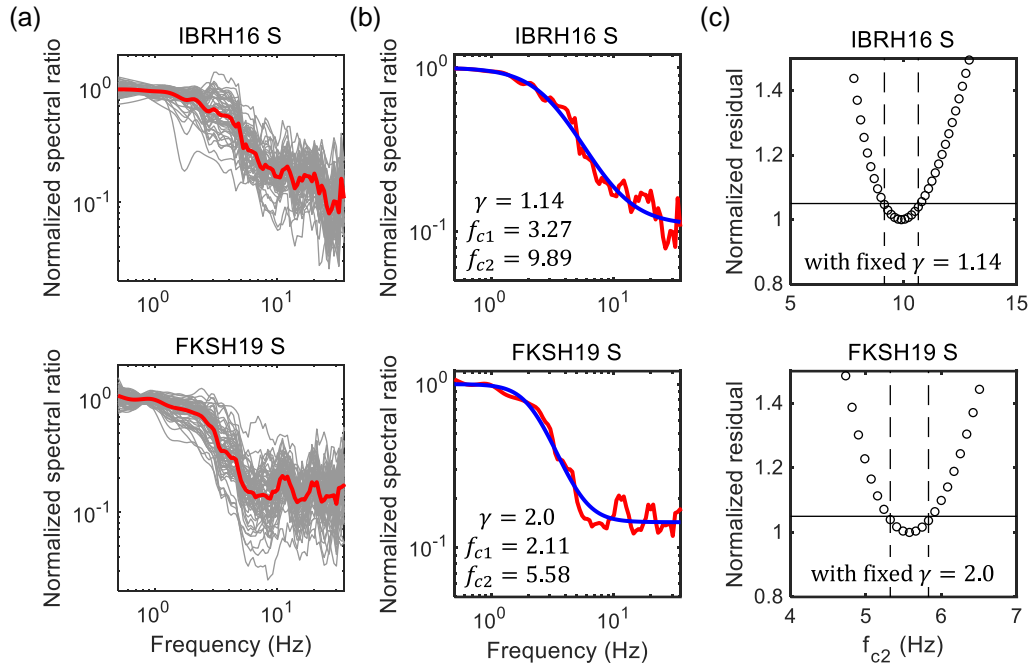


**Figure 3.4.** Examples of the preliminary fitting of spectral ratios with the omega-square model to determine the range of tested  $f_{c2}$  values. The results of the two S-wave spectral ratios for the different stations are shown. (a) Examples of stacking of spectral ratios. The red curves are the stacked spectral ratios and gray curves are individual spectral ratios used for stacking. (b) Comparison of the observed spectral ratios (red) with the optimal spectral ratio models (blue). (c) Example of determining the constraint range (vertical dotted lines) for  $f_{c2}$ . The horizontal black line shows the normalized residual of 1.05.

The parameters to be estimated are the rupture length  $L$ , aspect ratio  $AR(=L/W)$ , rupture speed  $C_{VS} = V_{rmax}/V_S$ , rupture start point ( $p$  and  $q$ ), fault plane (strike and dip), rupture orientation angle  $\Lambda$ , and corner frequencies  $f_{c2}$ . I conducted a grid search to minimize the residual  $F_{res}$ , equation (3.5), to determine the source parameters of a target earthquakes. Since we usually cannot avoid the parameter trade-off issues, one better approach is to limit the source parameters in advance so that they can only have the values within a physically reasonable range. It is difficult to estimate the rupture start point or source dimension simultaneously with rupture speed by the optimization due to the trade-off. Hence, I controlled  $C_{VS}$  by prescribing realistic values in the grid search. The  $C_{VS}$  was tested from 0.6 to 0.9 with an interval of 0.05 (e.g., Venkataraman & Kanamori, 2004). This study also prescribed the aspect ratios in the grid search to avoid obtaining an unrealistically narrow rupture area. The aspect ratios tested in the grid search were 1/3, 1/2, 1, 2, and 3.

The grid search estimated the optimal parameters ( $L$ ,  $p$ ,  $q$ , and corner frequencies  $f_{c2}$ ) for each combination of the prescribed rupture speed, aspect ratio, rupture orientation, strike, and dip under the constraints of  $f_{c2}$ . I used the strike and dip angles obtained for each earthquake's two possible fault planes indicated by their focal mechanism provided by F-net. The rupture orientation angles  $\Lambda$  of 0 and 45 degrees were tested since the square rupture front has the minimum rupture speed in the direction of 45 degrees oriented from that of the maximum rupture speed. The source parameters ( $L$ ,  $p$ ,  $q$ , and  $f_{c2}$ ) and residual ( $F_{res}$ ) were obtained for each combination of  $C_{VS}$ ,  $AR$ ,  $\Lambda$ ,  $\varphi_s$ , and  $\delta$ . I evaluated the model-dependent uncertainty of the stress drop estimates by calculating the stress drops from the source parameter sets whose residual ( $F_{res}$ ) is less than 1.05 times the minimum residual. The stress drop calculation is described in the following sections. In this study, the criterion that residuals ( $F_{res}$ ) are less than 1.05 times the minimum residual is called the minimum residual criterion. Figure 3.5 summarizes the source parameter estimation procedure.



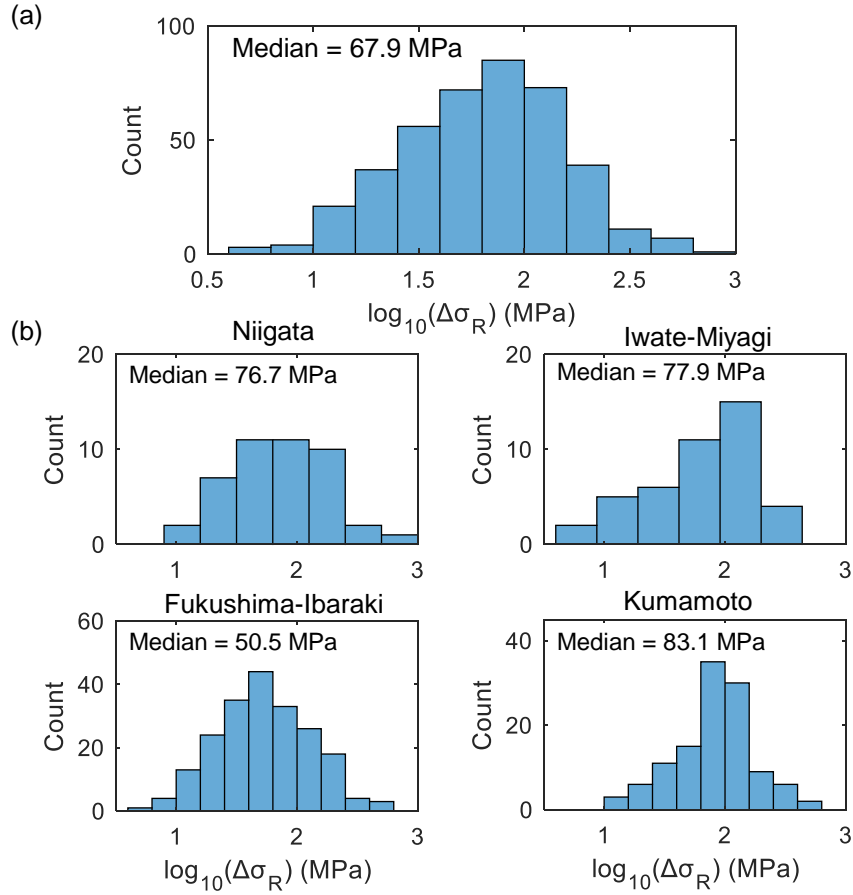


**Figure 3.6** Histograms of the stress drop  $\Delta\sigma_R$ . (a) Histogram of the stress drop  $\Delta\sigma_R$  for all events in the four target regions. (b) Histograms of the stress drops  $\Delta\sigma_R$  for each of the target regions.

### 3.4. RESULTS

This study provides the stress drop estimates for the 409 earthquakes. The stress drop  $\Delta\sigma_R$  was calculated from estimated rupture area  $LW$  by the following equation (Eshelby, 1957; Keilis-Borok, 1959).

$$\Delta\sigma_R = \frac{7M_0}{16(LW/\pi)^{3/2}} \quad (3.13)$$

The stress drops  $\Delta\sigma_R$  are in the range of 4.5 to 724 MPa with a median of 67.9 MPa (Figure 3.6a). The 89% of the stress drop estimates are within 10 to 200 MPa. Figure 3.6b shows the histogram of the stress drop  $\Delta\sigma_R$  for each of the target regions.

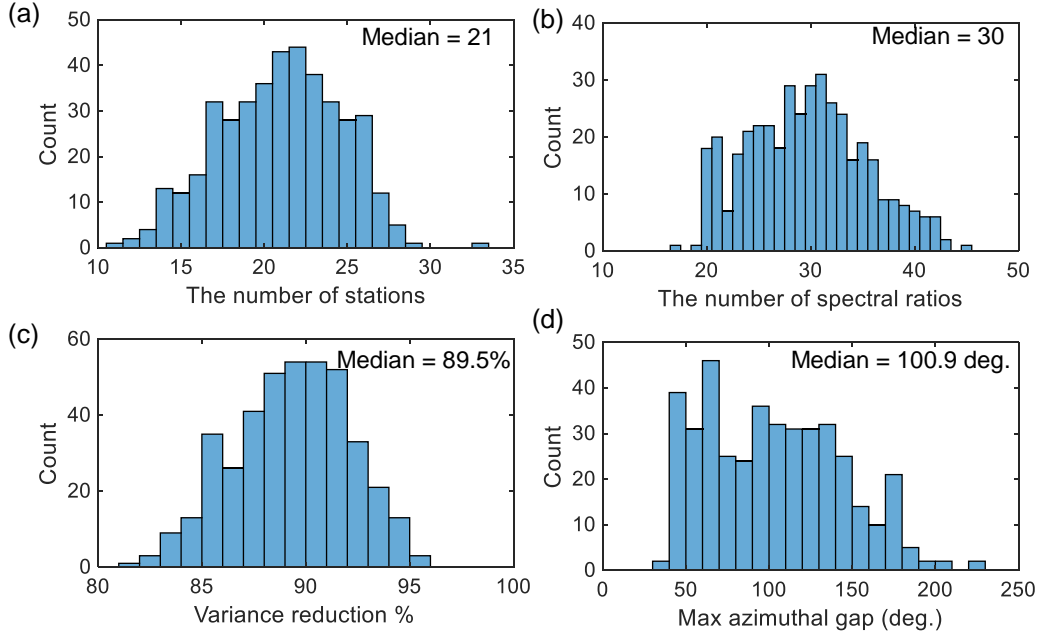


**Figure 3.7.** Histograms to summarize the results of the spectral ratio analysis: (a) The number of stations. (b) Number of stations used in the spectral ratio analysis. (c) Variance reduction. (d) Maximum azimuthal gaps.

To evaluate the accuracy of the spectral ratio fitting, I calculated the variance reduction defined as

$$VR_{env} = \left( 1 - \frac{F_{res}}{\sum_{i,j,c} (\log_{10} SR_{obs}^c(\mathbf{x}_j, f_i) - \overline{SR})^2} \right) \times 100 \quad (3.14)$$

where  $F_{res}$  is the residual in equation (3.5), and  $\overline{SR}$  is the average value for all components of the log spectral ratios,  $\log_{10} SR_{obs}^c(\mathbf{x}_j, f_i)$ . The 409 earthquakes have variance reductions of more than 80% (Figure 3.7a). Figure 3.7 also shows the number of stations (Figure 3.7b), the number of spectral ratios (Figure 3.7c), and maximum azimuthal gaps (Figure 3.7d). The spectral ratio fitting was conducted using events with a sufficient number of stations and spectral ratios with a broadband frequency range.

Table 3.1 and Figure 3.8 show a representative result of the spectral ratio analysis for an  $M_w$  3.8 event, whose source parameters, especially for rupture orientation angle and fault plane ambiguity, were well resolved. Figure 3.8a shows the stations used in the spectral ratio fitting and the best-fit rupture model. Figure 3.8 compares the envelope spectra,  $\Omega_{EN}(\mathbf{x}, f) = SR_E^c(\mathbf{x}, f) \times \Omega_{\omega_2}(\mathbf{x}, f)$ , with the synthesized source spectra,  $SR_{obs}^c(\mathbf{x}, f) \times \Omega_{\omega_2}(\mathbf{x}, f)$ , and shows the details of the spectrum shape for both the model and data. The model envelope spectra (gray curves) agree with the observed source

spectra (red curves) in the broadband frequency range (Figure 3.8). The variance reduction for the representative event is 91.4%. Appendix A2 provides additional representative results of the spectral ratio fitting. Table 3.1 shows the ensemble of the estimated source parameters whose residuals are less than 1.05 times the minimum residual, i.e., satisfying the minimum residual criterion. The source parameter ensemble was used to evaluate the uncertainty of the stress drop estimates.

**Table 3.1.** The ensemble of the estimated source parameters whose residuals are less than 1.05 times the minimum residual for the  $M_w$  3.8 event shown in Figure 3.7, i.e., satisfying the minimum residual criterion.

Residual	$L$ (m)	$W$ (m)	$AR$	$p$	$q$	$C_{vs}$	$A$ (deg.)	$\varphi_s$ (deg.)	$\delta$ (deg.)	$\Delta\sigma_R$ (MPa)
41.99	440	440	1	0.03	0.17	0.8	0	331	34	17.8
42.98	408	408	1	0.03	0.16	0.75	0	331	34	22.3
43.05	477	477	1	0.04	0.19	0.85	0	331	34	13.9
43.63	377	377	1	0.03	0.15	0.7	0	331	34	28.0



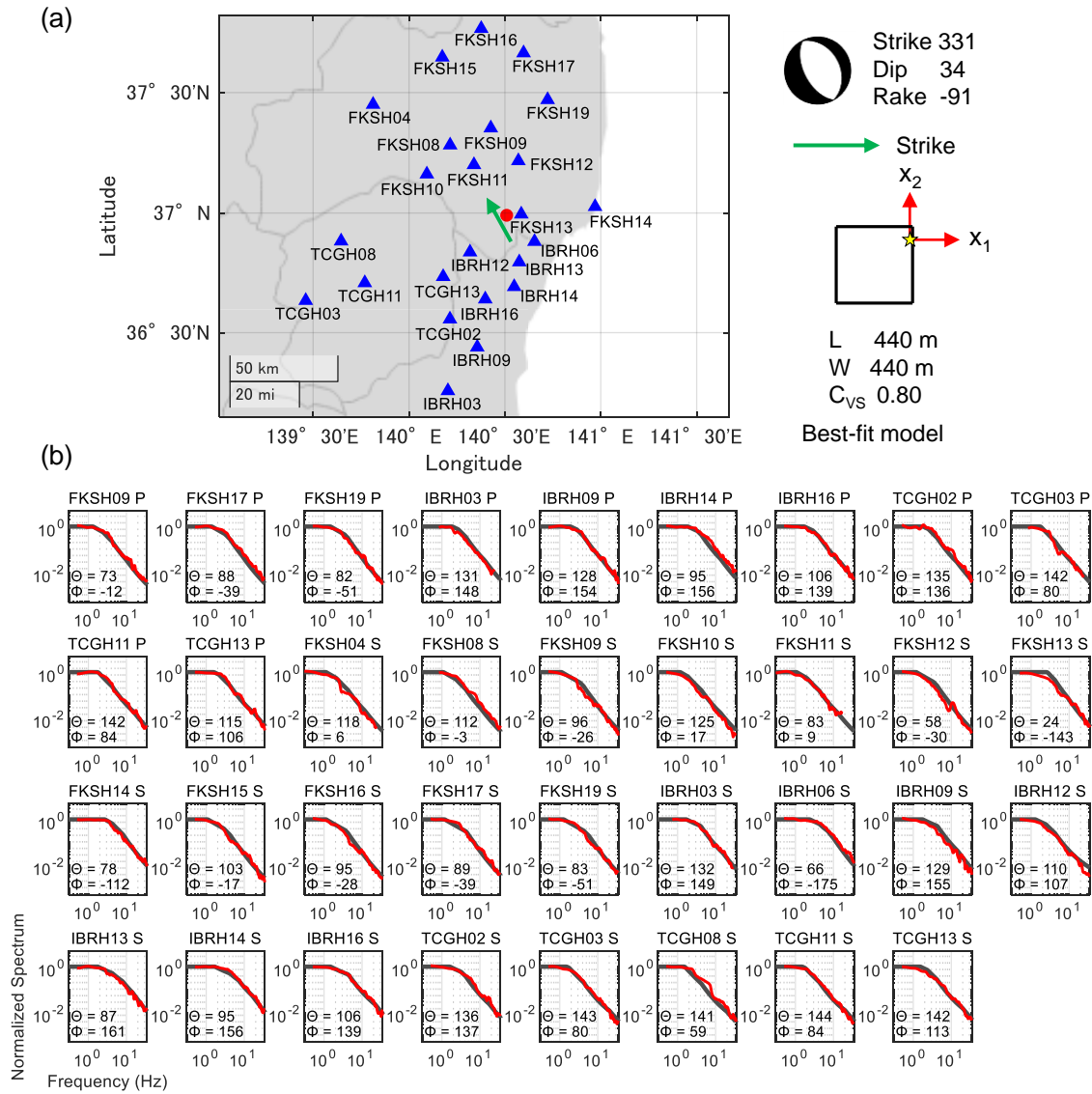


**Figure 3.8.** The result of the spectral ratio analysis for the  $M_w$  3.8 event that occurred on July 4th, 2011 in the Fukushima-Ibaraki region. (a) The stations (blue triangles) and the best-fit rupture model (top-left and top-right). The green arrow next to the red dot indicates the strike direction. The green arrow on the top of the best-fit model also shows the strike direction. (b) Comparison of the envelope spectra,  $\Omega_{EN}(\mathbf{x}, f)$ , (gray) and synthesized source spectra,  $SR_{obs}^c(\mathbf{x}, f) \times \Omega_{\omega_2}(\mathbf{x}, f)$ , (red) for the representative event (bottom). The synthesized source spectra correspond to the observation. The titles of each subplot designate the names of station and wave type. The polar coordinates are shown in each of the plots.

In the corner-frequency-based method, we usually assume a circular source with symmetric rupture propagation with a rupture speed of  $0.9V_S$ . It is useful to test if this assumption is generally valid. Thus, the spectral ratio analysis was conducted by assuming the square source ( $AR = 1$ ) whose rupture propagates from the center ( $p = q = 0.5$ ) with rupture speed of  $0.9V_S$  ( $C_{VS} = 0.9$ ). The bilateral–bidirectional source model with these assumptions (I call the standard source model) is not completely the same as the circular source but can be a good approximation. I call the source model estimated by the method originally proposed in this study the extended source model. I calculated the difference of the Akaike Information Criteria,  $\Delta AIC$ , following Yoshida (2019).

$$\Delta AIC = AIC_{stand} - AIC_{extend} = N \ln \left( \frac{F_{res}^{stand}}{F_{res}^{extend}} \right) - 2\Delta k \quad (3.15)$$

where  $AIC_{stand}$  and  $AIC_{extend}$  are the Akaike Information Criteria for the standard and extended source model.  $F_{res}^{stand}$  and  $F_{res}^{extend}$  are the residuals calculated from equation (3.5) for the standard and extended source model.  $\Delta k$  is the difference of the number of model parameters,  $\Delta k = 4$ .  $N$  is the total number of fitted frequencies in equation (3.5) calculated by adding fitted frequencies for all stations and wave types. Figure 3.9a shows that  $\Delta AIC$  for all the earthquakes exceeds 2.0 (the horizontal blue line), which indicates that all the analyzed earthquakes prefer the extended source model to the standard source model (Yoshida, 2019). Figure 3.8b shows the rupture start points ( $p$  and  $q$ ) estimated as the best-fit model. We see that most earthquakes rupture asymmetrically, which is consistent with the results by Yoshida (2019). The histograms of the aspect ratio and rupture speed are shown in Figures 3.9c and 3.9d. We see that  $AR = 1$  is less common. The rupture speed of  $C_{VS} = 0.9$  does not tend to occur more frequently than other rupture speeds. Thus, the standard source model is less common.

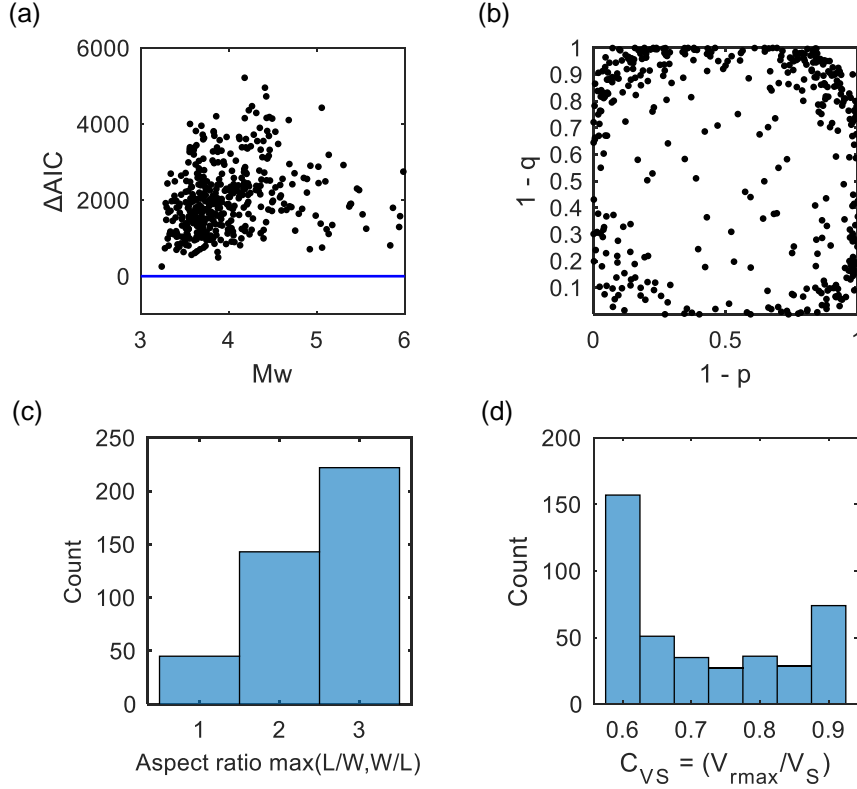


**Figure 3.9.** The  $\Delta AIC$  and source parameters estimated as the best-fit model. (a)  $\Delta AIC$  versus moment magnitude. The horizontal blue line indicates  $\Delta AIC = 2$ . (b) Distribution of the rupture start points on a rupture plane. The symmetric rupture is described as  $p = q = 0.5$ . For example,  $p = q = 1.0$  indicates that rupture asymmetrically propagates along length and width directions. (c) Histogram of aspect ratio. (d) Histogram of  $C_{VS}$ .

### 3.5. DISCUSSION

Compared to the typical range of 1 to 10 MPa observed for large earthquakes (Kanamori & Anderson, 1975; Kanamori & Brodsky, 2004; Venkataraman & Kanamori, 2004), the estimated stress drop values are one-order higher (10 to 200 MPa) (Figure 3.5). Table 3.2 compiles the source parameters of the large earthquakes (foreshock, mainshock, and aftershock) observed in the target regions. The stress drops  $\Delta\sigma_s$  were calculated from the source area  $S$  and the seismic moment  $M_0$ .

$$\Delta\sigma_s = \frac{7M_0}{16(S/\pi)^{3/2}} \quad (3.16)$$

The stress drops  $\Delta\sigma_s$  of the large earthquakes are within the typical 1 to 10 MPa range. This fact suggests that the stress drops estimated by the spectral ratio analysis are  $\Delta\sigma_R$  anomalously high. Another critical issue is the radiation efficiency  $\eta'_R$ , which is the ratio of the apparent stress  $\sigma_a$  to the average static stress drop  $\Delta\sigma_s$  multiplied by 2,  $\eta'_R = 2\sigma_a/\Delta\sigma_s$ . The radiation efficiency  $\eta'_R$  takes the value from 0.1 to 1.0 for typical earthquakes (e.g., Venkataraman & Kanamori, 2004). Suppose that the apparent stress is 1.5 MPa, which is a typical value (Hanks & Kanamori, 1979). Then, the stress drop  $\Delta\sigma_R$  of 67.9 MPa, which is the median estimate of  $\Delta\sigma_R$  (Figure 3.6), provides the (average) radiation efficiency  $\eta'_R = 2\sigma_a/\Delta\sigma_R$  of 0.04, which is too low compared with the typical range of 0.1 to 1.0.

In the Fukushima-Ibaraki region, Yoshida et al. (2015) estimated the differential stress and found that the range of the differential stress is 2 to 30 MPa. The 10 to 200 MPa stress drops appear inconsistent with the differential stress estimates by Yoshida et al. (2015). Uchide & Imanishi (2016) calculated the stress drops of some earthquakes in the Fukushima-Ibaraki region from corner frequency assuming the source model by Madariaga (1976). Their results show that the stress drops are 4 to 95 MPa with a median of 26 MPa. The Madariaga model assumes symmetric rupture propagation and high rupture speed,  $0.9V_s$ . However, the results in Figure 3.9 does not support the validity of using the Madariaga model for the earthquakes analyzed in this study. If we apply appropriate source geometry,

**Table 3.2.** The compiled source parameters for the large earthquakes in the target regions

Earthquake	$M_0$ (Nm)*	$L \times W$ (km)	$S$ (km <sup>2</sup> )	$\Delta\sigma_s$ (MPa)	References
Niigata Chuetsu 2004	7.5e+18	25 x 12	300	3.6	Miyazawa et al. (2005) Asano & Iwata. (2009)
Niigata Chuetsu 2004 aftershock	2.9e+18	12 x 12	144	4.1	Miyazawa et al. (2005)
Iwate Miyagi 2008	2.7e+19	40 x 18	720	3.4	Yokota et al. (2009) Suzuki et al. (2010)
Fukushima Hamadori 2011	9.6e+18	20 x 10 15 x 10	350**	3.6	Anderson et al. (2013) Tanaka et al. (2014)
Kumamoto foreshock 2016	1.7e+18	12 x 12	144	2.5	Asano et al. (2016)
Kumamoto 2016	4.4e+19	55 x 15	825	4.5	Yoshida et al. (2017) Asano & Iwata (2021)

\* The seismic moment values are obtained from F-net.

\*\* Two faults ruptured in the 2011 Fukushima Hamadori earthquake. The total rupture area was calculated by adding the rupture areas of two faults.

rupture speed, and rupture directivity in the corner-frequency-based stress drop estimation, the stress drops by Uchide & Imanishi (2016) can become higher. For example, the  $k_c$  value is generally smaller for asymmetric rupture propagation than symmetric rupture propagation and is also smaller for lower rupture speed (Kaneko & Shearer, 2015). The 10 to 200 MPa stress drop estimates are reasonable from a point of view of the corner-frequency-based method.

Our high stress drop estimates are inconsistent with the typical range of 1 to 10 MPa and the differential stress values by Yoshida et al. (2015) studies but are consistent with the corner-frequency-based study, such as Uchide & Imanishi (2016). The goodness of the spectral ratio fitting suggests that our estimated rupture areas should have some physical significance. However, when we calculate the stress drop using equation (3.13), we assume that the rupture area obtained from the spectral ratio fitting corresponds to the overall rupture area, which is necessary to calculate the static stress drop from equation (3.13). The rupture area estimated from the spectral ratio analysis may not be the overall rupture area but a smaller area that is generating strong seismic radiation. If this is true, the stress drops calculated from equation (3.13) with the rupture area  $LW$  will be systematically higher than an average stress drop for the entire fault plane.

### **3.6. CONCLUSIONS**

This chapter developed a procedure to estimate the source parameters (rupture size, shape, speed, and rupture start point) of the rectangular source model by the spectral ratio fitting with the envelope spectrum. The source parameters are estimated by fitting the model spectral ratios with the envelope spectrum to observed spectral ratios obtained by station and wave type. This spectral ratio fitting is different from the standard spectral ratio approach, which fits the model spectral ratio to an observed spectral ratio averaged over all stations to estimate the corner frequency. This difference is because the developed spectral ratio approach estimates more detailed source parameters than the standard one. It was confirmed that the model spectral ratio with the envelope spectrum fits the observed spectral ratios well. However, this chapter found a problem that the stress drops calculated from the rupture areas estimated by the spectral ratio approach are too high (about one order) compared with the typical stress drop range of 1 to 10 MPa despite good accuracy in the spectral ratio fitting.

## REFERENCES

- Abercrombie, R. E., (2014). Stress drops of repeating earthquakes on the San Andreas Fault at Parkfield. *Geophysical Research Letters*, **41**(24), 8784–8791.
- Abercrombie, R. E., Bannister, S., Ristau, J. & Doser, D., (2017). Variability of earthquake stress drop in a subduction setting, the Hikurangi Margin, New Zealand. *Geophysical Journal International*, **208**, 306–320.
- Aki, K. (1967). Scaling Law of Seismic Spectrum. *Journal of Geophysical Research*, **72**(4), 1217-1231.
- Anderson, J. G., Kawase, H., Biasi, G. P., Brune, J. N., & Aoi, S. (2013). Ground motions in the Fukushima Hamadori, Japan, normal-faulting earthquake. *Bulletin of the Seismological Society of America*, **103**, 1935–1951
- Asano, K. & Iwata, T. (2009), Source rupture process of the 2004 Chuetsu, Mid-Niigata prefecture, Japan, earthquake inferred from waveform inversion with dense strong-motion data. *Bulletin of the Seismological Society of America*, **99**, 123–140
- Asano, K. & Iwata, T. (2016). Source rupture processes of the foreshock and mainshock in the 2016 Kumamoto earthquake sequence estimated from the kinematic waveform inversion of strong motion data. *Earth Planets Space*, **68**,147
- Asano, K. & Iwata, T. (2021). Revisiting the source rupture process of the mainshock of the 2016 Kumamoto earthquake and implications for the generation of near-fault ground motions and forward directivity pulse. *Bulletin of the Seismological Society of America*, **111**, 2426–2440
- Boatwright, J. (1980). A spectral theory for circular sources: Simple estimates of source dimension, dynamic stress drop, and radiated seismic energy. *Bulletin of the Seismological Society of America*, **70**, 1–28.
- Boatwright, J. (2007). The persistence of directivity in small earthquakes. *Bulletin of the Seismological Society of America*, **97**(6), 1850-1861.
- Brune, J. N. (1970). Tectonic stress and the spectra of seismic shear waves from earthquakes, *Journal of Geophysical Research*, **75**(26), 4997–5009.
- Eshelby, J. D. (1957). The determination of the elastic field of an ellipsoidal inclusion, and related

- problems. *Proceedings of the Royal Society of London*, **241**(1226), 376-396.
- Geller, R. J. (1976). Scaling relations for earthquake source parameters and magnitudes, *Bulletin of the Seismological Society of America*, **66**(5), 1501–1523.
- Hanks, T. C., & Kanamori, H. (1979). A moment magnitude scale. *Journal of Geophysical Research*, **85**(B5), 2348–2350.
- Kanamori, H., & Anderson, D. L. (1975). Theoretical basis of some empirical relations in seismology. *Bulletin of the Seismological Society of America*, **65**(5), 1073–1095.
- Kanamori, H., & Brodsky, E. E. (2004). The physics of earthquakes. *Reports on Progress in Physics*, **67**(8), 1429–1496.
- Kaneko, Y., & Shearer, P. M. (2015). Variability of source spectra, estimated stress drop, and radiated energy, derived from cohesive-zone models of symmetrical and asymmetrical circular and elliptical ruptures. *Journal of Geophysical Research: Solid Earth*, **120**(2), 1053–1079.
- Keilis-Borok, V. (1959). On estimation of the displacement in an earthquake source and of source dimensions. *Annals of Geophysics*, **12**(12), 205–214.
- Koketsu, K., Miyake, H., & Suzuki, H. (2012). Japan Integrated Velocity Structure Model Version 1. *Proceedings of the 15th World Conference on Earthquake Engineering*, Paper No. 1773.
- Madariaga, R. (1976). Dynamics of an expanding circular fault. *Bulletin of the Seismological Society of America*, **66**(3), 639–666.
- Miyazawa, M., Mori, J., Iio, Y., Shibutani, T., Matsumoto, S., Katao, H., Ohmi, S., & Nishigami, K. (2005). Triggering sequence of large aftershocks of the mid Niigata prefecture, Japan earthquake in 2004 by static stress changes. *Earth Planets and Space*, **57**, 1109–1113
- National Research Institute for Earth Science and Disaster Resilience (2019a), NIED Hi-net, doi:10.17598/NIED.0003.
- National Research Institute for Earth Science and Disaster Resilience (2019b), NIED F-net, doi:10.17598/NIED.0005.
- Okada, Y., Kasahara, K., Hori, S., Obara, K., Sekiguchi, S., Fujiwara, H., & Yamamoto, A. (2004). Recent progress of seismic observation networks in Japan—Hi-net, F-net, K-NET and KiK-net. *Earth, Planets and Space*, **56**, xv–xxviii.
- Park, J., Lindberg, C. R., & Vernon, F. L. (1987). Multitaper spectral analysis of high-frequency seismograms. *Journal of Geophysical Research: Solid Earth*, **92**(B12), 12675–12684.

- Ross, Z. E., & Ben-Zion, Y. (2016). Toward reliable automated estimates of earthquake source properties from body wave spectra. *Journal of Geophysical Research: Solid Earth*, **121**(6), 4390–4407.
- Shearer, P. M., Prieto, G. A., & Hauksson, E. (2006). Comprehensive analysis of earthquake source spectra in southern California. *Journal of Geophysical Research: Solid Earth*, **111**, B06303.
- Shimmoto, S. (2020). An earthquake source spectrum model considering rupture directivity and its application for obtaining Green's functions. *Bulletin of the Seismological Society of America*, **110**(6), 2711–2727.
- Shimmoto, S. (2022). Stress drop estimates for small to moderate earthquakes in Tohoku, Japan considering rupture geometry, speed, and directivity. *Journal of Geophysical Research: Solid Earth*, **127**, e2022JB025157.
- Suzuki, W., Aoi, S. & Sekiguchi, H. (2010). Rupture process of the 2008 Iwate–Miyagi Nairiku, Japan, earthquake derived from near-source strong-motion records. *Bulletin of the Seismological Society of America*, **100**, 256–266
- Tanaka, M., Asano, K., Iwata, T., & Kubo, H. (2014). Source rupture process of the 2011 Fukushima-ken Hamadori earthquake: how did the two subparallel faults rupture? *Earth Planets Space*, **66**, 101.
- Thomson, D. J. (1982). Spectrum estimation and harmonic analysis, *Proceeding of the IEEE*, **70**(9), 1055–1096.
- Uchide, T. & Imanishi, K. (2016). Small earthquakes deviate from the omega-square model as revealed by multiple spectral ratio analysis. *Bulletin of the Seismological Society of America*, **106**(3), 1357–1363.
- Venkataraman, A., & Kanamori, H. (2004). Observational constraints on the fracture energy of subduction zone earthquakes. *Journal of Geophysical Research*, **109**, B05302.
- Viegas, G., Abercrombie, R. E., & Kim, W.Y. (2010). The 2002 M5 Au Sable Forks, NY, earthquake sequence: Source scaling relationships and energy budget. *Journal of Geophysical Research: Solid Earth*, **115**(B7).
- Ye, L., Lay, T., Kanamori, H., & Rivera, L. (2016). Rupture characteristics of major and great ( $M_w \geq 7.0$ ) megathrust earthquakes from 1990 to 2015: 1. Source parameter scaling relations. *Journal of Geophysical Research: Solid Earth*, **121**, 826–844.



- Yokota, Y., Koketsu, K., Hikima, K., & Miyazaki, S. (2009). Ability of 1-Hz GPS data to infer the source process of a medium-sized earthquake: The case of the 2008 Iwate-Miyagi Nairiku, Japan, earthquake. *Geophysical Research Letters*, **36**, L12301.
- Yoshida, K. (2019). Prevalence of asymmetrical rupture in small earthquakes and its effect on the estimation of stress drop: a systematic investigation in inland Japan. *Geoscience Letters*, **6**, 16.
- Yoshida, K., Hasegawa, A., & Okada, T. (2015). Spatially heterogeneous stress field in the source area of the 2011 Mw 6.6 Fukushima-Hamadori earthquake, NE Japan, probably caused by static stress change. *Geophysical Journal International*, **206**(2), 1062–1071.
- Yoshida, K., Miyakoshi, K., Somei, K. & Irikura, K. (2017). Source process of the 2016 Kumamoto earthquake (Mj7.3) inferred from kinematic inversion of strong-motion records. *Earth Planets Space*, **69**, 64.

## Chapter 4

# SEISMIC SPECTRA AND SOURCE HETEROGENEITY

## 4.1. BACKGROUND AND OVERVIEW

In the previous chapter, we saw that the stress drops  $\Delta\sigma_R$  calculated from the rupture area estimated by the spectral ratio analysis are too high compared with the typical range. A hypothesis is that the rupture area estimated from the spectral analysis is not the overall rupture area but is a much smaller area. This chapter clarifies the physical meaning of the estimated rupture area.

The source model developed in Chapter 2 does not incorporate slip heterogeneity and can still be too simple to represent a realistic earthquake rupture. Some studies suggest that the slip distribution of small earthquakes, similar to large earthquakes, is heterogeneous rather than uniform (Dreger et al., 2007; Kim et al., 2016; Yamada et al., 2005). The heterogeneous stress drop distribution can cause high-stress drops locally but a low average stress drop (Dreger et al., 2007; Kim et al., 2016; Brown et al., 2015). The source heterogeneity may affect the rupture area estimated by the spectral ratio analysis. The high-stress drop estimates in the previous chapter may correspond to the stress drop on a localized area with large slip.

This chapter demonstrates that the rupture area  $LW$  estimated by the spectral ratio method corresponds to a localized area with large slip rather than the overall rupture area. This consequence suggests that a localized area with large slip controls the shapes of the seismic source spectrum rather than the total rupture area. Hence, the stress drops,  $\Delta\sigma_R$ , calculated with the rupture area obtained from

this spectral ratio method are systematically higher than the actual average stress drop for the entire rupture area. This chapter proposes a procedure to correct the bias in the stress drop estimation and calculate the stress drops. Then, their scaling relation, focal mechanism dependence, depth dependence, rupture speed dependence, uncertainty, and relationship to the corner-frequency-based stress drop are studied.

## **4.2. WHAT IS THE ESTIMATED RUPTURE AREA?**

Firstly, I compared the slip inversion results of the two  $M_w$  5.9 events by JMA with the best-fit rupture models in the spectral ratio method (Shimmoto, 2022). The rupture speeds of the best-fit rupture models are almost the same as those used in the finite source inversions (Figure 4.1). The rupture areas estimated by the spectral ratio method are significantly smaller than the overall rupture area (Figure 4.1). The rupture areas estimated from the spectral ratio method seem to correspond to the areas of the large slip regions in the finite fault inversions.

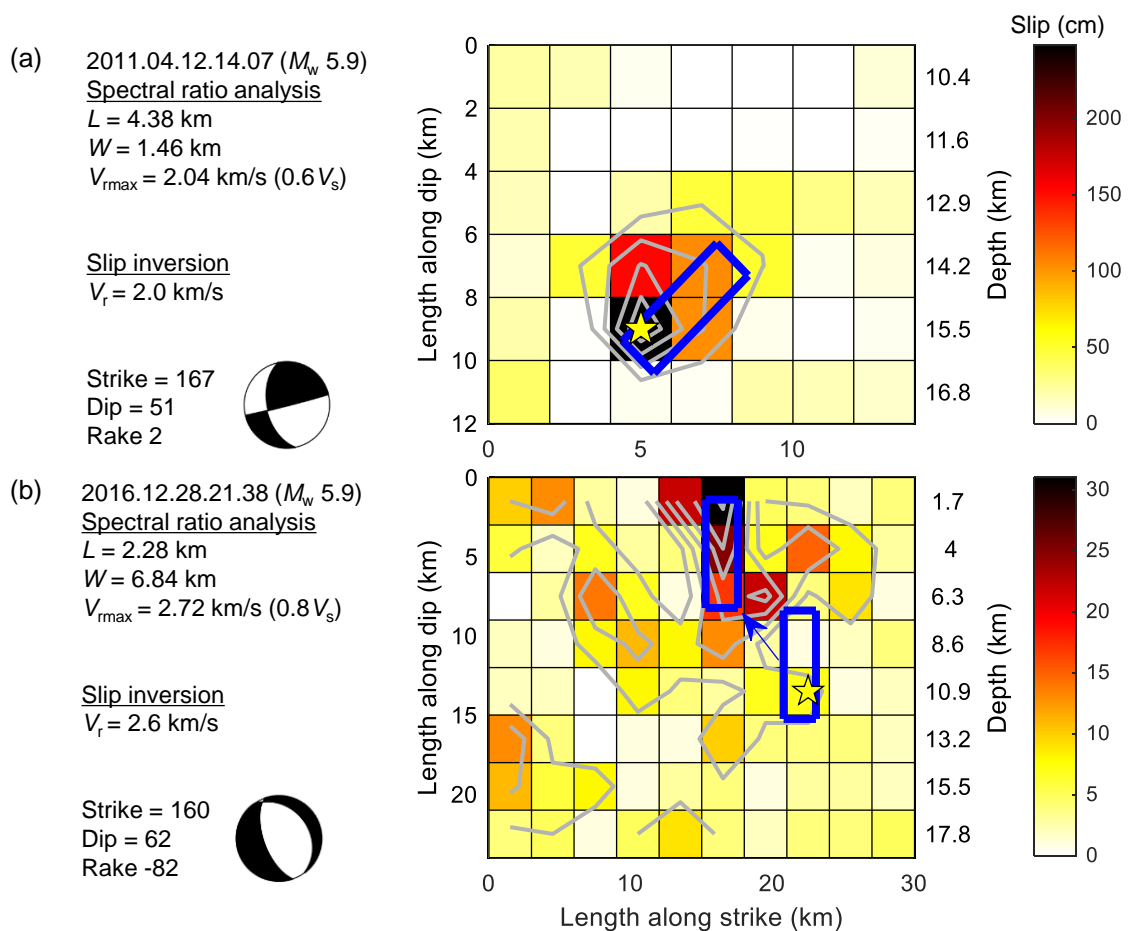
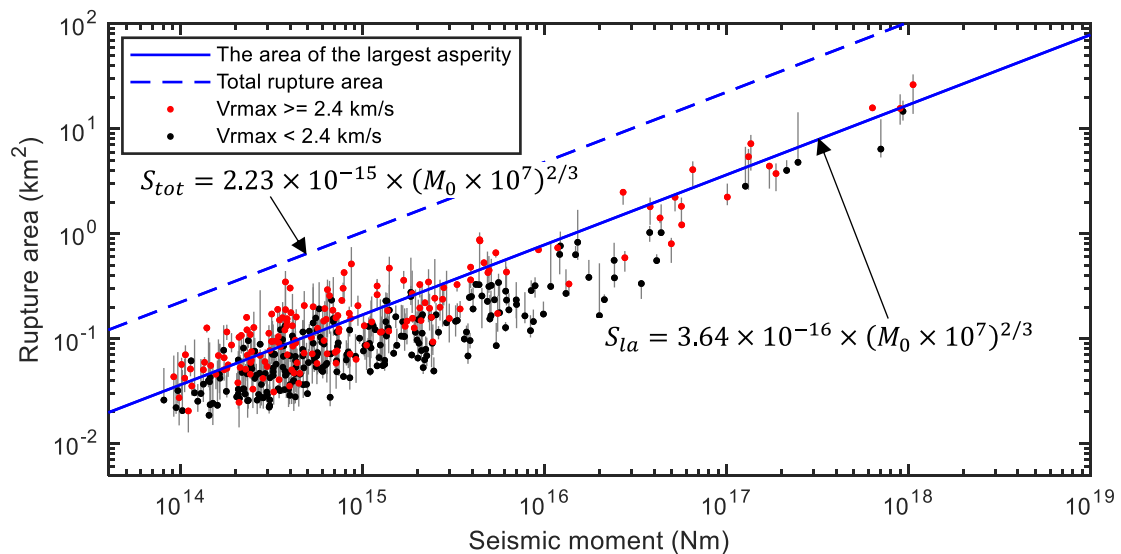


**Figure 4.1.** Comparison of the estimated rupture area with the slip distribution for two  $M_w$  5.9 events. The information on the spectral ratio analysis and slip inversion is described on the left. The results of the slip inversion were provided by JMA. The yellow stars are the hypocenters used in the slip inversion. The blue rectangular areas correspond to the estimated rupture area and are plotted assuming the hypocenters coincide with those used in the slip inversion. (a) 2011  $M_w$  5.9 event. (b) 2016  $M_w$  5.9 event. The blue rectangular rupture area for Figure 4.1b is shifted to the region with a large slip for easy comparison. These plots were made based on the slip inversion result by JMA.

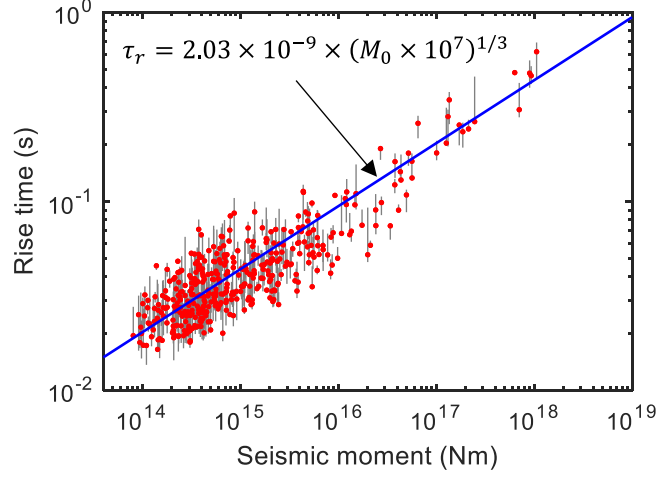
Figure 4.1a: <https://www.data.jma.go.jp/svd/eqev/data/sourceprocess/event/2011041214074228near.pdf>

Figure 4.1b: <https://www.data.jma.go.jp/svd/eqev/data/sourceprocess/event/2016122821384904near.pdf>

Secondly, I compared the estimated rupture areas of the two large earthquakes with those of the other earthquakes. Somerville et al. (1999) provide the regression results of the relationships between the total rupture area and seismic moment, also the area of the largest asperity and seismic moment. The rupture areas estimated in this study are consistent with the regression line for the area of the largest asperity, rather than the total rupture area (Figure 4.2). Note that  $M_w$  5.9 ( $M_0 = 7.9 \times 10^{17}$  Nm) is within the magnitude range treated by Somerville et al. (1999). The rupture speeds of the earthquakes analyzed by Somerville et al. (1999) are limited to 2.4 to 3.0 km/s. Looking at the results for rupture speeds greater than or equal to 2.4 km/s (red dots in Figure 4.2), they appear even more consistent with the regression curve for the largest asperity area. These results also indicate that the rupture area estimated by the spectral ratio method corresponds to the localized area with large slip.



**Figure 4.2.** The relationship between the rupture area and seismic moment for this study. The dashed and solid blue lines are the regression results of the total rupture area and the area of the largest asperity, respectively, by Somerville et al. (1999). The red and black dots are the results obtained by the spectral ratio method and are classified by the rupture speed. The gray bars stand for the upper and lower bound of the estimated rupture areas.



**Figure 4.3.** The relationship between the rise time and the seismic moment for this study. The blue line is the regression result by Somerville et al. (1999). The gray bars stand for the upper and lower bound.

The rise time was calculated from the rupture area  $LW$  with equation (3.12). The rise times obtained in this study are consistent with the regression curve obtained by Somerville et al. (1999) (Figure 4.3). This result suggests that the rise time is more comparable to the rupture duration in a localized area with large slip rather than an overall rupture duration. Somerville et al. (1999) pointed out that the rise time is similar to the rupture duration of the largest asperity.

### 4.3. REVISE OF STRESS DROP CALCULATION METHOD

Since we saw that the estimated rupture area  $LW$  is much smaller than the overall rupture area, the stress drop calculated by equation (3.13) represents a much higher value than the average static stress drop. Somerville et al. (1999) reported that the ratio of the rupture area of the largest asperity to the overall rupture area is 17.5% on average. We can use this average area ratio to estimate the average stress drop for the entire fault. Assuming that the estimated rupture areas occupy 17.5% of the overall rupture area for all the target earthquakes, we can calculate the average static stress drop  $\Delta\sigma_s$  as:

$$\Delta\sigma_s = \frac{7M_0}{16(S/\pi)^{3/2}} = 0.175^{3/2}\Delta\sigma_R \quad (4.1)$$

where  $S$  is the overall rupture area,  $S = LW/0.175$ . The stress drop  $\Delta\sigma_s$  is one order smaller than the stress drop  $\Delta\sigma_R$ . Note that the stress drop estimation with equation (4.1) corrects only the bias from the interpretation of the areas of the asperity and total rupture. There is also the uncertainty in the stress drop estimates due to not knowing the actual ratios of the estimated rupture areas to the overall rupture areas for each individual events. Therefore, we should treat only the statistical trend of the stress drop  $\Delta\sigma_s$  and not the individual values of each event.

I interpret the results as an earthquake source with a single asperity and heterogeneous stress drop distribution (Boatwright, 1988; Das & Kostrov, 1986; McGarr, 1981; Rudnicki & Kanamori, 1981). The stress drop is concentrated on a small area located in the overall rupture area and is zero outside of this area. Consequently, the stress drop averaged over the overall rupture area is much lower than that on the small region. The stress drop on the small area, the local stress drop  $\Delta\sigma_{la}$ , can be calculated as follows (Madariaga, 1979; Miyake et al., 2003).

$$\Delta\sigma_{la} = \frac{7M_0}{16Rr^2} = \frac{1}{0.175} \Delta\sigma_s = \sqrt{0.175} \Delta\sigma_R \quad (4.2)$$

The local stress drop  $\Delta\sigma_{la}$  is approximately half of the stress drop  $\Delta\sigma_R$  and is a factor of 5.7 larger than the average static stress drop  $\Delta\sigma_s$ .

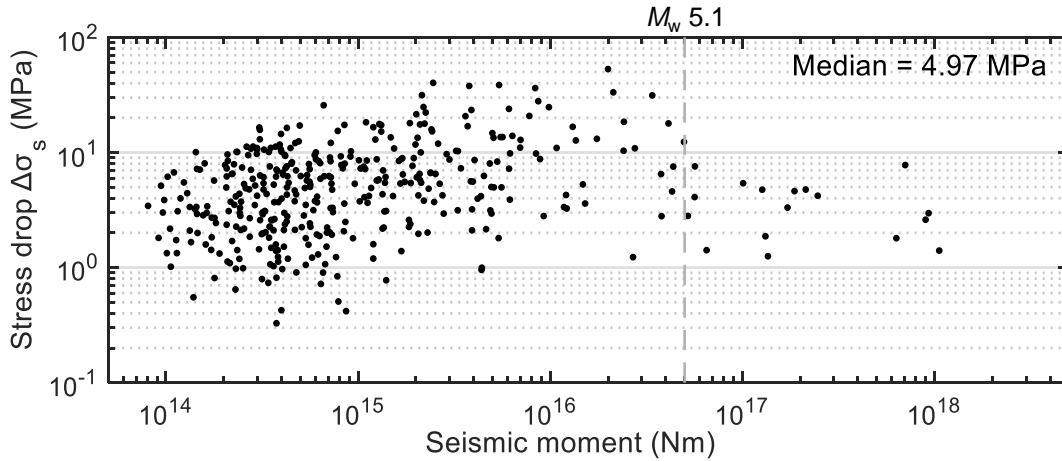


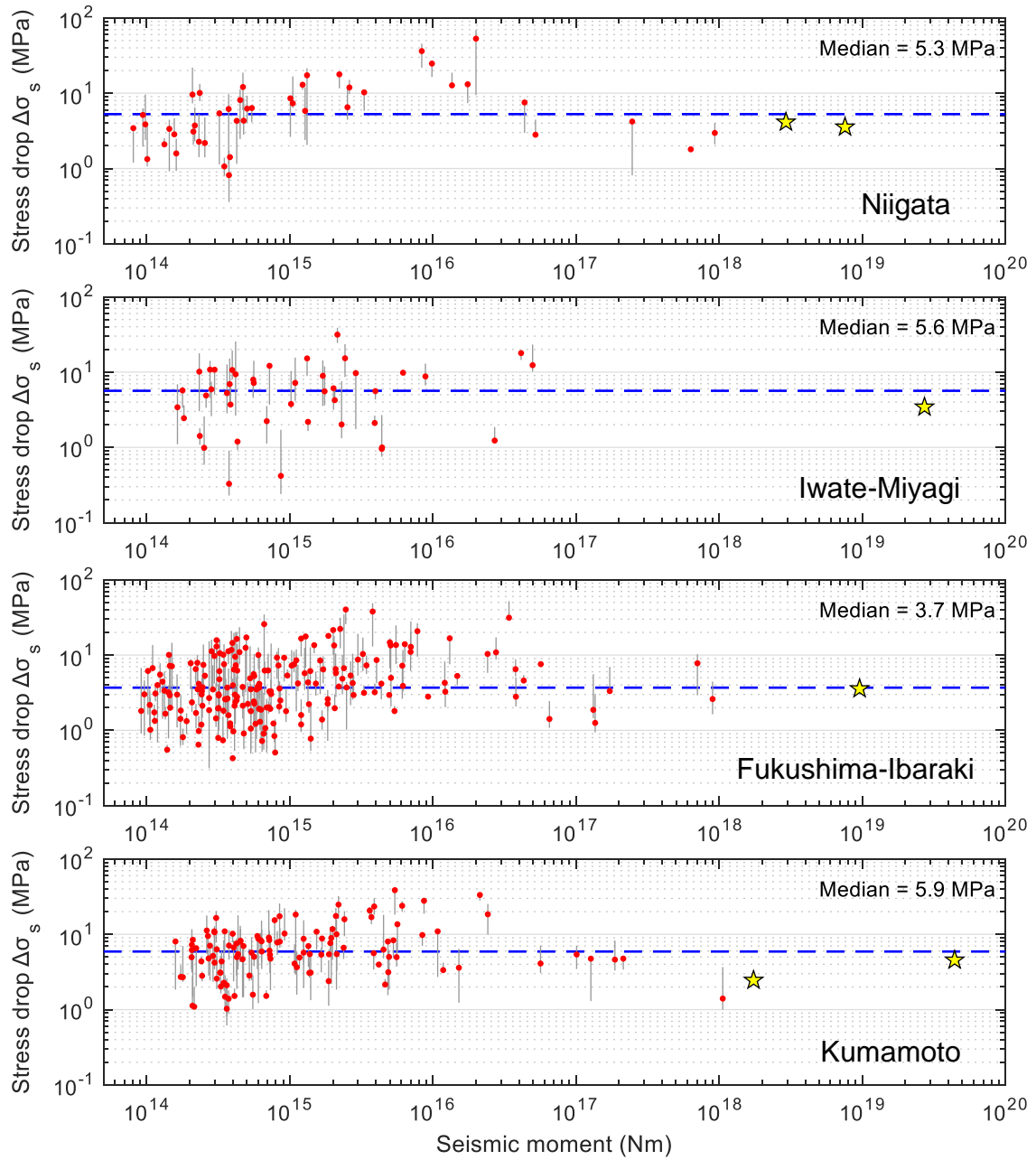
**Figure 4.4.** The average static stress drops  $\Delta\sigma_s$  versus the seismic moment  $M_0$ . The black dots are the best-fit stress drops estimated by the spectral ratio analysis.

## 4.4. STRESS DROP RESULTS

### 4.4.1. Seismic Moment Dependence

The revised stress drops  $\Delta\sigma_s$  calculated for the best-fit models range from 0.33 to 53 MPa with a median of 4.97 MPa, and 91% of the stress drop estimates are within a typical range of 1 to 20 MPa (Figure 4.4). The median stress drop is 4.91 MPa (the best-fit model) if the large earthquakes in Table 3.2 are included. The scale dependence of the stress drop is somewhat complicated. In the range of  $M_0 < 5.0 \times 10^{16}$  Nm ( $M_w < 5.1$ ), the stress drop increases as the seismic moment increases. However, we may also interpret that stress drop is relatively scale-independent in  $M_0 < 1.0 \times 10^{15}$  Nm. From near  $M_0 = 5.0 \times 10^{16}$  Nm, the stress drop decreases and seems to become independent of the seismic moment in the range of  $M_0 > 5.0 \times 10^{16}$  Nm. The local stress drops  $\Delta\sigma_{la}$  range from 1.9 to 303 MPa with a median of 28.4 MPa, and 91% of the local stress drops  $\Delta\sigma_{la}$  are in 5 to 100 MPa.





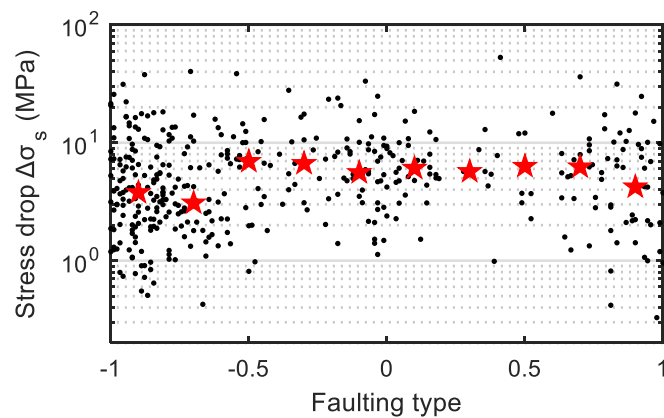
**Figure 4.5** The stress drops  $\Delta\sigma_s$  for each of the target regions. The gray lines indicate the estimation uncertainty. The yellow stars are the compiled data in Table 3.2. The blue dashed lines show the median values calculated for the best-fit model.

Figure 4.5 shows the stress drops  $\Delta\sigma_s$  for each of the target regions with the uncertainties of the stress drop estimates. The stress drops were calculated for all source parameters that satisfy the residual criterion to evaluate the uncertainties of stress drop estimates (e.g., see Table 3.1) (gray lines in Figure 4.5). In the Niigata, Fukushima-Ibaraki, and Kumamoto, the stress drop increases with the seismic

moment in  $M_0 < 5.0 \times 10^{16}$  Nm and becomes nearly scale-independent in  $M_0 > 5.0 \times 10^{16}$  Nm. This tendency holds even if the estimation uncertainties are considered (gray lines in Figure 4.5). In the Iwate-Miyagi, it is difficult to confirm this tendency because the stress drops of earthquakes with  $M_0 > 5.0 \times 10^{16}$  Nm are absent.

#### 4.4.2. Faulting Type Dependence

Figure 4.6 summarizes the focal mechanism-dependency of the stress drops  $\Delta\sigma_s$  for the best-fit models. The stress drop  $\Delta\sigma_s$  appears not to depend on the faulting types. However, the normal and reverse faults have slightly lower median stress drops (red stars). The normal-faulting earthquakes are found mainly in the Fukushima-Ibaraki, and the reverse-faulting earthquakes are dominant in the Niigata and Iwate-Miyagi (Figure 3.1).



**Figure 4.6** (a) The focal mechanism dependence of the stress drops. The normal faulting, strike-slip, and reverse faulting correspond to the values on the x-axis -1.0, 0, and 1.0, respectively. The values classifying faulting types (x-axis) were divided into bins with 0.2 widths to calculate the median values for different faulting types (the red stars).

### 4.4.3. Rupture Speed Dependence

The relationship between the rupture speed and the stress drop is significant in engineering seismology (e.g., Causse & Song, 2015) and in understanding the physics of earthquakes (e.g., Kanamori & Rivera, 2004). Figure 4.7 shows the relationships between the rupture speed and the stress drop for the best-fit rupture models. The rupture speed and the stress drop are inversely correlated. The coefficient of correlation between  $\log_{10}V_{rmax}$  and  $\log_{10}\Delta\sigma_s$  is  $-0.55$ . The linear regression in log space suggests that the stress drop is inversely proportional to the cube of rupture speed in a statistical manner (Kanamori & Rivera, 2004).

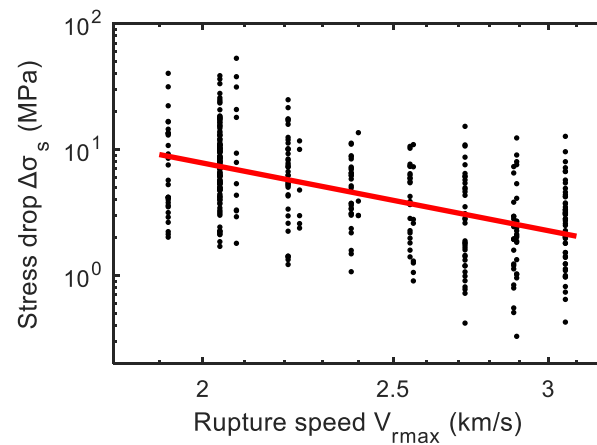


**Figure 4.7** The relationship between the rupture speed and the stress drops. The red line is the regression result.

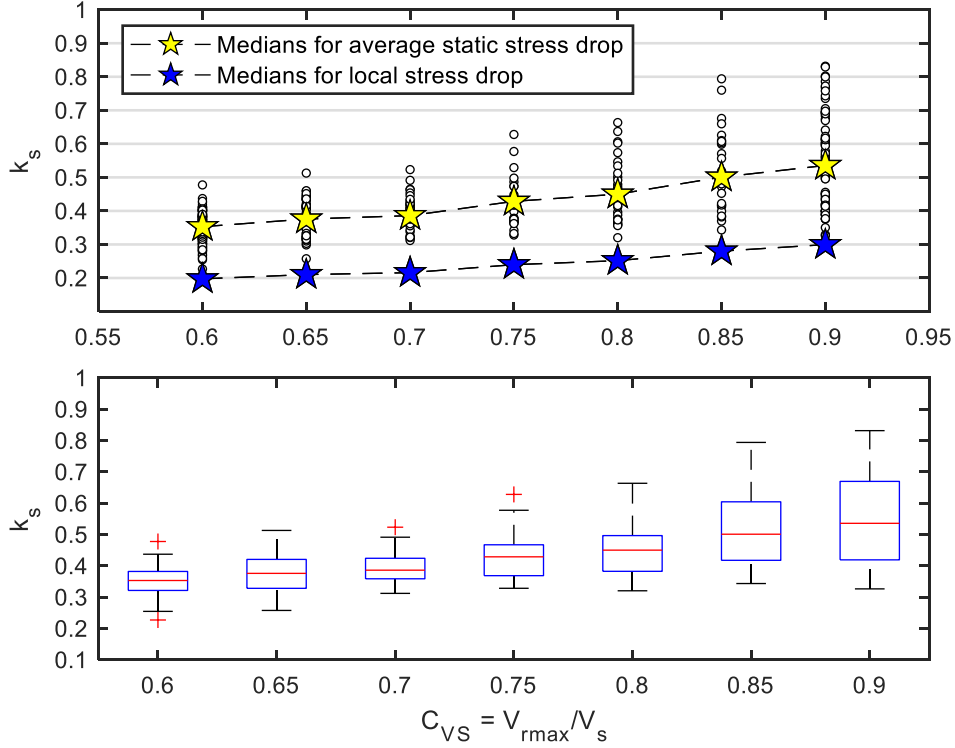


**Figure 4.8** The rupture speed versus the estimated  $k_s$  values. Top panel shows all estimated  $k_s$  values with their median values calculated for each rupture speed. The  $k_s$  values provided for the average static stress drop (white dots and yellow stars) and the local stress drop (the blue stars). The bottom panel is the box plot of the  $k_s$  values for the average static stress drop. The horizontal red line indicates the median, and the bottom and top edges stand for the 25th and 75th percentiles, respectively (the horizontal blue lines). The horizontal black lines indicate the maximum and minimum values. The symbol “+” indicates an outlier.

#### 4.4.4. Stress Drop and Corner Frequency

The stress drop is calculated from the corner frequency  $f_c$  in the standard approach (Chapter 1).

$$\Delta\sigma_{fc} = \frac{7M_0}{16} \left( \frac{f_c}{k_c V_s} \right)^3 \quad (4.3)$$

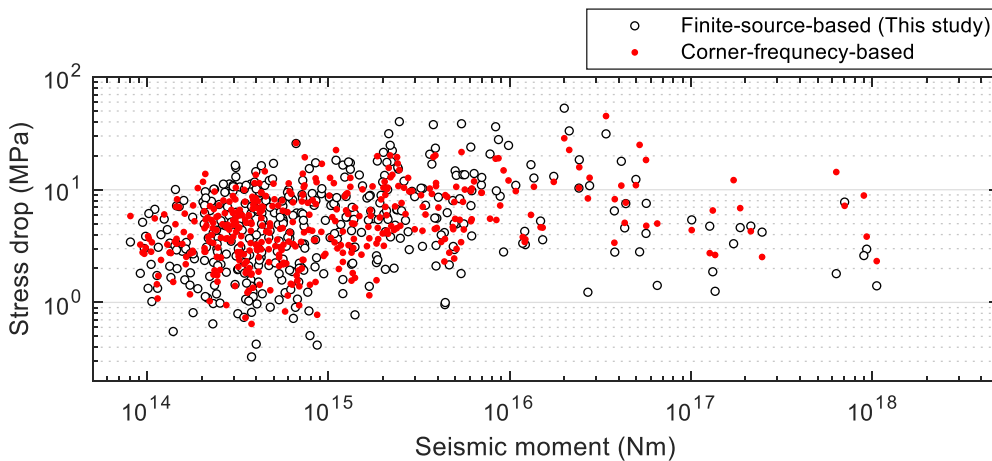
Estimating the  $k_c$  value from the estimated stress drop  $\Delta\sigma_s$  and the corner frequency should be useful for comparison with the corner-frequency-based method. Thus, I fitted the spectral ratio calculated from the omega-square model to the S-wave spectral ratio averaged over the stations and estimated the corner frequency assuming  $1 \leq \gamma \leq 2$ . From equation (4.3) and equation (4.1), we can obtain the  $k_c$  value for S-wave,  $k_s$ , as

$$k_s = \frac{f_c \sqrt{LW}}{V_s \sqrt{0.175\pi}} \quad (4.4)$$

where  $f_c$  is the corner frequency of the average spectrum for S-wave. We can obtain the  $k_s$  value to estimate the local stress drop by  $k_s \times 0.175^{1/3}$ .

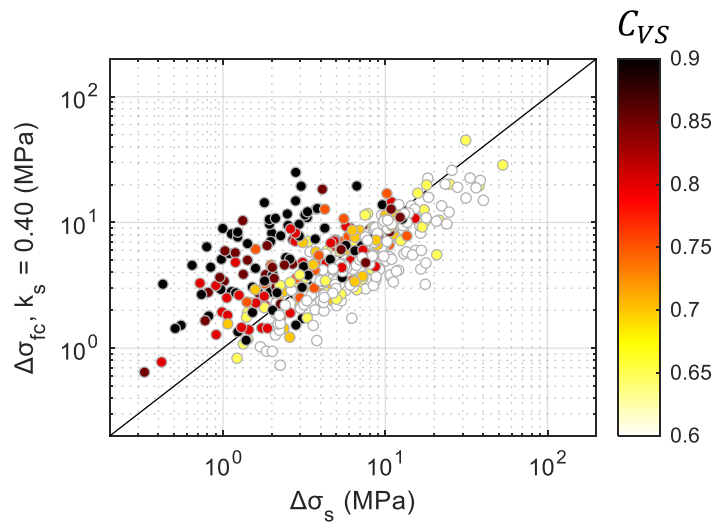
Figure 4.8 provides the estimated  $k_s$  values. The median  $k_s$  value for the average static stress drop  $\Delta\sigma_s$  is 0.388, which is close to the  $k_s$  values by Brune (1970) ( $k_s = 0.372$ ). The mean of  $k_s$  value for is 0.420. The  $k_s$  values are highly variable for different earthquakes, from 0.227 to 0.832. The standard deviation is 0.112. The median  $k_s$  value for the local stress drop is 0.217, which is consistent with Madariaga (1976) ( $k_s = 0.21$ ). The  $k_s$  value for the local stress drop increases as rupture speed increases, and the medians calculated for each rupture speed approximately from 0.2 to 0.3 (blue stars), which is consistent with Kaneko & Shearer (2015). Figure 4.10 compares the stress drops derived from equation (4.1) and equation (4.3) with the corner frequencies by assuming  $k_s = 0.40$  (i.e., constant  $k_s$  value assumption). I chose this  $k_s = 0.40$  so that the median stress drop estimated from the corner frequency would be consistent with the median of the stress drop  $\Delta\sigma_s$ . Figure 4.9 shows that the range of the stress drops estimated from the corner frequency (0.64 to 45 MPa with a median of 4.79 MPa, red dots) is approximately consistent with the range of the stress drops  $\Delta\sigma_s$  (0.33 to 53 MPa with a median of 4.97 MPa, white dots).

Figure 4.10 compares the stress drop  $\Delta\sigma_s$  to the corner-frequency-based stress drop  $\Delta\sigma_{f_c}$ . I calculated  $\Delta\sigma_{f_c}$  by assuming  $k_s = 0.40$ . The color map indicates the rupture speed. The rupture speed-



**Figure 4.9** The comparison with the average static stress drops to the corner-frequency-based stress drops calculated by assuming  $k_s = 0.40$ .

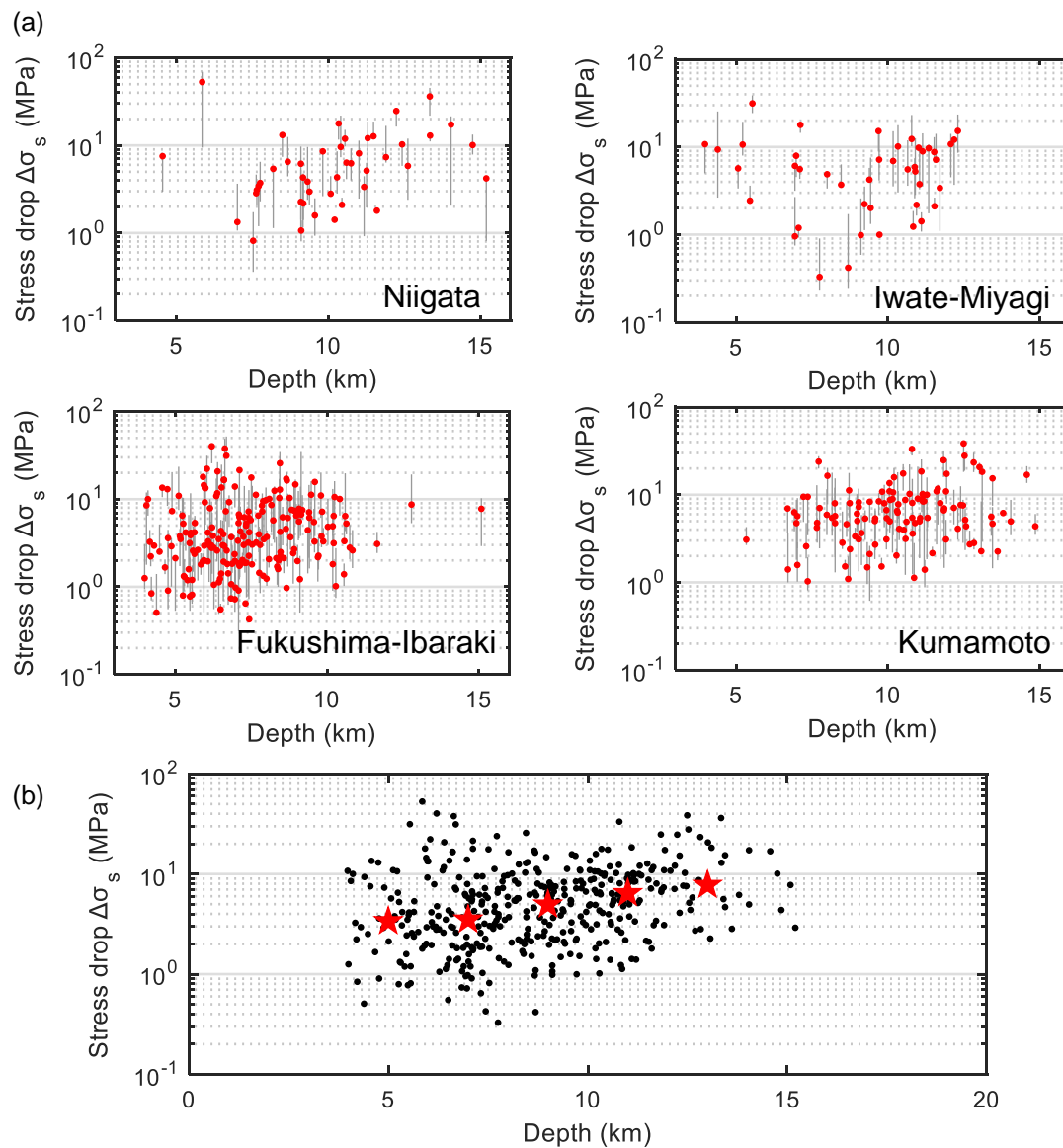
dependence of  $\Delta\sigma_s$  is useful to see the difference between  $\Delta\sigma_s$  and  $\Delta\sigma_{fc}$ . For example, Figure 4.10 demonstrates that a high rupture speed causes a low value of  $\Delta\sigma_s$  (e.g., 1.0 MPa) but a high value of  $\Delta\sigma_{fc}$  (e.g., 1.0 MPa). The essential cause of this discrepancy is the assumption of the proportionality of the cube of the corner frequency to the stress drop in the corner-frequency-based approach. This assumption does not hold if rupture speed varies with earthquakes.



**Figure 4.10** Relationship between the stress drop  $\Delta\sigma_s$  and the corner-frequency-based stress drop  $\Delta\sigma_{fc}$ . The rupture speed is shown by the color map.

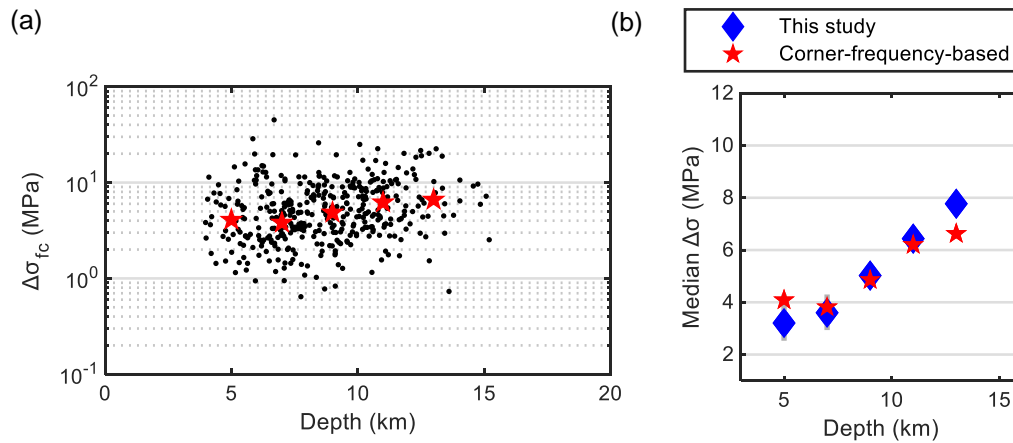
### 4.4.5. Depth Dependence

Figure 4.11 shows the relationship between the stress drops  $\Delta\sigma_s$  and depth. The depth-dependence tendency is not clear in the four target regions (Figure 4.11a). Figure 4.12b summarizes the results of the depth-dependence for the four target regions. The median stress drops calculated for each depth bin (red stars) tend to increase with depth slightly. The median of  $\Delta\sigma_s$  increases from 3.4 to 7.8, a factor of 2.3, as depth increases from 5 to 13 km.



**Figure 4.11** The relationship between depth and stress drops. (a) The depth-dependence in each target region. (b) The depth-dependence for all target regions. The red stars are the median values calculated for each bin.

Figure 4.12a shows the depth-dependence of the corner-frequency-based stress drop  $\Delta\sigma_{fc}$ . The median of  $\Delta\sigma_{fc}$  increases from 4.1 to 6.6 MPa, a factor of 1.6, as depth increases from 5 to 13 km. The medians of  $\Delta\sigma_{fc}$  (red stars) tend to increase as similar to  $\Delta\sigma_s$  (Figure 4.12b). The depth dependences of  $\Delta\sigma_{fc}$  and  $\Delta\sigma_s$  may be overestimated due to the constant S-wave velocity in the 1-D velocity structure model assumed in this study. The S-wave velocity in the Kumamoto region is 3.4 km/s from 3.0 up to 15.5 km depth, and the one in the other regions is 3.4 km/s from 6.7 up to 17 km depth. For example, if we assume the S-wave velocity is 3.7 km/s at 13 km depth, the median  $\Delta\sigma_{fc}$  at this depth decreases to 5.2 MPa, which is a factor of 1.3 higher than the median  $\Delta\sigma_{fc}$  at 5 km depth. We may apply a similar discussion for  $\Delta\sigma_s$  because the S-wave velocity controls the rupture speed in the grid search. Thus, the depth dependence of the stress drop is probably not remarkable in this study.



**Figure 4.12** The relationship between depth and the corner-frequency-based stress drops  $\Delta\sigma_{fc}$  ( $k_s = 0.40$ ). (a) The depth dependence of  $\Delta\sigma_{fc}$ . The red stars are the median values calculated for each bin. (b) Comparison of the depth-dependences of the medians of  $\Delta\sigma_s$  and  $\Delta\sigma_{fc}$ . The blue diamonds were obtained from the best-fit model.



## 4.5. STRESS DROP UNCERTAINTY

I investigated the stress drop uncertainty considering a number of other parameters in my model. The resolution of the other parameters influences the stress drop uncertainty. This study treats only the statistical tendency of the relationship between the stress drop uncertainty and the uncertainty of other parameters. The source parameter ensembles were obtained for each event based on the minimum residual criterion, the criterion that residuals ( $F_{res}$ ) are less than 1.05 times the minimum residual, in the grid search (e.g., Table 3.1). The working hypothesis is that the source parameter uncertainty is evaluated based only on this minimum residual criterion in the grid search. Figure 4.13a shows the histograms of the uncertainties of the rupture speed  $C_{VS}$ , the aspect ratio  $AR' = \max(L/W, W/L)$ , and the rupture start point  $I_{pq}$ .

$$I_{pq} = |p - 0.5| + |q - 0.5| \quad (4.5)$$

$I_{pq}$  takes the value from 0 to 1.0 and represents the L1 distance from the center of the rupture area. The uncertainties of  $C_{VS}$ ,  $AR'$ , and  $I_{pq}$  are defined as the difference between the upper and lower bounds obtained from the minimum residual criterion (e.g.,  $upperC_{VS} - lowerC_{VS} = 0.15$  in Table 3.1). Figure 4.13b shows the relationship between the stress drop uncertainty and the uncertainty of  $C_{VS}$ ,  $AR'$ , and  $I_{pq}$ . The  $AR'$  uncertainty does not correlate to the stress drop uncertainty. The uncertainty of  $C_{VS}$  or  $I_{pq}$  is correlated positively to the stress drop uncertainty. This result is due to the parameter trade-off: (1)  $C_{VS}$  versus the rupture area (or  $\Delta\sigma_s$ ) and (2)  $C_{VS}$  versus  $I_{pq}$  (Boatwright, 2007). The median uncertainty of  $C_{VS}$  is 0.15. This study could distinguish high rupture speed ( $C_{VS} \geq 0.75$  for 73 events) and low rupture speed ( $C_{VS} \leq 0.75$  for 141 events) for about half of the analyzed earthquakes although some events have low resolutions of  $C_{VS}$  (Figure 4.13a). The median uncertainty of  $I_{pq}$  is 0.13, and the resolution  $I_{pq}$  of relatively well under the working hypothesis.

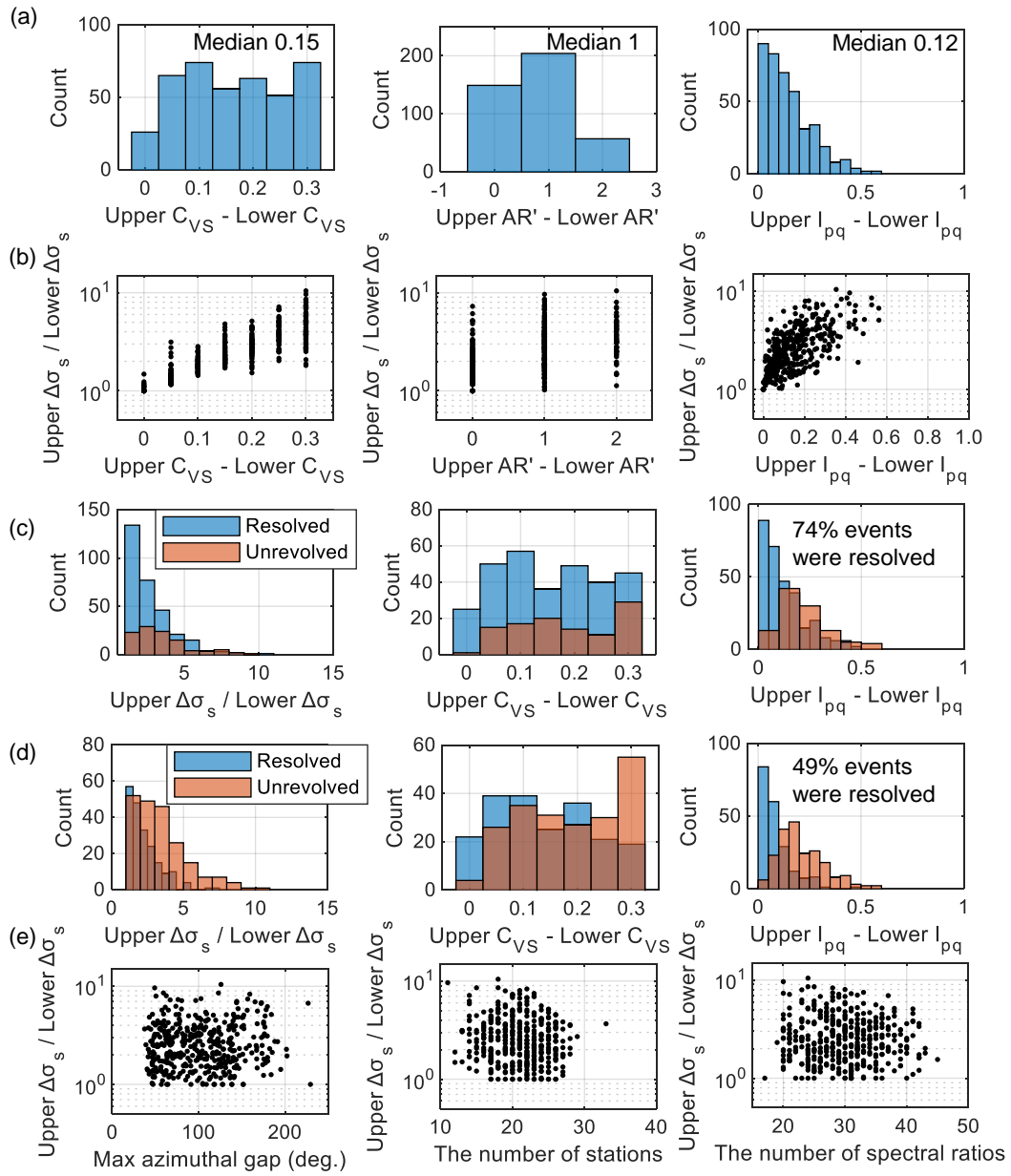


**Figure 4.13** Summary of the source parameter uncertainties. (a) Histograms of the uncertainties of the rupture speed  $C_{VS}$  (left), aspect ratio  $AR'$  (middle), and the rupture start point  $I_{pq}$  (right). (b) The relationships between the stress drop uncertainty and the uncertainties of other parameters. (c) The source parameter uncertainties and resolution of the fault plane solution. The histograms show the uncertainties of stress drop (left), rupture speed (middle), and the rupture start point (right). (d) The source parameter uncertainties and resolution of the rupture orientation angle  $\lambda$ . (e) The relationship between the stress drop uncertainty and the observation limitation.

The grid search tested the two possible nodal planes of the fault plane solution and the two cases of the rupture orientation angles  $\Lambda$  (0 or 45 degrees). The rupture orientation angle characterizes the orientation angle of the estimated rupture area (the large-slip asperity area) on the nodal plane. For example, Figures 4.1a and 4.1b illustrate the cases of  $\Lambda = 45$  and  $\Lambda = 0$ , respectively. The two nodal planes of the fault plane solution or rupture orientation angles were sometimes resolved uniquely based on the minimum residual criterion (e.g., Table 3.1). The resolution of the fault plane or rupture orientation angle  $\Lambda$  affects the uncertainty of  $\Delta\sigma_s$ ,  $C_{VS}$ , and  $I_{pq}$  (Figures 4.13c and 4.13d). However, the stress drop uncertainty was low for some events even though their fault planes or  $\Lambda$  could not be resolved. This result implies that the ambiguities of fault planes and  $\Lambda$  were not the direct factors in increasing the stress drop uncertainty. The resolution of  $\Lambda$  (0 or 45 degrees in this study) was relatively low (Figure 4.13d). This low resolution can be partly because the actual angles of  $\Lambda$  for some events have intermediate values of 0 and 45 degrees. Figure 4.13e shows the relationship between the stress drop uncertainty and the observation conditions (the maximum azimuthal gaps, the number of stations, and the number of spectral ratios). Improving these observation conditions seems not significant for reducing the stress drop uncertainty.

I investigated the effect of  $f_{c2}$  on the stress drop estimates by conducting the spectral ratio analysis by fixing these parameters as specific values (Figure 4.14). For example, Shearer et al. (2019) showed that  $f_{c2}$  is sometimes hard to constrain well and affects the corner frequency of a target earthquake. I only focused on the effect of  $f_{c2}$  on the systematic error in the stress drop estimates by assuming that the spectral ratios were well estimated. This study demonstrates the two cases: (1) fix  $f_{c2}$  as low values, and (2) fix  $f_{c2}$  as high values. In this study, the fixed values of  $f_{c2}$  were determined as the multiplication of 1/1.5 (low) or 1.5 (high) to the best-fit  $f_{c2}$  values in the initial spectral ratio fitting (e.g., Figure 3.4b).

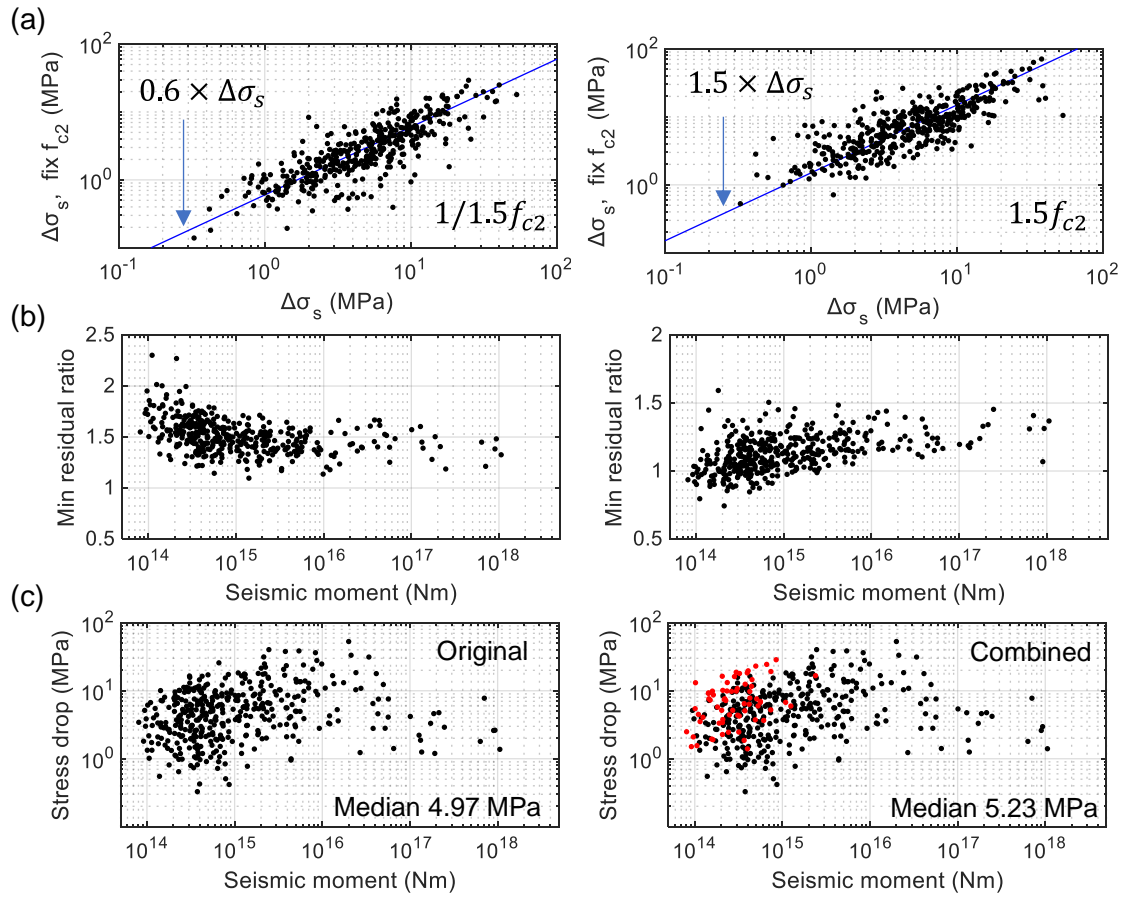


**Figure 4.14** Effect of  $f_{c2}$  on the stress drop estimates. (a) Stress drop comparison. The horizontal axis shows the stress drop obtained without fixing  $f_{c2}$ . The vertical axis shows the stress drop obtained with fixed  $f_{c2}$ . (b) Seismic moment versus the minimum residual ratio. The denominator of the minimum residual ratio is the minimum residual obtained without fixing  $f_{c2}$ . (c) Seismic moment versus stress drop for best-fit model. The left panel is the same as Figure 4.4 (best-fit model). The right panel is the combined result of the stress drops without fixing and  $f_{c2}$  and with fixing  $f_{c2}$  as high values. The red dots are the replaced results, and the black dots are the same as the original results. The replaced stress drops in the right panel were determined based on the minimum residuals.

Figure 4.14a compares the (best-fit) stress drops  $\Delta\sigma_s$  without and with fixing  $f_{c2}$ . If  $f_{c2}$  values are fixed as high (low), the stress drops become systematically higher (lower). Figure 4.14b shows the relationship between the seismic moment and the ratio of the minimum residuals obtained without and with fixing  $f_{c2}$ . The minimum residuals without fixing  $f_{c2}$  are systematically smaller than those with fixing  $f_{c2}$  as the low values (the left panel). This result suggests that the stress drops obtained by forcing low values of  $f_{c2}$  are not plausible. Besides, we see that the systematic errors of the stress

drops are less than a factor of 2.0 (the blue lines in Figure 4.14a). Therefore, the low resolutions of  $f_{c2}$  cannot cause the high values of the stress drop  $\Delta\sigma_R$  (the median of 67.9 MPa) compared to the typical values of 1 to 10 MPa. The minimum residuals without fixing  $f_{c2}$  are greater than those obtained by fixing  $f_{c2}$  as high values for 68 events (the right panel in Figure 4.14b). This tendency is remarkable in the events with  $M_0 < 10^{15}$  Nm. Figure 4.14c shows the relationships between the seismic moment and the stress drop  $\Delta\sigma_s$  for the best-fit model. The left panel shows the same result as Figure 4.4. The right panel shows the result of replacing the stress drops of the 68 events with those obtained by fixing  $f_{c2}$  as the high values. The effect of the stress drop replacement is not significant for the conclusion of the stress drop scaling relation (Figure 4.14c). The difference in the median values is about 5% (4.97 and 5.23 MPa).

## 4.6. DISCUSSION

### 4.6.1. Stress Drops

The rupture area estimated in this analysis is small compared with the overall rupture area and can be interpreted as corresponding to a local region with large slip (asperity). Thus, the developed spectral ratio approach is suitable for obtaining the rupture area with large slip (the largest asperity area). The average stress drops  $\Delta\sigma_s$  for the entire faults are obtained as 1 to 20 MPa with a median of 4.97 MPa by assuming the rupture area estimated from the spectral ratio analysis occupies 17.5% of the overall rupture area based on the result by Somerville et al., (1999). This result assumes that the average ratio of the asperity area to the overall rupture area does not vary significantly. For example, if the average area ratio varies to 22.5% or 12.5% from 17.5%, the stress drop estimates systematically change by a factor of 1.46 or 0.60, respectively, which does not alter the conclusions. The stress drops observed for the earthquakes with  $M_w$  3.2 to 6.0 are similar to those observed for large earthquakes (e.g., Aki, 1972; Kanamori & Anderson, 1975; Venkataraman & Kanamori, 2004). The stress drop estimates are consistent with the differential stress of 2 to 30 MPa (the shear stress of 1 to 15 MPa) obtained by Yoshida et al. (2015) in the Fukushima-Ibaraki region. This differential stress should be regarded as the regional average, and hence, it is compared with the median stress drop in this region (3.7 MPa).

In the source model incorporated in this study, the local stress drop is 5.7 times higher than the average static stress drop. The two different stress drop estimates ( $\Delta\sigma_s$  and  $\Delta\sigma_{la}$ ) may be helpful to reconcile some inconsistent stress drop values estimated from the different approaches. For example, the stress drop inferred from the laboratory friction experiment is more comparable to the local stress drop  $\Delta\sigma_{la}$  than the average static stress drop  $\Delta\sigma_s$  (Zielke et al., 2017). Another example can be found in Dreger et al. (2007).

One of the advantages of the developed stress drop estimation method over the single corner-frequency approach is that we can reduce the model-dependent bias and evaluate the model-dependent uncertainty. The corner frequency cannot be uniquely related to the stress drop  $\Delta\sigma_s$  (Figures 4.8 and 4.10). Considering the rupture speed in stress drop estimation is significant for calculating the radiation efficiency and the fracture energy (e.g., Kanamori & Brodsky, 2004; Kaneko & Shearer, 2015). The inverse correlation between rupture speed and stress drop is important in predicting ground motion (Causse & Song, 2015; Chounet et al., 2018). An earthquake with a high-stress drop does not necessarily cause a ground motion with high spectral amplitudes at high frequencies, i.e., it does not always have a high corner frequency (Atkinson & Beresnev, 1997).

The minimum residuals without fixing  $f_{c2}$  are usually better than with fixing  $f_{c2}$  for the earthquakes with  $M_w > 4.0$  ( $M_0 > 1.0 \times 10^{15}$  Nm) (Figure 4.14b). The corner frequency for earthquakes with  $M_w = 4.0$  is about 3.0 Hz which is approximately 1/10 times the high-frequency limit. Thus, a recommended high-frequency limit is more than 10.0 times the corner frequency of a target earthquake if the magnitudes of EGF events are about 1.0 to 2.0 units lower than the target event. The result obtained by fixing  $f_{c2}$  as high values showed better misfit values for 68 events with  $M_w < 4.0$  (right panels in Figure 4.14b). This result is probably because the high-frequency limit in the analysis (mostly 35 Hz) is inadequately low for evaluating  $f_{c2}$  for some events. However, Figure 4.14c shows that the influence of this result was not significant for the statistical tendency of the stress drop results, at least for the studied case. Note also that the misfit values without fixing  $f_{c2}$  are better for 70% of the earthquakes with  $M_w < 4.0$ . The maximum corner frequency for the analyzed earthquakes was 7.5 Hz, about 1/5 times the high-frequency limit. Hence, when the high-frequency limit is between 5.0 and 10.0 times the corner frequency of a target earthquake, the results may not often be biased significantly, but we need to check the stress drop result carefully. If the recommended value of 10.0 is

not satisfied, one better approach may be to test by fixing the high-frequency limits in the constraint ranges of  $f_{c2}$  as high values.

#### **4.6.2. Seismic Spectra and Localized Area with Large Slip**

The results of the spectral ratio fitting indicate that a compact area compared to the overall rupture area mainly controls the shape of a broadband seismic spectrum. The origin of this observation is the earthquake stress drop heterogeneity (e.g., Boatwright, 1988; Miyake et al., 2003). While important information about the total rupture area appears in the low-frequency spectral level, i.e., the value of the seismic moment, Miyake et al. (2003) showed that the characteristics of a strong motion generation area (SMGA), which is a compact area compared with the overall rupture area, can sufficiently reproduce near-source ground motions in a broadband frequency. They defined the SMGA as the area with relatively large slip velocities within a total rupture area and showed that the size and position of the SMGA match well with those of the area with large slips. The features of the SMGA are similar to those of the rupture area estimated in our spectral ratio analysis. The relationship between earthquake source heterogeneity and strong motion generation supports the conclusion that the small areas obtained by the spectral ratio analysis correspond to the localized regions with large slips that dominate the strong ground motions. In conclusion, I think that it is important to consider the heterogeneity of stress drop (or slip) distribution in addition to the rupture geometry, speed, and directivity when estimating the stress drops from seismic spectra.

Most of the analyzed earthquakes were estimated to rupture asymmetrically (Figure 3.8). Mai et al. (2005) showed that few earthquake ruptures start within the region of very-large-slip asperity. After an earthquake rupture nucleates at the hypocenter, the earthquake rupture starts to propagate and reach an area of large-slip-asperity. Then, the dynamic stress concentration at the rupture front breaks the large-slip asperity from its edge. Thus, the localized area with large slip often ruptures asymmetrically. Considering the discussion in the previous paragraph, it is plausible that we often observe earthquakes with asymmetric (unilateral) rupture propagations from seismic spectrum analysis. It is important to notice that the asymmetry of the earthquake rupture estimated from seismic spectra may not be the characteristic of an overall fault rupture but that of a localized area with large slip.

Often stress drop for small earthquakes is estimated by the source dimension derived from the shape of the seismic source spectrum (e.g., the corner frequency). In general, however, this extracted source dimension may not correspond to the overall rupture area, as discussed above, and needs to be corrected by considering the effect of the earthquake source heterogeneity. This problem was discussed in the pioneering work by Boatwright (1984). However, this problem has been less focused on in the analysis of small-to-moderate earthquakes, probably because the standard approach relates a corner frequency to a source dimension by assuming a source model *a priori*. The second moment approach is another tool to obtain the stress drops of small-to-moderate earthquakes considering the source geometry, rupture speed, and rupture directivity (McGuire, 2004; McGuire & Kaneko, 2018). The second moment approach estimates the finite source properties from the apparent characteristic duration (McGuire, 2004). Meng et al. (2020) applied the second moment approach to the small-to-moderate earthquakes in southern California and obtained relatively high values of the stress drop (4.5 to 186 MPa with a median of 41.8 MPa). In light of the results in this study, these high-stress drop estimates may imply a small area compared to the total rupture area controls the apparent characteristic duration.

### 4.6.3. Corner-Frequency-Based Stress Drop

In the corner-frequency-based stress drop estimation, the  $k_c$  value by Brune (1970) is useful to calculate average static stress drop, and the one obtained from the dynamic simulation of a crack model with a uniform stress drop (e.g., Madariaga, 1976; Kaneko & Shearer, 2015) is useful to calculate local stress drop (assuming the single asperity model). For example, Uchide & Imanishi et al. (2016) estimated the stress drops using the Madariaga model as 4 to 95 MPa with a median of 26 MPa in the Fukushima-Ibaraki region. Their stress drop estimates are consistent with the local stress drop  $\Delta\sigma_{la}$  (5 to 100 MPa with a median of 21 MPa in the Fukushima-Ibaraki region) rather than the average static stress drop  $\Delta\sigma_s$ . The dynamic crack simulation approach provides the  $k_c$  value by relating the corner frequency to the source radius of the crack model. If a large-slip asperity area controls the spectral shape of a natural earthquake, it should also dominate the corner frequency value. Hence, it may be reasonable that the stress drop estimated from the corner frequency and the  $k_s$  value derived by the dynamic crack simulation tends to be close to  $\Delta\sigma_{la}$  rather than  $\Delta\sigma_s$ .



The  $k_s$  value by Brune (1970) was derived differently from the dynamic simulation approach. Brune (1970) derived the spectral model at first. Then, he made an ad hoc assumption that the circular source radiates the model spectra. The radiation efficiency  $\eta'_R = 2\sigma_a/\Delta\sigma_s$  ( $\sigma_a$ : the apparent stress) helps explain why  $\Delta\sigma_{fc}$  calculated with the  $k_s$  value by Brune (1970) tends to be close to  $\Delta\sigma_s$  rather than  $\Delta\sigma_{la}$ . Only  $\Delta\sigma_{fc}$  calculated with the  $k_c$  value by Brune (1970) provides the plausible value of the radiation efficiency, 0.466, for the omega-square model (e.g., Ji et al., 2022). This radiation efficiency value is consistent with the previous study of large earthquakes on average (e.g., Venkataraman & Kanamori, 2004). Therefore, the  $k_s$  value by Brune (1970) provides the average static stress drop rather than the local stress drop. For example, the radiation efficiency becomes about 0.08 when using the  $k_s$  value by Madariaga (1976) for the apparent stress calculated with the omega-square spectrum by Brune (1970). There is no inherent reason that a simple circular source model explains all aspects of a heterogeneous earthquake. The radiation efficiency of about 0.4 to 0.6, often implied from a standard circular crack simulation, appears to be a good approximation of the average radiation efficiency of typical crustal earthquakes. However, the relationship between the corner frequency and source radius obtained using a uniform stress drop crack model may not be appropriate to estimate the total rupture area of a heterogeneous earthquake.

The corner-frequency-based approach can be used to estimate the average of the stress drop of numerous earthquakes only if the  $k_c$  value is appropriate. A plausible median of the  $k_s$  value for the shallow crustal earthquakes implied in this study was 0.40, which is higher than 0.372 by Brune (1970). Recently, Ji et al. (2022) implied that the  $k_s$  value of 0.41 is plausible for shallow crustal earthquakes. The result of this study is consistent with the implication by Ji et al. (2022).

## 4.7. CONCLUSIONS

This chapter revealed that the rupture area estimated by the spectral ratio approach developed in this study is small compared with the total rupture area and can be interpreted as a localized rupture area with large slip. Thus, a compact rupture area compared with the total rupture area dominantly controls the source spectral shapes in a broadband range. This conclusion implies that the idea of the strong motion generation area (SMGA) is significant for small-to-moderate earthquakes. Since an earthquake

rupture often initiates from outside the localized area with large slip, the rupture front tends to break the large-slip asperity area from its edge. Combining this fact with the result that a compact area compared with the overall rupture area controls the shape of a source spectrum dominantly, it is plausible that most of the analyzed earthquakes were estimated to have asymmetric rupture propagation, as found in the previous chapter.

The comparison of the estimated rupture area  $LW$  with the result by Somerville et al. (1999) suggests that the estimated rupture area can be 17.5% of the total rupture area on average. The average static stress drops  $\Delta\sigma_s$  were calculated using the 17.5% area ratio and are within a typical range of 1 to 20 MPa. They increase with the seismic moment in  $M_0 > 5.0 \times 10^{16}$  Nm ( $M_w > 5.1$ ) and tend to be scale-independent in  $M_0 < 5.0 \times 10^{16}$  Nm. They are not strongly dependent on faulting type but increase with depth weakly. Comparing the stress drops of the large earthquakes in Table 3.1 with the estimated stress drops  $\Delta\sigma_s$  supports the validity of the stress drop calculation. Thus, I conclude that the spectral ratio approach developed in this study is effective for estimating the average static stress drop considering the rupture speed, geometry, and rupture start point.

The  $\log_{10}V_{rmax}$  and  $\log_{10}\Delta\sigma_s$  are inversely correlated with a correlation coefficient of  $-0.55$ . Specifically,  $\Delta\sigma_s \propto V_{rmax}^{-3}$ . An earthquake with a high value of the stress drop  $\Delta\sigma_s$  does not necessarily cause ground motions with high spectral amplitudes at high frequencies due to the inverse correlation between the stress drop and rupture speed. Obvious dependences of the stress drop  $\Delta\sigma_s$  on depth and focal mechanism were not found.

The  $k_s$  values were estimated from the corner frequencies and the estimated rupture area. The median and mean of the  $k_s$  value are 0.388 and 0.42, respectively. The  $k_s$  value of 0.40 provides the median value of  $\Delta\sigma_{fc}$  similar to that of  $\Delta\sigma_s$ . The  $k_s$  value by Brune (1970) is useful to calculate average static stress drop, and the one obtained from the dynamic simulation of a crack model with a uniform stress drop (e.g., Madariaga, 1976) is useful to calculate local stress drop under the assumption of the single asperity model. The corner-frequency-based approach may be helpful to the stress drop variability investigation (Figure 4.9). However, we should recognize that the between event variability of the  $k_s$  value is significantly large (Figure 4.8). The standard deviation of the  $k_s$  value is 0.112. In conclusion, the rupture geometry, speed, directivity, and source heterogeneity should be considered when estimating the stress drops from seismic spectra.

## REFERENCES

- Aki, K. (1972). Earthquake mechanism. *Tectonophysics*, **13**, 423–446.
- Atkinson, G. M., & Beresnev, I. (1997). Don't call it stress drop. *Seismological Research Letters*, **68**(1), 3–4.
- Boatwright, J. (1984). The effect of rupture complexity on estimates of source size. *Journal of Geophysical Research: Solid Earth*, **89**(B2), 1132–1146.
- Boatwright, J. (1988). The seismic radiation from composite models of faulting. *Bulletin of the Seismological Society of America*, **78**(2), 489–508.
- Boatwright, J. (2007). The persistence of directivity in small earthquakes. *Bulletin of the Seismological Society of America*, **97**(6), 1850–1861.
- Brown, L., Wang, K., and Sun, T. (2015). Static stress drop in the  $M_w$  9 Tohoku-oki earthquake: Heterogeneous distribution and low average value. *Geophysical Research Letters*, **42**, 10,595–10,600.
- Brune, J. N. (1970). Tectonic stress and the spectra of seismic shear waves from earthquakes, *Journal of Geophysical Research*, **75**(26), 4997–5009.
- Causse, M., & Song, S. G. (2015). Are stress drop and rupture speed of earthquakes independent? Insight from observed ground motion variability. *Geophysical Research Letters*, **42**(18), 7383–7389.
- Chounet, A., Vallée, M., Causse, M., & Courboulex, F. (2018). Global catalog of earthquake rupture velocities shows anticorrelation between stress drop and rupture speed. *Tectonophysics*, **733**, 148–158.
- Das, S., & Kostrov B. V. (1986). Fracture of a single asperity on a finite fault: a model for weak earthquakes? in *Earthquake Source Mechanics*, S. Das, J. Boatwright, and C. H. Scholz (Editors), American Geophysical Monograph, **37**, 91–96.
- Dreger, D., Nadeau, R. M., & Chung, A. (2007). Repeating earthquake finite source models: Strong asperities revealed on the San Andreas Fault. *Geophysical Research Letters*, **34**, L23302.
- Ji, C., Archuleta, R. J., & Wang, Y. (2022). Variability of spectral estimates of stress drop reconciled by radiated energy. *Bulletin of the Seismological Society of America*, **112**, 1871–1885.

- Kanamori, H., & Anderson, D. L. (1975). Theoretical basis of some empirical relations in seismology. *Bulletin of the Seismological Society of America*, **65**(5), 1073–1095.
- Kanamori, H., & Brodsky, E. E. (2004). The physics of earthquakes. *Reports on Progress in Physics*, **67**(8), 1429–1496.
- Kanamori, H., & Rivera, L. (2004). Static and dynamic scaling relations for earthquakes and their implications for rupture speed and stress drop. *Bulletin of the Seismological Society of America*, **94**(1), 314–319.
- Kaneko, Y., & Shearer, P. M. (2015). Variability of source spectra, estimated stress drop, and radiated energy, derived from cohesive-zone models of symmetrical and asymmetrical circular and elliptical ruptures. *Journal of Geophysical Research: Solid Earth*, **120**(2), 1053–1079.
- Kim, A., Dreger, D. S., Taira, T., & Nadeau, R. M. (2016). Changes in repeating earthquake slip behavior following the 2004 Parkfield main shock from waveform empirical Green's functions finite-source inversion. *Journal of Geophysical Research: Solid Earth*, **121**, 1910–1926.
- Madariaga, R. (1976). Dynamics of an expanding circular fault. *Bulletin of the Seismological Society of America*, **66**(3), 639–666.
- Madariaga, R. (1979). On the relation between seismic moment and stress drop in the presence of stress and strength heterogeneity. *Journal of Geophysical Research: Solid Earth*, **84**(B5), 2243–2250.
- Mai, P. M., Spudich, P., & Boatwright, J. (2005). Hypocenter locations in finite-source rupture models. *Bulletin of the Seismological Society of America*, **95**(3), 965–980.
- McGarr, A. (1981). Analysis of peak ground motion in terms of a model of inhomogeneous faulting. *Journal of Geophysical Research: Solid Earth*, **86**(B5), 3901–3912.
- McGuire, J. J. (2004). Estimating finite source properties of small earthquake ruptures. *Bulletin of the Seismological Society of America*, **94**(2), 377–393.
- McGuire, J. J. & Kaneko, Y. (2018). Directly estimating earthquake rupture area using second moments to reduce the uncertainty in stress drop. *Geophysical Journal International*, **214**(3), 2224–2235.
- Meng, H., McGuire, J. J., & Ben-Zion, Y. (2020). Semiautomated estimates of directivity and related source properties of small to moderate southern California earthquakes using second seismic moments. *Journal of Geophysical Research: Solid Earth*, **125**, e2019JB018566.
- Miyake, H., Iwata, T., & Irikura, K. (2003). Source characterization for broadband ground-motion

- simulation: kinematic heterogeneous source model and strong motion generation area. *Bulletin of the Seismological Society of America*, **93**(6), 2531–2545.
- Rudnicki, J. W., & Kanamori, H. (1981). Effects of fault interaction on moment, stress drop, and strain energy release. *Journal of Geophysical Research: Solid Earth*, **92**(B12), 1785–1793.
- Shearer, P. M., Abercrombie, R. E., Trugman, D. T., & Wang, W. (2019). Comparing EGF methods for estimating corner frequency and stress drop from P wave spectra. *Journal of Geophysical Research: Solid Earth*, **124**(4), 3966–3986.
- Shimmoto, S. (2022). Stress drop estimates for small to moderate earthquakes in Tohoku, Japan considering rupture geometry, speed, and directivity. *Journal of Geophysical Research: Solid Earth*, **127**, e2022JB025157.
- Somerville, P., Irikura K., Graves R., Sawada S., Wald D., Abrahamson N., Iwasaki Y., Kagawa T., Smith N., & Kowada A. (1999). Characterizing crustal earthquake slip models for the prediction of strong ground motion. *Seismological Research Letters*, **70**(1), 59–80.
- Uchide, T. & Imanishi, K. (2016). Small earthquakes deviate from the omega-square model as revealed by multiple spectral ratio analysis. *Bulletin of the Seismological Society of America*, **106**(3), 1357–1363.
- Venkataraman, A., & Kanamori, H. (2004). Observational constraints on the fracture energy of subduction zone earthquakes. *Journal of Geophysical Research*, **109**, B05302.
- Yamada, T., Mori, J., Ide S., Kawakata, H., Iio, Y., & Ogasawara, H (2005). Radiation efficiency and apparent stress of small earthquakes in a South African gold mine. *Journal of Geophysical Research: Solid Earth*, **110**, B01305.
- Yoshida, K., Hasegawa, A., & Okada, T. (2015). Spatially heterogeneous stress field in the source area of the 2011 Mw 6.6 Fukushima-Hamadori earthquake, NE Japan, probably caused by static stress change. *Geophysical Journal International*, **201**(2), 1062–1071.
- Zielke, O., Galis, M., & Main, P., M. (2017). Fault roughness and strength heterogeneity control earthquake size and stress drop. *Geophysical Research Letters*, **44**, 777–783.

## Chapter 5

# EARTHQUAKE ENERGY BUDGET AND SOURCE PARAMETER SCALING RELATIONS

### 5.1. OVERVIEW

The previous chapter studied the average static stress drop  $\Delta\sigma_s$ . Another observable physical quantity in seismology is the radiated energy  $E_R$ . The average static stress drop and radiated energy are fundamental for understanding the energy budget during an earthquake. For example, the radiation efficiency is calculated from the apparent stress and the average static stress drop. However, the stress drop calculated from the seismic moment and rupture area, the moment-based stress drop  $\Delta\sigma_s$ , can be inappropriate for studying the earthquake energy budget, e.g., the evaluation of the radiation efficiency (Noda et al., 2013). Thus, at first, this chapter proposes a way to obtain the energy-related stress drop  $\Delta\sigma_E$ , which is appropriate for studying the earthquake energy partitioning, based on the single asperity model introduced in the previous chapter. Then, this chapter provides the radiated energy estimates for the shallow crustal earthquakes analyzed in the previous chapters and investigates the relationship between the seismic moment and the stress drop, the scaled energy  $E_R/M_0$  (or the apparent stress  $\sigma_a$ ), and the radiation efficiency. Furthermore, the relationship between the fracture energy and slip is studied.

## 5.2. EARTHQUAKE ENERGY BUDGET AND STRESS DROP

The overview of the earthquake energy budget is described briefly. More detailed descriptions can be found in, for example, Kostrov & Das (1988), Kanamori & Brodsky (2004), and Kanamori & Rivera (2006). The occurrence of an earthquake releases the potential energy  $E_p$  (the elastic strain energy accumulated by crustal deformation and gravitational energy) as the radiated energy  $E_R$ , fracture energy (or breakdown energy)  $E_G$ , and frictional energy (or thermal energy),  $E_F$ . The fracture energy is the energy involved with all resistance to rupture propagation, e.g., cracking, yielding, and latent heat due to thermal pressurization or melting. The frictional energy is interpreted as the remaining energy dissipated other than the radiated energy and the fracture energy,  $E_F = E_p - E_R - E_G$ . The potential energy change before and after an earthquake is expressed as follows.

$$\Delta W = \frac{1}{2}(\sigma_0 + \sigma_1)DS = \frac{1}{2}\overline{\Delta\sigma}DS + \sigma_1DS = E_R + E_G + E_F \quad (5.1)$$

where  $\sigma_0$  is the average initial stress,  $\sigma_1$  is the average final stress,  $D$  is the average slip,  $S$  is the rupture area. The average static stress drop is  $\overline{\Delta\sigma} = \sigma_0 - \sigma_1$ . The radiation efficiency  $\eta_R$  is the ratio of the radiated energy to the sum of the radiated energy and the fracture energy,  $\eta_R = E_R/(E_R + E_G)$ .

Figure 5.1 illustrates the relationship between stress and slip during an earthquake for a simple stress relaxation model (a slip-weakening model). Figure 5.1a shows a simple slip-weakening model in which there is no stress undershoot and overshoot, i.e., the dynamic stress  $\sigma_d$  is equal to the final stress  $\sigma_1$ . In this case, we can evaluate the radiation efficiency from seismologically observable quantities:

$$\eta_R = \frac{E_R}{E_R + E_G} = \frac{E_R}{1/2\overline{\Delta\sigma}DS} = 2\mu \frac{E_R}{M_0} \frac{1}{\overline{\Delta\sigma}} = 2 \frac{\sigma_a}{\overline{\Delta\sigma}} \quad (5.2)$$

where  $M_0$  is the seismic moment, and  $\sigma_a$  is the apparent stress  $\sigma_a = \mu E_R/M_0$  ( $\mu$ : shear rigidity). The sum of the radiated energy and fracture energy is called the available energy,  $\Delta W_0 = E_R + E_G$  (Husseini & Randall, 1976). Figure 5.1 illustrates that the available energy per unit area  $\Delta W_0/S$  is equal to  $1/2\overline{\Delta\sigma}D$ . The radiation efficiency  $\eta_R$  quantifies the ratio of the radiated energy to the available energy. For example, a low radiation efficiency implies that a large amount of the available energy is dissipated as the fracture energy. The fracture energy per unit area for the stress relaxation model in Figure 5.1 is defined as:

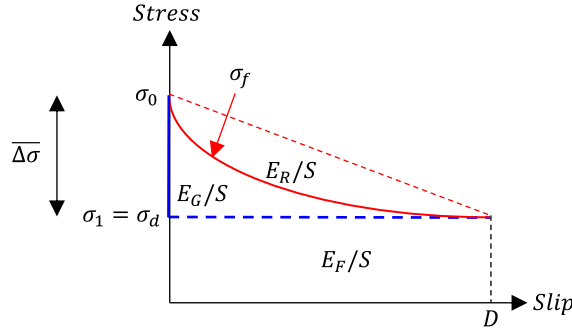


**Figure 5.1** Graphic descriptions of the earthquake energy budget without stress overshoot and undershoot. The solid red curve represents the frictional stress  $\sigma_f$ . The radiated energy per unit area  $E_R/S$  is enclosed by the dashed red line and solid red curve. The fracture energy per unit area  $E_G/S = G$  is enclosed by the solid red curve, solid blue line, and dashed blue curve.

$$G = \frac{E_G}{S} = \int_0^D (\sigma_f(u) - \sigma_d) du = \frac{1}{2}(\overline{\Delta\sigma} - 2\sigma_d)D \quad (5.3)$$

where  $\sigma_f$  is the frictional stress (the shear stress on fault during slip) and  $\sigma_d = \sigma_1 = \sigma_f(D)$  indicates the residual stress level (Abercrombie & Rice, 2005). The frictional energy is  $E_F = \sigma_1 DS$ , which is not seismologically measurable. Equations (5.2) and (5.3) were derived under the assumption of the simple slip-weakening model, although a real earthquake can have a more complex stress relaxation process. However, it is advantageous that we can evaluate the radiation efficiency and fracture energy from seismologically inferable source parameters ( $M_0$ ,  $\overline{\Delta\sigma}$ ,  $E_R$ , and  $D$ ) using equations (5.2) and (5.3).

The physical quantities in Figure 5.1 are average values, and there are several ways to calculate an average value of stress drop. A common approach is to calculate average static stress drop from the seismic moment  $M_0$  and the rupture area  $S$  (the moment-based stress drop). An example of the moment-based stress drop is (Eshelby, 1957; Kanamori & Anderson, 1975).

$$\Delta\sigma_s = \frac{7M_0}{16(S/\pi)^{3/2}} \quad (5.4)$$

In the previous chapter, the average static stress drops  $\Delta\sigma_s$  were calculated based on equation (5.4) using the rupture area estimated from the spectral ratio analysis, see equation (4.1). The moment-based stress drop has been used frequently since equation (5.4) requires only simple physical quantities  $M_0$  and  $S$ . The stress drop calculated with equation (5.4) corresponds to the spatial average of the stress drop weighted by the slip distribution calculated for the circular crack model with a uniform stress drop (Madariaga, 1979; Noda, 2013). The critical point is that the moment-based stress drop is not the spatial



average of the stress drop weighted by the actual slip distribution. The radiation efficiency calculated with  $\Delta\sigma_s$  is expressed as  $\eta'_R = 2\sigma_a/\Delta\sigma_s$  in this study.

The average static stress drop  $\Delta\sigma_E$  calculated by weighting the stress drop by the actual slip distribution (obtained from a finite fault inversion in practice) is necessary useful for investigating the energy partitioning during an earthquake (Noda et al., 2013). In this study, this average stress drop is called the energy-related stress drop,  $\Delta\sigma_E$ . The energy-related stress drop  $\Delta\sigma_E$  is calculated as

$$\Delta\sigma_E = \frac{\int_{\Sigma} \Delta\sigma_1 \Delta u_1 dS}{\int_{\Sigma} \Delta u_1 dS} \quad (5.5)$$

where  $\Delta\sigma_1$  and  $\Delta u_1$  are (local) stress drop and slip at each point of the studied fault, and  $\Sigma$  indicates that the integral is taken over the entire fault plane (Noda et al., 2013; Ye et al., 2016). Noda et al. (2013) showed the energy-related stress drop is always greater than or equal to the moment-based stress drop. The energy-related stress drop and the moment-based stress drop take similar values if the stress drop distribution is relatively uniform. Since earthquakes have heterogeneous stress drop distribution mostly, the radiation efficiency calculated with  $\Delta\sigma_s$ ,  $\eta'_R = 2\sigma_a/\Delta\sigma_s$ , can cause systematic overestimations. The radiation efficiency is preferred to be calculated with the energy-based stress drop  $\Delta\sigma_E$ , that is,  $\eta_R^E = 2\sigma_a/\Delta\sigma_E$ .

The single asperity model, introduced in the previous chapter, enables us to calculate the energy-related stress drop by using the seismic moment and the rupture area estimated from the spectral ratio analysis. The single asperity model assumes that the stress drop is concentrated on the localized area (the asperity area) and is zero outside this localized area. Suppose that the ratio of the asperity area  $S_1$  to the total rupture area  $S$  is 17.5%,  $S_1 = 0.175S$  (Chapter 4). In this case, under the assumption of the single asperity model, the average stress drop on the asperity area is  $\Delta\sigma_{la} = \Delta\sigma_s/0.175$ . The stress drop distribution on the large-slip asperity area estimated by the spectral ratio analysis is expected to be relatively homogeneous. Therefore, the stress drop on the asperity area is assumed to be uniform as  $\Delta\sigma_{la}$ . Since the seismic moment released on the asperity area is  $\sqrt{0.175}M_0$ , the slip on the asperity area is

$$D_1 = \frac{\sqrt{0.175}M_0}{\mu 0.175S} = \frac{D}{\sqrt{0.175}} \quad (5.6)$$

where  $D = M_0/(\mu S)$ . Similarly, the slip on the rupture region outside the asperity area is

$$D_2 = \frac{1(1 - \sqrt{0.175})M_0}{\mu(1 - 0.175)S} = 0.705D \quad (5.7)$$

Finally, the energy-related stress drop  $\Delta\sigma_E$  for the single asperity model is

$$\Delta\sigma_E = \frac{\Delta\sigma_{ta}D_1S_1 + 0 \cdot D_2S_2}{D_1S_1 + D_2S_2} = \frac{1}{\sqrt{0.175}}\Delta\sigma_s \approx 2.4\Delta\sigma_s \quad (5.8)$$

where  $S_2 = (1 - 0.175)S$ . The result suggests that  $\eta'_R = 2.4\eta_R^E$  under the single asperity model assumption. This chapter provides the radiation efficiency  $\eta_R^E$  calculated from the seismic moment and source area by assuming the relation  $\eta_R^E = \eta'_R/2.4$ .

### 5.3. METHOD OF RADIATED ENERGY ESTIMATION

The radiated energy is computed from the following equation (Venkataraman & Kanamori, 2004).

$$E_R = \left[ \frac{8\pi}{15\rho V_P^5} + \frac{8\pi}{10\rho V_S^5} \right] \int_0^\infty f^2 |\Omega(f)|^2 df \quad (5.9)$$

where  $\rho$  is the density,  $f$  is the frequency, and  $V_P$  and  $V_S$  are the P- and S-wave velocities, respectively. The S-wave velocity is typically 3.4 km/s.  $|\Omega(f)|$  is the displacement source spectral amplitude. I obtained  $|\Omega(f)|$  from the spectral ratios stacked over all stations. A difficulty in evaluating the radiated energy is a limited frequency bandwidth. For example, Ide & Beroza (2001) show that a limited frequency bandwidth can cause systematic underestimation of the radiated energy. Prieto et al. (2004) calculated  $|\Omega(f)|$  using the model-predicted spectrum rather than the observed data. Then, they conducted the integration by extending the upper integration limit to avoid underestimating the radiated energy. Following Prieto et al. (2004), I calculated the radiated energy using the model-predicted spectrum of equation (5.10).

$$|\Omega(f)| = \frac{M_0}{\left\{ 1 + \left( \frac{f}{f_{c1}} \right)^{2\gamma} \right\}^{\frac{1}{\gamma}}} \quad (5.10)$$

where  $M_0$  is the seismic moment,  $f_{c1}$  is the corner frequency of a target earthquake, and  $\gamma$  indicates the sharpness of spectral corner, assuming  $1.0 \leq \gamma \leq 2.0$ . The falloff rate was assumed to be 2.0 since the falloff rate of the envelope spectrum is proportional to  $f^{-2}$  at a high frequency range. I fitted the spectral ratio model of equation (5.11) to the normalized average spectral ratios for S-wave in order to estimate  $f_{c1}$  and  $\gamma$ .

$$SR_{\omega 2} = \left\{ \frac{1 + \left(\frac{f}{f_{c2}}\right)^{2\gamma}}{1 + \left(\frac{f}{f_{c1}}\right)^{2\gamma}} \right\}^{\frac{1}{\gamma}} \quad (5.11)$$

where  $f_{c2}$  is the corner frequency of a stacked spectrum of EGFs. The radiated energies were computed from equation (5.9) and the source spectrum model of equation (5.10). The  $f_{c1}$  and  $\gamma$  of the source spectrum model were estimated from S-wave spectra. Figure 5.2a shows the spectral ratio fitting to the average spectral ratio. Figure 5.2b demonstrates three average source spectra: observed (red),  $|\Omega(f)|/M_0$  (dashed blue), and the envelope spectrum (green). The observed spectrum in Figure 5.2b was synthesized by multiplying the normalized omega-square model calculated using  $f_{c2}$  and  $\gamma$ , estimated by the spectral ratio fitting, to the observed average spectral ratio (the red curve in Figure 5.2a).

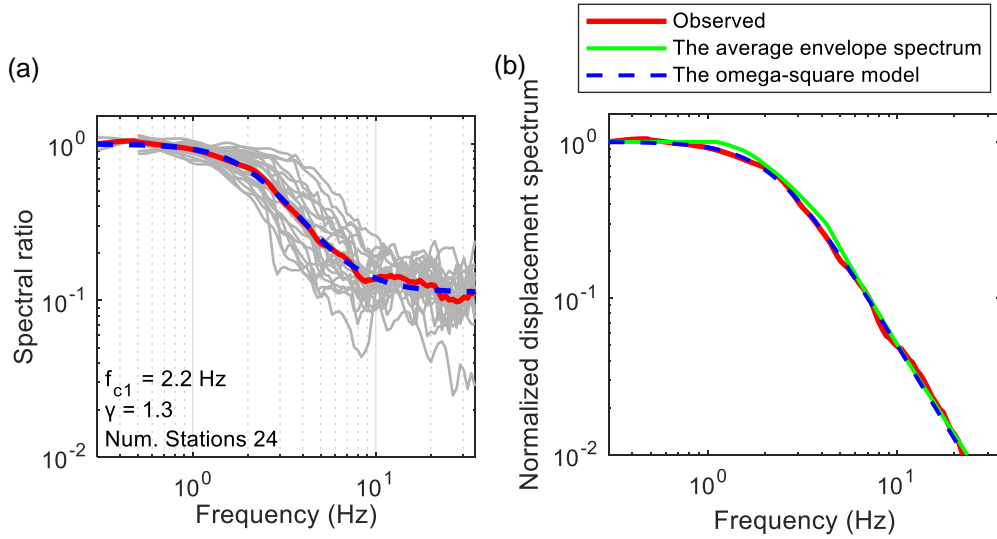


**Figure 5.2** Example of estimating the average source spectrum. (a) Spectral ratio fitting result. The red curve is the average observed spectral ratio, and the dashed blue curve is the prediction from the omega-square model. The gray curves are the observed spectral ratios obtained for each station. (b) Comparison between the observed average spectrum (red), the average envelope spectrum (green), and the normalized omega-square model  $|\Omega(f)|/M_0$  (dashed blue).

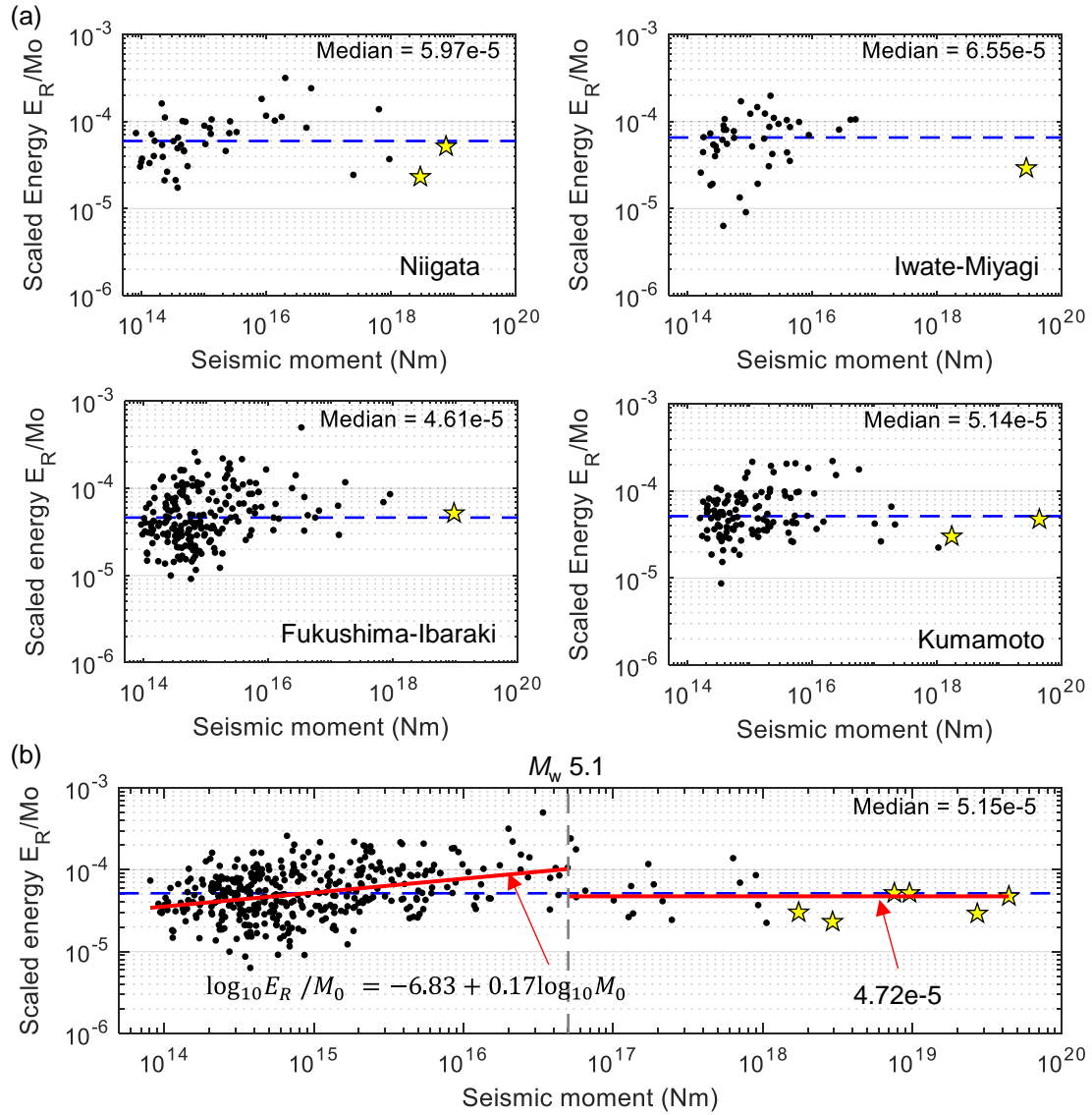


**Figure 5.3** The relationship between the scaled energy and the seismic moment. (a) Results for each target region. (b) Results combined for all target regions. The black dots are the estimates in this study, and the yellow stars are the estimates by Kanamori et al. (2020). The red inclined line shows the regression result obtained for  $M_w < 5.1$ . The horizontal red line indicates the median value at  $M_w > 5.1$ .

## 5.4. RESULTS

### 5.4.1. Radiated Energy and Stress Drop

Figure 5.3 shows the relationship between the radiated energy divided by the seismic moment (the scaled energy  $E_R/M_0$ ) and the seismic moment. The yellow stars in Figure 5.3 are the scaled energies calculated for the large earthquakes observed in the target regions by referring to Kanamori et al. (2020).

Table 5.1 summarizes the source parameters for the large earthquakes used in this study. The Fukushima-Ibaraki (normal faulting) and Kumamoto (strike-slip) regions have slightly smaller scaled energies than other regions (reverse faulting) (Figure 5.3a). The scaled energies estimated in this study are consistent with ones obtained by Kanamori et al. (2020) (the yellow stars).

Figure 5.3b summarizes the scaling relation of the scaled energy for all regions. The median is  $5.15 \times 10^{-5}$ . The scaled energy increases with the seismic moment and becomes relatively independent of the seismic moment at near  $M_0 = 5.0 \times 10^{16}$  Nm ( $M_w = 5.1$ ), as we saw for the stress drop scaling relation in the previous chapter. I conducted the regression analysis for the events with  $M_w < 5.1$ . The regression result between the scaled energy and the seismic moment (the red line for  $M_w < 5.1$  in Figure 5.3b) is

$$\log_{10} E_R / M_0 = -6.83 + 0.17 \log_{10} M_0 \quad (5.12)$$

Several studies suggest that the scaled energy (or the apparent stress) is independent of the seismic moment at a large magnitude range (e.g., Choy & Boatwright, 1995; Kanamori et al., 2020; Ye et al.,

**Table 5.1.** Source parameters of large earthquakes in the target regions.

Earthquake	$M_0$ (Nm)*	$E_R$ (J)**	$S$ (km <sup>2</sup> )	$D$ (m)†	$\Delta\sigma_s$ (MPa) ††	References
Mid Niigata (Chuetsu) 2004	7.5e+18	3.9e+14	300	0.8	3.6	Kanamori et al. (2020) Miyazawa et al. (2005) Asano & Iwata. (2009)
Mid Niigata (Chuetsu) 2004 aftershock	2.9e+18	6.8e+13	144	0.7	4.1	Kanamori et al. (2020) Miyazawa et al. (2005)
Iwate Miyagi 2008	2.7e+19	7.9e+14	720	1.3	3.4	Kanamori et al. (2020) Yokota et al. (2009) Suzuki et al. (2010)
Fukushima Hamadori 2011	9.6e+18	5.0e+14	350	0.9	3.6	Kanamori et al. (2020) Anderson et al. (2013) Tanaka et al. (2014)
Kumamoto foreshock 2016	1.7e+18	5.2e+13	144	0.4	2.5	Kanamori et al. (2020) Asano et al. (2016)
Kumamoto 2016	4.4e+19	2.9e+15	825	1.8	4.5	Kanamori et al. (2020) Yoshida et al. (2016) Asano & Iwata (2021)

\* The seismic moment values were obtained from F-net.

\*\*The apparent stress can be calculated as  $\mu E_R / M_0$ , where  $\mu$  is the shear rigidity (assumed to be 30 GPa).

† The values of slip  $D$  were calculated as  $M_0 / (\mu S)$ , where  $\mu$  is assumed to be 30 GPa.

††The stress drops were calculated with equation (5.4)

2016). Therefore, I regarded that the scaled energy is scale-independent in  $M_w \geq 5.1$  (the horizontal red line in Figure 5.3b). Note that the choice of the reference magnitude  $M_w = 5.1$  is just for simplicity and not conclusive.

As described in the previous chapter, the stress drops tend to increase with the seismic moment in  $M_w < 5.1$  and become independent of the seismic moment from near  $M_w = 5.1$  (Figure 5.4a). I conducted the regression analysis for the data where  $M_w < 5.1$  and obtained the trend of the stress drop increase with the magnitude (the red line for  $M_w < 5.1$ ). The regression result shows the relation  $\Delta\sigma_s \propto M_0^{0.25}$ :

$$\log_{10}\Delta\sigma_s = -3.07 + 0.25\log_{10}M_0 \quad (5.13)$$

For  $M_w > 5.1$ , Figure 5.4a and the previous studies (e.g., Aki, 1972; Kanamori & Anderson, 1975; Ye et al., 2016) suggest that the stress drop is independent of the seismic moment.

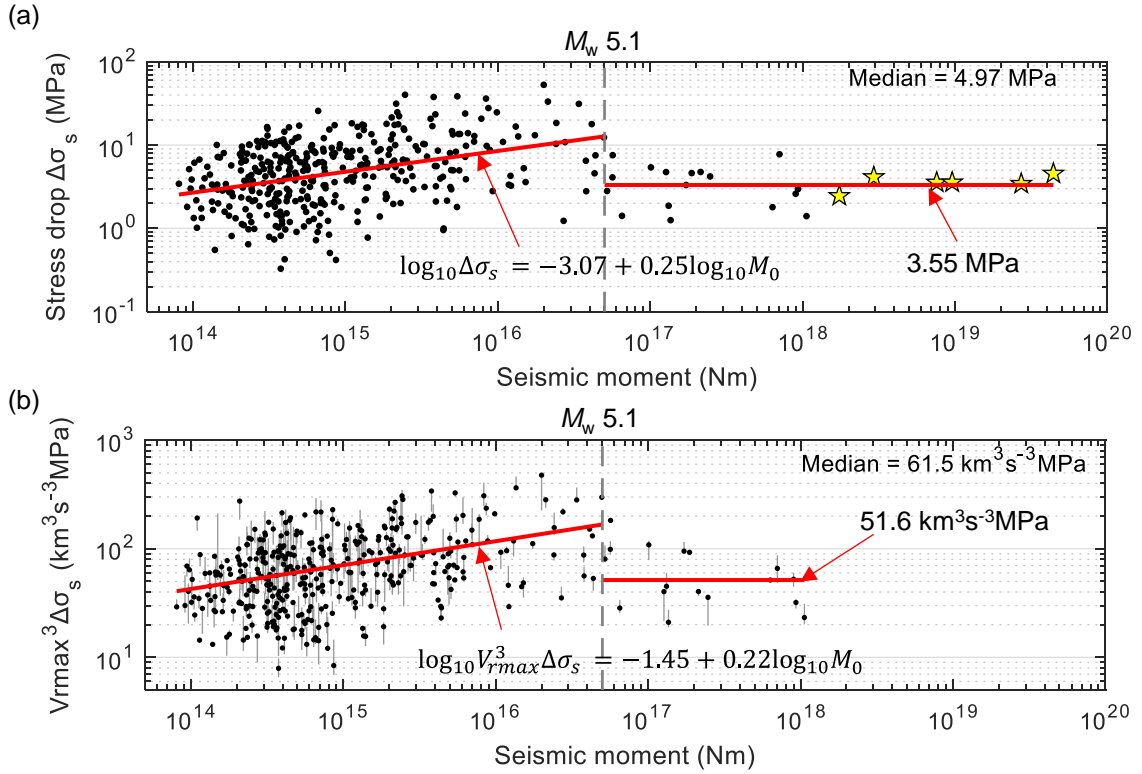


**Figure 5.4** The scaling relations of the moment-based stress drop  $\Delta\sigma_s$  and the produce of the cube of rupture speed and the moment-based stress drop,  $V_{rmax}^3\Delta\sigma_s$ . (a) The relationship between the seismic moment and  $\Delta\sigma_s$  (the best-fit models). The yellow stars are from Table 5.1. (b) The relationship between the seismic moment and  $V_{rmax}^3\Delta\sigma_s$ . The vertical gray lines show the uncertainties (the upper and lower bounds). The inclined red line shows the regression result obtained for  $M_w < 5.1$ . The horizontal red line indicates the median value at  $M_w > 5.1$ .

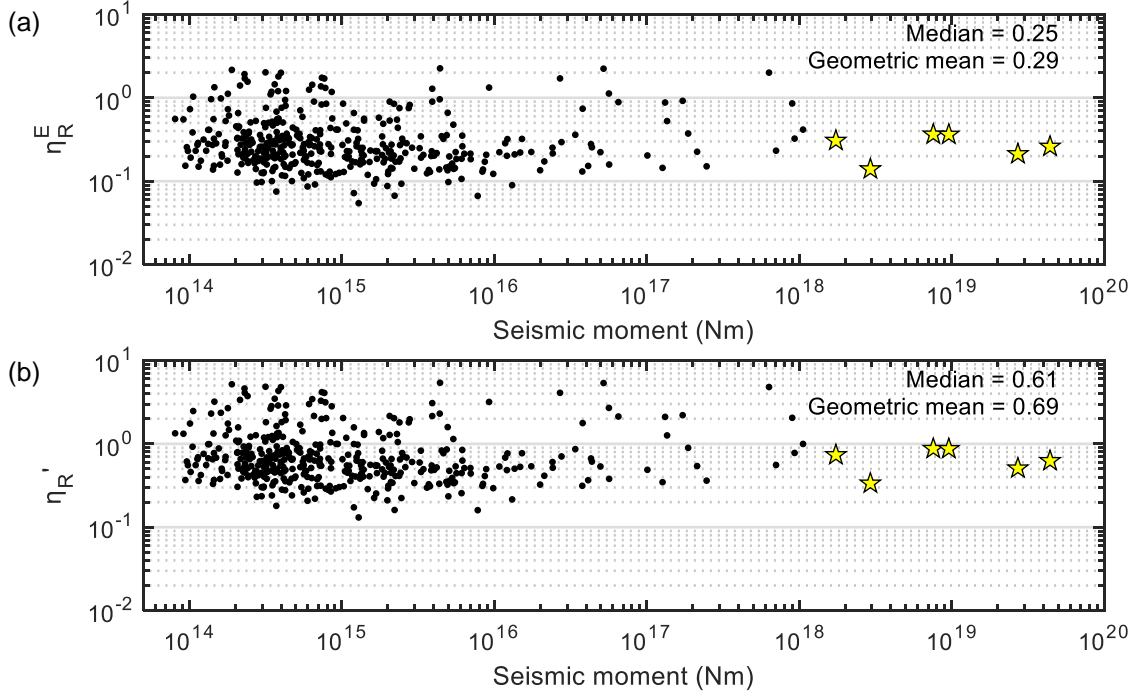


**Figure 5.5** The relationship between the seismic moment and radiation efficiencies (a)  $\eta_R^E = 2\sigma_a/\Delta\sigma_E$  and (b)  $\eta_R' = 2\sigma_a/\Delta\sigma_s = 2.4\eta_R^E$ . The yellow stars are the radiation efficiencies calculated for the earthquakes in Table 5.1. The dashed-horizontal blue lines indicate the median values.

The scaling relation of the product of the cube of the rupture speed  $V_{rmax}$  and the stress drop  $\Delta\sigma_s$ ,  $V_{rmax}^3\Delta\sigma_s$ , is similar to that of the stress drop  $\Delta\sigma_s$  (Figure 5.4b). Ye et al. (2016) observed that the product  $V_{rmax}^3\Delta\sigma_s$  is stable (small uncertainty) due to the trade-off between the  $\Delta\sigma_s$  and  $V_{rmax}$  in the source parameter estimation. The same tendency was observed in this study. Hence, the existence of the transition of the scale dependence of  $V_{rmax}^3\Delta\sigma_s$  is reliable. The relationship between the seismic moment and  $V_{rmax}^3\Delta\sigma_s$  in  $M_w < 5.1$  is

$$\log_{10} V_{rmax}^3 \Delta\sigma_s = -1.45 + 0.22 \log_{10} M_0 \quad (5.14)$$

The seismic moment dependency,  $V_{rmax}^3\Delta\sigma_s \propto M_0^{0.22}$ , is similar to that of  $\Delta\sigma_s$ ,  $\Delta\sigma_s \propto M_0^{0.25}$ .

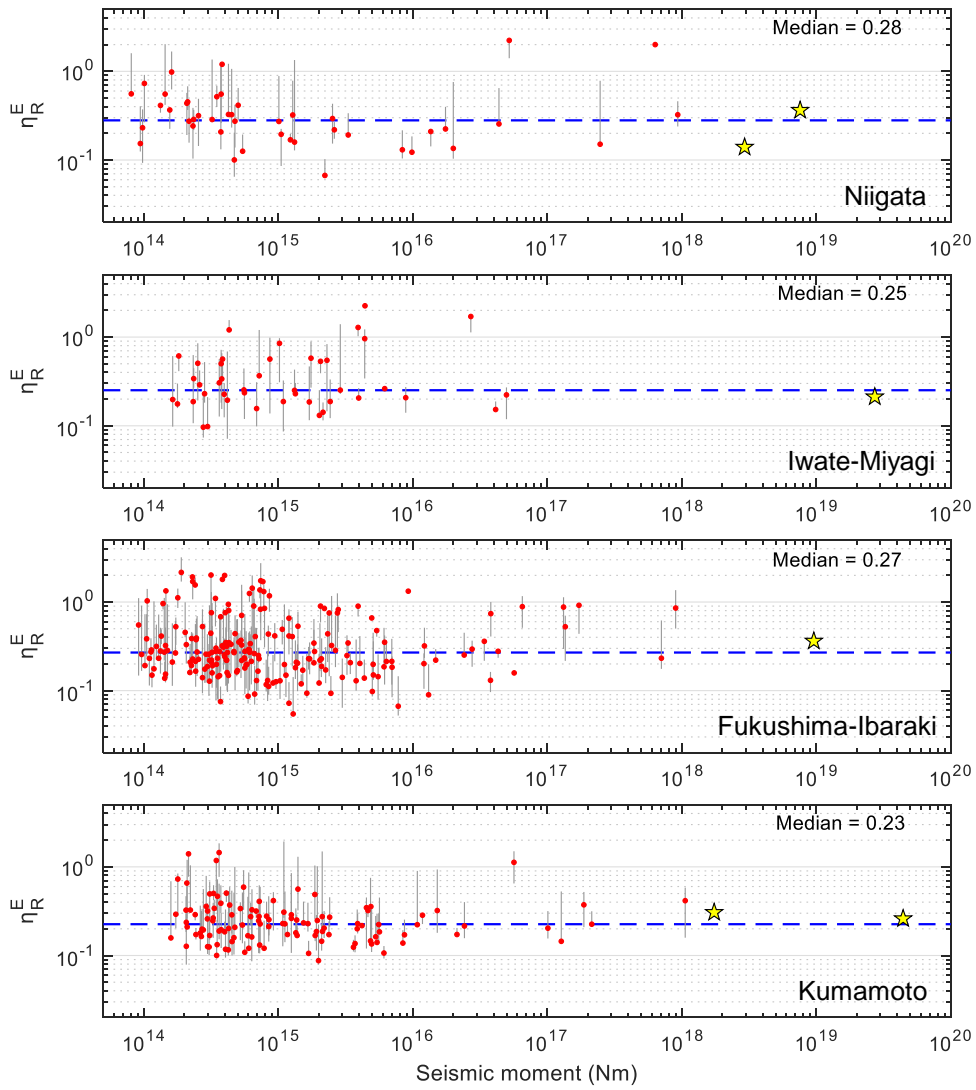
## 5.4.2. Radiation Efficiency

Figure 5.5 shows the relationship between the seismic moment and the radiation efficiencies,  $\eta_R^E = 2\sigma_a/\Delta\sigma_E$  (Figure 5.5a) and  $\eta_R' = 2\sigma_a/\Delta\sigma_s$  (Figure 5.5b). The radiation efficiencies were calculated for the best-fit model. The radiation efficiencies  $\eta_R^E$  of the large earthquake in Table 5.1 were calculated by assuming  $\eta_R^E = \eta_R'/2.4 = \sigma_a/(1.2\Delta\sigma_s)$  (Figure 5.5a). The radiation efficiency is independent of

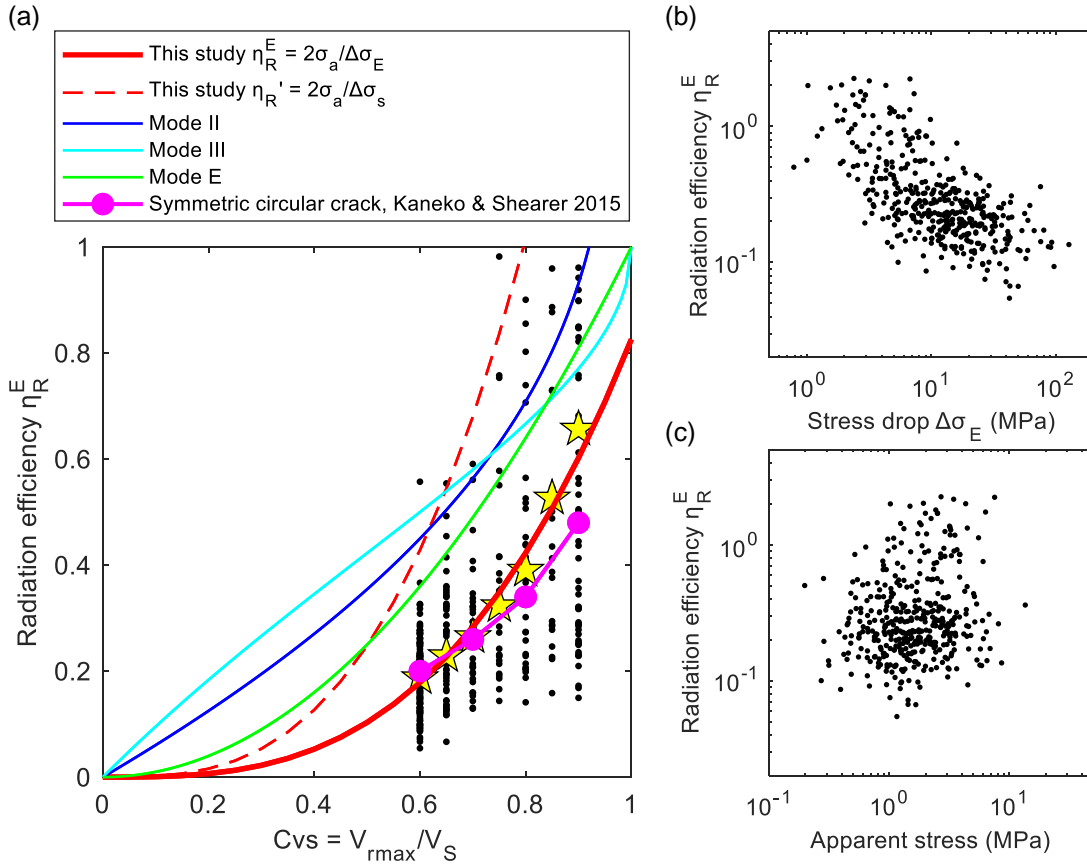
the seismic moment. This result is due to the similar scale dependencies of the stress drop and scaled energy (Figures 5.3 and 5.4). The radiation efficiency  $\eta_R^E$  varies from 0.05 to 2.5 and is more than 1.0 for 7% of the analyzed earthquakes (Figure 5.5a). On the other hand, the radiation efficiency  $\eta'_R$  varies from 0.1 to 6.0 and is more than 1.0 for 22% of the analyzed earthquakes (Figure 5.5b).

Figure 5.6 shows the scaling relation of the radiation efficiency  $\eta_R^E$  for each target region. Regional differences in the radiation efficiency  $\eta_R^E$  are not significant. Thus, the radiation efficiency  $\eta_R^E$  is relatively independent of the seismic moment. The scale independence of radiation efficiency implies that the ratio of the radiated energy to the fracture energy is similar between small and large earthquakes. Since rupture speed is directly relevant to the radiation efficiency, the constancy of the radiation efficiency implies that of the rupture speed. Although the resolution of rupture speed was low, the seismic moment dependencies of the stress drop  $\Delta\sigma_s$  and the product  $V_{rmax}^3\Delta\sigma_s$  were relatively well resolved. Since  $\Delta\sigma_s$  and  $V_{rmax}^3\Delta\sigma_s$  are similarly scaled with the seismic moment, the rupture speed is considered to be independent of the seismic moment.





**Figure 5.6** The relationship between the seismic moment and radiation efficiency  $\eta_R^E = \eta'_R/2.4$ . The red dots are from the best-fit model. The gray lines indicate the upper and lower bounds of  $\eta_R^E$ . The yellow stars are the radiation efficiencies calculated for the earthquakes in Table 5.1. The dashed horizontal blue lines indicate the median values.



**Figure 5.7** Relationship between the radiation efficiency  $\eta_R^E$  and other source parameters. (a) The radiation efficiency  $\eta_R^E$  versus rupture speed  $C_{VS}$ . The black dots show the observations for the best-fit model, and the yellow stars are the medians calculated for each rupture speed. For comparison, the relation  $\eta_R'$  and  $C_{VS}$  is also shown (the dashed red curve). Other curves are from a mode II (longitudinal shear) crack (Fossum & Freund, 1975), a mode III (transverse shear) crack (Eshelby, 1969; Kostrov, 1966), an energy-based model (mode E, Kanamori & Brodsky, 2004), and the result for symmetric circular crack by Kaneko & Shearer (2015). (b) The radiation efficiency  $\eta_R^E$  versus the energy-related stress drop  $\Delta\sigma_E$ . (c) The radiation efficiency  $\eta_R^E$  versus the apparent stress  $\sigma_a$ .

Figure 5.7 shows the relationship between the radiation efficiency  $\eta_R^E$  and other source parameters. This study found the rupture speed dependency of the radiation efficiency  $\eta_R^E$  (Figure 5.7a). The regression result between the log radiation efficiency  $\log_{10}\eta_R^E$  and log rupture speed  $\log_{10}C_{VS}$  shows that  $\eta_R^E$  is proportional to the cube of  $C_{VS}$ :

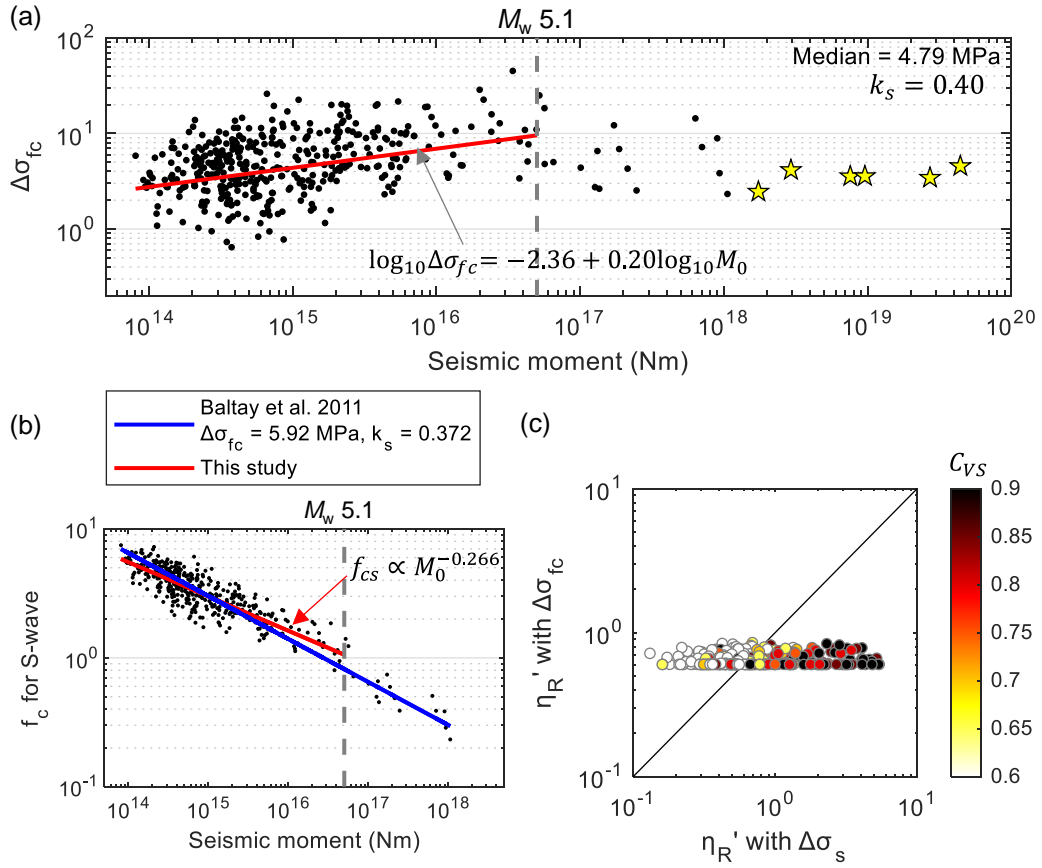
$$\eta_R^E = 0.83C_{VS}^{3.0} \quad (5.15)$$

Figure 5.7a compares the relation of equation (5.15) to the radiation efficiency derived as a function of rupture speed for a mode II (longitudinal shear) crack (Fossum & Freund, 1975), a mode III (transverse shear) crack (Eshelby, 1969; Kostrov, 1966), an energy-based model derived by Kanamori & Brodsky

(2004), and the result for a symmetric circular crack by Kaneko & Shearer (2015). The relation by equation (5.15) is comparable to the result by Kaneko & Shearer (2015). Figure 5.7a shows the relationship between the radiation efficiency  $\eta'_R = 2\sigma_a/\Delta\sigma_s$  and rupture speed  $C_{VS}$ ,  $\eta'_R = 1.98C_{VS}^{3.0}$  (the dashed red curve). The relation  $\eta'_R = 1.98C_{VS}^{3.0}$  suggests that the value of the radiation efficiency  $\eta'_R$  tends to exceed 1.0 for  $C_{VS} > 0.8$ . Kanamori & Rivera (2004) has implied a similar tendency. That is, we can obtain the relation  $\eta'_R = 1.74C_{VS}^{3.0}$  from equation (9) of Kanamori & Rivera (2004). Figure 5.7b suggests that the log radiation efficiency  $\log_{10}\eta_R^E$  is inversely correlated to the log stress drop  $\log_{10}\Delta\sigma_E$  (the correlation coefficient is  $-0.66$ ). This relationship indicates that the higher the stress drop, the greater the fraction of the available energy dissipated as the fracture energy. Figure 5.6c suggests that the log apparent stress  $\log_{10}\sigma_a$  is not correlated to the log radiation efficiency  $\log_{10}\eta_R^E$  strongly (the correlation coefficient of 0.17). Ye et al. (2016) have reported the similar tendencies to Figures 5.7b and 5.7c.

### 5.4.3. Corner-Frequency-Based Stress Drop

The scaling of corner-frequency-based stress drop  $\Delta\sigma_{fc}$  also appears to change from near  $M_w = 5.1$  (Figure 5.8a). The median stress drop  $\Delta\sigma_{fc}$  is 4.79 MPa, calculated including the stress drops of the large earthquakes (the yellow stars), for  $k_s = 0.40$ . The seismic moment dependency of  $\Delta\sigma_{fc}$ ,  $\Delta\sigma_{fc} \propto M_0^{0.20}$ , is similar to that of  $\Delta\sigma_s$  in  $M_w < 5.1$ . Figure 5.8b shows the relationship between the seismic moment and corner frequency. Baltay et al. (2011) analyzed the earthquakes in Japan, including the Iwate-Miyagi and Niigata regions, and obtained the average stress drop of 5.92 MPa using the Brune source model  $k_s = 0.372$ . Figure 5.8b compares the result in this study (the black dots and red line) with the corner frequency derived from a constant stress drop of 5.92 MPa using the Brune source model (the blue line). Although this study shows the transition of the scaling relation, the corner frequency with the 5.92 MPa stress drop appears to be consistent with the result in this study if we see the overall trend. For  $M_w < 5.1$ , the scaling relation of the corner frequency is  $f_c \propto M_0^{-0.266}$  approximately (the red line in Figure 5.8b).



**Figure 5.8** (a) The scaling relation of the corner-frequency-based stress drop. The stress drops were calculated using  $k_s = 0.40$ . The red line shows the regression result. The blue dashed line shows the median. The yellow stars are from Table 5.1. (b) The scaling relation of the corner-frequency. The red line shows the regression result in this study. The blue solid line is obtained from  $\Delta\sigma_{fc} = 5.92$  MPa and  $k_s = 0.372$ . (c) The radiation efficiencies  $\eta'_R$  calculated by  $\Delta\sigma_{fc}$  and  $\Delta\sigma_s$ .  $\Delta\sigma_{fc}$  were calculated with  $k_s = 0.40$ . The color bar describes the rupture speed.

The essential difference between  $\Delta\sigma_{fc}$  and  $\Delta\sigma_s$  appears in the radiation efficiency estimates (Figure 5.8c). The radiation efficiency obtained from  $\Delta\sigma_{fc}$ ,  $\eta'_R = 2\sigma_a/\Delta\sigma_{fc}$ , is approximately constant since  $\Delta\sigma_{fc}$  is correlated strongly with the apparent stress. For example, if we calculate  $\sigma_a$  from the omega-square model by Brune (1970) and  $\Delta\sigma_{fc}$  assuming  $k_s = 0.372$ , we obtain a constant radiation efficiency value of 0.47. Some observational studies found that strong correlation between  $\sigma_a$  and  $\Delta\sigma_{fc}$  (e.g., Baltay et al., 2011; Ide et al., 2003; Oth et al., 2010). On the other hand, the radiation efficiency obtained from  $\Delta\sigma_s$ ,  $\eta'_R = 2\sigma_a/\Delta\sigma_s$ , varies considerably compared with that obtained  $\Delta\sigma_{fc}$  due to the between-event variability of the finite source properties, especially rupture speed (Figure 5.8c).

#### 5.4.4. Comparison with Other Crustal Earthquakes

Comparing with previous studies can help confirm if the scaling relations found in this study can be plausible or not. The stress drop and apparent stress were compiled from shallow crustal earthquakes with  $M_w < 3.0$  and  $M_w > 6.0$  from previous studies. Then, the scaling relations of the stress drop, apparent stress, and radiation efficiency are investigated for a wide seismic moment range. Furthermore, the relationship between the fracture energy is studied for the compiled earthquakes.

The selected large crustal earthquakes and their source parameters are shown Tables 5.1 and 5.2. The radiation efficiencies  $\eta_R^E$  for the large earthquakes were calculated assuming  $\Delta\sigma_E = 2.4\Delta\sigma_s$ . The source parameters of small earthquakes ( $M_w < 3.0$ ) are provided by Abercrombie & Rice (2005), Ide et al. (2003), Oye et al. (2005), Venkataraman et al. (2006), and Yamada et al. (2007). The stress drops were obtained from the corner frequency. The value of the stress drop  $\Delta\sigma_{fc}$  can be different depending on the assumption of a source model, i.e., the choice of the  $k_c$  value, significantly (e.g., Kaneko & Shearer, 2015). This model dependency problem causes difficulty in comparing the stress drop  $\Delta\sigma_{fc}$  to the stress drop  $\Delta\sigma_s$  derived for large earthquakes. On the other hand, this study showed that  $\Delta\sigma_{fc}$  calculated with the S-wave corner frequency and  $k_s = 0.40$  provides a comparable value to  $\Delta\sigma_s$  on average. Thus, I re-calculated  $\Delta\sigma_{fc}$  provided the previous studies by using  $k_s = 0.40$ . The radiation efficiencies  $\eta_R^E$  for the small earthquakes were calculated from the corner frequencies assuming  $\Delta\sigma_E = 2.4\Delta\sigma_{fc}$ . The source parameters of the aftershocks of the 1994 Northridge earthquake by Mori et al. (2003) were compared to the results in this study. The magnitudes of the Northridge aftershocks are similar to the earthquakes analyzed in this study. The radiation efficiencies of the Northridge aftershocks were calculated by assuming  $\Delta\sigma_E = 2.4\Delta\sigma_s$ . I used the stress drop  $\Delta\sigma_s$  of the Northridge aftershocks compiled by Abercrombie & Rice (2005).

**Table 5.2** List of the source parameters of large crustal earthquakes. Most earthquakes are compiled by referring to Abercrombie & Rice (2005) and Lambert et al. (2021), which are omitted in the reference list.

Earthquake	$M_0$ (Nm)	$E_R$ (J)**	$L \times W$ (km)	$S$ (km <sup>2</sup> )	$D$ (m) †	$\Delta\sigma_s$ (MPa)	References
San Fernando, 1971	7.0e+18	1.5e+15	12 x 14	168	1.2	8.1	Bolt (1986) Heaton (1990) Smith et al. (1991)
Imperial Valley 1979	6.7e+18	5.9e+14	35 x 15	525	0.4	1.7	Archuleta (1984)
Morgan Hill 1986	2.1e+18	1.4e+14	20 x 8	160	0.4	2.9	Bolt (1986) Heaton (1990) Smith et al. (1990)
Loma Prieta 1989	3.1e+19	2.7e+15	40 x 17	680	1.5	4.8	Wald et al. (1991)
Landers 1992	7.7e+19	1.2e+16	65 x 15	975	2.6	7.6	Kanamori et al. (1993) Wald & Heaton (1994)
Northridge 1994	1.3e+19	1.2e+15	15 x 20	300	1.4	6.3	McGarr & Fletcher (2000) Wald et al. (1996)
Kobe 1995	2.4e+19	1.5e+15	60 x 20	1200	0.7	1.7	Wald (1995)
Hector Mine 1999	6.3e+19	3.2e+15	30 x 15 30 x 15 20 x 15	1200*	1.8	3.7	Venkataraman et al. (2004) Ji et al. (2002)
Izmit 1999	2.1e+20	6.0e+15	100 x 20	2000	3.5	7.0	Bouchon et al. (2000) Yagi & Kikuchi (2000) Tibi et al. (2001) Kanamori & Ross (2019)
Western Tottori 2000	1.2e+19	9.3e+14	30 x 20	600	0.7	2.3	Tinti et al. (2005) Choy & Boatwright (2009) Kanamori et al. (2020)
Denali 2002	7.6e+20	3.6e+16	292 x 18	5256	4.8	10.4	Asano et al. (2005) Choy & Boatwright (2004)
Fukuoka 2005	1.2e+19	6.2e+14	26 x 18	468	0.9	3.3	Kanamori et al. (2020) Asano & Iwata (2006)
Noto 2007	1.4e+19	8.7e+14	25 x 15	375	1.2	4.7	Kanamori et al. (2020) Asano & Iwata (2011)
Niigata Chuetsu- oki 2007	9.3e+18	3.4e+14	30 x 24	720	0.4	1.2	Aoi et al. (2008) Kanamori et al. (2020)

\*The total rupture area was calculated as the sum of the rupture areas of the three fault segments shown by Ji et al. (2002).

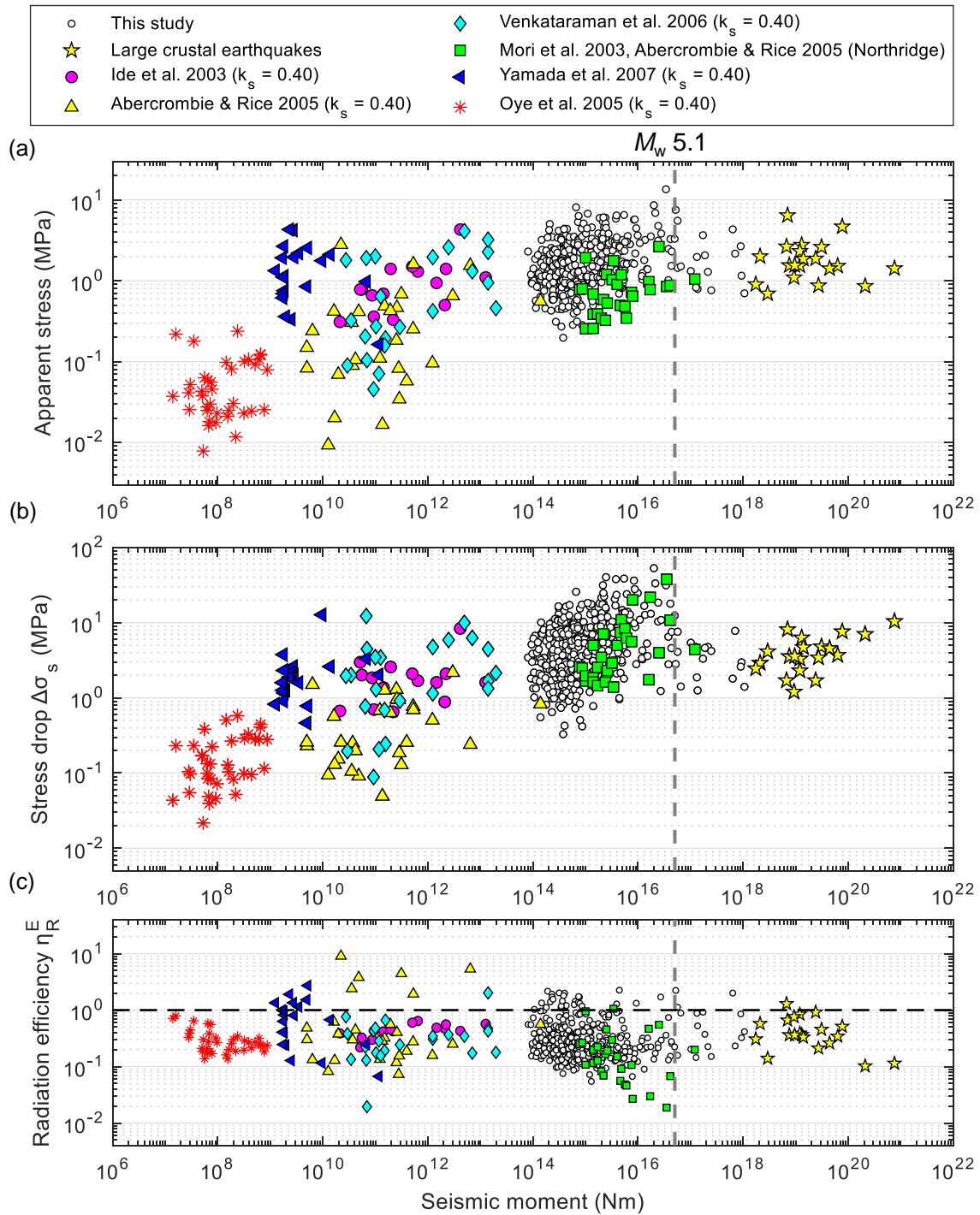
\*\*The apparent stress can be calculated as  $\mu E_R/M_0$ , where  $\mu$  is assumed to be 30 GPa.

† The values of slip  $D$  were calculated as  $M_0/(\mu S)$ , where  $\mu$  is assumed to be 30 GPa.

Figure 5.9 compiles the seismic moment dependences of the apparent stress  $\sigma_a$ , the stress drop  $\Delta\sigma_s$ , and the radiation efficiency  $\eta_R^E$ . The apparent stresses of the large earthquakes in this study (the white circles) are comparable to those of the compiled large crustal earthquakes (the yellow stars) and are independent of the seismic moment (Figure 5.9a). It is usually observed that the apparent stresses of large earthquakes (e.g.,  $M_w > 7.0$ ) are independent of the seismic moments (Choy & Boatwright, 1995; Kanamori et al., 2020; Ye et al., 2016). The stress drops of the large earthquakes in this study (the white circles) are comparable to those of the compiled large crustal earthquakes (the yellow stars) and are independent of the seismic moment (Figure 5.9b). The stress drops  $\Delta\sigma_s$  of the large earthquakes ( $M_w > 5.1$ ) are within 1 to 10 MPa (Figure 5.9b). This result is consistent with the previously proposed scaling relation (e.g., Aki, 1972; Kanamori & Anderson, 1975).

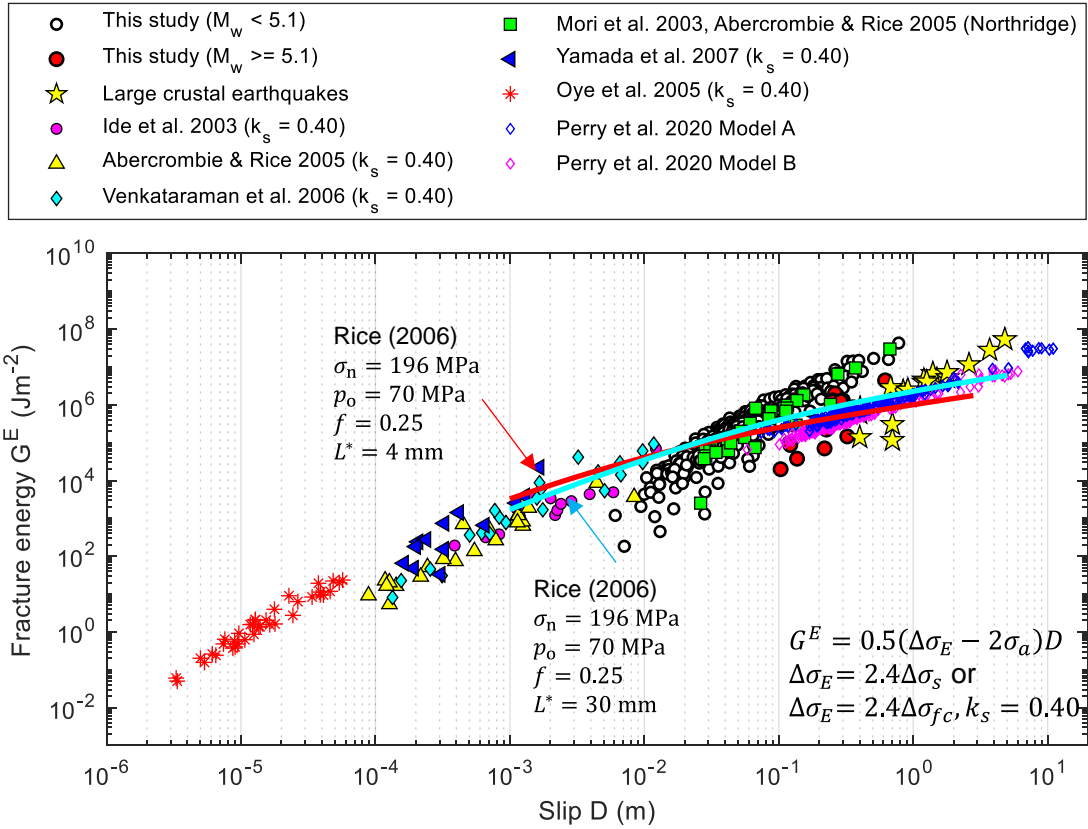
The scaling relations of the compiled stress drops and apparent stresses for the small earthquakes with  $M_w < 3.0$  are relatively complex. We see that the stress drop (or apparent stress) increases with the seismic moment in  $M_w < 5.1$  (Figures 5.9a and 5.9b), which are approximately consistent with the scaling relations found in the shallow crustal earthquakes analyzed in this study (the white circles). However, we can also see that the stress drop and apparent stress results by Ide et al. (2003) and Yamada et al. (2007) appear independent of the seismic moment. A more reliable fact may be that the variability of the stress drop (or apparent stress) values is higher for earthquakes with  $M_w < 5.1$  than those with  $M_w > 5.1$ . Another confident result is that we do not see the scaling relation that the stress drop (or apparent stress) becomes lower as the seismic moment increases for earthquakes with  $M_w < 5.1$ .

Figure 5.9c suggests that the radiation efficiency  $\eta_R^E$  is relatively independent of the seismic moment over the entire magnitude range. The radiation efficiencies obtained in this study for events with  $M_w > 5.1$  (the white circles) are similar to those of the large crustal earthquakes in Tables 5.1 and 5.2 (the yellow stars) (Figure 5.9c). The radiation efficiency  $\eta_R^E$  of the two earthquakes (the 1999 Izmit and 2002 Denali earthquakes) with  $M_w > 7.5$  ( $M_0 > 1.8 \times 10^{20}$  Nm) have relatively low values. The low radiation efficiencies for the two earthquakes with  $M_w > 7.5$  may be due to the long narrow fault geometry, i.e., large aspect ratios. For example, some studies showed that the radiation efficiencies of elliptical cracks are generally lower than those of circular cracks (e.g., Kaneko & Shearer, 2015).



**Figure 5.9** Source parameter scaling relations for crustal earthquakes. (a) The relationship between the seismic moment and the apparent stress  $\sigma_a$ . (b) The relationship between the seismic moment and the moment-based stress drop  $\Delta\sigma_s$ . (c) The relationship between the seismic moment and the radiation efficiency  $\eta_R^E$ . The horizontal dashed line indicates  $\eta_R^E = 1.0$ .





**Figure 5.10** The fracture energy  $G^E$  versus slip  $D$ . The differences between models A and B for the results of Perry et al. (2020) are effective normal stress (50 and 25 MPa) and coupling coefficient (0.1 and 0.34 MPa/K). The coupling coefficient gives pore pressure change per unit temperature change under undrained conditions. The solid red and cyan lines are the theoretical predictions by Rice (2006).

Figure 5.10 shows the relationship between fracture energies per unit area,  $G^E$ , and slip  $D$ . The fracture energies  $G^E$  were calculated from the energy-related stress drop  $\Delta\sigma_E$  and the apparent stress  $\sigma_a$ .

$$G^E = 0.5(\Delta\sigma_E - 2\sigma_a)D \quad (5.16)$$

Equation (5.16) assumes the slip-weakening model whose dynamic stress and final stress levels are the same (i.e., no stress undershoot and overshoot). The value of  $G^E$  becomes negative if there is stress undershoot. In Figure 5.10, the fracture energies with negative values were ignored. The fracture energy  $G^E$  increases with increasing slip. Since the scaling relations of the stress drop and apparent stress change around  $M_w = 5.1$ , the different markers are used for illustrating the fracture energy results for  $M_w < 5.1$  (the white circles) and  $M_w > 5.1$  (the red circles). We can see a branch of the slip

dependency of  $G^E$  at near  $D = 0.1$  m (the white circles versus the red circles). This branch is relevant to the scaling transition observed in the stress drop and the apparent stress in Figure 5.9. The fracture energy results of the numerical simulations of crack-like earthquake sequences on faults with rate-and-state friction and thermal pressurization by Perry et al. (2020) are consistent with the observational results for  $M_w > 5.1$  compiled in this study (Figure 5.10). Besides, the trend of the increasing fracture energy with slip is consistent with the theoretical predictions by Rice (2006). The relationship between  $G^E$  and  $D$  deviates from the predictions by Rice (2006) and Perry et al. (2020) for earthquakes with  $D > 0.1$  m and  $M_w < 5.1$  (the white circles and green squares).

I conducted a regression analysis to investigate the relationship between  $G^E$  and  $D$  for earthquakes with  $M_w < 5.1$ . The regression results of the relationship between  $G^E$  and  $D$  for  $M_w < 5.1$  was obtained as:

$$\log_{10} G^E = 7.29 + 1.50 \log_{10} D \quad (5.17)$$

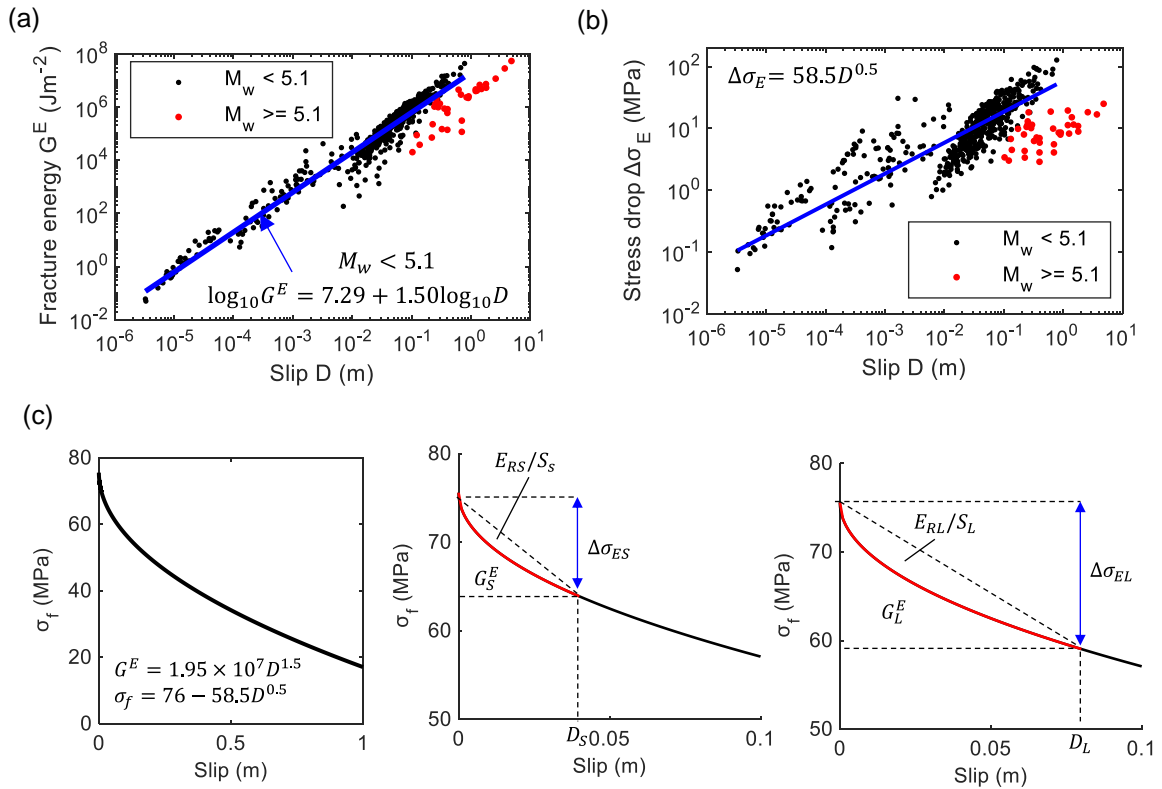


**Figure 5.11** (a) The fracture energy  $G^E$  versus slip  $D$ . The solid blue line is the regression result for earthquakes with  $M_w < 5.1$  (the black dots). (b) The energy-related stress drop  $\Delta\sigma_E$  versus slip  $D$ . The blue solid line is obtained from equation (5.19). (c) Examples of the relationship between shear stress and slip from the power law fracture energy scaling  $G^E \propto D^{1.5}$ . The middle and right panels compare the cases of small and large slips. The solid red curves correspond to the slip histories.

Figure 5.11a illustrates the regression result. Following Abercrombie & Rice (2005), the frictional stress can be obtained from equations (5.3) and (5.17) as:

$$\sigma_f(D) = \sigma'_0 - 58.5D^{0.5} \quad (5.18)$$

where  $\sigma'_0$  is a constant. The unit of  $\sigma_f(D)$  is MPa, and that of  $D$  is m. The constant  $\sigma'_0$  may be interpreted as the peak strength at onset of failure (Abercrombie & Rice, 2005). Suppose that there is no stress undershoot and overshoot. Besides, I assume to interpret the constant  $\sigma'_0$  the initial stress. Then, the stress drop is expressed as:

$$\Delta\sigma_E(D) = \sigma'_0 - \sigma_f(D) = 58.5D^{0.5} \quad (5.19)$$

Figure 5.11b shows the relationship between the energy-related stress drop  $\Delta\sigma_E(D)$  and slip  $D$  with the relation from equation (5.19) (the solid blue line). The stress drop  $\Delta\sigma_E$  increases with increasing slip for earthquakes with  $M_w < 5.1$ . Equation (5.19) predicts a stress drop value of 52.3 MPa for the average slip of 0.8 m (the upper limit in the regression analysis), which can be close to the shear strength of a fault in a shallow depth of 5–10 km. Figure 5.11c exemplifies the relationship between the frictional stress  $\sigma_f(D)$  and slip  $D$  derived by assuming the shear strength of  $\sigma'_0 = 76$  MPa, calculated by multiplying the effective normal stress 126 MPa by the friction coefficient 0.6. Although stress drop increases with slip (the middle and right panels in Figure 5.11c), the radiation efficiency has a constant value of 0.33 if the relation  $G^E \propto D^{1.5}$  holds.

$$\eta_R^E = \frac{0.5\Delta\sigma_E(D) \cdot D - G^E}{0.5\Delta\sigma_E(D) \cdot D} = \frac{1}{3} \quad (5.20)$$

The radiation efficiency of 0.33 is consistent with the median (or geometric mean) of  $\eta_R^E$  found in this study (median: 0.25, geometric mean: 0.29) (Figure 5.5a). A more general form of the power law in fracture energy scaling,  $G^E \propto D^\alpha$ , provides a constant radiation efficiency as:

$$\eta_R^E = 1 - \frac{2(\alpha - 1)}{\alpha} \quad (5.21)$$

A physical requirement  $\eta_R^E < 1.0$  suggests that the exponent  $\alpha$  must satisfy  $1 < \alpha < 2$ . Finally, it is noted that the results in this paragraph hold under some assumptions and are only inapplicable for large earthquakes with  $M_w > 5.1$ . Also, the fracture energy scaling discussed in this paragraph expresses an approximate statistical trend and needs not to be valid for individual events.

### 5.4.5. Comparison with Subduction Zone Interplate Earthquakes

Figure 5.12 compares the apparent stress  $\sigma_a$ , the energy-related stress drop  $\Delta\sigma_E$ , and the radiation efficiency  $\eta_R^E$  for the crustal earthquakes (this study and Tables 5.1 and 5.2) and the subduction zone interplate earthquakes by Ye et al. (2016). Most of the results by Ye et al. (2016) were obtained by assuming a rupture speed of 2.5 km/s. Figure 5.12a shows that the apparent stress of the crustal earthquakes is higher than that of subduction zone earthquakes. Similar to the apparent stress result, the energy-related stress drop  $\Delta\sigma_E$  of the large crustal earthquakes ( $M_w > 5.1$ ) is higher than that of subduction zone earthquakes ( $M_w > 7.0$ ). The radiation efficiency  $\eta_R^E$  is similar in the crustal and subduction zone earthquakes and is independent of the seismic moment. Table 5.3 summarizes the results of the apparent stress  $\sigma_a$ , the stress drop  $\Delta\sigma_E$ , and the radiation efficiency  $\eta_R^E$  for the crustal earthquakes with  $M_w > 5.1$  and the subduction zone earthquakes. The median apparent stress of the large crustal earthquakes is 1.6 MPa and is 2.6 time higher than that of the subduction zone earthquakes. The difference in the apparent stress of the crustal and subduction zone interplate earthquakes corresponds to the difference in the stress drop  $\Delta\sigma_E$  rather than the radiation efficiency (Table 5.3).

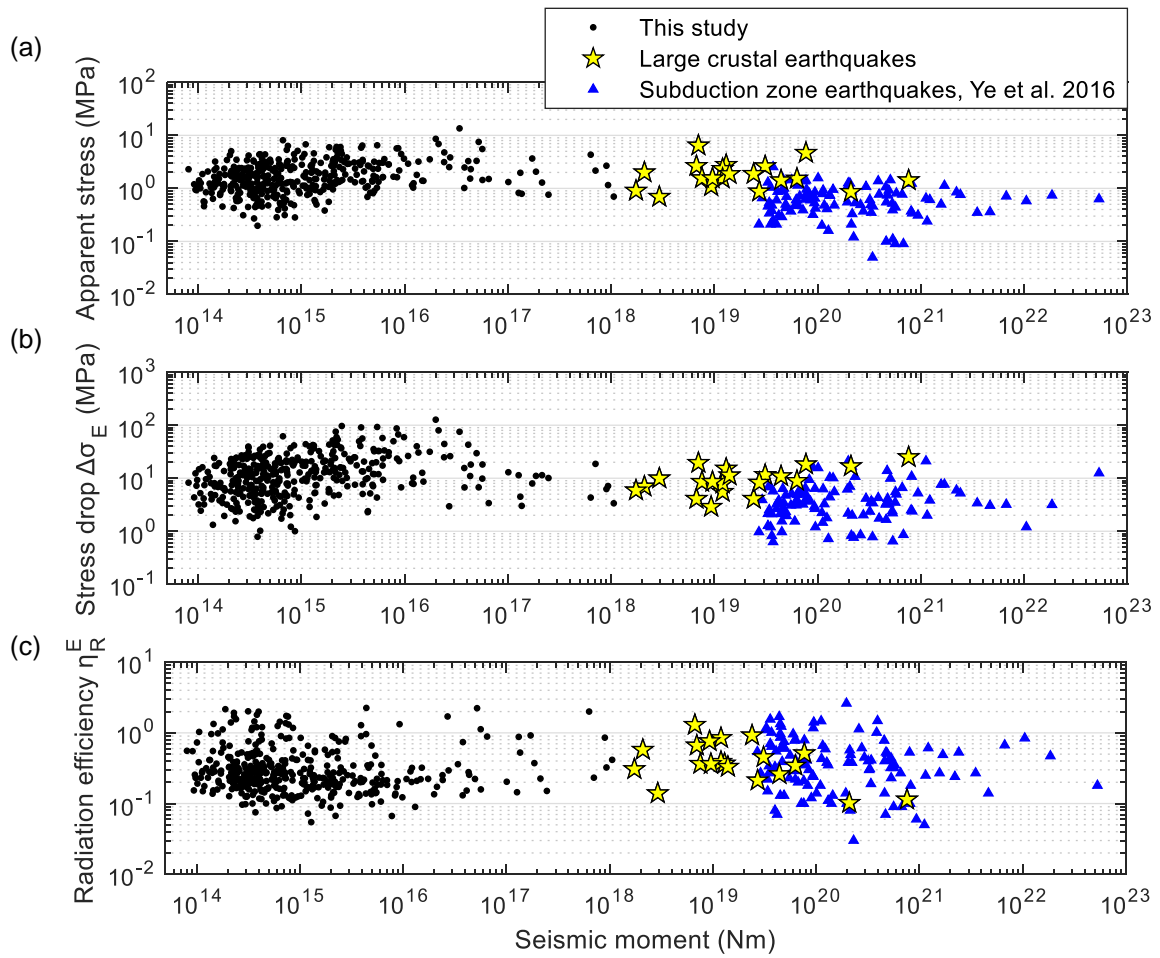


**Figure 5.12** Comparison of the source parameter scaling relations between crustal earthquakes and subduction zone interplate earthquakes. The seismic moment versus (a) the apparent stress  $\sigma_a$ , (b) the energy-related stress drop  $\Delta\sigma_E$ , and (c) the radiation efficiency  $\eta_R^E$ .

**Table 5.3** Summary of the source parameters of large crustal earthquakes ( $M_w > 5.1$ ) and subduction zone interplate earthquakes ( $M_w > 7.0$ ).

	Large crustal ( $M_w > 5.1$ )	Large subduction zone interplate
Apparent stress $\sigma_a$	0.7 to 5.0	0.1 to 1.5
(MPa)	Median 1.55, Geometric mean 1.76	Median 0.61, Geometric mean 0.56
Stress drop $\Delta\sigma_E$	2 to 20	1.0 to 10
(MPa)	Median 8.55, Geometric mean 8.38	Median 3.43, Geometric mean 3.44
Radiation efficiency $\eta_R^E$	0.1 to 1.0	0.1 to 1.0
	Median 0.37, Geometric mean 0.42	Median 0.38, Geometric mean 0.34

## 5.5. DISCUSSION

### 5.5.1. Radiation Efficiency and Earthquake Rupture Dynamics

This study confirmed that the moment-based stress drops  $\Delta\sigma_s$  and the apparent stress  $\sigma_a$  obtained in this study are consistent with those obtained for large crustal earthquakes shown in Tables 5.1 and 5.2 (the white circles and yellow stars in Figures 5.9a and 5.9b). This result supports the validity of the statistical trends obtained for  $\Delta\sigma_s$  and  $\sigma_a$  by the spectral analysis in this study. This study found that the value of the radiation efficiency  $\eta_R^E$  is typically within 0.1 to 1.0 for shallow crustal earthquakes (the white circles and the yellow stars and 5.9c). This result is reliable if the assumption of the single asperity model, whose asperity area is 17.5% of the total rupture area, is valid, i.e.,  $\Delta\sigma_E = 2.4\Delta\sigma_s$ . We may need to consider the following two factors: (1) the assumption of a 17.5% area ratio and (2) the influence of the existence of multiple asperities. The consistency of moment-based stress drops,  $\Delta\sigma_s$ , obtained by the spectral ratio analysis and Tables 5.1 and 5.2 support that the 17.5% area ratio is valid (the white circles and yellow stars in Figures 5.9b). Chapters 3 and 4 (and Appendix A2) showed that the single localized area is usually adequate to explain the observed spectral ratios. Thus, the single asperity model may be a good approximation of small-to-moderate earthquakes and sufficient for investigating the statistical properties of their source parameters. For large earthquakes, Somerville et al. (1999) showed that while the area of the largest asperity is 17.5% of the total rupture area on average, the combined asperity area is 22% of the total rupture area. This result implies that the area of the largest asperity often occupies most of the combined asperity area. The influence of the remaining asperity areas other than the largest asperity area may not be so significant for the statistical trends of  $\Delta\sigma_E$ ,  $\eta_R^E$ , and  $G^E$ . Thus, the statistical trend that  $\eta_R^E$  of the shallow crustal earthquakes (the white circles and the yellow stars and 5.9c) is typically within 0.1 to 1.0 is considered to be approximately valid. A multiple asperity model is more complex than a single asperity model. Hence, the radiation efficiency calculated by the single asperity model may be an overestimate, but it is unlikely that it is an underestimate. Thus, the conclusion that the radiation efficiency  $\eta_R^E$  is typically less than 1.0 is robust.

The result that  $\eta_R^E$  is mostly less than 1.0 suggests that stress undershoot, which indicates the dynamic stress level during seismic slip is lower than the final shear stress, is probably rare. Figure 5.13

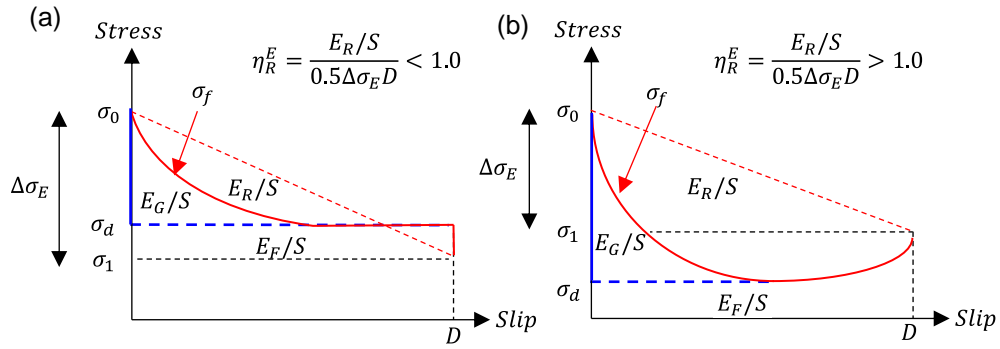


**Figure 5.13** Graphic descriptions of the earthquake energy budget with (a) stress overshoot and (b) undershoot. Crack-like ruptures typically have stress overshoot and provide  $\eta_R^E$  of less than 1.0. The kinematic feature of crack-like ruptures is a long slip duration comparable to the rupture duration of overall rupture area. Self-healing pulse-like ruptures have stress undershoot and typically provide  $\eta_R^E$  of more than 1.0. The kinematic feature of pulse-like ruptures is short slip duration compared to the rupture duration. Geometrically-constrained pulse-like ruptures are energetically crack-like (i.e.,  $\eta_R^E < 1.0$ ) but kinematically pulse-like (i.e., short slip duration).

shows the illustrative descriptions of stress overshoot and undershoot. Lambert et al. (2021) demonstrates that self-healing pulse-like ruptures usually cause significant stress undershoots. Hence, the self-healing pulse-like ruptures typically provide the values of the radiation efficiency  $\eta_R^E$  greater than 1.0. On the other hand, crack-like ruptures are typically characterized by stress overshoot and provide the value of the radiation efficiency  $\eta_R^E$  less than 1.0 (e.g., Lambert et al., 2021). Thus, the ruptures of the studied small-to-moderate earthquakes are energetically crack-like.

The slip duration of a dynamic crack (with a uniform stress drop) is comparable to the rupture duration of the overall rupture area. However, the slip durations (or rise time) of observed earthquakes are often significantly shorter than the rupture duration (e.g., Heaton, 1990; Somerville et al., 1999; Dreger et al., 2007). The studied small-to-moderate earthquakes are also expected to have short slip duration, implied in Chapter 4. Heaton (1990) considers short slip durations observed in the finite fault inversion results of seven shallow earthquakes as evidence of self-healing pulse-like rupture. On the other hand, Beroza & Mikumo (1996) shows that short-length-scale stress drop (and slip) heterogeneity can also cause short rise time. In a heterogeneous earthquake source, there are several localized areas with large slips, sometimes called asperities (e.g., Somerville et al., 1999). The short slip duration in a heterogeneous source can be because the slips on asperity areas are arrested by unloading from arrest waves generated by the local rupture boundaries around these asperities. In this case, the rupture of each

asperity area is expected to be crack-like. For example, Somerville et al. (1999) found that the average rise time is similar to the rupture duration of the largest-asperity area. The numerical simulation results by Lambert (2021) demonstrate that the radiation efficiency of a pulse-like rupture whose slip duration is short due to arresting wave generated from the rupture boundary is consistent with a crack-like rupture rather than a self-healing pulse-like rupture. Thus, the rupture style of the studied small-to-moderate earthquakes can be consistent with the pulse-like rupture caused by geometrical constraints due to source heterogeneity, which is energetically crack-like.

### 5.5.2. Source Parameter Scaling Relations

The stress drop and the apparent stress of the earthquakes analyzed in this study increase with the seismic moment in  $3.2 < M_w < 5.1$  but are independent of the seismic moment in  $5.1 < M_w < 6.0$  (Figures 5.3 and 5.4). Some studies observed that the apparent stress (or the corner-frequency-based stress drop) increases with the seismic moment (e.g., Abercrombie, 1995; Abercrombie & Rice, 2005; Mayeda et al., 2005 and 2007; Mori et al., 2003; Trugman & Shearer, 2017). On the other hand, some other studies suggest the apparent stress does not vary with the seismic moment (e.g., Baltay et al., 2011; Choy & Boatwright, 1995; Ide & Beroza, 2001; Kanamori et al., 2020; McGarr, 1999; Prieto et al., 2004; Shearer et al., 2006; Ye et al., 2016). This study suggests that we should investigate the scaling relations separately for small (e.g.,  $M_w < 5.1$ ) and large earthquakes.

The rupture speed is an important parameter for investigating the source parameter scaling relations in addition to the stress drop (Kanamori & Rivera, 2004). Recently, Ji & Archuleta (2020) suggested that the stress drop can increase with the magnitude in  $M_w < 5.3$  and decrease with increasing the magnitude in  $M_w > 5.3$  if rupture speed is independent of the magnitude. Ji & Archuleta (2020) also suggested another possibility that the stress drop is independent of the magnitude if rupture speed depends on the magnitude. This study is consistent with the first scenario by Ji & Archuleta (2020). This study estimates both stress drop and rupture speed and found that the stress drop depends on the magnitude while rupture speed is relatively independent of the magnitude (Figure 5.4). Thus, the results of this study are consistent with the first scenario of the stress drop scaling relation by Ji & Archuleta (2020). In contrast to the scaling relations of the stress drop and the apparent stress, this study found that the radiation efficiency is relatively independent of the magnitude (Figure 5.5). This result is the



consequence of the magnitude independence of rupture speed.

The relation between the fracture energy per unit area and slip predicted by Rice (2006) and Perry et al. (2020) are consistent with the observed slip dependency of the fracture energy  $G^E$  for earthquakes with  $M_w > 5.1$  (e.g., the red circles in Figure 5.10). This consistency implies the importance of thermal weakening, such as thermal pressurization. Perry et al. (2020) found that earthquakes with larger magnitude with enhanced dynamic weakening due to thermal pressurization (i.e., a larger amount of slip) weaken the frictional strength further and have lower final stress, i.e., the fracture energy increases with increasing slip. They also found that earthquakes with larger magnitudes have lower average initial stress levels. Since the frictional strength of large earthquakes is weakened further due to dynamic weakening, the rupture of large earthquakes can propagate over regions with lower prestress levels. As a consequence of rupturing regions with lower prestress, the average initial stress of large earthquakes can become lower compared to small earthquakes. Since both initial and final stress levels become lower for large earthquakes with enhanced dynamic weakening due to thermal pressurization, the stress drop can be independent of the seismic moment (or slip) while the fracture energy increases with slip.

The slip-weakening model in Figure 5.12c was derived based on the power law scaling of the fracture energy  $G^E$  and some assumptions for earthquakes with  $M_w < 5.1$ . This slip-weakening model describes the statistical characteristics of the source parameter scaling relation for earthquakes with  $M_w < 5.1$  consistently. First, the fracture energy  $G^E$  increases with increasing slip. Second, the radiation efficiency  $\eta_R^E$  is independent of the seismic moment and is 0.33. Third, the stress drop increases with increasing slip (Figure 5.13b), which is different from the results by Perry et al. (2020). The slip-weakening model in Figure 5.12c assumes that while the final stress level becomes lower as the slip increases, the average initial stress level does not depend on the amount of slip. Hence, the stress drop and the fracture energy increases with slip. A small amount of frictional strength weakening for small earthquakes may often be insufficient to rupture the regions with lower prestress levels, unlike the case of large earthquakes demonstrated by Perry et al. (2020).

As we saw in Figure 5.9, the source parameter scaling relations for small earthquakes are more complex than those of large earthquakes. At least, Figure 5.9 supports the existence of such scaling relations. This study found that the variabilities of the stress drop and apparent stress are higher for earthquakes with  $M_w < 5.1$  than those with  $M_w > 5.1$  (Figures 5.9a and 5.9b). Malagnini et al.

(2014) found a similar trend with the threshold magnitude of 5.5. The source properties of small earthquakes are influenced by local fault properties (e.g., friction coefficient, normal stress, pore pressure, and permeability) in a heterogeneous fault zone. On the other hand, the source properties of large earthquakes are the average over a large area in the fault zone. The variability of average rupture characteristics over a large area is expected to be smaller than that of local rupture characteristics in a heterogeneous fault zone. Consequently, small earthquakes can have a larger variability of their source parameters.

There is a possibility that for small-to-moderate earthquakes ( $M_w < 5.1$ ), the following two types of scaling relations coexist: (1) the stress drop increases with the seismic moment, and (2) the stress drop is relatively independent of the seismic moment (1 to 10 MPa in  $\Delta\sigma_s$ ). However, the first scaling relation seems to disappear in  $M_w > 5.1$ . From the regression results for the relationship between  $\Delta\sigma_s$  and  $M_0$ , equation (5.13), the energy-related stress drop  $\Delta\sigma_E$  ( $\Delta\sigma_E = 2.4\Delta\sigma_s$ ) for  $M_w = 5.1$  is 30.6 MPa on average, which may be close to fault shear strength (i.e., nearly complete stress drop), see also Figure 5.12b. If  $\Delta\sigma_E$  for  $M_w = 5.1$  is close to a fault shear strength (the upper limit of stress drop),  $\Delta\sigma_E$  is difficult to increase more. Several studies suggest that the influence of thermal effect starts to be significant from the average slip of about 0.1 to 0.3 m (e.g., Kanamori & Heaton, 2000; Viesca & Garagash, 2015), which corresponds to the average slip of earthquakes with near  $M_w = 5.1$ . Thus, thermal weakening effects due to frictional heating can be important for understanding the transition of the source parameter scaling relation starting from near  $M_w = 5.1$ . We need further investigation based on multiple approaches, such as numerical simulation and experiment, to reveal the cause of the source parameter scaling relations observed in this study. Besides, for small earthquakes, some scaling relations of the apparent stress (or the corner-frequency-based stress drop) may be artifacts due to observational limitations, such as limited frequency bandwidth or analysis methods (Abercrombie, 2021; Ide & Beroza, 2001). Therefore, accumulating reliable data on the source parameters for small earthquakes (e.g.,  $M_w < 3.0$ ) is necessary for establishing the scaling law of the source parameters for a wide magnitude range.

## 5.6. CONCLUSIONS

The energy-related stress drop  $\Delta\sigma_E$  is required in studying the earthquake energy budget, and the moment-based stress drop  $\Delta\sigma_S$  is inadequate. The single asperity model, whose asperity area is 17.5% of the overall rupture area, was introduced to calculate the energy-related stress drop. The use of the single asperity model is based on the results in Chapter 4. The single asperity model assumed in this study provides the relation  $\Delta\sigma_E = 2.4\Delta\sigma_S$ .

This chapter investigated the scaling relation of the source parameters for the shallow crustal earthquakes in Japan (Figures 5.3 to 5.7). The stress drop increases with the seismic moment up to near  $M_w = 5.1$  and becomes independent of the seismic moment in  $M_w > 5.1$ . Also, the apparent stress increases with the seismic moment in  $M_w < 5.1$  and becomes independent of the seismic moment in  $M_w > 5.1$ . The stress drop variability for earthquakes with  $M_w > 5.1$  is smaller than that for earthquakes with  $M_w < 5.1$ . The seismic moment dependency of the product  $V_{rmax}^3\Delta\sigma_S$  is similar to that of the stress drop  $\Delta\sigma_S$ . This result implies that rupture speed is relatively independent of the seismic moment. The radiation efficiency  $\eta_R^E = 2\sigma_a/\Delta\sigma_E$  is relatively independent of the seismic moment. This result suggests that the ratio of the radiated energy to the fracture energy is similar in small and large earthquakes. The radiation efficiency  $\eta_R^E$  takes a value typically from 0.1 to 1.0. The (average) rupture speed dependency  $\eta_R^E = 0.83C_{VS}^{3.0}$  is comparable to that predicted from typical crack models and appears to predict plausible values given  $C_{VS}$ . The stress drop estimation in this study enables us to consider the rupture speed dependency of the radiation efficiency, which is an improvement against previous corner-frequency-based stress drop estimation. The fracture energy per unit area  $G^E$  increases with increasing slip.

This study found that the apparent stress and the stress drop of subduction zone interplate earthquakes are lower than those of large crustal earthquakes. The radiation efficiency between large crustal earthquakes and large subduction zone interplate earthquakes is relatively similar. The difference in the apparent stress of the crustal and subduction zone interplate earthquakes corresponds to the difference in the stress drop  $\Delta\sigma_E$  rather than the radiation efficiency  $\eta_R^E$ .

## REFERENCES

- Abercrombie, R. E. (1995). Earthquake source scaling relationships from -1 to 5 ML using seismograms recorded at 2.5 km depth. *Journal of Geophysical Research: Solid Earth*, **100**, 24015–24036.
- Abercrombie, R. E. (2021). Resolution and uncertainties in estimates of earthquake stress drop and energy release. *Philosophical Transactions of the Royal Society A*, **379**, 20200131.
- Abercrombie R. E., & Rice, J. R. (2005). Small earthquake scaling revisited: can it constrain slip weakening? *Geophysical Journal International*, **162**(2), 406–424.
- Aki, K. (1972). Earthquake mechanism. *Tectonophysics*, **13**, 423–446.
- Aoi, S., Sekiguchi, H., Morikawa, N. & Kunugi, T. (2008). Source process of the 2007 Niigata-ken Chuetsu-oki earthquake derived from near-fault strong motion data. *Earth, Planets and Space*, **60**, 1131–1135.
- Asano, K., Iwata, T. & Irikura, K. (2005). Estimation of source rupture process and strong ground motion simulation of the 2002 Denali, Alaska, earthquake. *Bulletin of the Seismological Society of America*, **95**, 1701–1715.
- Asano, K. & Iwata, T. (2006). Source process and near-source ground motions of the 2005 West Off Fukuoka Prefecture earthquake. *Earth, Planets and Space*, **58**, 93–98.
- Asano, K. & Iwata, T. (2009). Source rupture process of the 2004 Chuetsu, Mid-Niigata prefecture, Japan, earthquake inferred from waveform inversion with dense strong-motion data. *Bulletin of the Seismological Society of America*, **99**, 123–140.
- Asano, K. & Iwata, T. (2011). Source rupture process of the 2007 Noto hanto, Japan, earthquake estimated by the joint inversion of strong motion and GPS data, *Bulletin of the Seismological Society of America*, **101**, 2467–2480.
- Asano, K. & Iwata, T. (2016). Source rupture processes of the foreshock and mainshock in the 2016 Kumamoto earthquake sequence estimated from the kinematic waveform inversion of strong motion data. *Earth, Planets and Space*, **68**, 147.
- Asano, K. & Iwata, T. (2021). Revisiting the source rupture process of the mainshock of the 2016 Kumamoto earthquake and implications for the generation of near-fault ground motions and forward directivity pulse. *Bulletin of the Seismological Society of America*, **111**, 2426–2440.

- Baltay, A., Ide, S., Prieto, G., & Beroza, G. (2011). Variability in earthquake stress drop and apparent stress. *Geophysical Research Letters*, **38**(6), L06303.
- Beroza, G. C., & Mikumo, T. (1996). Short slip duration in dynamic rupture in the presence of heterogeneous fault properties. *Journal of Geophysical Research: Solid Earth*, **101**(B10), 22449–22460.
- Bolt, B. A. (1986). Seismic energy release over a broad frequency band. *Pure and Applied Geophysics*, **124**, 919–930.
- Bouchon, M., Toksoz, N., Karabulut, H., Bouin, M., Dietrich, M., Aktar, M., & Edie, M. (2000). Seismic imaging of the 1999 Izmit (Turkey) rupture inferred from the near-fault recordings, *Geophysical Research Letters*, **27**, 3013–3016.
- Brune, J. N. (1970). Tectonic stress and the spectra of seismic shear waves from earthquakes, *Journal of Geophysical Research*, **75**(26), 4997–5009.
- Choy, G. L., & Boatwright, J. (1995). Global patterns of radiated seismic energy and apparent stress. *Journal of Geophysical Research*, **100**(B9), 18,205–18,228.
- Choy, G. L. & Boatwright, J. (2004). Radiated energy and the rupture process of the Denali fault earthquake sequence of 2002 from broadband teleseismic Body Waves. *Bulletin of the Seismological Society of America*, **94**, S269–S277.
- Choy, G. L. & Boatwright (2009), J. Differential energy radiation from two earthquakes in Japan with identical Mw: The Kyushu 1996 and Tottori 2000 earthquakes. *Bulletin of the Seismological Society of America*, **99**, 1815–1826.
- Dreger, D., Nadeau, R. M., & Chung, A. (2007). Repeating earthquake finite source models: Strong asperities revealed on the San Andreas Fault. *Geophysical Research Letters*, **34**, L23302.
- Eshelby, J. D. (1957). The determination of the elastic field of an ellipsoidal inclusion, and related problems. *Proceedings of the Royal Society of London*, **241**(1226), 376–396.
- Eshelby, J. D. (1969). The elastic field of a crack extending non-uniformly under general anti-plane loading. *Journal of the Mechanics and Physics of Solids*, **17**, 177–199.
- Fossum, A. F., & Freund, L. B. (1975). Nonuniformly moving shear crack model of a shallow focus earthquake mechanism, *Journal of Geophysical Research*, **80**, 3343–3347.
- Heaton, T. H. (1990). Evidence for and implications of self-healing pulses of slip in earthquake rupture. *Physics of the Earth and Planetary Interiors*, **64**, 1–20.

- Husseini M. I., & Randall, M. J. (1976). Rupture velocity and radiation efficiency. *Bulletin of the Seismological Society of America*, **66**(4), 1173–1187.
- Ide, S., & Beroza, G. C. (2001). Does apparent stress vary with earthquake size? *Geophysical Research Letters*, **28**(17), 3349–3352.
- Ide, S., Beroza, G. C., Prejean, S. G., & Ellsworth, W. L. (2003). Apparent break in earthquake scaling due to path and site effects on deep borehole recordings. *Journal of Geophysical Research*, **108**(B5), 2271.
- Ji, C. & Archuleta, R. J. (2020). Two empirical double-corner-frequency source spectra and their physical implications. *Bulletin of the Seismological Society of America*, **111** (2), 737–761.
- Ji, C., Wald, D. J. & Helmberger, D. V. (2002). Source Description of the 1999 Hector Mine, California, Earthquake, Part II: Complexity of Slip History. *Bulletin of the Seismological Society of America*, **92**, 1208–1226.
- Kanamori, H., & Anderson, D. L. (1975). Theoretical basis of some empirical relations in seismology. *Bulletin of the Seismological Society of America*, **65**(5), 1073–1095.
- Kanamori, H., Mori, J., Hauksson, E., Heaton, T. H., Hutton, L. K. & Jones, L. M. (1993). Determination of earthquake energy release and  $M_L$  using TERRAScope, *Bulletin of the Seismological Society of America*, **83**(2), 330–346.
- Kanamori H, Heaton T. H. (2000). Microscopic and macroscopic physics of earthquakes. In Geocomplexity and the physics of earthquakes, pp. 147–163. *American Geophysical Union Geophysical Monograph*, **120**. Washington, DC: AGU.
- Kanamori, H., & Brodsky, E. E. (2004). The physics of earthquakes. *Reports on Progress in Physics*, **67**(8), 1429–1496.
- Kanamori, H. & Rivera, L., (2006). Energy partitioning during an earthquake. *Earthquakes: Radiated Energy and the Physics of Faulting* (pp. 3–13), eds Abercrombie, R. McGarr, A. Di Toro, G. & Kanamori, H., American Geophysical Union.
- Kanamori, H. & Ross, Z. E. (2019). Reviving mB. *Geophysical Journal International*, **216**, 1798–1816.
- Kanamori, H., Ross, Z. E., & Rivera, L. (2020). Estimation of radiated energy using the KiK-net downhole records—old method for modern data, *Geophysical Journal International*, **221**(2), 1029–1042.
- Kaneko, Y., & Shearer, P. M. (2015). Variability of source spectra, estimated stress drop, and radiated

- energy, derived from cohesive-zone models of symmetrical and asymmetrical circular and elliptical ruptures. *Journal of Geophysical Research: Solid Earth*, **120**(2): 1053–1079.
- Kostrov, B. V. (1966). Unsteady propagation of longitudinal shear cracks, *Journal of Applied Mathematics and Mechanics*, **30**, 1241–1248.
- Kostrov, B. V., & Das, S. (1988). *Principles of Earthquake Source Mechanics*, Cambridge University Press, Cambridge, pages 308.
- Lambert, V. (2021). *Constraining Earthquake Source Processes Through Physics-Based Modeling*. Dissertation (Ph.D.), California Institute of Technology.
- Lambert, V., Lapusta, N. & Perry, S. (2021). Propagation of large earthquakes as self-healing pulses or mild cracks. *Nature*, **591**, 252–258.
- Madariaga, R. (1979). On the relation between seismic moment and stress drop in the presence of stress and strength heterogeneity. *Journal of Geophysical Research: Solid Earth*, **84**(B5), 2243–2250.
- Malagnini, L., Mayeda, K., Nielsen, S., Yoo, S-H, Munafo', I., Rawles, I. C., & Boschi, E. (2014). Scaling transition in earthquake sources: a possible link between seismic and laboratory measurements. *Pure and Applied Geophysics*, **171**, 2685–2707.
- Mayeda, K., Gök, R., Walter, W. R., & Hofstetter, A. (2005). Evidence for non-constant energy/moment scaling from coda-derived source spectra. *Geophysical Research Letters*, **32**, L10306.
- Mayeda, K., Malagnini, L., & Walter W. R. (2007). A new spectral ratio method using narrow band coda envelopes: evidence for non-self-similarity in the Hector Mine. *Geophysical Research Letters*, **34**, L11303.
- McGarr, A. (1999). On relating apparent stress to the stress causing earth-quake slip. *Journal of Geophysical Research*, **104**(B2), 3003–3011.
- McGarr, A., & Fletcher, J. B. (2000). A method for mapping apparent stress and energy radiation applied to the 1994 Northridge earthquake fault zone. *Geophysical Research Letters*, **27**, 1953–1956.
- Miyazawa, M., Mori, J., Iio, Y., Shibutani, T., Matsumoto, S., Katao, H., Ohmi, S., & Nishigami, K. (2005). Triggering sequence of large aftershocks of the mid Niigata prefecture, Japan earthquake in 2004 by static stress changes. *Earth Planets and Space*, **57**, 1109–1113.
- Mori, J., Abercrombie R. E., Kanamori, H. (2003). Stress drops and radiated energies of aftershocks of the 1994 Northridge, California, earthquake. *Journal of Geophysical Research: Solid Earth*, **108**(B11), 2545.

- Noda, H., Lapusta, N. & Kanamori, H. (2013). Comparison of average stress drop measures for ruptures with heterogeneous stress change and implications for earthquake physics. *Geophysical Journal International*, **193**(3), 1691–1712.
- Oye, V., Bungum, H., & Roth, M. (2005). Source parameters and scaling relations for mining-related seismicity within the Pyhasalmi Ore Mine, Finland. *Bulletin of the Seismological Society of America*, **95**, 1011–1026.
- Oth, A., Bindi, D., Parolai, S. & Di Giacomo, D., (2010). Earthquake scaling characteristics and the scale-(in) dependence of seismic energy-tomoment ratio: insights from KiK-net data in Japan. *Geophysical Research Letters*, **37**, L19304.
- Prieto, G. A., Shearer, P. M., Vernon, F. L. & Kilb, D. (2004). Earthquake source scaling and self-similarity estimation from stacking P and S spectra, *Journal of Geophysical Research: Solid Earth*, **109**, B08310.
- Perry, S. M., Lambert, V., & Lapusta, N. (2020). Nearly magnitude-invariant stress drops in simulated crack-like earthquake sequences on rate-and-state faults with thermal pressurization of pore fluids. *Journal of Geophysical Research: Solid Earth*, **125**, e2019JB018597.
- Rice, J. R. (2006). Heating and weakening of faults during earthquake slip. *Journal of Geophysical Research*, **111**, B05311.
- Shearer, P. M., Prieto, G. A., & Hauksson, E. (2006). Comprehensive analysis of earthquake source spectra in southern California. *Journal of Geophysical Research: Solid Earth*, **111**, B06303.
- Smith, K. D., Brune, J. N. & Priestley, K. F. (1991). The seismic spectrum, radiated energy, and the Savage and Wood inequality for complex earthquakes. *Tectonophysics*, **188**, 303–320.
- Somerville, P., Irikura K., Graves R., Sawada S., Wald D., Abrahamson N., Iwasaki Y., Kagawa T., Smith N., & Kowada A. (1999). Characterizing crustal earthquake slip models for the prediction of strong ground motion. *Seismological Research Letters*, **70** (1), 59–80.
- Suzuki, W., Aoi, S. & Sekiguchi, H. (2010). Rupture process of the 2008 Iwate–Miyagi Nairiku, Japan, earthquake derived from near-source strong-motion records. *Bulletin of the Seismological Society of America*, **100**, 256–266.
- Tanaka, M., Asano, K., Iwata, T., & Kubo, H. (2014). Source rupture process of the 2011 Fukushima-ken Hamadori earthquake: how did the two subparallel faults rupture? *Earth Planets Space*, **66**,



- Tibi, R., Bock, G., Xia, Y., Baumbach, M., Grosser, H., Milkereit, C., Karakisa, S., Zünbül, S., Kind, R., & Zschau, J. (2001). Rupture processes of the 1999 August 17 Izmit and November 12 Düzce (Turkey) earthquakes, *Geophysical Journal International*, **144**(2), F1–F7.
- Tinti, E., Spudich, P. & Cocco, M. (2005). Earthquake fracture energy inferred from kinematic rupture models on extended faults. *Journal of Geophysical Research: Solid Earth*, **110**, B12303.
- Trugman, D. T., & Shearer, P. M. (2017). Application of an improved spectral decomposition method to examine earthquake source scaling in Southern California. *Journal of Geophysical Research: Solid Earth*, **122**(4), 2890–2910.
- Venkataraman, A., & Kanamori, H. (2004). Observational constraints on the fracture energy of subduction zone earthquakes. *Journal of Geophysical Research*, **109**, B05302.
- Venkataraman, A., Beroza, G. C., Ide, S., Imanishi, K., Ito, H. & Iio, Y., (2006). Measurements of spectral similarity for microearthquakes in western Nagano, Japan, *Journal of Geophysical Research: Solid Earth*, **111**, B03303.
- Viesca, R., & Garagash, D. (2015). Ubiquitous weakening of faults due to thermal pressurization. *Nature Geoscience*, **8**, 875–879.
- Wald, D. J. (1995). A preliminary dislocation model for the 1995 Kobe (Hyogo-ken nanbu), Japan, earthquake determined from strong motion and teleseismic waveforms. *Seismological Research Letters*, **66**, 22–28.
- Wald, D. J., Helmberger, D. V. & Heaton, T. H. (1991). Rupture model of the 1989 Loma Prieta earthquake from the inversion of strong-motion and broadband teleseismic data. *Bulletin of the Seismological Society of America*, **81**, 1540–1572.
- Wald, D. J. & Heaton, T. H. (1994). Spatial and temporal distribution of slip for the 1992 Landers California, earthquake. *Bulletin of the Seismological Society of America*, **84**, 668–691.
- Wald, D. J., Heaton, T. H. & Hudnut, K. W. (1996). The slip history of the 1994 Northridge, California, earthquake determined from strong-motion, teleseismic, GPS, and leveling data. *Bulletin of the Seismological Society of America*, **86**, S49–S70.
- Yagi, Y., & Kikuchi, M. (2000). Source rupture process of the Kocaeli, Turkey, earthquake of August 17, 1999, obtained by joint inversion of near-field data and teleseismic data, *Geophysical Research Letters*, **27**, 1969–1972.

- Yamada, T., Mori, J. J., Ide, S., Abercrombie, R. E., Kawakata, H., Nakatani, M., Iio, Y., & Ogasawara, H. (2007). Stress drops and radiated seismic energies of microearthquakes in a South African gold mine. *Journal of Geophysical Research*, **112**, B03305.
- Ye, L., Lay, T., Kanamori, H., & Rivera, L. (2016). Rupture characteristics of major and great ( $M_w \geq 7.0$ ) megathrust earthquakes from 1990 to 2015: 1. Source parameter scaling relations. *Journal of Geophysical Research: Solid Earth*, **121**, 826–844.
- Yokota, Y., Koketsu, K., Hikima, K., & Miyazaki, S. (2009). Ability of 1-Hz GPS data to infer the source process of a medium-sized earthquake: The case of the 2008 Iwate-Miyagi Nairiku, Japan, earthquake. *Geophysical Research Letters*, **36**, L12301.
- Yoshida, K., Miyakoshi, K., Somei, K. & Irikura, K. (2017). Source process of the 2016 Kumamoto earthquake ( $M_j7.3$ ) inferred from kinematic inversion of strong-motion records. *Earth Planets Space*, **69**, 64.

## Chapter 6

# CONCLUSIONS AND FUTURE STUDIES

## 6.1. CONCLUSIONS

This dissertation develops a new spectral ratio approach to estimate the stress drop of small-to-moderate earthquakes considering rupture geometry, speed, and directivity to improve the standard corner frequency method. Applying the developed spectral ratio approach to the shallow crustal earthquakes in Japan reveals that the rupture area estimated by the spectral ratio analysis corresponds to the large-slip asperity area rather than the overall rupture area. The localized rupture with large slip controls the shape of source spectra in a broadband frequency range. The results of this study encourage us to describe an earthquake source as a simple heterogeneous source model, the single asperity model. The localized area with concentrated stress drop, which generates strong ground motions, corresponds to the rupture area estimated by the spectral ratio analysis. This study proposes a procedure to calculate the energy-related stress drop based on the spectral ratio analysis and the single asperity model. The single asperity model consists of a localized area with a concentrated stress drop and the remaining region (outside the localized area but within the entire rupture domain) with zero stress drop. The single asperity model is more detailed than the standard circular source model but is still simple. The energy-related stress drop is usually estimated using slip distribution obtained from finite fault inversion. Since finite fault inversion is often hard to conduct for small-to-moderate earthquakes, estimating the energy-related stress drop based on the spectral ratio analysis and the single asperity model is convenient.

This study introduced three types of stress drops, the local stress drop  $\Delta\sigma_{la}$ , the moment-based

stress drop  $\Delta\sigma_s$ , and the energy-related stress drop  $\Delta\sigma_E$ . This study implied that a localized area with large slip dominates strong motion generation rather than the overall rupture area. Therefore, the local stress drop  $\Delta\sigma_{la}$  can be one of the most significant source parameters in ground motion prediction. The moment-based stress drop  $\Delta\sigma_s$  is an effective parameter to characterize the relationship between the seismic moment and source dimension, which is important for earthquake engineering. The energy-related stress drop  $\Delta\sigma_E$  rather than the moment-based stress drop  $\Delta\sigma_s$  is appropriate for calculating the radiation efficiency. The radiation efficiency can be used to investigate the rupture style of earthquakes. For example, the radiation efficiency for self-healing pulse-like rupture tends to be more than 1.0, although one for crack-like rupture is less than 1.0 (Lambert et al., 2021). Appropriate observational constraints of radiation efficiency are helpful for precise ground motion prediction based on dynamic source modeling or physics-based earthquake simulation.

The developed spectral ratio approach enables us to investigate more detailed source characteristics, e.g., rupture speed, of small-to-moderate earthquakes (e.g.,  $M_w < 6.0$ ) compared with the previous corner-frequency-based method. Applying the developed spectral ratio approach to small-to-moderate earthquakes is helpful for obtaining the joint probability distribution of the source parameters for physics-based probabilistic seismic hazard analysis since the number of small-to-moderate earthquakes is greater than that of large earthquakes. For example, understanding the source properties of small-to-moderate earthquakes can be significant for aftershock seismic hazard assessment. Aftershock seismic hazard assessment helps prepare post-earthquake recovery plans for expected earthquakes in advance, which is expected to contribute to mitigating social loss due to earthquake disasters.

Notable conclusions in this dissertation are summarized as follows.

### ***Chapter 2: Source Spectrum Model Considering Rupture Directivity Effect***

- (1) A source spectrum model incorporating the effect of rupture size, geometry, speed, and rupture start point was developed. The mathematical representation of the source spectrum for the kinematic rectangular source model with bilateral–bidirectional rupture propagation was derived. This source spectrum has the  $\omega^{-2}$  high-frequency falloff rate. The source spectrum incorporates the effect of rupture size, geometry, speed, and rupture start point.
- (2) The source spectrum derived for the rectangular source model was approximated as its envelope (the envelope spectrum). The envelope spectrum has a smooth spectral shape (i.e., without spectral holes). For example, this smooth spectral shape is advantageous for spectral ratio fitting, in which

we often use observed spectral ratios smoothed by applying a tapering or stacking technique.

### ***Chapter 3: Spectral Ratio Method***

- (1) A spectral ratio approach incorporating the envelope spectrum was developed to estimate the stress drop of small-to-moderate earthquakes considering rupture geometry, speed, and directivity. The source parameters are estimated by fitting the model spectral ratios with the envelope spectrum to observed spectral ratios obtained by station and wave type. This spectral ratio fitting is different from the standard spectral ratio approach, which fits the model spectral ratio to an observed spectral ratio averaged over all stations to estimate the corner frequency. Applying this spectral ratio approach to the shallow crustal earthquakes in Japan showed that the model spectral ratio using the envelope spectrum could fit observed spectral ratios well.
- (2) The stress drops, calculated from the seismic moment and the rupture area estimated by the spectral ratio analysis, were systematically much higher than expected, albeit with good fits of spectral ratios.

### ***Chapter 4: Seismic Spectra and Source Heterogeneity***

- (1) The rupture area estimated by the spectral ratio approach is small compared with the overall rupture area. The rupture area obtained by the spectral ratio approach corresponds to the localized rupture area with large slip (the largest-asperity area). This localized rupture area dominates the source spectral shapes in a broadband range. This conclusion suggests that the idea of the strong motion generation area is also significant for small-to-moderate earthquakes (e.g.,  $M_w < 6.0$ ).
- (2) The comparison of the estimated rupture area  $LW$  with the result by Somerville et al. (1999) suggests that the estimated rupture area can be 17.5% of the total rupture area on average. The average static stress drops  $\Delta\sigma_s$  are estimated using the 17.5% area ratio and are within a typical range of 1 to 20 MPa. The consistency with the stress drops estimated for large earthquakes supports the validity of the stress drop calculation.
- (3) The rupture speed and stress drop are inversely correlated. The correlation coefficient between the  $\log_{10}V_{rmax}$  and  $\log_{10}\Delta\sigma_s$  is  $-0.55$ . The depth dependence and focal mechanism dependence of the stress drop  $\Delta\sigma_s$  are not obvious.
- (4) The  $k_s$  values were estimated from the estimated rupture areas and the corner frequencies. The median and mean of the  $k_s$  value are 0.400 and 0.433, respectively. The  $k_s$  value of 0.40 provides the median value of  $\Delta\sigma_{fc}$  similar to that of  $\Delta\sigma_s$ . The corner-frequency-based approach is useful to observe the average trend of stress drop if an appropriate  $k_s$  value is used. However, it should

be recognized that the between event variability of the  $k_c$  value is significantly large. The standard deviation of the  $k_s$  value is 0.119.

### ***Chapter 5: Earthquake Energy Budget and Source Parameter Scaling Relations***

- (1) The energy-related stress drop  $\Delta\sigma_E$  is theoretically required in studying the earthquake energy budget, and the moment-based stress drop  $\Delta\sigma_s$  is inadequate. Hence, the single asperity model, whose asperity area is 17.5% of the overall rupture area, is introduced to calculate the energy-related stress drop. The asperity area corresponds to the rupture area estimated by the spectral ratio analysis developed in this study. The single asperity model assumed in this study provides the relation  $\Delta\sigma_E = 2.4\Delta\sigma_s$ .
- (2) The stress drop increases with the seismic moment up to near  $M_w = 5.1$  and becomes independent of the seismic moment for earthquakes with  $M_w > 5.1$ . The stress drops of the earthquakes with  $M_w > 5.1$  are 1 to 10 MPa. The seismic moment dependency of the product  $V_{rmax}^3\Delta\sigma_s$  is similar to that of the stress drop  $\Delta\sigma_s$ . The apparent stress increases with the seismic moment up to near  $M_w = 5.1$  and becomes independent of the seismic moment for earthquakes with  $M_w > 5.1$ . The variabilities of stress drop and apparent stress for earthquakes with  $M_w > 5.1$  is smaller than those for earthquakes with  $M_w < 5.1$ . The radiation efficiency  $\eta_R^E = 2\sigma_a/\Delta\sigma_E$  is relatively independent of the seismic moment. The fracture energy  $G^E$  increases with increasing slip.
- (3) The radiation efficiency  $\eta_R^E$  takes a value typically from 0.1 to 1.0. The short slip duration and  $\eta_R^E < 1.0$  suggest that the rupture mode of the studied earthquakes is consistent with pulse-like rupture due to geometrical constraints, such as source heterogeneity. The (average) rupture speed dependency  $\eta_R^E = 0.83C_{VS}^{3.0}$  is comparable to that predicted from typical crack models and appears to predict plausible values given  $C_{VS}$ . The stress drop estimation in this study enables us to consider the rupture speed dependency of the radiation efficiency, which is an improvement against previous corner-frequency-based stress drop estimation.
- (4) This study found that the apparent stress and the stress drop of subduction zone interplate earthquakes are lower than those of large crustal earthquakes. The radiation efficiency between large crustal earthquakes and large subduction zone interplate earthquakes is relatively similar.

## 6.2. FUTURE STUDIES

This study found that the scaling relation of source parameters (e.g., the stress drop) changes around  $M_w = 5.1$ . Since the scaling law of source parameters is significant for seismic hazard assessment, the existence of the source scaling transition should be confirmed by further investigation. Some studies found that the relationship between the magnitude and peak ground acceleration (PGA) or peak ground velocity (PGV) changes around  $M_w$  of 5.0 to 5.5 (Abrahamson et al., 2014; Boatwright et al., 2003; Ji et al., 2021). If the source scaling transition observed in this study is true, it should appear in the magnitude dependence of PGA and PGV for shallow crustal earthquakes. Therefore, an important future work is investigating the magnitude dependence of PGA and PGV for shallow crustal earthquakes in Japan.

This study demonstrated that the envelope spectrum fits observed spectral ratios effectively. This result suggests that a localized area with large slip dominates the shape of seismic spectra. I think the conclusion that the spectral ratio approach developed in this study estimates the largest asperity area is reasonable and valid. However, the envelope spectrum may become inappropriate at a very high-frequency range. For example, Somerville et al. (1997) showed that the rupture directivity effect diminishes in a high-frequency range for all directions. Gusev (2014) simulated an earthquake with heterogeneous slip distribution and a complex rupture front. His result suggested that the rupture complexity would diminish the high-frequency rupture directivity effect. Although this study considered source heterogeneity, the rupture directivity effect exists at high frequencies since the rupture propagation in the rectangular source model is smooth. A deeper understanding of the behavior of seismic source spectra over broadband frequencies is essential for engineering seismology and earthquake source physics.

## REFERENCES

- Abrahamson, N. A., Silva, W. J., & Kamai, R. (2014). Summary of the ASK14 ground motion relation for active crustal regions. *Earthquake Spectra*, **30**(3), 1025–1055.
- Boatwright, J., Bundock, H., Luetgert, J., Seekins, L., Gee, L., & Lombard, P. (2003). The Dependence

- of PGA and PGV on Distance and Magnitude Inferred from Northern California ShakeMap Data. *Bulletin of the Seismological Society of America*, **93**(5), 2043–2055.
- Brune, J. N. (1970). Tectonic stress and the spectra of seismic shear waves from earthquakes. *Journal of Geophysical Research*, **75**, 4997–5009.
- Gusev, A. A. (2014). Doubly stochastic earthquake source model: “Omega-square” spectrum and low high-frequency directivity revealed by numerical experiments. *Pure and Applied Geophysics*, **171**(10), 2581–2599.
- Ji, C. & Archuleta, R. J. (2020). Two empirical double-corner-frequency source spectra and their physical implications. *Bulletin of the Seismological Society of America*, **111**(2), 737–761.
- Lambert, V., Lapusta, N. & Perry, S. (2021). Propagation of large earthquakes as self-healing pulses or mild cracks. *Nature*, **591**, 252–258.
- Somerville, P. G., Smith, N. F., Graves, R. W., & Abrahamson, N. A. (1997). Modification of empirical strong ground motion attenuation relations to include the amplitude and duration effects of rupture directivity. *Seismological Research Letters*, **68**(1), 199–222.



# ACKNOWLEDGMENT

I would like to thank the many people who helped me in completing my doctoral dissertation.

- Professor Yoshiki Ikeda. I would like to thank Prof. Ikeda greatly for allowing me to work independently to complete my doctoral research on my own. When writing my doctoral dissertation, he carefully read and commented on the detail of the dissertation.
- Professor Masahiro Kurata. I thank him for instructing my research in my bachelor's and master's courses. His broad interest in research has allowed me to experience a wide range of things, e.g., shaking table experiments to field damage surveys for the 2016 Kumamoto earthquake.
- Prof. Masayoshi Nakashima. He gave me opportunities to join international workshops and talk with many students and researchers from diverse countries. These opportunities have been very stimulating for my research activities.
- Prof. Masumi Yamada. I am grateful to her for helping me when I started the study of seismology. Her advice was helpful in deepening my understanding of seismology. She gave me opportunity to interact with many researchers working on seismology and earthquake engineering.
- Prof. Hiroe Miyake. Her seminar on strong-motion seismology was the inspiration for the topic of my doctoral dissertation.
- Prof. Jim Mori. The discussion with Prof. Mori was stimulating, and I could learn a lot. He shared with me his knowledge and experience. He not only gave me many valuable comments on the content of my paper but also gave me much advice on my writing.
- Prof. Shinichi Matsushima and Prof. Izuru Takewaki. I thank them for reviewing my dissertation and suggesting thoughtful comments for improvement.
- Mrs. Chisato Gamou. I am grateful for her support in my daily life in the lab. Thanks to her help, I could concentrate on my research.
- The members of Ikeda & Kurata lab and Nakashima & Kurata lab. I spent time in this laboratory with many students and researchers. I could have precious experiences and learn a lot of things from them.
- My family. I would thank my mother and grandmother for their dedicated support and encouragement. Without their patient help, I could never have completed my doctoral dissertation.

# APPENDICES

## A1. CALCULATION NOTES FOR CHAPTER 2

### A1.1. Derivation of $K$

The recommended value of  $K = 3$  was derived so that the area of the two slip functions represented by equations (2.2) and (2.4) would be equal (Figure A1).

$$D_1(t) = \begin{cases} 0, & t \leq 0 \\ \frac{D}{K}H(t) + \frac{K-1}{K} \frac{D}{\tau_r} t, & 0 < t \leq \tau_r \\ D, & \tau_r < t \end{cases} \quad (2.2)$$

$$D_r(t) = \begin{cases} 0, & t \leq 0 \\ \frac{D}{\sqrt{\tau_r}} \sqrt{t}, & 0 < t \leq \tau_r \\ D, & \tau_r < t \end{cases} \quad (2.4)$$

The problem is to determine the value of  $K$  that Area 1 and Area 2 in Figure A1 become equal. The equilibrium of the two area is represented as

$$\int_0^a \left\{ \frac{D}{\tau_r} \left( \frac{K-1}{K} \right) t + \frac{D}{K} - \frac{D}{\sqrt{\tau_r}} \sqrt{t} \right\} dt - \int_a^{\tau_r} \left\{ \frac{D}{\sqrt{\tau_r}} \sqrt{t} - \frac{D}{\tau_r} \left( \frac{K-1}{K} \right) t - \frac{D}{K} \right\} dt = 0 \quad (A1.1)$$

where  $a$  designates the time at the intersection point in Figure A1, and the first and second integrals calculate Area 1 and Area 2 in Figure A1, respectively. By substituting  $\tau_r = D^2/4$ , the left side becomes

$$\begin{aligned} & \int_0^a \left\{ \frac{D}{\tau_r} \left( \frac{K-1}{K} \right) t + \frac{D}{K} - \frac{D}{\sqrt{\tau_r}} \sqrt{t} \right\} dt - \int_a^{\tau_r} \left\{ \frac{D}{\sqrt{\tau_r}} \sqrt{t} - \frac{D}{\tau_r} \left( \frac{K-1}{K} \right) t - \frac{D}{K} \right\} dt \\ &= \frac{D}{2\tau_r} \left( \frac{K-1}{K} \right) a^2 + \frac{D}{K} a - \frac{2D}{3\sqrt{\tau_r}} a^{\frac{3}{2}} - \frac{2D}{3\sqrt{\tau_r}} \left\{ (\tau_r)^{\frac{3}{2}} - a^{\frac{3}{2}} \right\} + \frac{D}{2\tau_r} \left( \frac{K-1}{K} \right) \{ (\tau_r)^2 + a^2 \} + \frac{D}{K} (\tau_r - a) \end{aligned}$$

$$= \frac{D}{2} \left( \frac{K-1}{K} \right) \tau_r + \frac{D}{K} \tau_r - \frac{2D}{3} \tau_r$$

Therefore, we equation (A1.1) becomes,

$$\begin{aligned} \frac{D}{2} \left( \frac{K-1}{K} \right) \tau_r + \frac{D}{K} \tau_r - \frac{2D}{3} \tau_r &= 0 \\ \Rightarrow \frac{1}{2} \left( \frac{K-1}{K} \right) + \frac{1}{K} - \frac{2}{3} &= 0 \end{aligned} \quad (\text{A1.2})$$

Finally, we obtain  $K = 3$  by solving equation (A1.2).

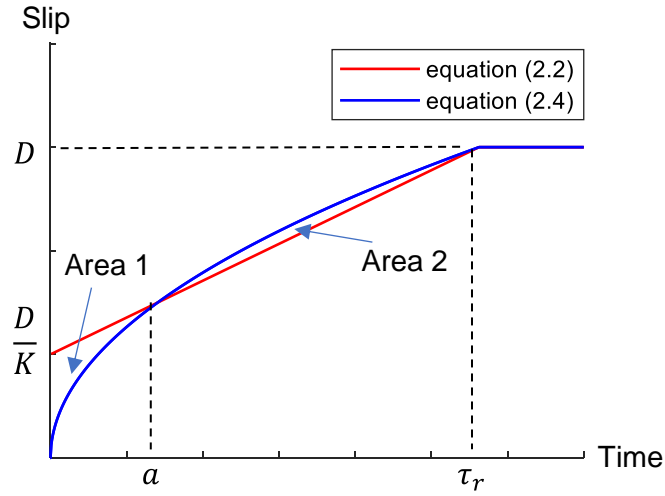


**Figure A1** Comparison of the slip functions of equations (2.2) and (2.4). Areas 1 and 2 are enclosed by the red line and blue curve.

## A1.2. Solution of the Source Spectrum

The source spectrum was the Fourier transform of equation (2.5)

$$\Omega(\mathbf{x}, t) = \mu \int_{-(1-q)W}^{qW} \int_{-(1-p)L}^{pL} \dot{D}_1[t - T_v - T_r] d\xi_1 d\xi_2 \quad (2.5)$$

where  $\dot{D}_1[t - T_v - T_r]$  is the slip velocity with time delays  $T_v$  and  $T_r$ . Before taking the Fourier transform, equation (2.5) was deformed as

$$\begin{aligned} \Omega(\mathbf{x}, t) &= \mu \int_0^{qW} \int_0^{pL} \dot{D}_1 \left[ t - \frac{\xi_1 \sin \theta + \xi_2 \cos \theta}{V_r} - \frac{r_h - (\xi_1 \sin \theta \cos \Phi + \xi_2 \sin \theta \sin \Phi)}{V_c} \right] d\xi_1 d\xi_2 \\ &+ \mu \int_0^{qW} \int_{-(1-p)L}^0 \dot{D}_1 \left[ t - \frac{-\xi_1 \sin \theta + \xi_2 \cos \theta}{V_r} - \frac{r_h - (\xi_1 \sin \theta \cos \Phi + \xi_2 \sin \theta \sin \Phi)}{V_c} \right] d\xi_1 d\xi_2 \\ &+ \mu \int_{-(1-q)W}^0 \int_{-(1-p)L}^0 \dot{D}_1 \left[ t - \frac{-\xi_1 \sin \theta - \xi_2 \cos \theta}{V_r} - \frac{r_h - (\xi_1 \sin \theta \cos \Phi + \xi_2 \sin \theta \sin \Phi)}{V_c} \right] d\xi_1 d\xi_2 \end{aligned}$$

$$+\mu \int_{-(1-q)W}^0 \int_0^{pL} \dot{D}_1 \left[ t - \frac{\xi_1 \sin \theta - \xi_2 \cos \theta}{V_r} - \frac{r_h - (\xi_1 \sin \theta \cos \Phi + \xi_2 \sin \theta \sin \Phi)}{V_c} \right] d\xi_1 d\xi_2 \quad (\text{A1.3})$$

For example, we can deform the first integral term as

$$\begin{aligned} & \mu \int_0^{qW} \int_0^{pL} \dot{D}_1 \left[ t - \frac{\xi_1 \sin \theta + \xi_2 \cos \theta}{V_r} - \frac{r_h - (\xi_1 \sin \theta \cos \Phi + \xi_2 \sin \theta \sin \Phi)}{V_c} \right] d\xi_1 d\xi_2 \\ &= \mu \dot{D}_1 \left[ t - \frac{r_h}{V_c} \right] * \int_0^{pL} \delta_D \left[ t - \frac{\xi_1 \sin \theta}{V_r} + \frac{\xi_1 \sin \theta \cos \Phi}{V_c} \right] d\xi_1 * \int_0^{qW} \delta_D \left[ t - \frac{\xi_2 \cos \theta}{V_r} + \frac{\xi_2 \sin \theta \sin \Phi}{V_c} \right] d\xi_2 \\ &= \mu \dot{D}_1 \left[ t - \frac{r_h}{V_c} \right] * \frac{pL}{\tau_{L1}} (H(t) - H(t - \tau_{L1})) * \frac{qW}{\tau_{W1}} (H(t) - H(t - \tau_{W1})) \end{aligned} \quad (\text{A1.4})$$

where the symbol \* is the convolution operator,  $\delta_D(t)$  is Dirac's delta function, and  $H(t)$  is Heaviside step function. The apparent rupture times were defined in Chapter 2 as

$$\tau_{L1} = pL \left( \frac{\sin \theta}{V_r} - \frac{\sin \theta \cos \Phi}{V_c} \right) \quad (\text{2.9d})$$

$$\tau_{L2} = (1 - p)L \left( \frac{\sin \theta}{V_r} + \frac{\sin \theta \cos \Phi}{V_c} \right) \quad (\text{2.9e})$$

$$\tau_{W1} = qW \left( \frac{\cos \theta}{V_r} - \frac{\sin \theta \sin \Phi}{V_c} \right) \quad (\text{2.9f})$$

$$\tau_{W2} = (1 - q)W \left( \frac{\cos \theta}{V_r} + \frac{\sin \theta \sin \Phi}{V_c} \right) \quad (\text{2.9g})$$

After deforming the second to fourth integral terms similar to the first integral term, the Fourier transform of  $\Omega(\mathbf{x}, t)$  was calculated as

$$\begin{aligned} \Omega(\mathbf{x}, \omega) = & pqM_0 \exp \left\{ i\omega \left( \frac{r_h}{V_c} - \frac{\tau_{L1}}{2} - \frac{\tau_{W1}}{2} \right) \right\} \frac{\sin \left( \frac{\omega \tau_{L1}}{2} \right) \sin \left( \frac{\omega \tau_{W1}}{2} \right)}{\frac{\omega \tau_{L1}}{2} \frac{\omega \tau_{W1}}{2}} F_\tau(\omega) \\ & + (1 - p)qM_0 \exp \left\{ i\omega \left( \frac{r_h}{V_c} - \frac{\tau_{L2}}{2} - \frac{\tau_{W1}}{2} \right) \right\} \frac{\sin \left( \frac{\omega \tau_{L2}}{2} \right) \sin \left( \frac{\omega \tau_{W1}}{2} \right)}{\frac{\omega \tau_{L2}}{2} \frac{\omega \tau_{W1}}{2}} F_\tau(\omega) \\ & + (1 - p)(1 - q)M_0 \exp \left\{ i\omega \left( \frac{r_h}{V_c} - \frac{\tau_{L2}}{2} - \frac{\tau_{W1}}{2} \right) \right\} \frac{\sin \left( \frac{\omega \tau_{L2}}{2} \right) \sin \left( \frac{\omega \tau_{W1}}{2} \right)}{\frac{\omega \tau_{L2}}{2} \frac{\omega \tau_{W1}}{2}} F_\tau(\omega) \\ & + p(1 - q)M_0 \exp \left\{ i\omega \left( \frac{r_h}{V_c} - \frac{\tau_{L2}}{2} - \frac{\tau_{W1}}{2} \right) \right\} \frac{\sin \left( \frac{\omega \tau_{L2}}{2} \right) \sin \left( \frac{\omega \tau_{W1}}{2} \right)}{\frac{\omega \tau_{L2}}{2} \frac{\omega \tau_{W1}}{2}} F_\tau(\omega) \end{aligned} \quad (\text{A1.5})$$

where the symbol exp is the exponential function,  $i = \sqrt{-1}$ ,  $M_0$  is the seismic moment  $M_0 = \mu LWD$ , and  $F_\tau(\omega)$  is the Fourier transform of the slip velocity  $\dot{D}_1(t)$  of equation (2.1).

$$F_{\tau}(\omega) = \left( \frac{1}{K} - \frac{K-1}{K} \exp\left(-\frac{i\omega\tau_r}{2}\right) \frac{\sin\left(\frac{\omega\tau_r}{2}\right)}{\frac{\omega\tau_r}{2}} \right) \quad (\text{A1.6})$$

By deforming equation (A1.5), we can obtain the mathematical representation of the source spectrum with equations (2.8) and (2.9).

### A1.3. Envelope Approximation of the Source Spectrum

The envelope of the source spectrum was derived heuristically rather than rigorously. This section provides the derivations of the envelopes  $F_{E\tau}$  and  $F_{EL}$ . A basic approach is to find possible functions by referring to the original theoretical solution and test them by comparing the derived envelopes with the original theoretical spectra.

The amplitude spectrum of the slip velocity is

$$|F_{\tau}(\omega)| = \left| \frac{1}{K} - \frac{K-1}{K} \exp\left(-\frac{i\omega\tau_r}{2}\right) \frac{\sin\left(\frac{\omega\tau_r}{2}\right)}{\frac{\omega\tau_r}{2}} \right| \quad (\text{A1.7})$$

The low-frequency asymptote of  $|F_{\tau}(\omega)|$  is 1.0. This result can be obtained considering  $\omega \rightarrow 0$  in equation (A1.7). The amplitude spectrum of equation (A3.1) can be deformed as

$$|F_{\tau}(\omega)| = \frac{1}{K} \sqrt{1 + \sqrt{\left(\frac{K-1}{\frac{\omega\tau_r}{2}}\right)^2 + \left(\frac{(K-1)^2}{2\left(\frac{\omega\tau_r}{2}\right)^2}\right)^2} \sin(\omega\tau_r + \alpha) + \frac{(K-1)^2}{2\left(\frac{\omega\tau_r}{2}\right)^2}} \quad (\text{A1.8})$$

$$\alpha = \tan^{-1}\left(\frac{1-K}{4\omega\tau_r}\right)$$

The term  $\sin(\omega\tau_r + \alpha)$  suggests that the amplitude spectrum has local maximum values periodically. I obtained the envelope of  $|F_{\tau}(\omega)|$  at a high-frequency range by connecting the local maximum values indicated by  $\sin(\omega\tau_r + \alpha) = 1$ . Thus, the envelope  $F_{E\tau}$  at a high-frequency range is

$$F_{E\tau} = \frac{1}{K} \sqrt{1 + \sqrt{\left(\frac{K-1}{\frac{\omega\tau_r}{2}}\right)^2 + \left(\frac{(K-1)^2}{2\left(\frac{\omega\tau_r}{2}\right)^2}\right)^2} + \frac{(K-1)^2}{2\left(\frac{\omega\tau_r}{2}\right)^2}} \quad (\text{A1.9})$$

The envelope of equation (A1.9) is inappropriate at a low-frequency range. At a low-frequency range, the envelope of  $|F_\tau(\omega)|$  can be approximated well by  $F_{E\tau} = 1.0$ . The intersection frequency between equation (A1.9) and  $F_{E\tau} = 1.0$  can be derived as

$$\omega = \frac{2K}{\tau_r(K + 1)} \quad (\text{A1.10})$$

Finally, the envelope of  $|F_\tau(\omega)|$  is proposed as equation (2.11) (also, see Figure 2.2).

$$F_{E\tau} = \begin{cases} 1, & \omega < \frac{2K}{\tau_r(K + 1)} \\ \frac{1}{K} \sqrt{1 + \sqrt{\left(\frac{K-1}{\frac{\omega\tau_r}{2}}\right)^2 + \left(\frac{(K-1)^2}{2\left(\frac{\omega\tau_r}{2}\right)^2}\right)^2} + \frac{(K-1)^2}{2\left(\frac{\omega\tau_r}{2}\right)^2}}, & \frac{2K}{\tau_r(K + 1)} \leq \omega \end{cases} \quad (\text{2.11})$$

The amplitude spectrum of  $F_L$  is

$$|F_L| = \left| p \exp\left(-i\omega \frac{\tau_{L1}}{2}\right) \frac{\sin\left(\frac{\omega\tau_{L1}}{2}\right)}{\frac{\omega\tau_{L1}}{2}} + (1-p) \exp\left(-i\omega \frac{\tau_{L2}}{2}\right) \frac{\sin\left(\frac{\omega\tau_{L2}}{2}\right)}{\frac{\omega\tau_{L2}}{2}} \right| \quad (\text{A1.11})$$

The envelope of  $|F_L|$  is more complicated than  $F_{E\tau}$ , see equation (2.12). The envelope of  $|F_L|$  could be obtained similarly to  $F_{E\tau}$  partly. However, the envelope of  $|F_L|$  was difficult to obtain if the apparent rupture time,  $\tau_{L1}$  or  $\tau_{L2}$ , is less than zero. The derivations of equations (2.12a) and (2.12b), which are the case that  $\tau_{L1}$  and  $\tau_{L2}$  are more than zero, were relatively simple. This appendix provides the derivation of equation (2.12a), which is the case of  $1 \leq \tau_{L1}/\tau_{L2}$ , since the derivations of equations (2.12a) and (2.12b) are similar. At a low-frequency range, the following approximation holds.

$$\frac{\sin(\omega\tau_{L1}/2)}{\omega\tau_{L1}/2} = 1.0 \quad (\text{A1.12})$$

Equations (A1.11) and (A1.12) suggest that the low-frequency asymptote of  $|F_L|$  is 1.0. On the other hand, the following approximation holds at a high-frequency range.

$$\frac{\sin(\omega\tau_{L1}/2)}{\omega\tau_{L1}/2} = \frac{1}{\omega\tau_{L1}/2} \quad (\text{A1.13})$$

The high-frequency asymptote may be obtained from equations (A1.11) and (A1.13) as

$$F_{EL} = \frac{p}{\omega\tau_{L1}/2} + \frac{1-p}{\omega\tau_{L2}/2} \quad (\text{A1.14})$$

The mathematical representation of the envelope of  $|F_L|$  at an intermediate frequency range is also necessary (see Figure 2.3). The derivation of the envelope of  $|F_L|$  at an intermediate frequency range was based on a somewhat heuristic way. Considering the condition of  $\tau_{L2} \leq \tau_{L1}$ , I assumed that the following equations hold approximately at an intermediate frequency range.

$$\frac{\sin(\omega\tau_{L1}/2)}{\omega\tau_{L1}/2} = \frac{1}{\omega\tau_{L1}/2} \quad (A1.15)$$

$$\frac{\sin(\omega\tau_{L2}/2)}{\omega\tau_{L2}/2} = 1.0 \quad (A1.16)$$

By assuming  $\exp(-i\omega\tau_{L1}/2) = 1.0$  and  $\exp(-i\omega\tau_{L2}/2) = 1.0$  and by using equations (A1.15) and (A1.16), we can obtain the envelope of  $|F_L|$  at an intermediate frequency range as

$$F_{EL} = 1 - p + \frac{p}{\omega\tau_{L1}/2} \quad (A1.17)$$

After determining the intersection frequencies, the envelope of  $|F_L|$  was obtained as

(i)  $1 \leq \tau_{L1}/\tau_{L2}$

$$F_{EL} = \begin{cases} 1.0, & \omega < \frac{2}{\tau_{L1}} \\ 1 - p + \frac{p}{\omega\tau_{L1}/2}, & \frac{2}{\tau_{L1}} \leq \omega < \frac{2}{\tau_{L2}} \\ \frac{p}{\omega\tau_{L1}/2} + \frac{1-p}{\omega\tau_{L2}/2}, & \frac{2}{\tau_{L2}} \leq \omega \end{cases} \quad (2.12a)$$

Since equation (2.12a) was derived somewhat heuristically, I confirmed the validity of equation (2.12a) by comparing the original theoretical solution of equation (A1.11) to the envelope of equation (2.12a). Equation (2.12b) was derived similarly to equation (2.12a). Equations (2.12c) to (2.12g) were derived by testing some possible functions prepared by referring to the original theoretical solution of equation (A1.11). I compared several functions with the original theoretical solution and obtained the preferred representations.

## A2. SPECTRAL RATIO FITTING RESULTS

This appendix provides representative results of the spectral ratio fitting to show the effectiveness of the envelope spectrum. Figure caption is as follows.

### *Figure caption*

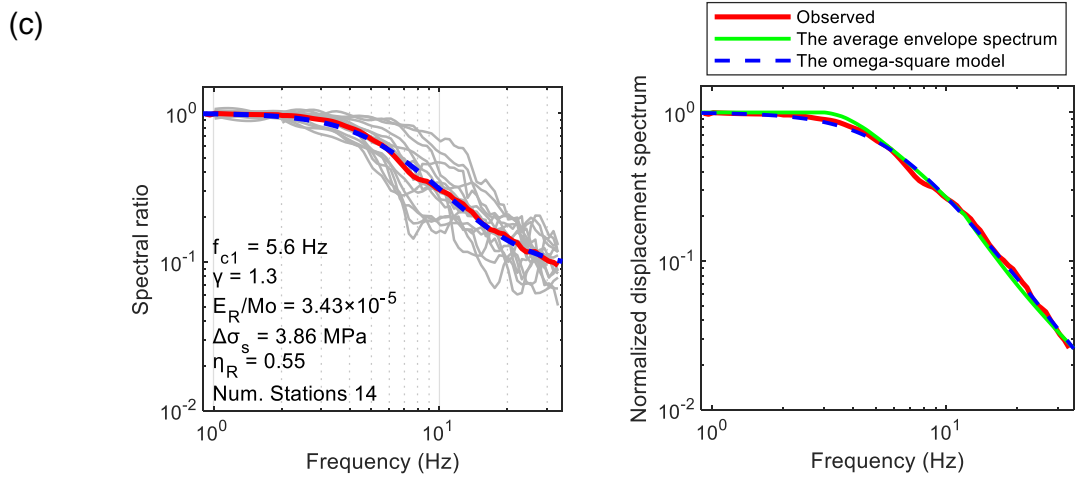
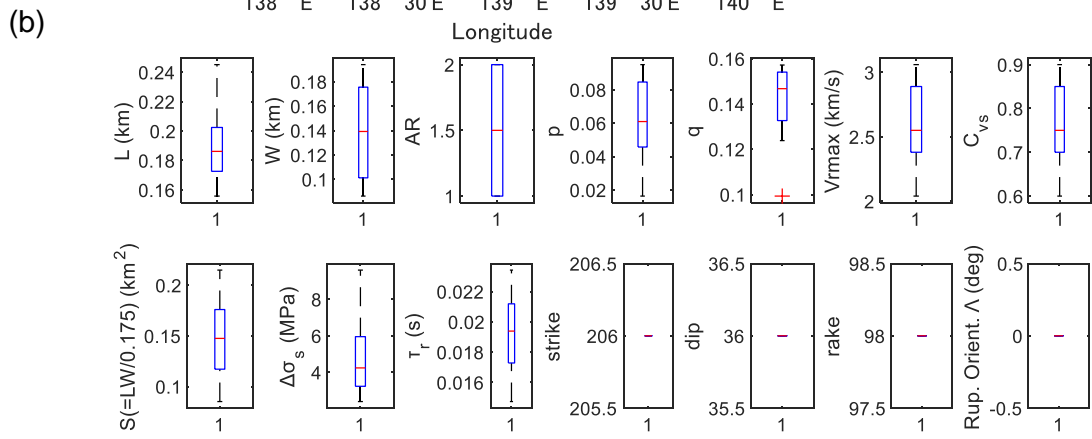
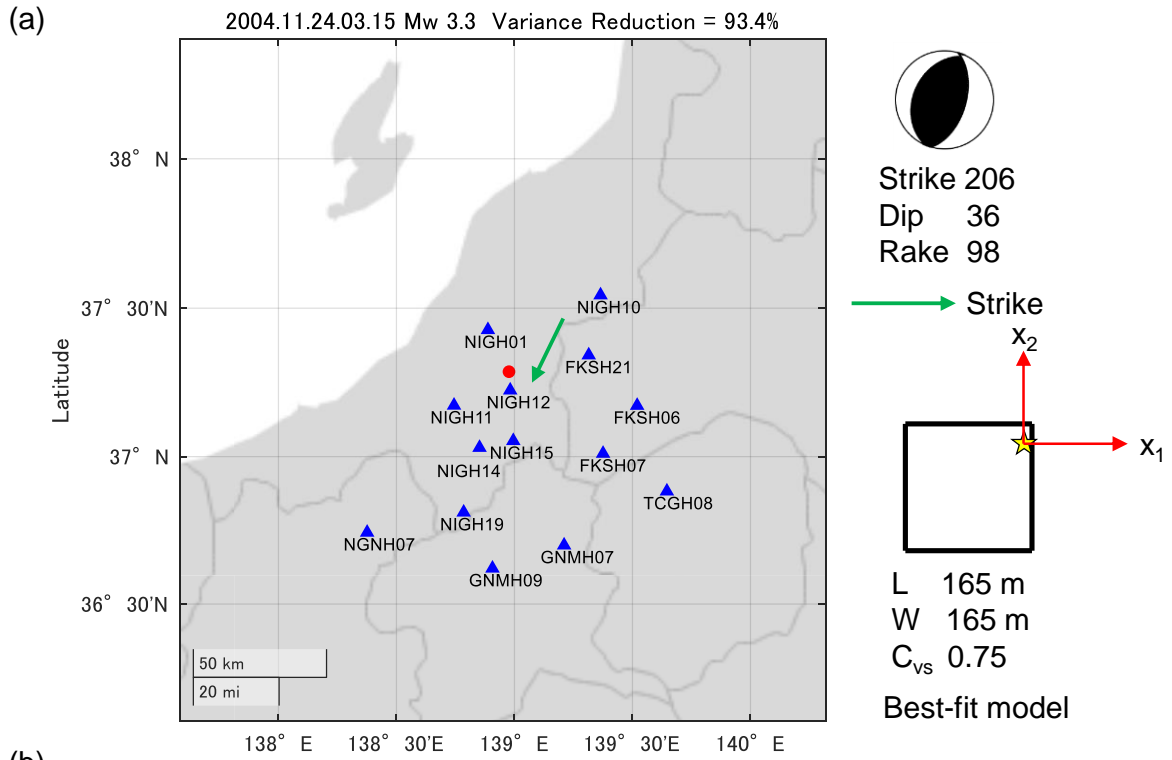
(a) The stations (blue triangles) and the best-fit rupture model (top-left and top-right). The green arrow next to the red dot indicates the strike direction. The green arrow on the top of the best-fit model also shows the strike direction. The  $x_1$  axis is rotated depending on the rupture orientation angle. If the rupture orientation angle is 45 degrees, the  $x_1$  axis is rotated 45 degrees from the strike direction in the best-fit model. The rupture start point (yellow star) for the best-fit model corresponds to the hypocenter. The red dot on the map is the epicenter of a target earthquake. Figure 4.1 may help understand the rupture orientation angle. The date of earthquake occurrence, the moment magnitude, and the variance reduction are shown at the top of the map.

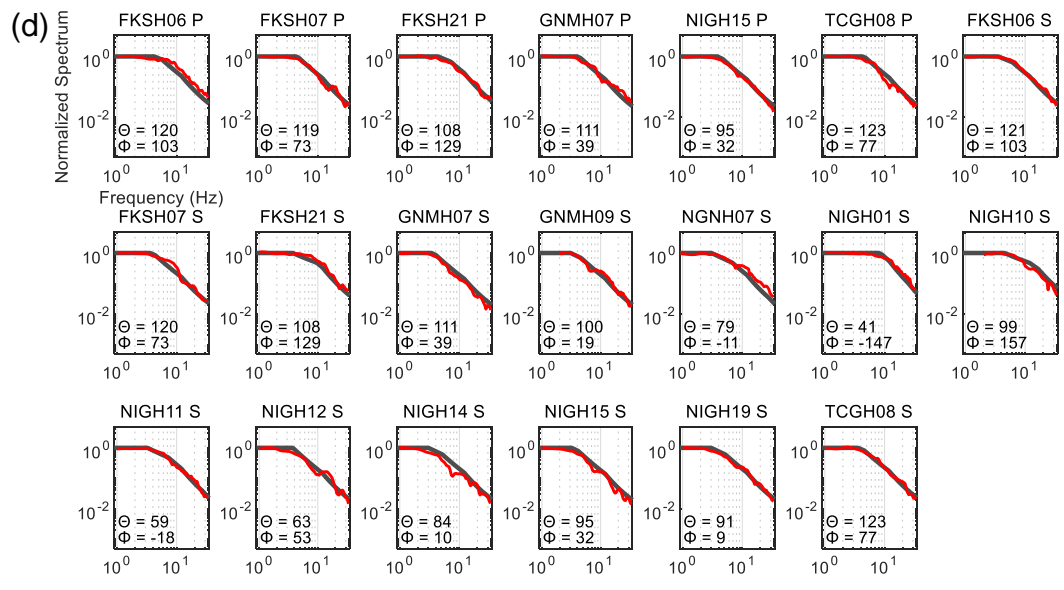
(b) The box plot of the estimated source parameters. The horizontal red line indicates the median, and the bottom and top edges indicate the 25th and 75th percentiles, respectively (the blue lines). The black lines indicate the maximum and minimum values. The symbol “+” indicates an outlier.

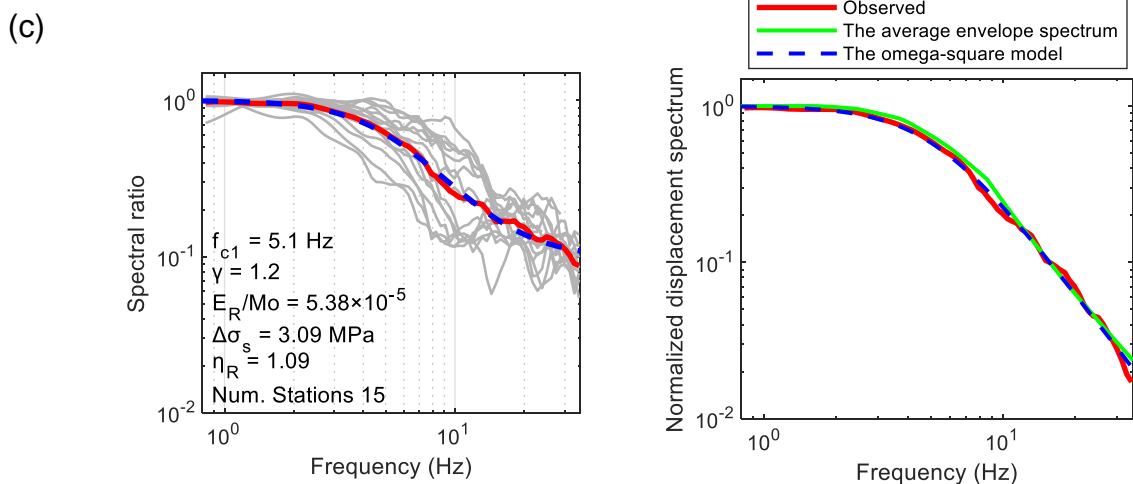
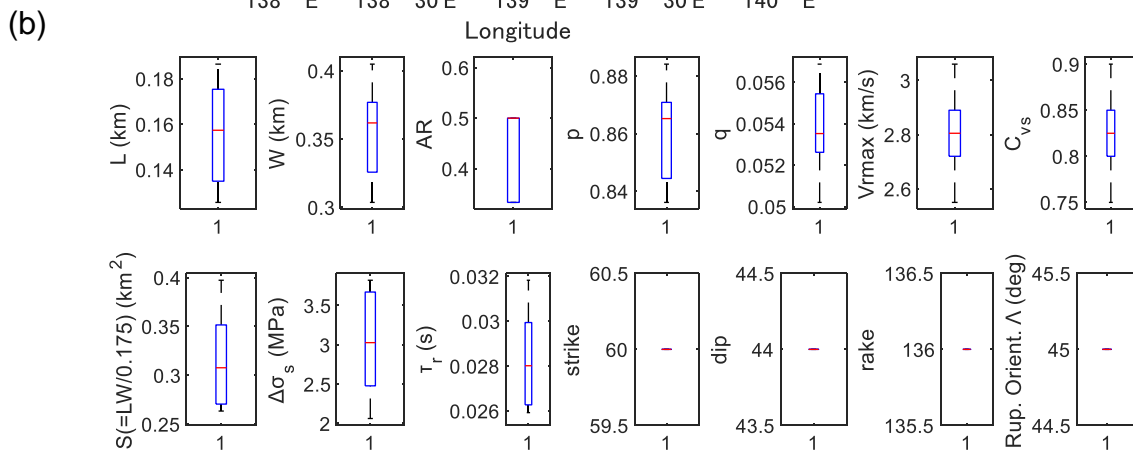
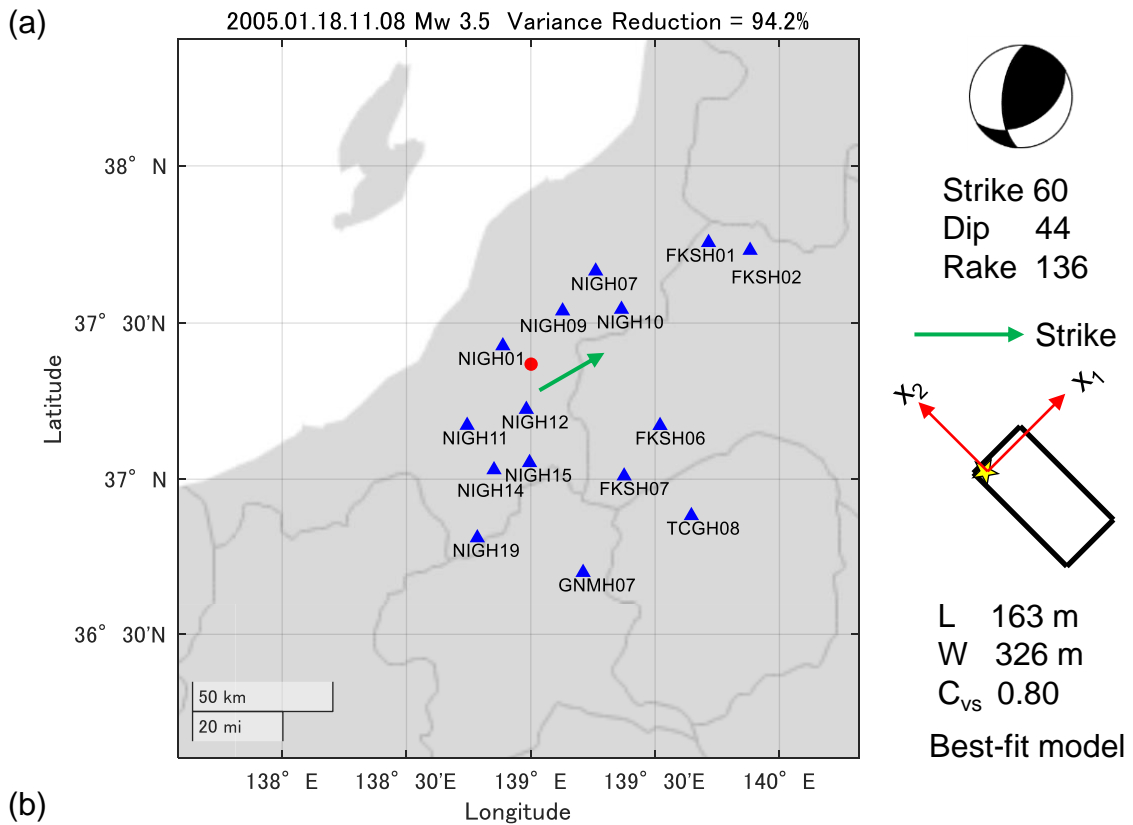
(c) The spectral ratio fitting results for the average spectral ratios. This spectral ratio analysis is conducted to estimate the radiated energy and corner-frequency-based stress drop. The left panel shows the spectral ratio fitting result. The red curve is the average observed spectral ratio, and the dashed blue curve is the prediction from the omega-square model. The gray curves are the observed spectral ratios obtained for each station. The right panel shows the comparison between the observed average spectrum (red), the average envelope spectrum (green), and the normalized omega-square model  $|\Omega(f)|/M_0$ . The red and blue curves in the right panel are obtained from the average spectral ratio (red and blue dashed curves) in the right panel. The green curve is obtained from the spectral ratio fitting shown in (d).

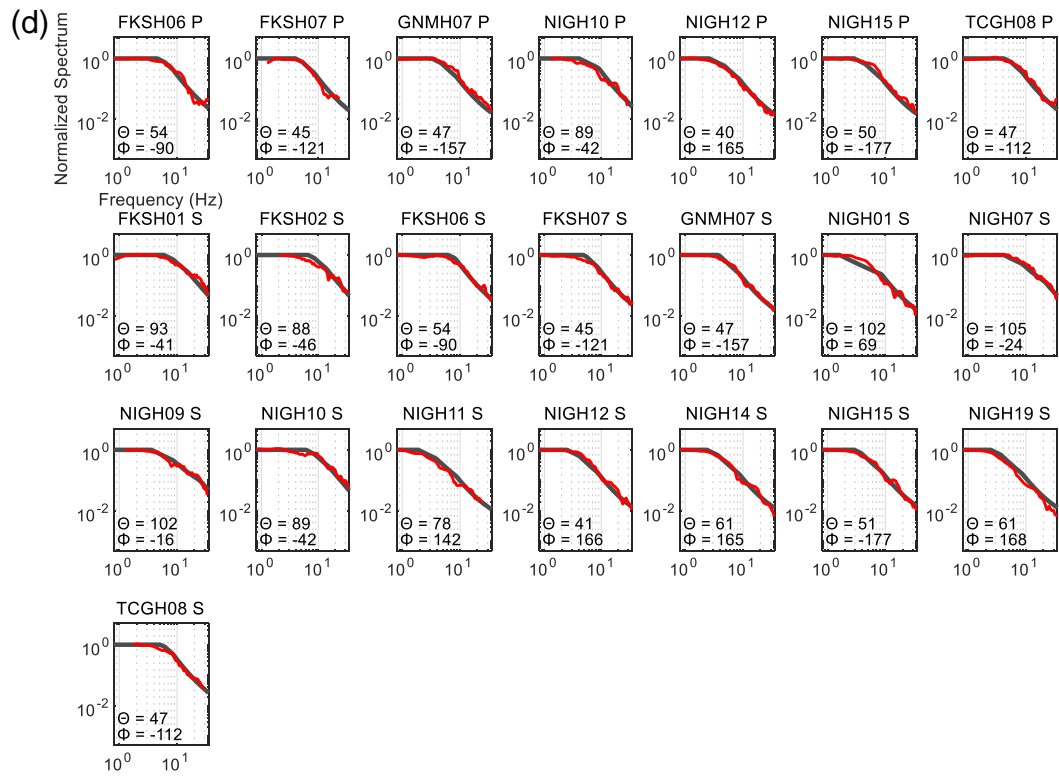


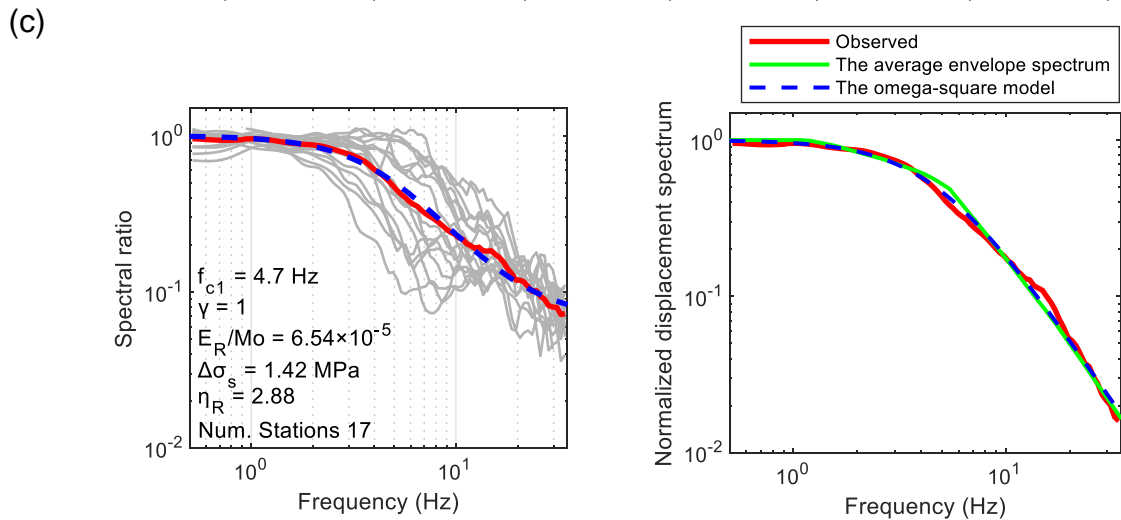
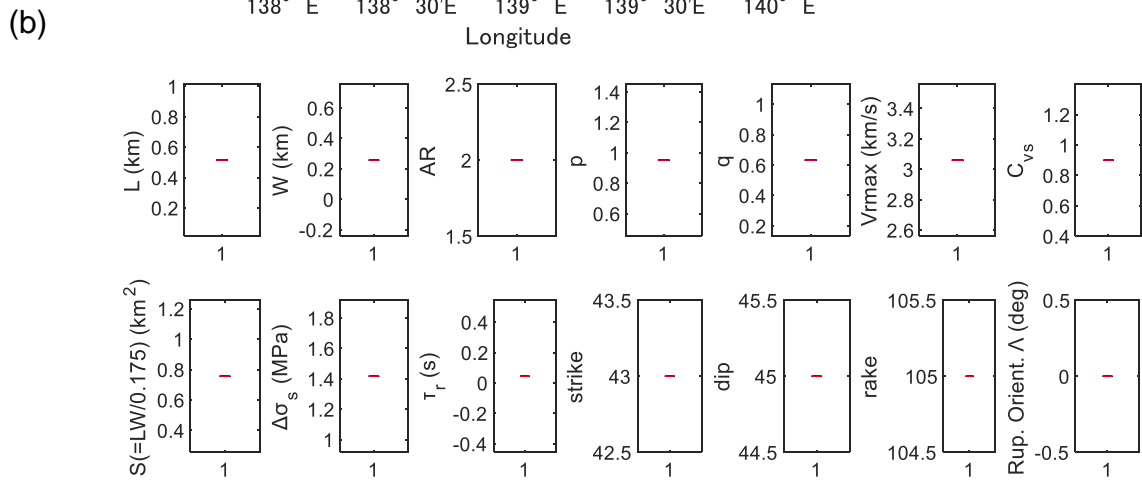
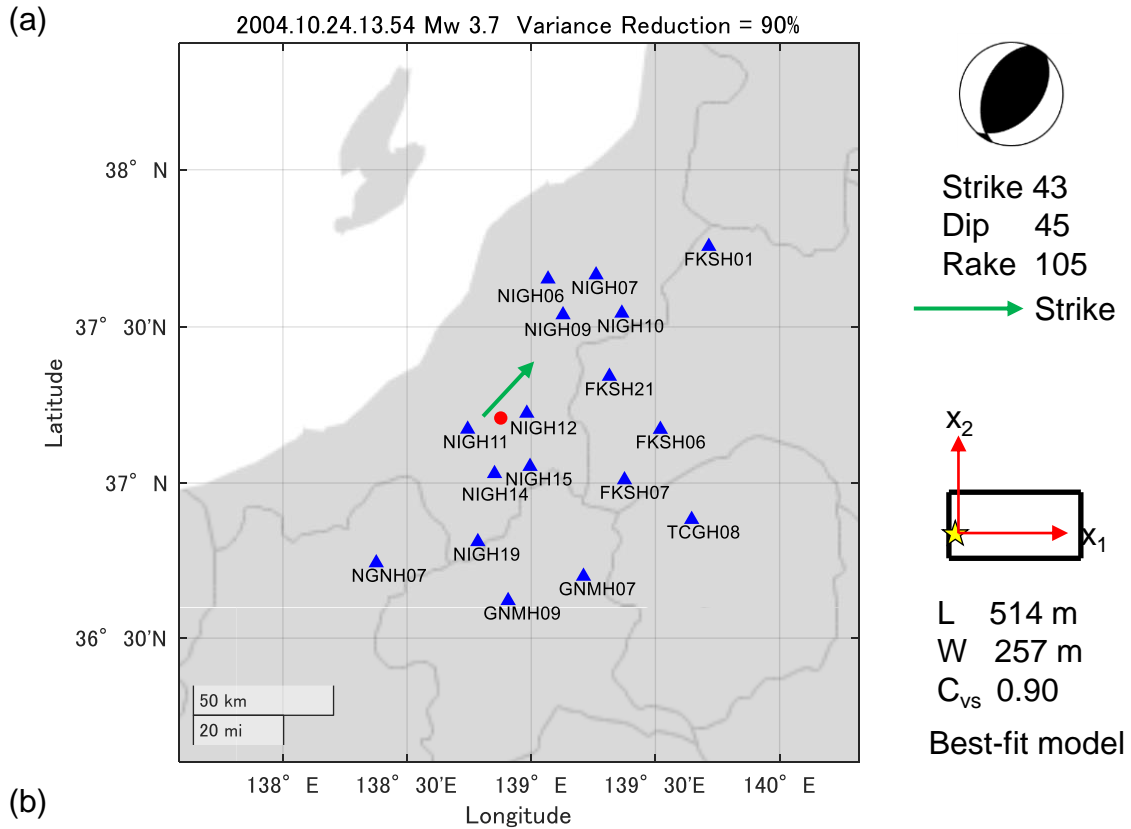
(d) The result of the fitting to the spectral ratios obtained by station and wave type. The panels show the comparison of the envelope spectra,  $\Omega_{EN}(\boldsymbol{x}, f)$ , (gray) and synthesized source spectra,  $SR_{obs}^c(\boldsymbol{x}, f) \times \Omega_{\omega 2}(\boldsymbol{x}, f)$ , (red) for the representative event (bottom). The synthesized source spectra correspond to the observation. The titles of each subplot designate the names of stations and wave type. The polar coordinates are shown in each panel.

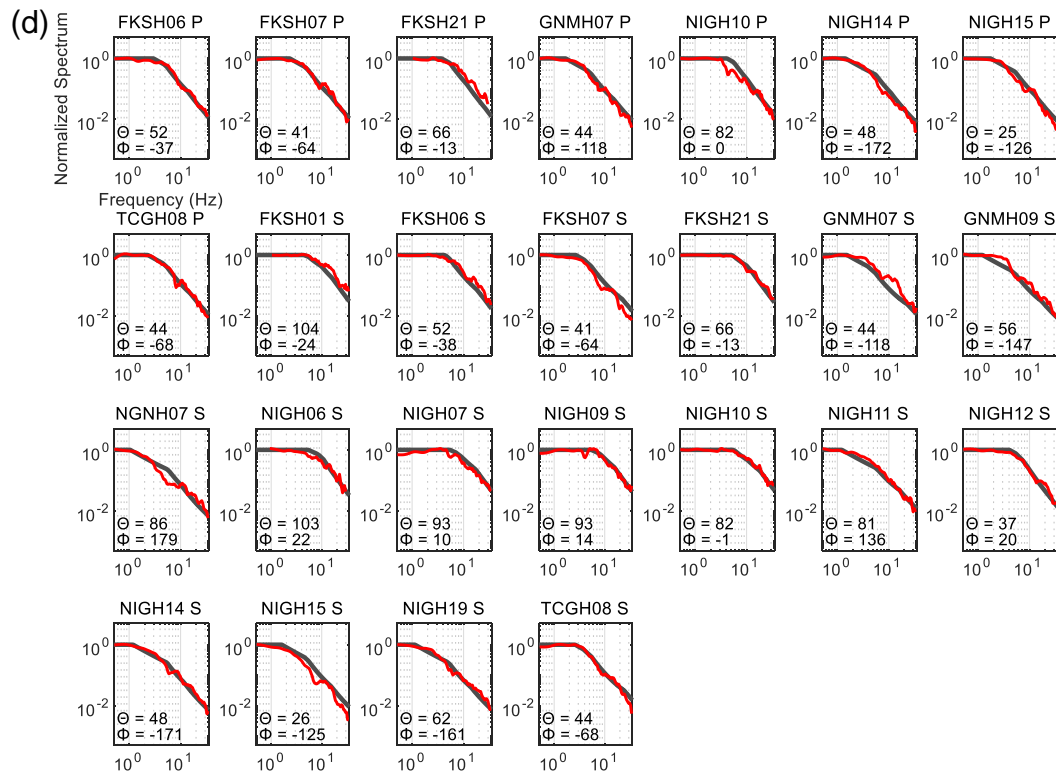


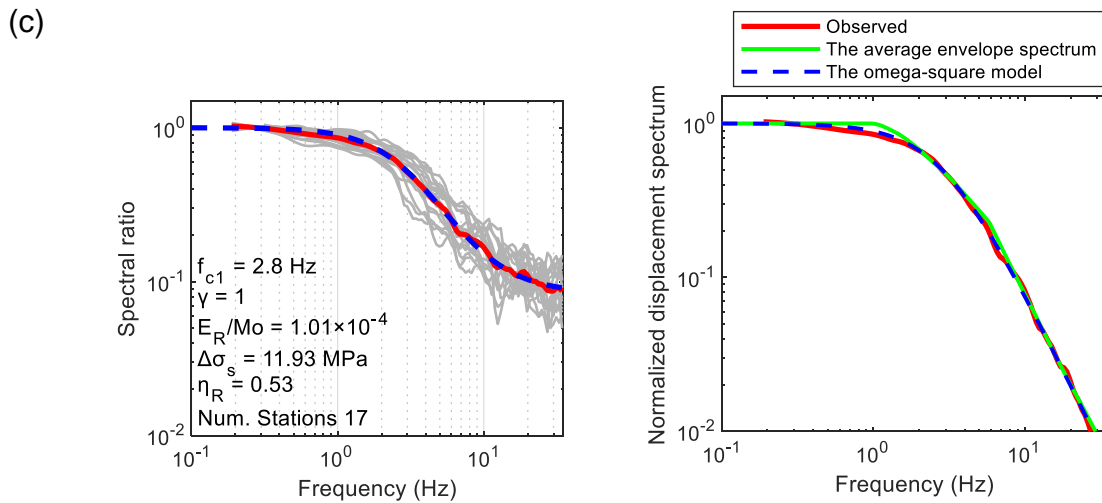
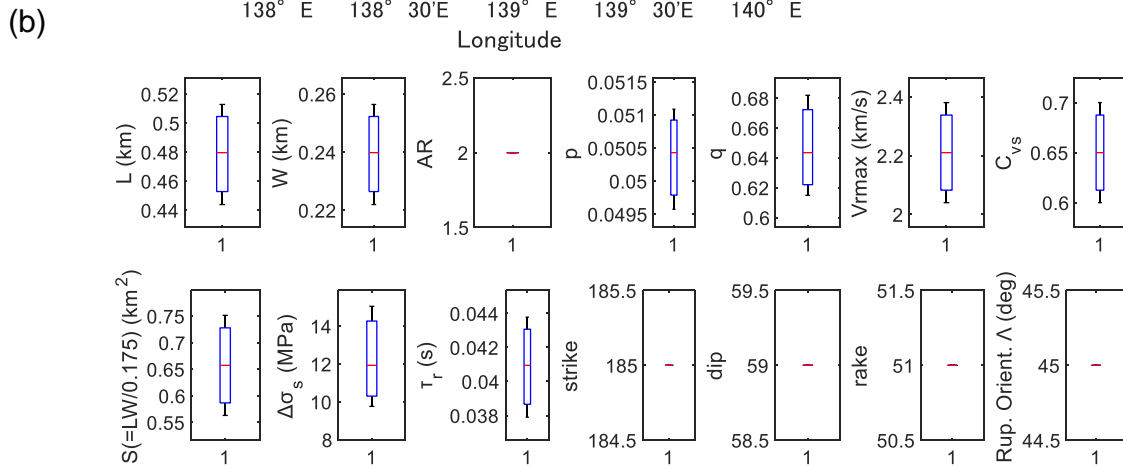
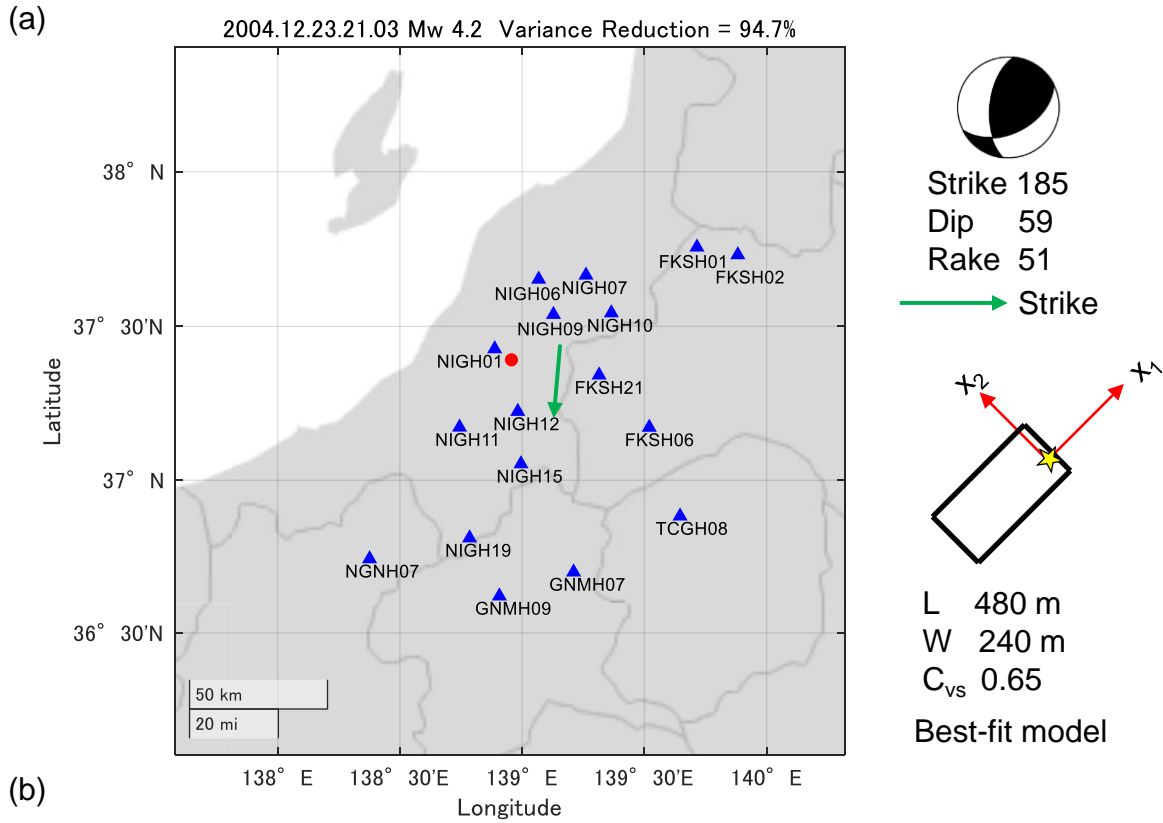




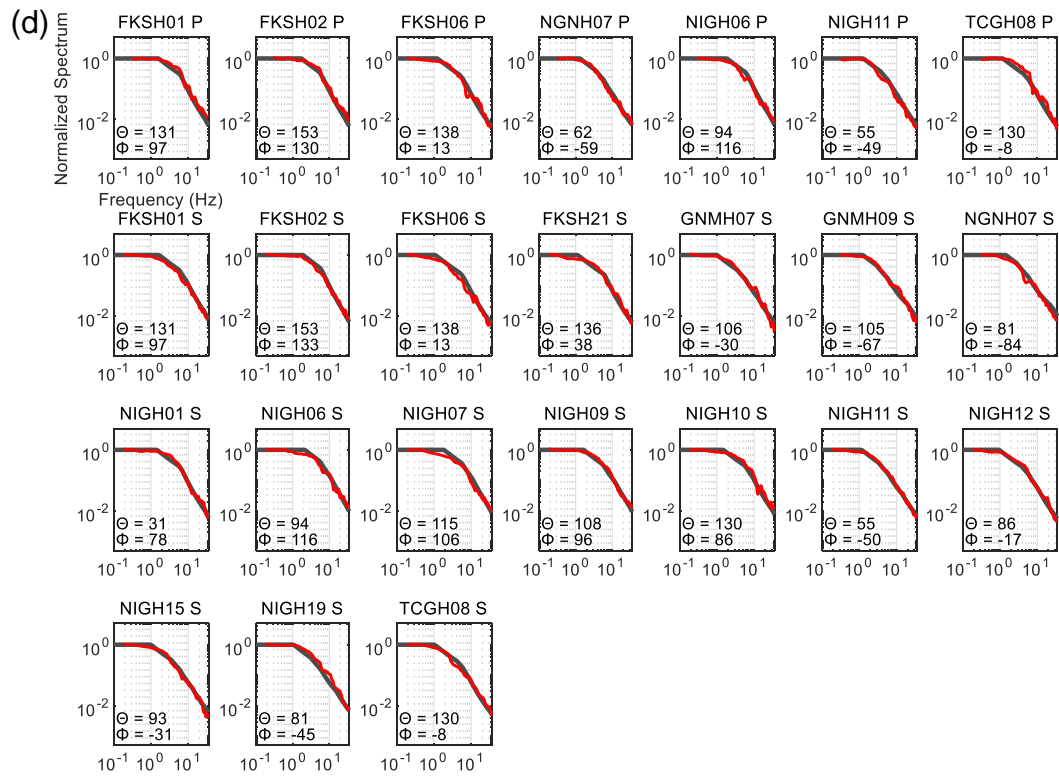


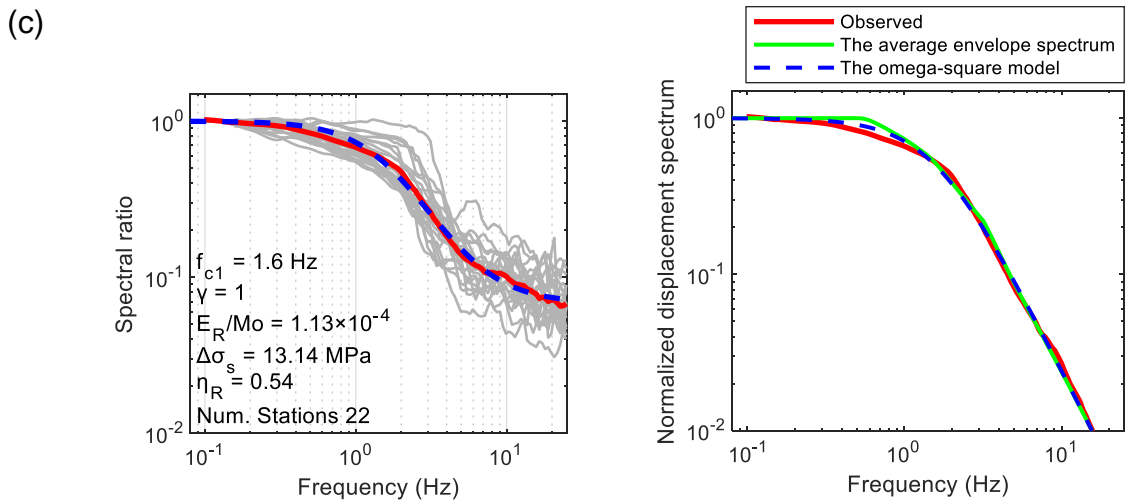
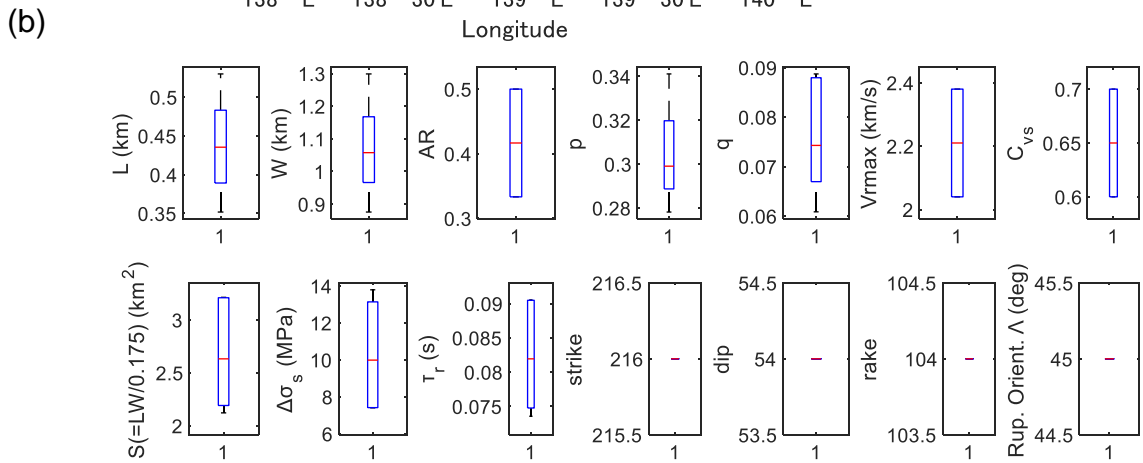
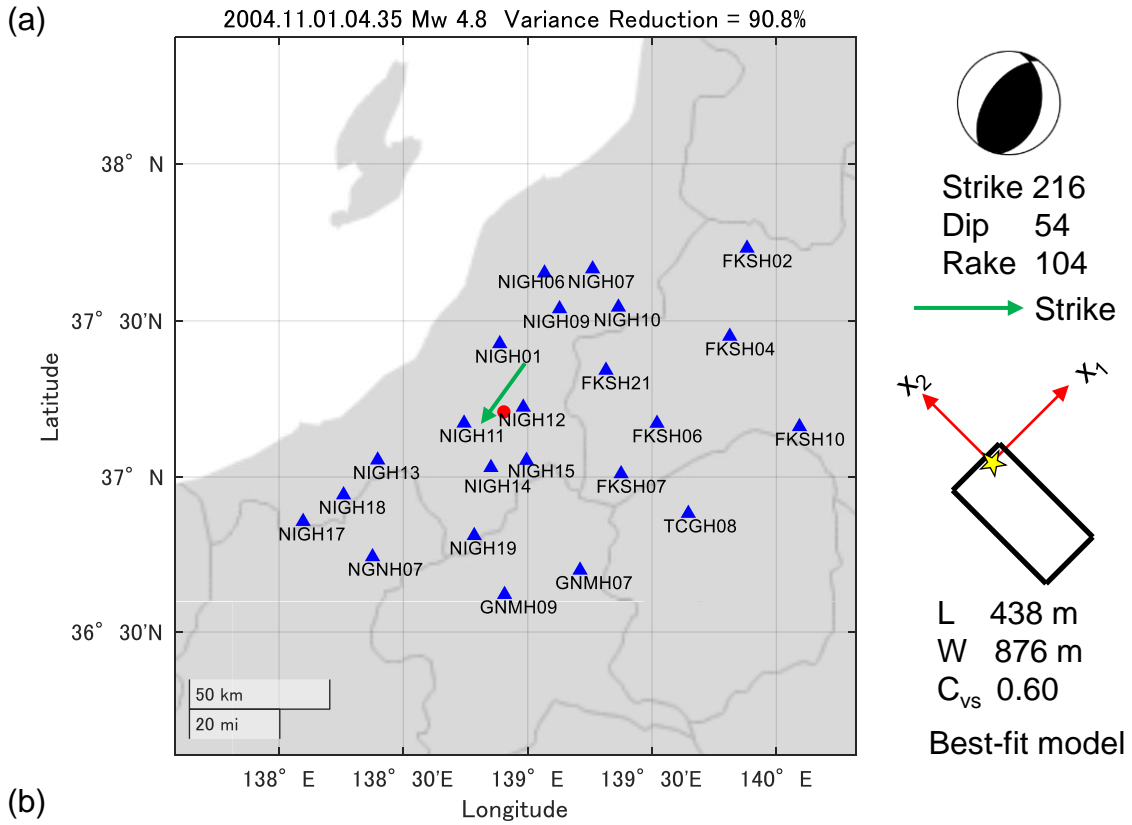


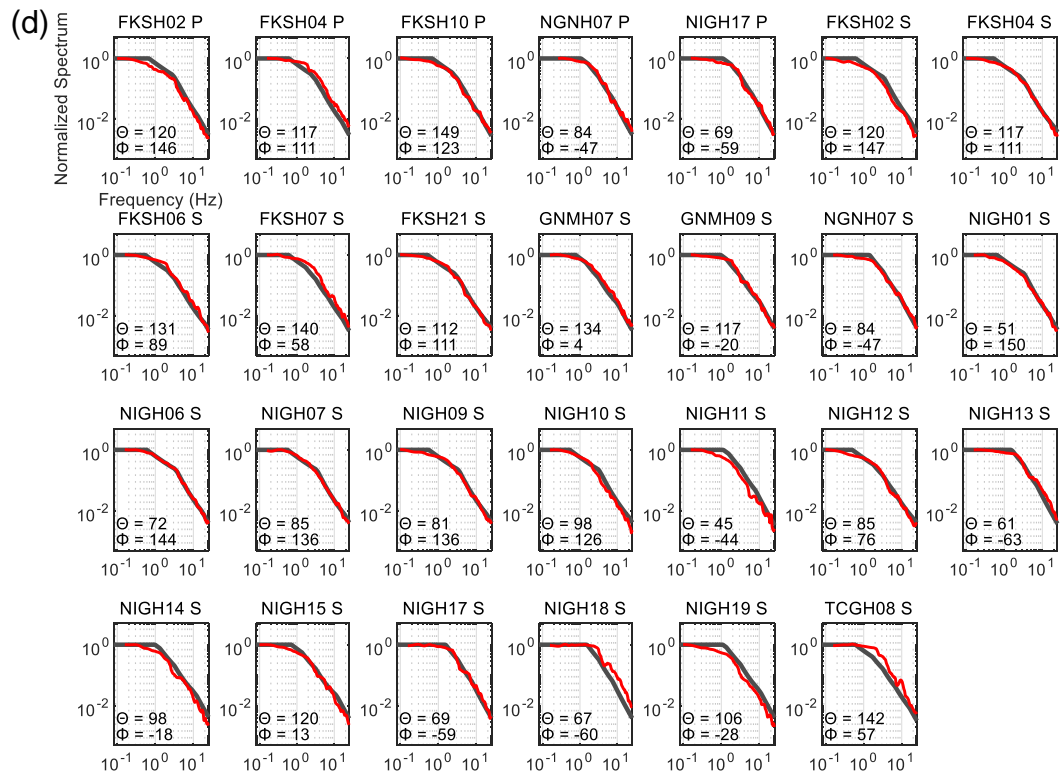


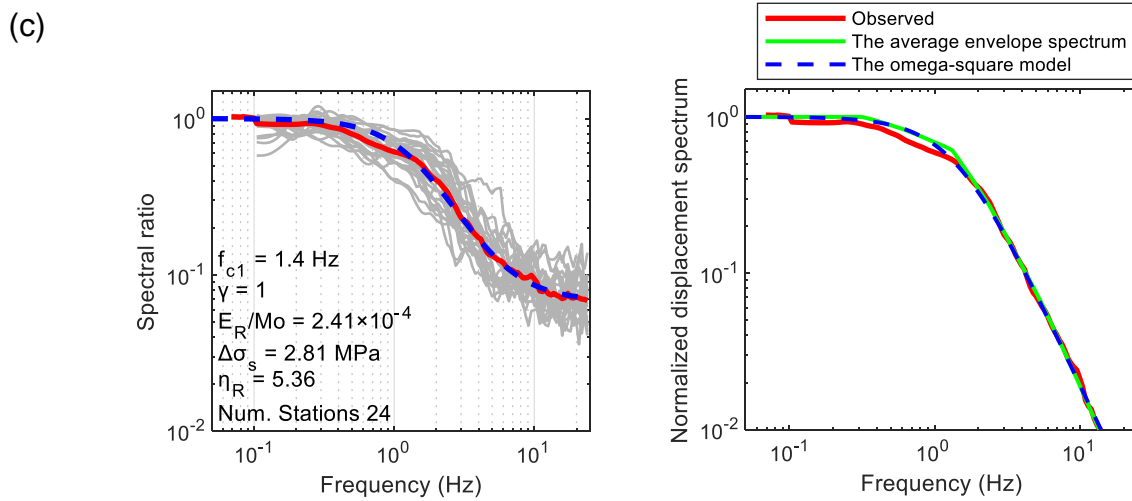
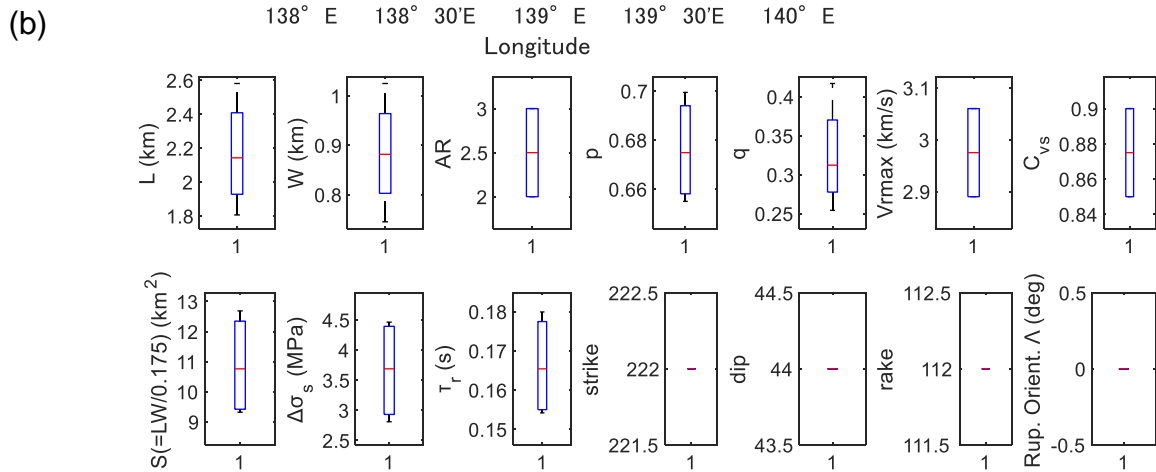
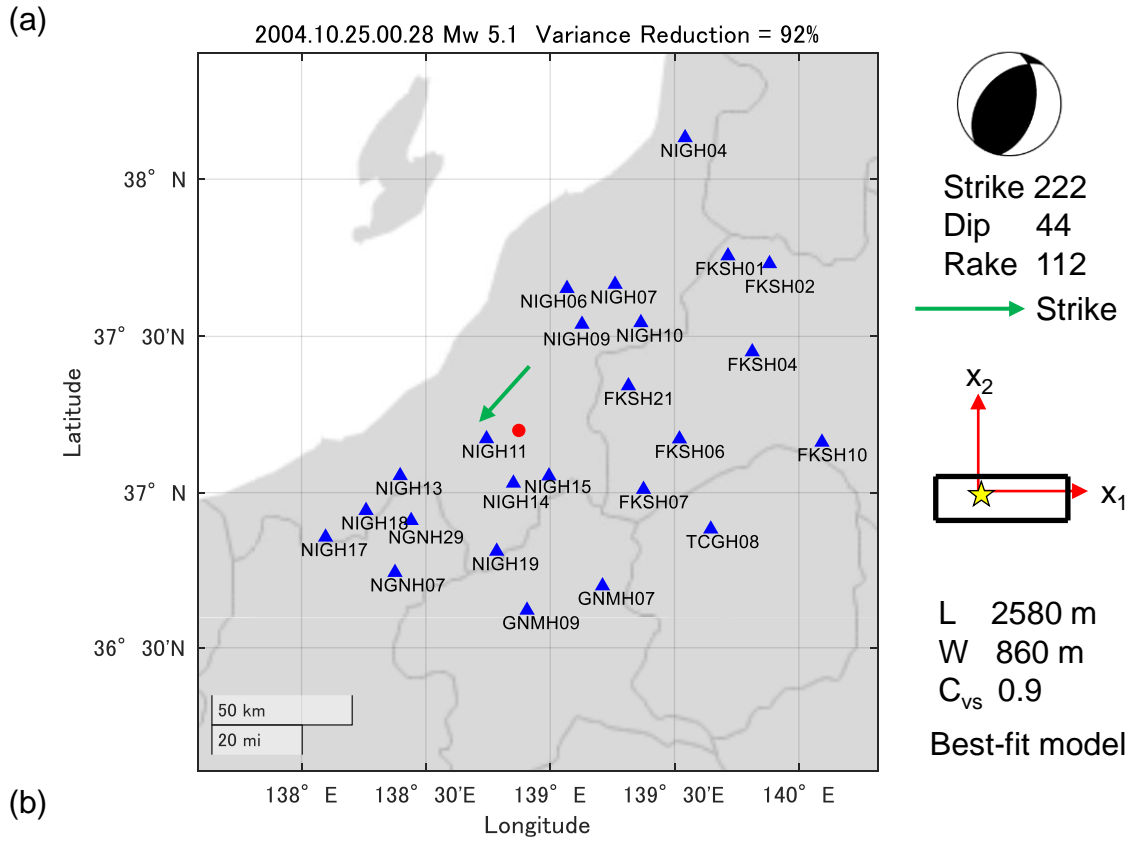


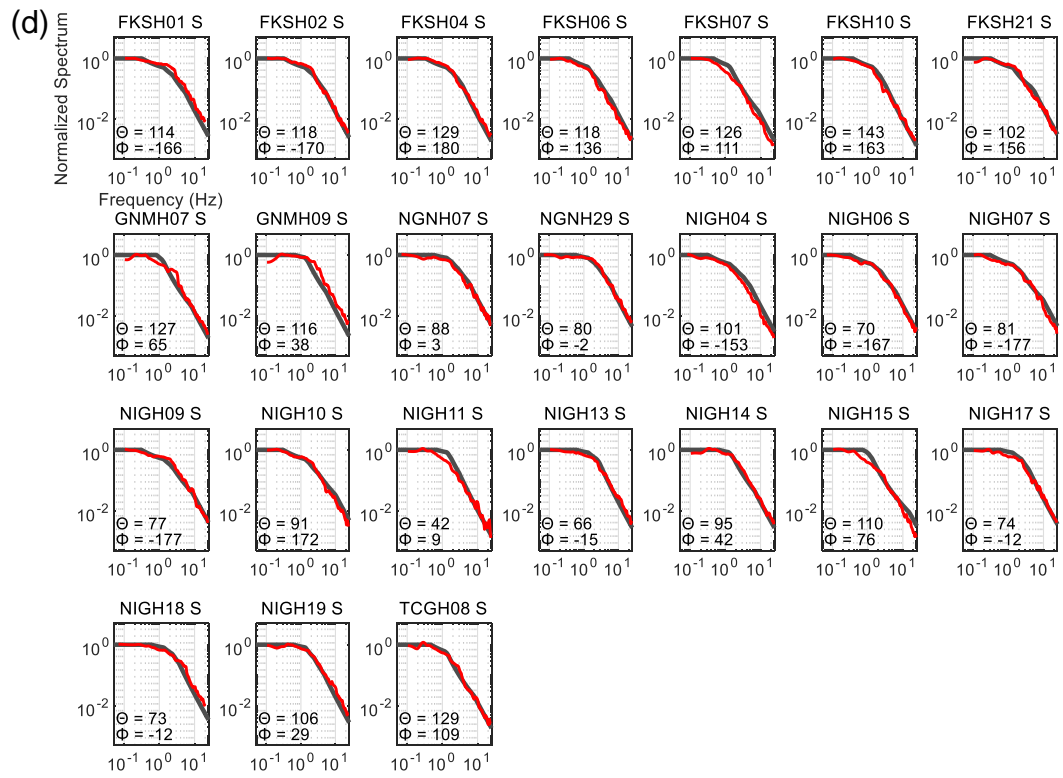


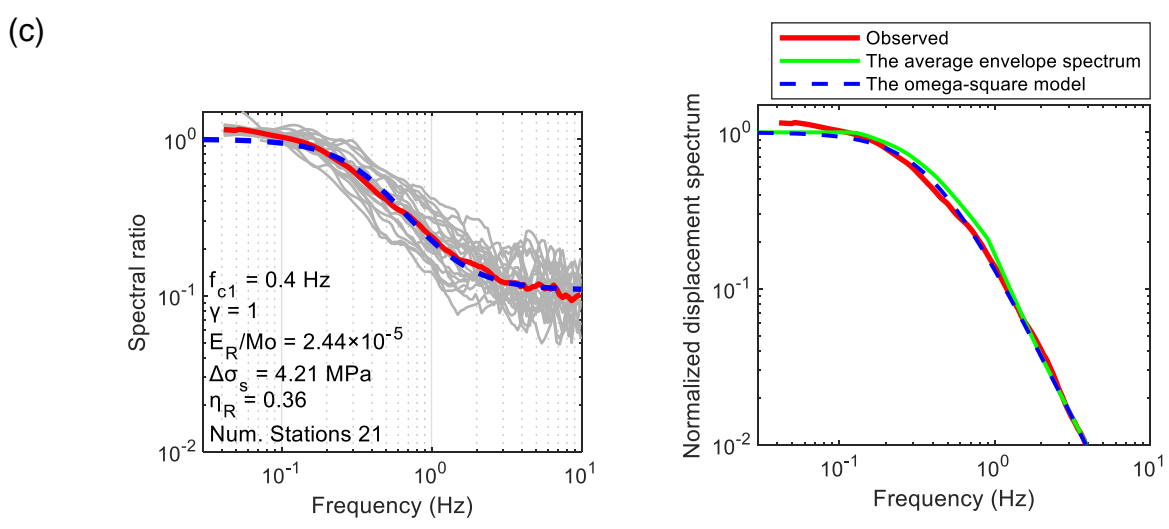
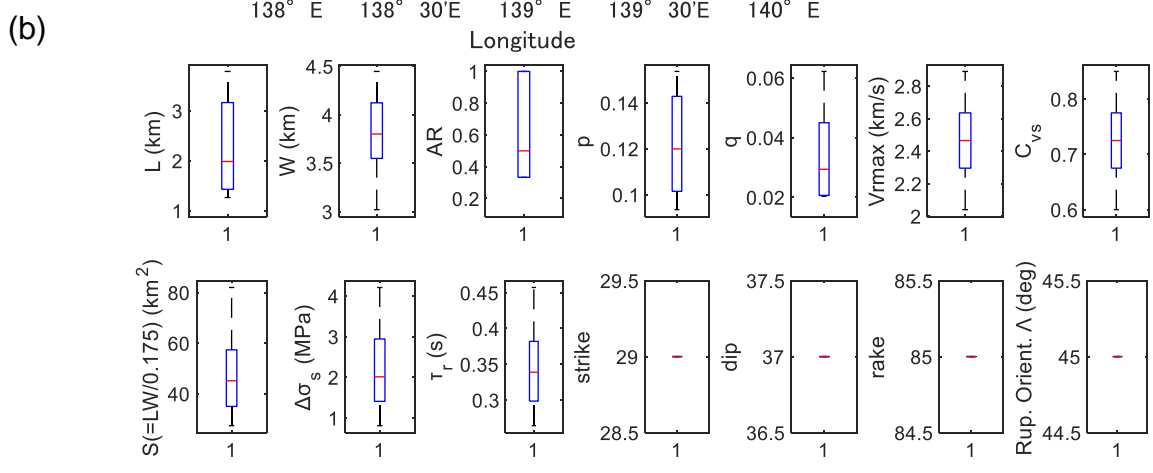
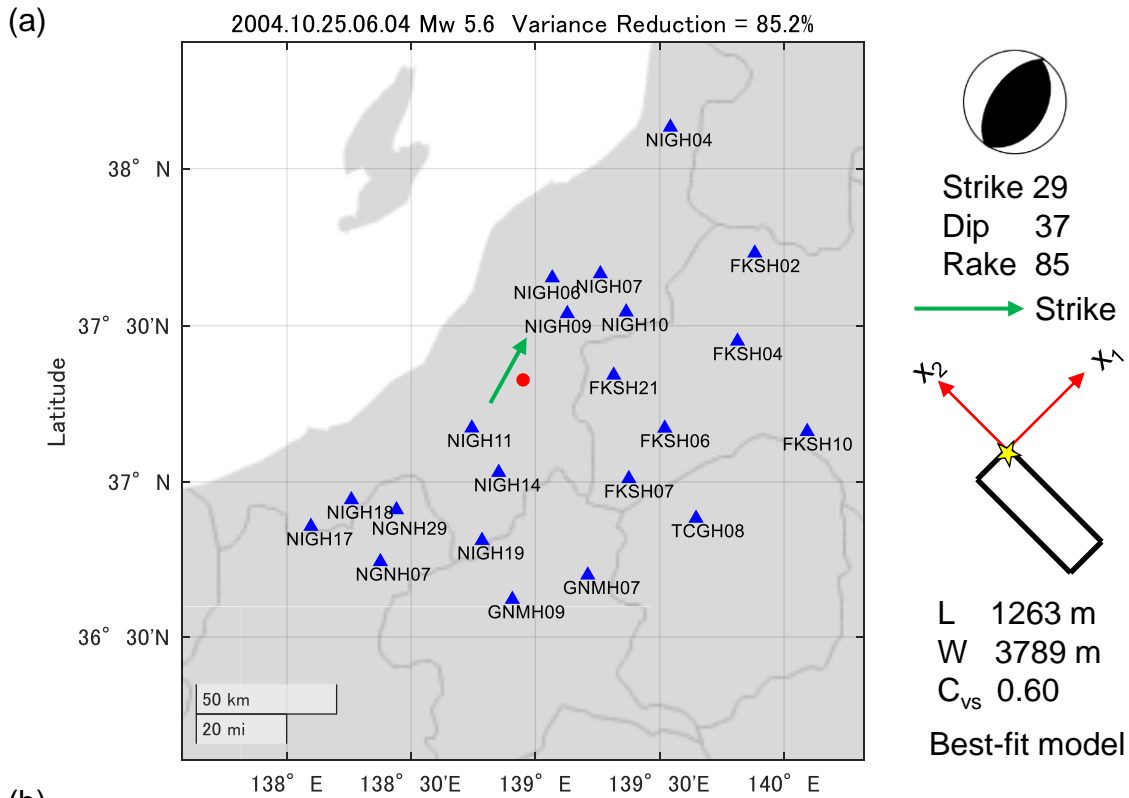


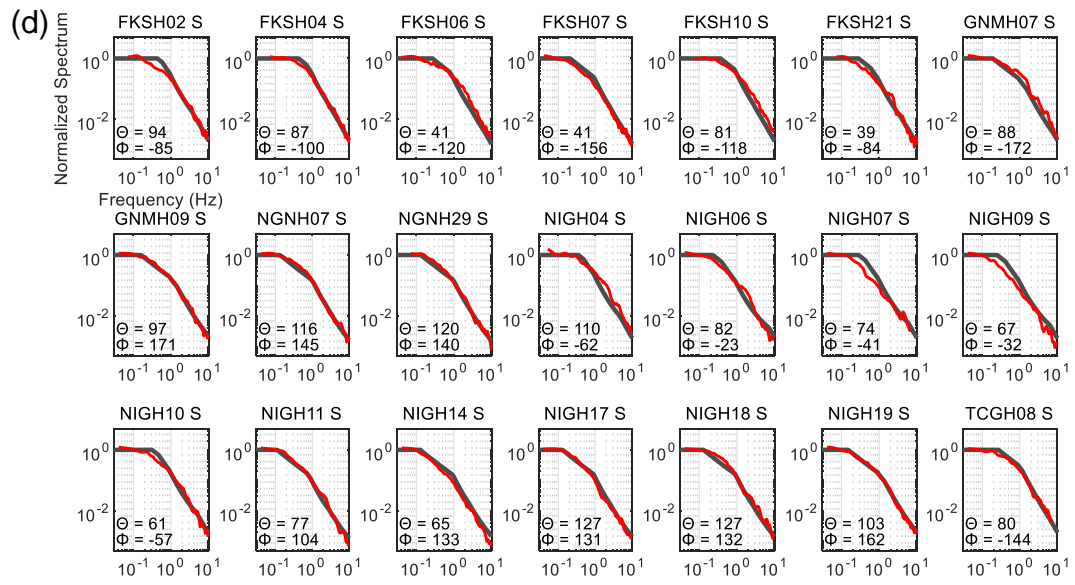


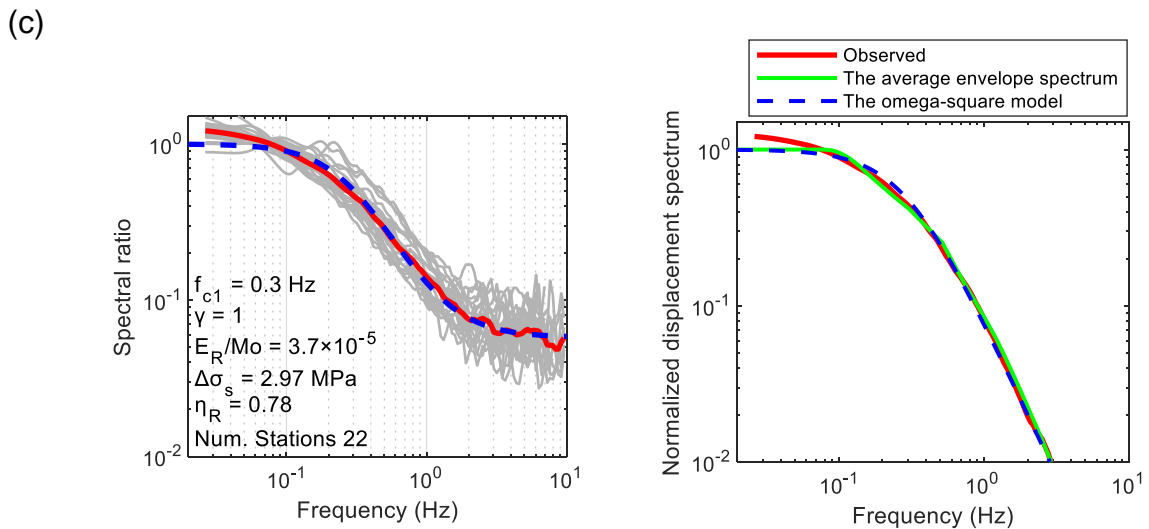
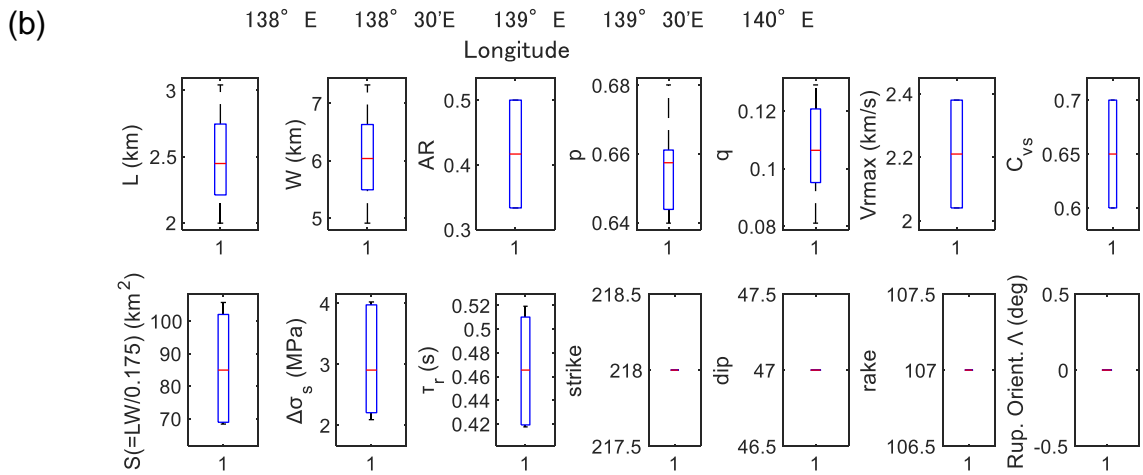
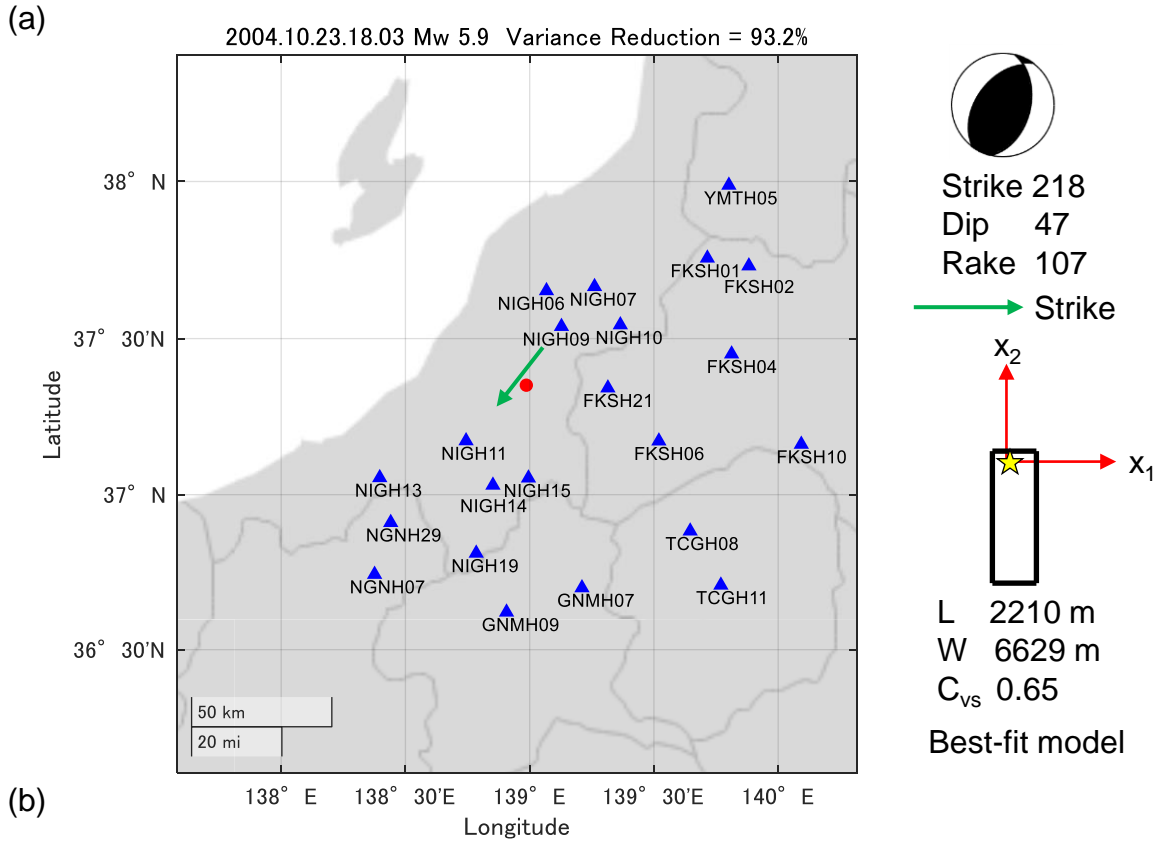




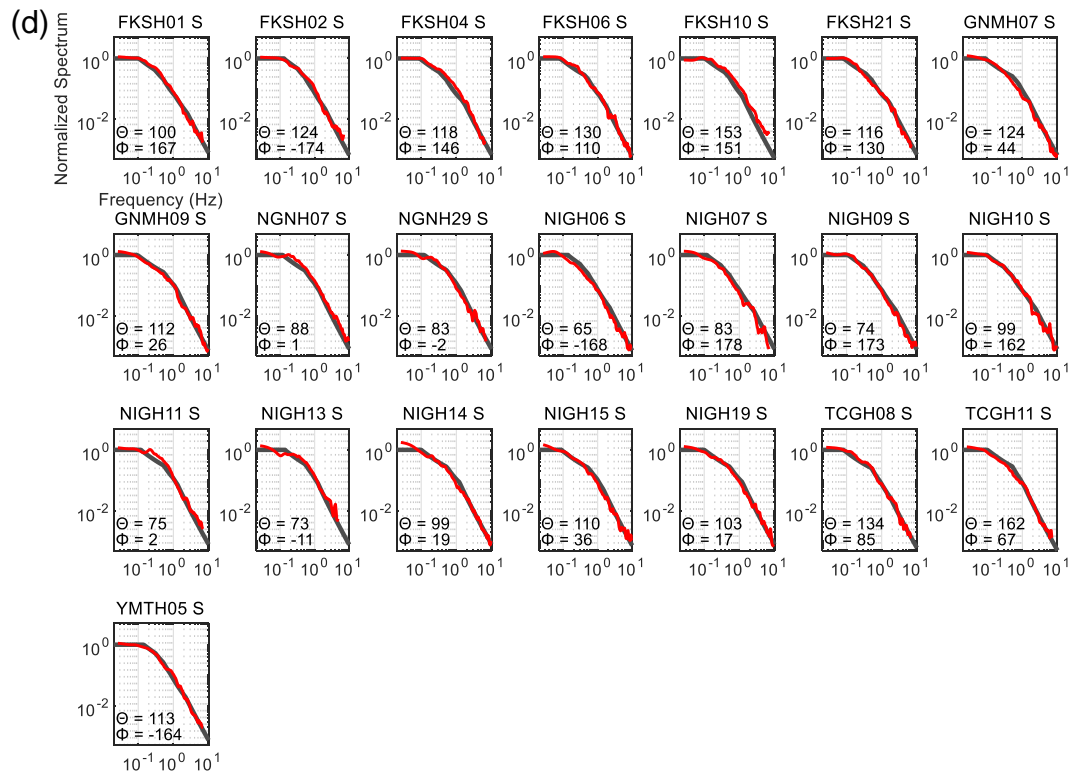


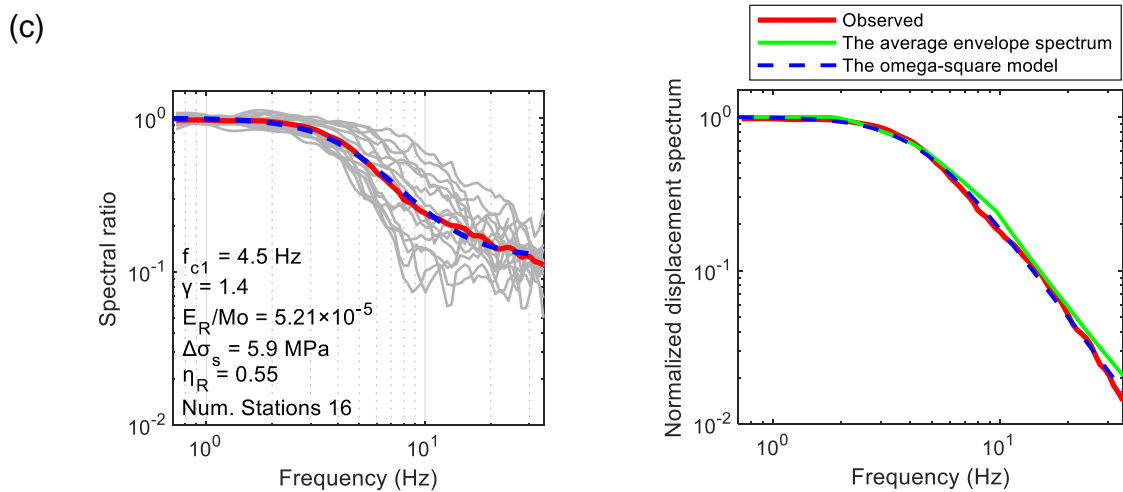
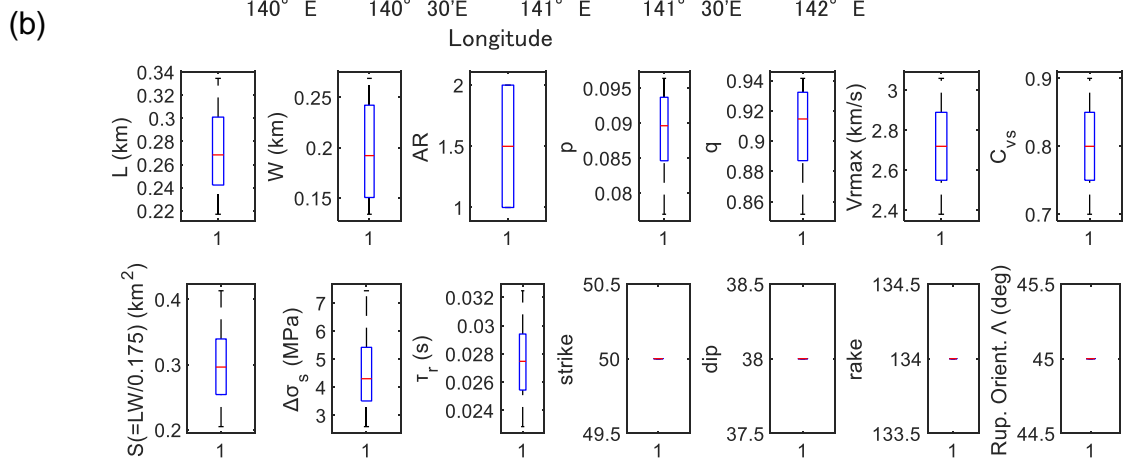
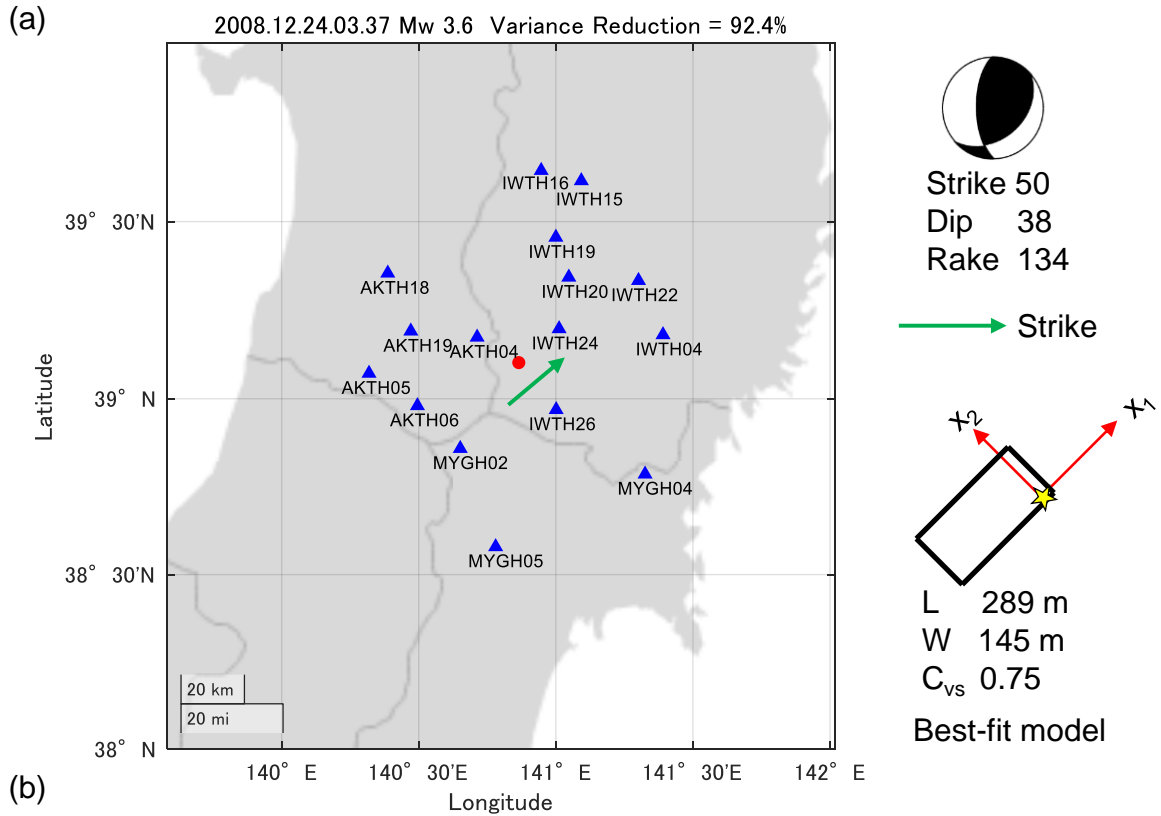


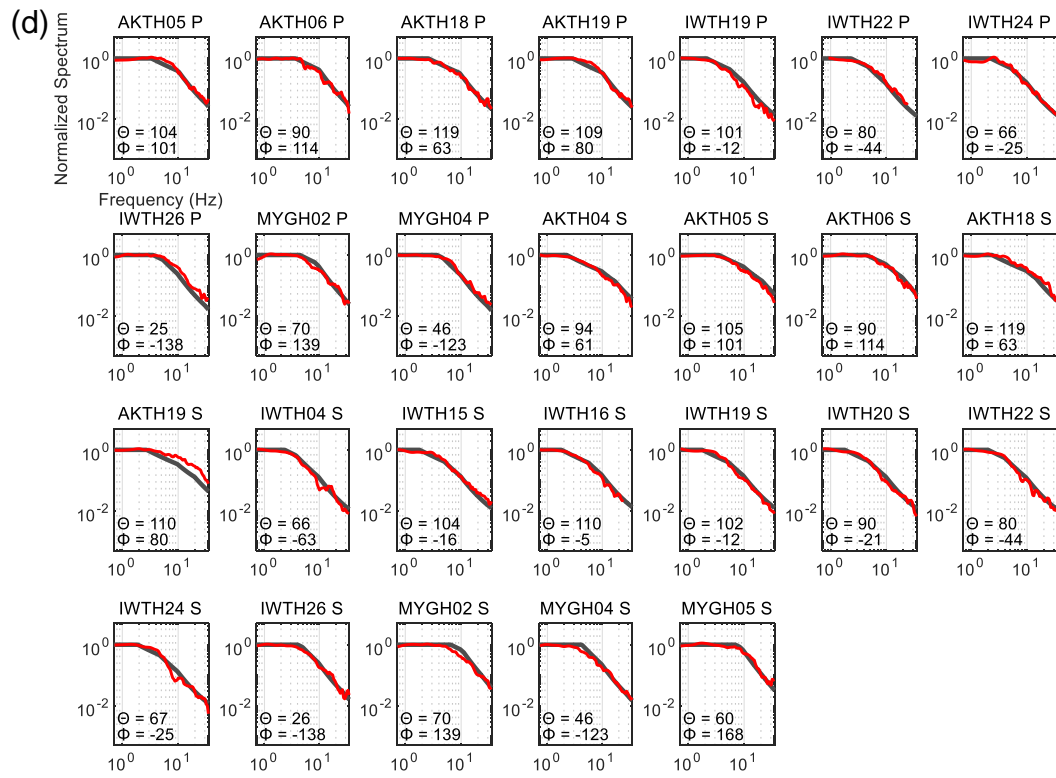


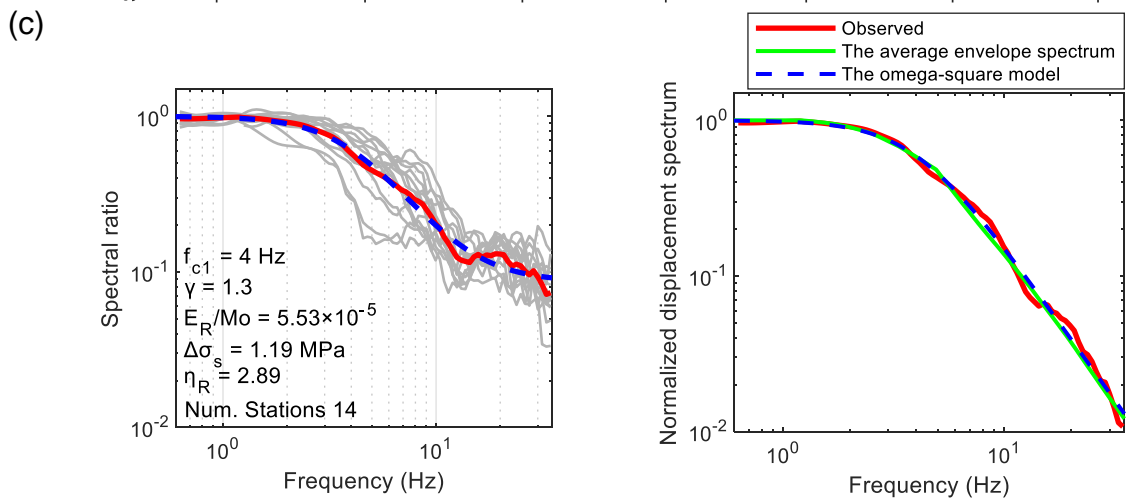
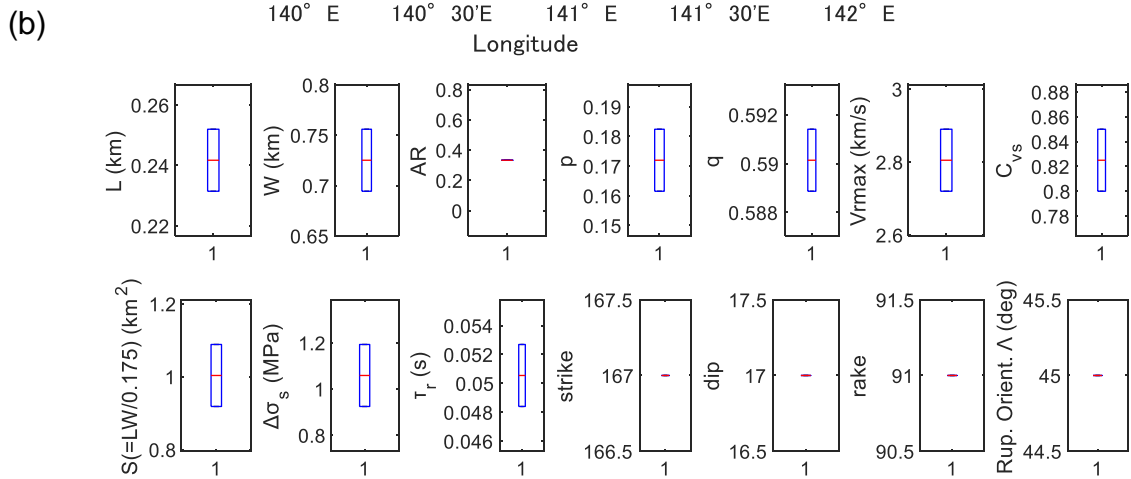
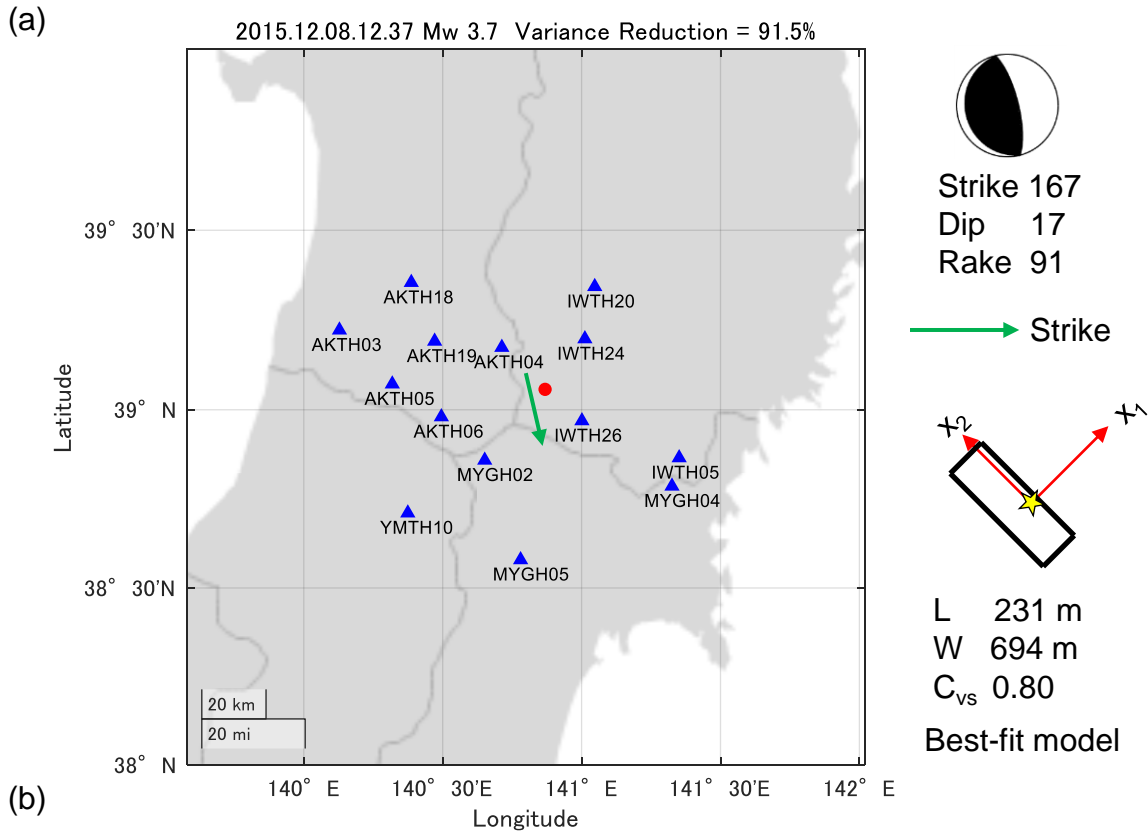


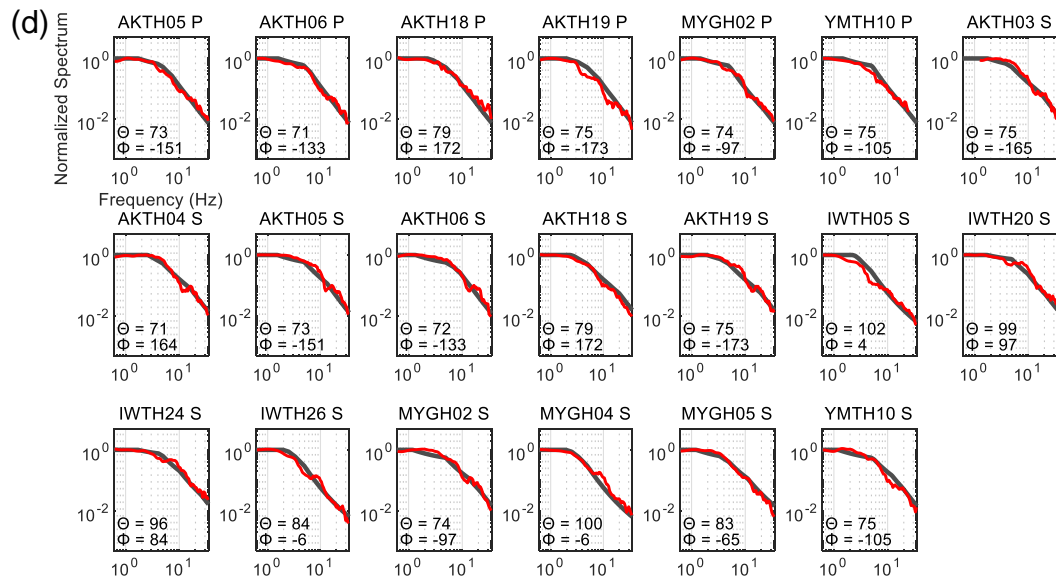


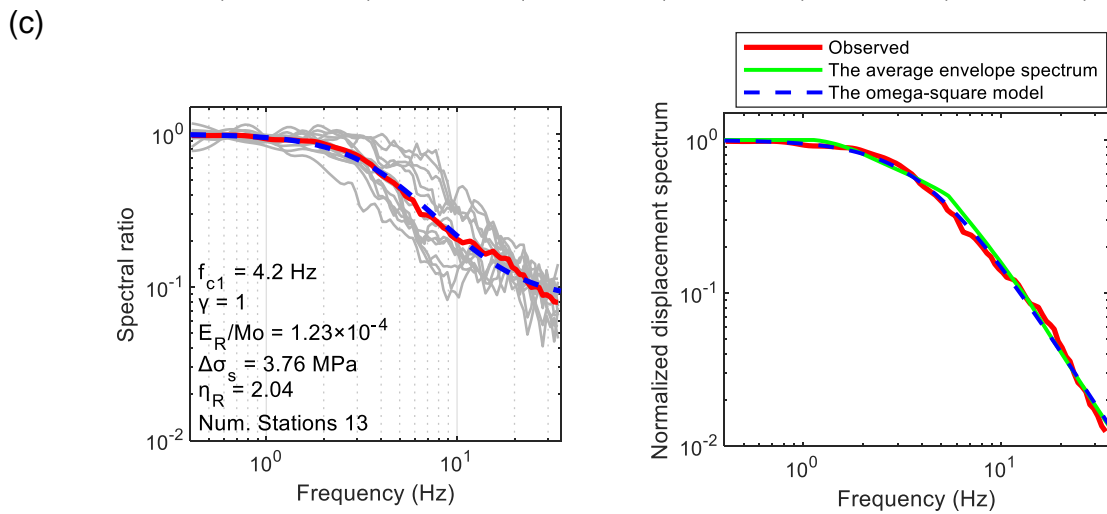
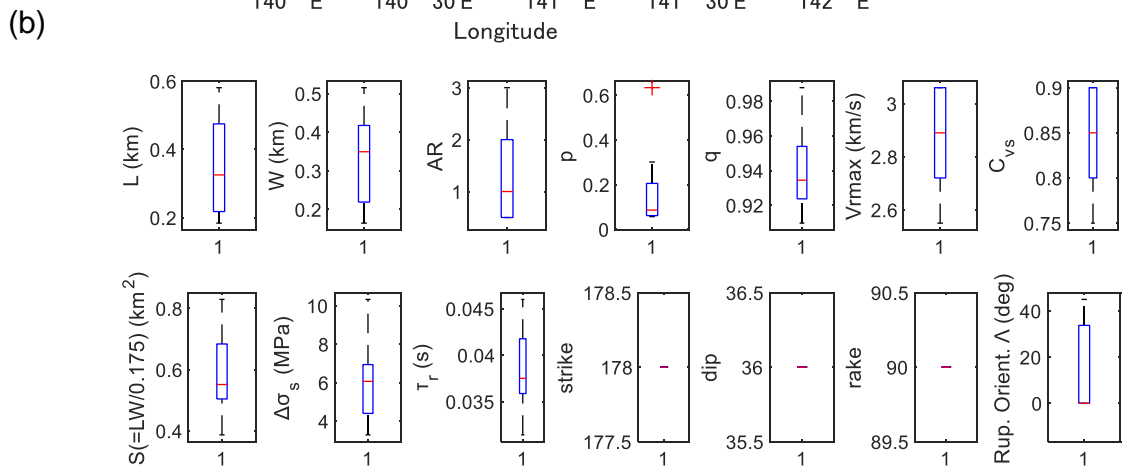
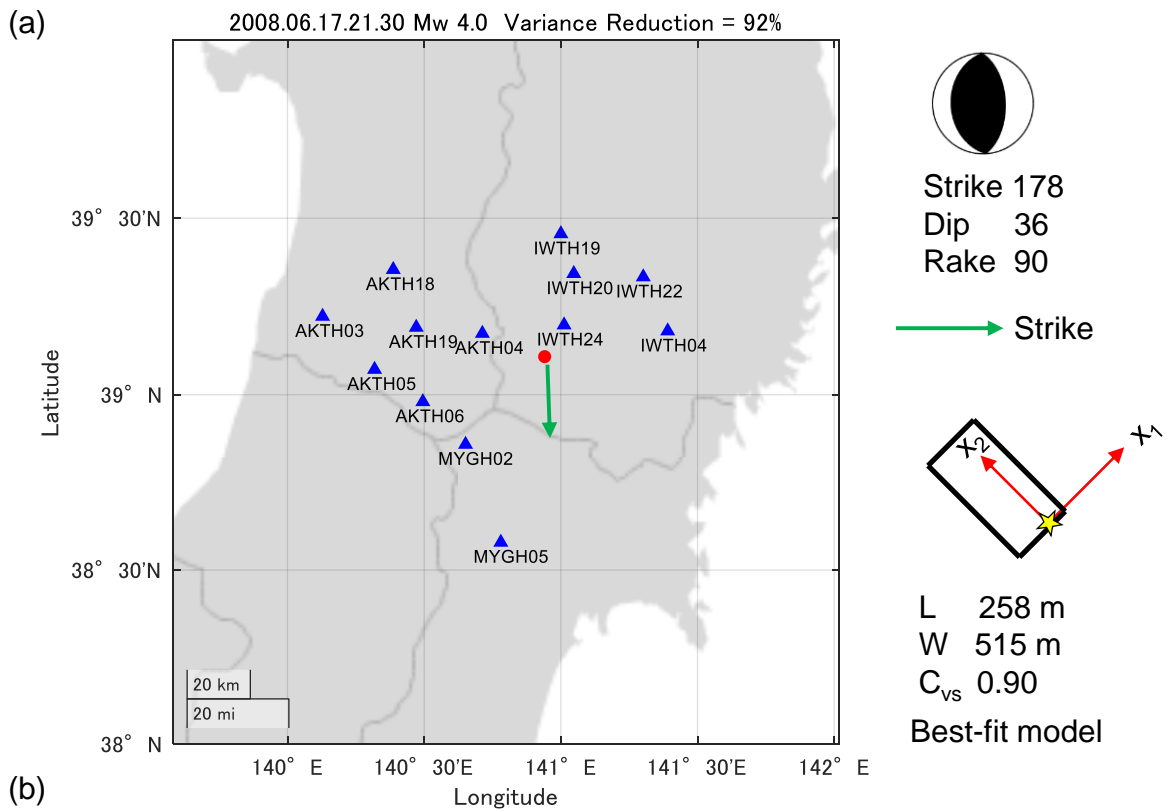


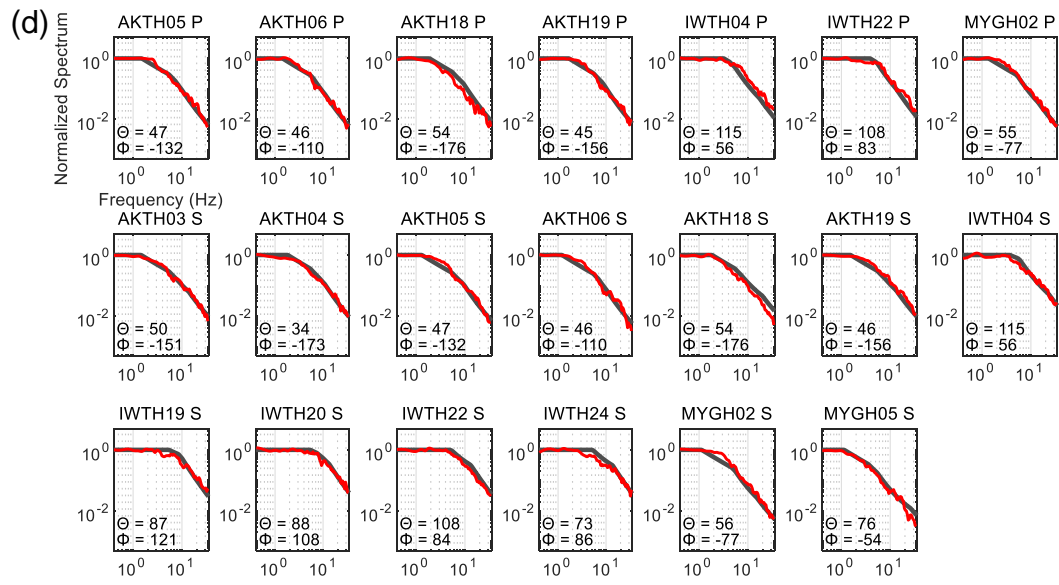


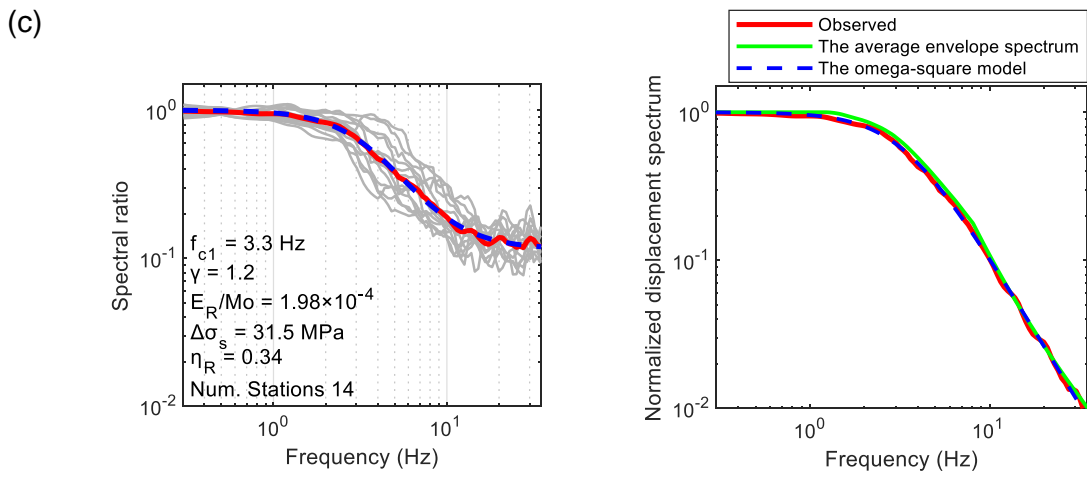
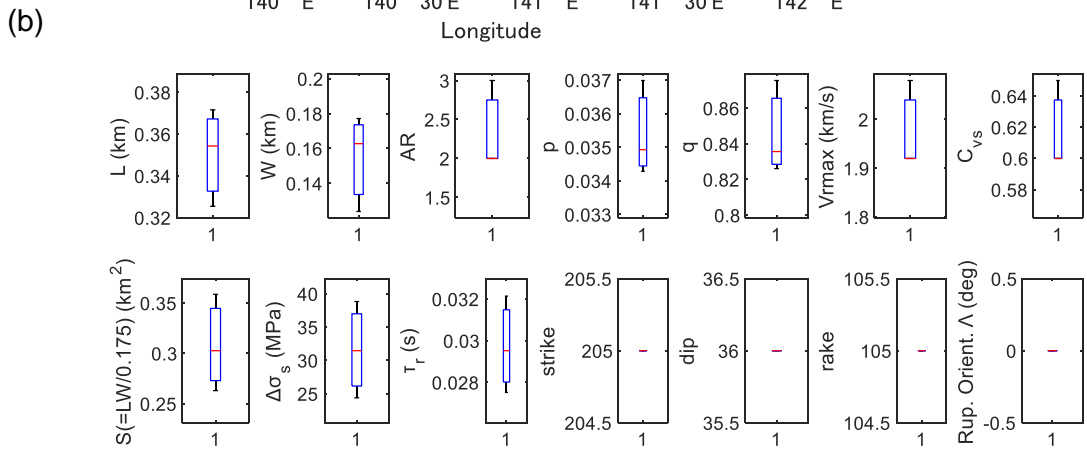
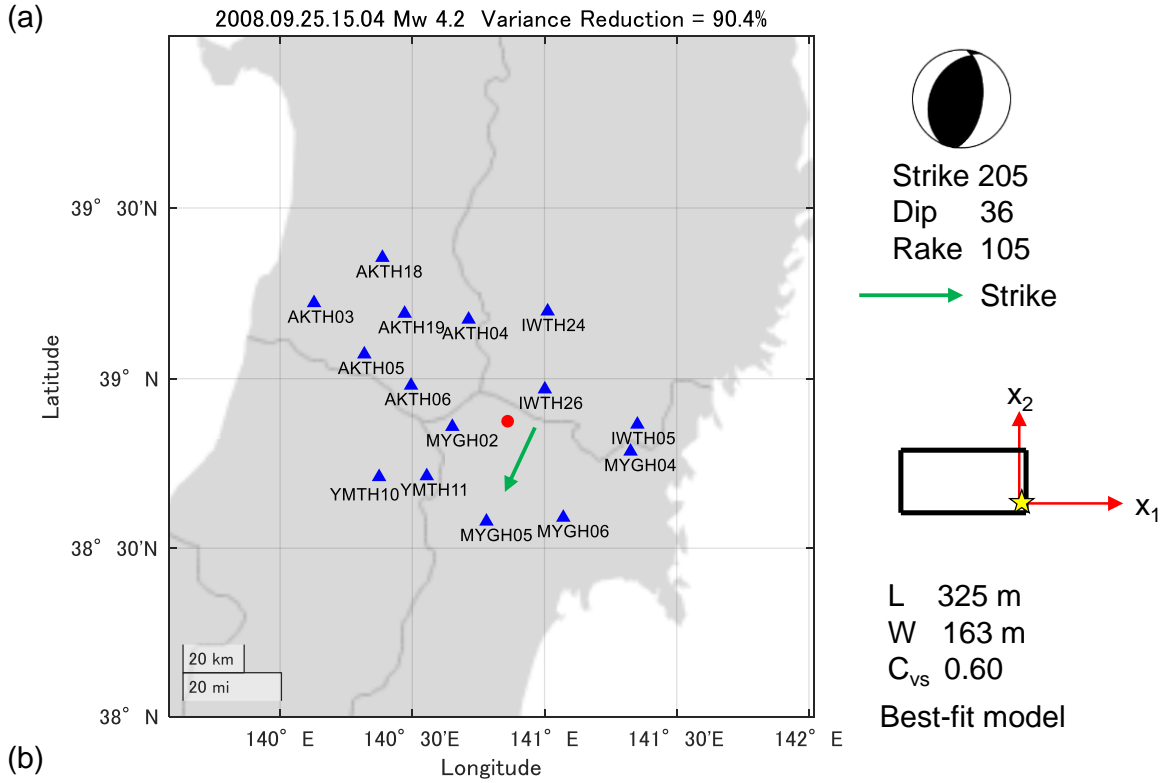




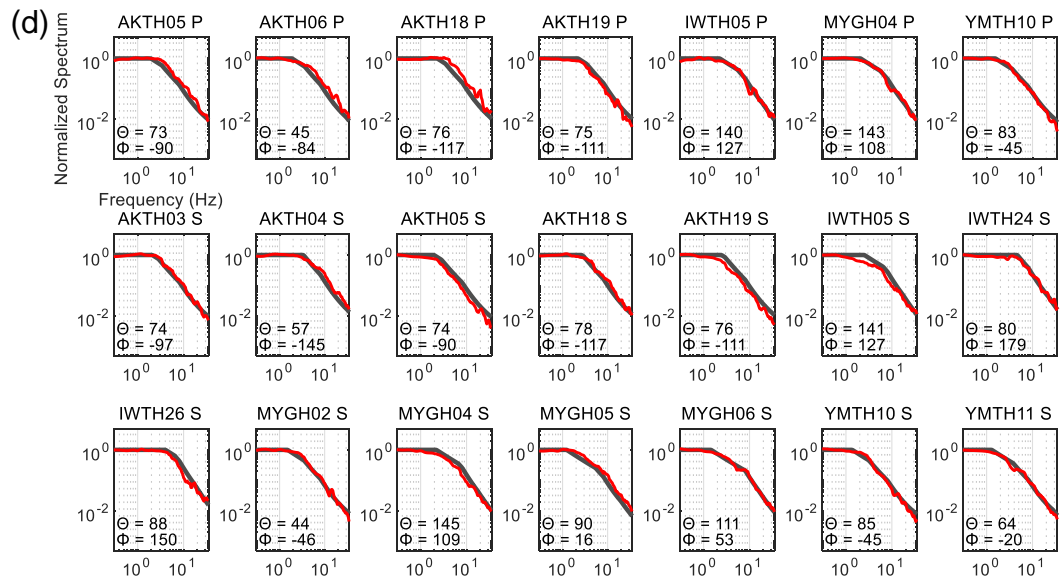


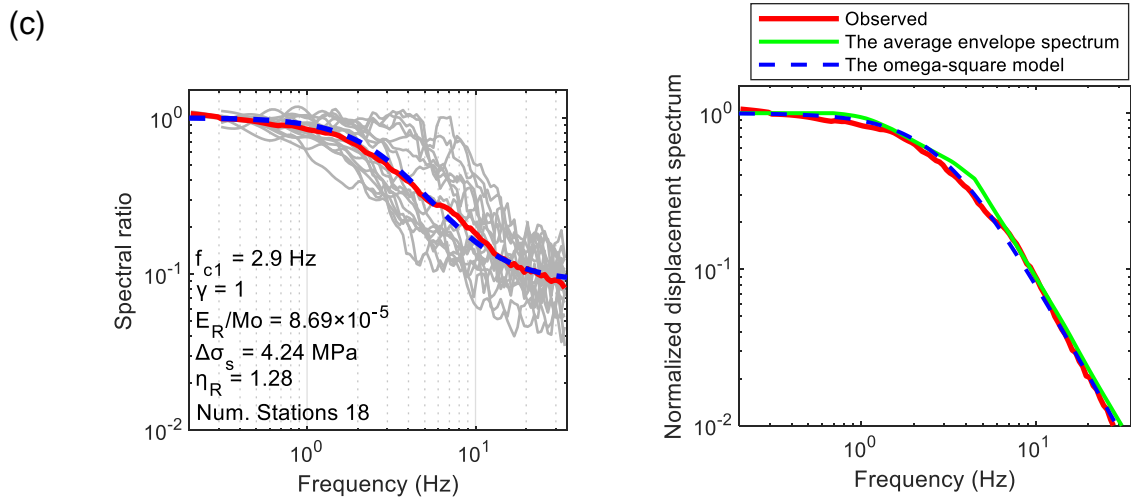
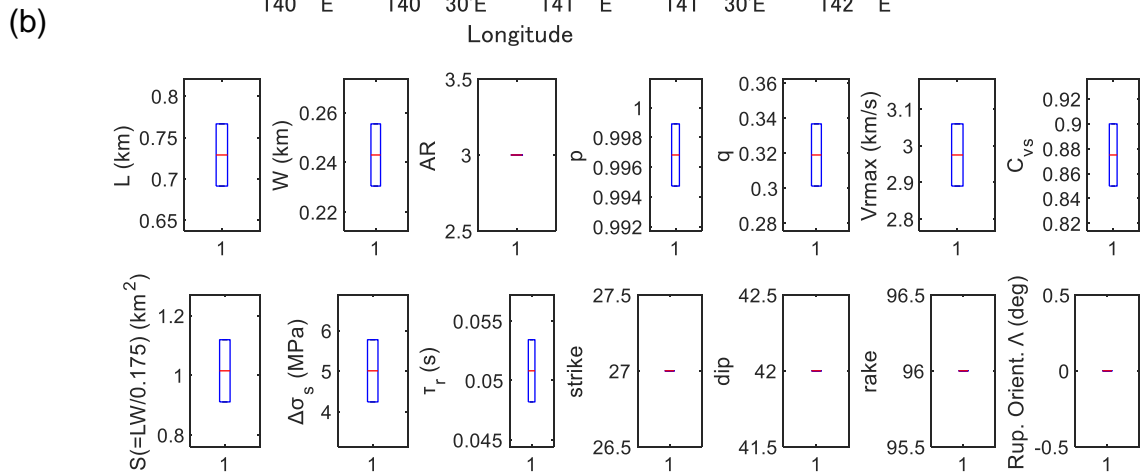
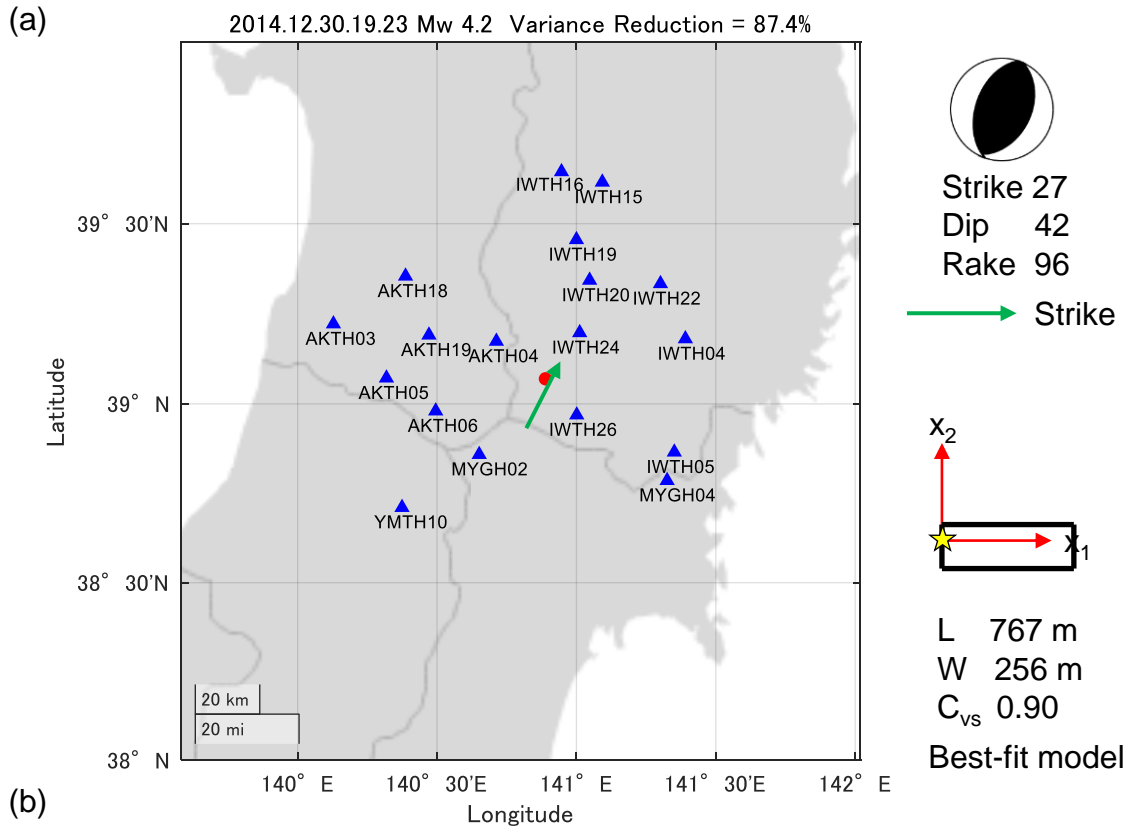


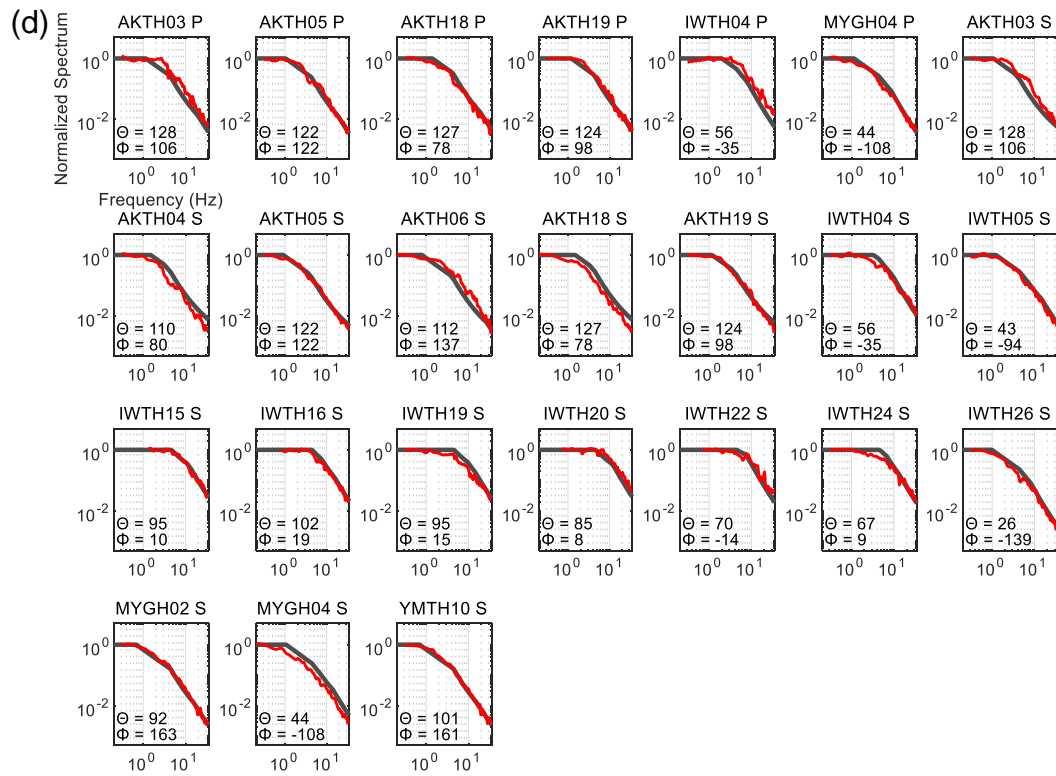


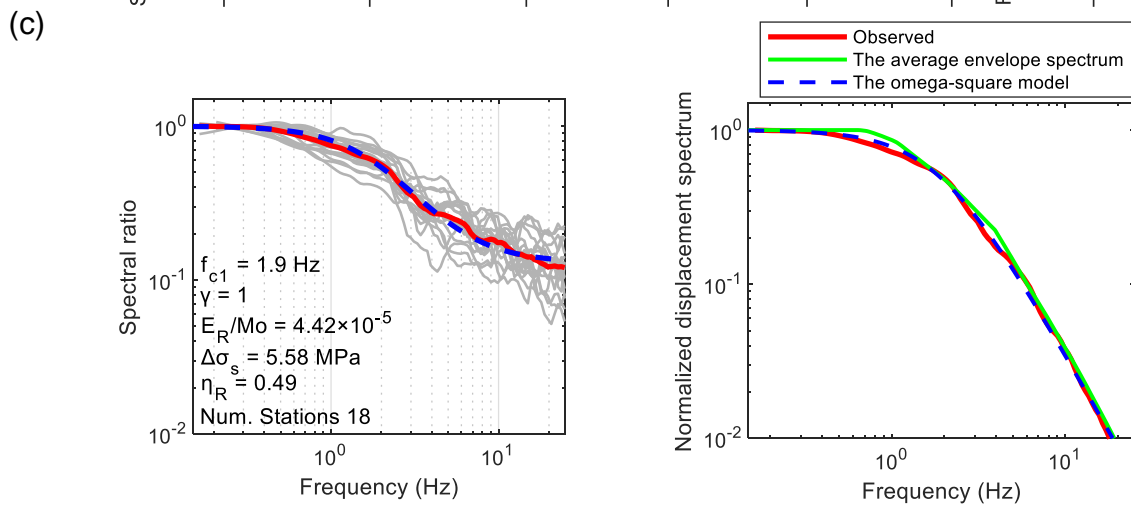
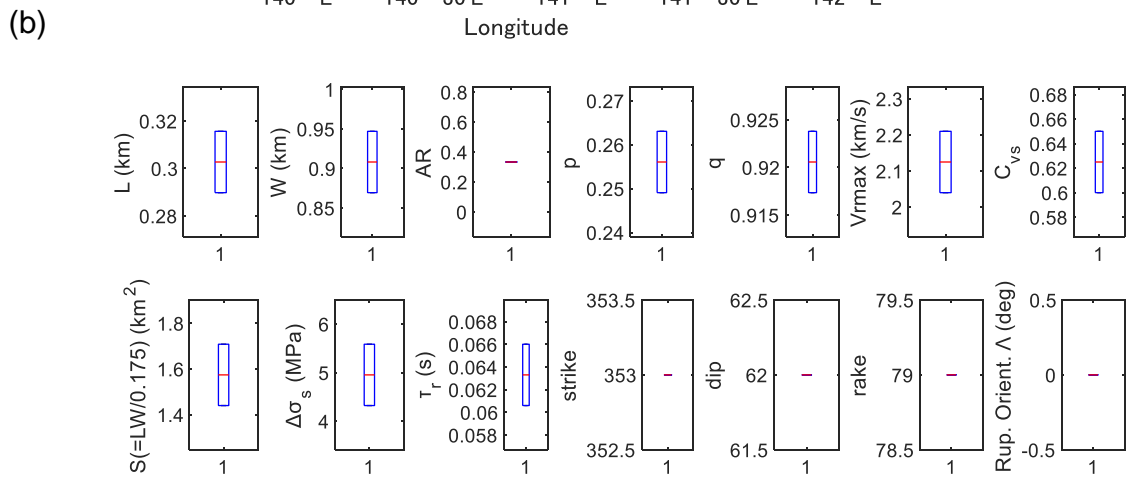
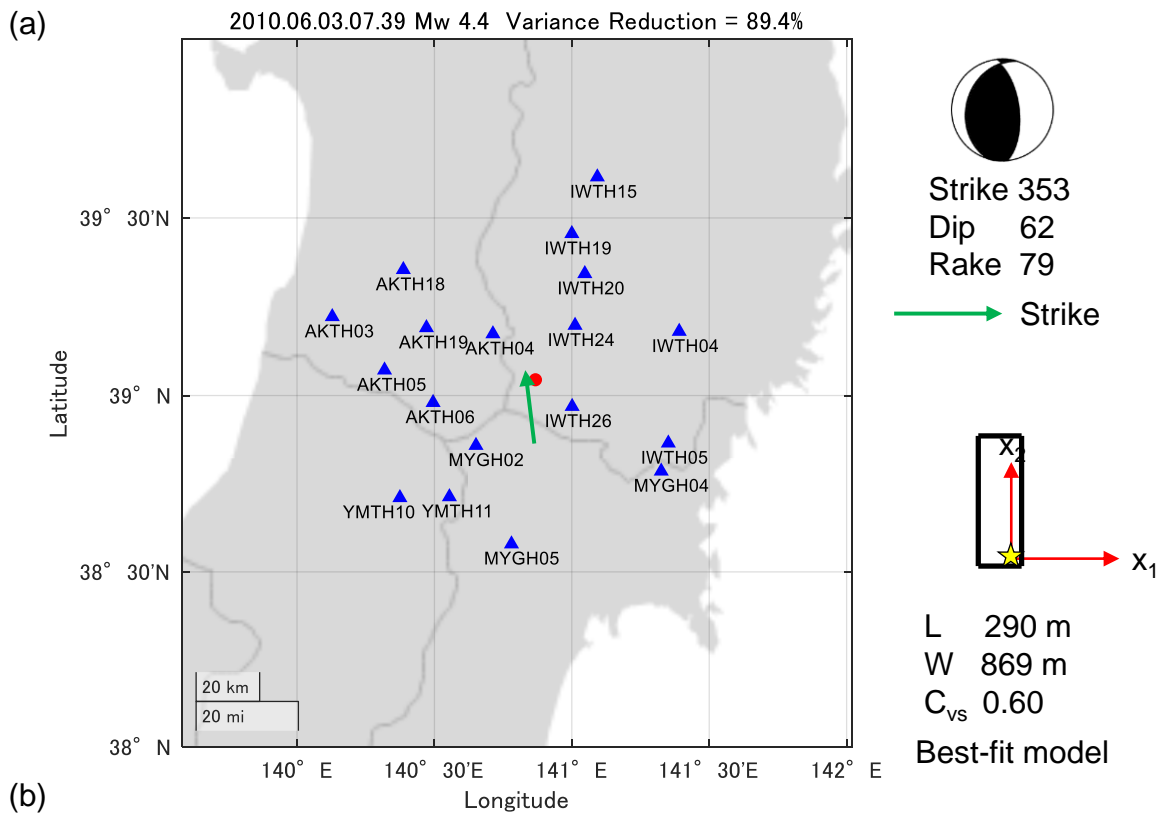


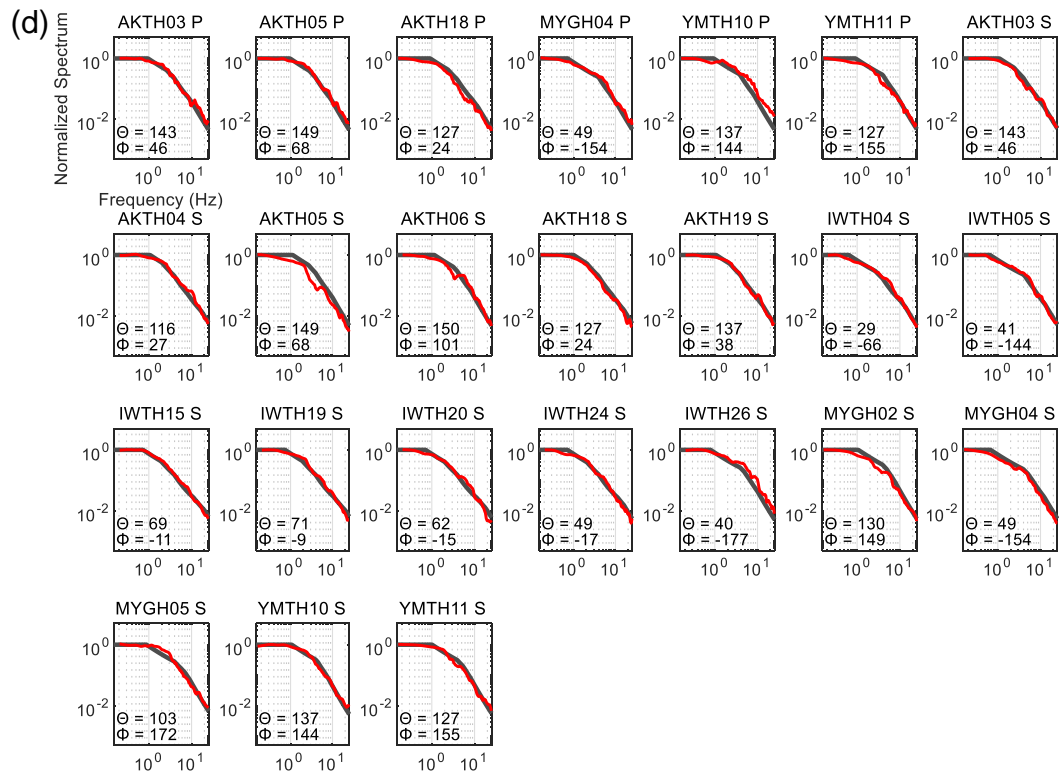


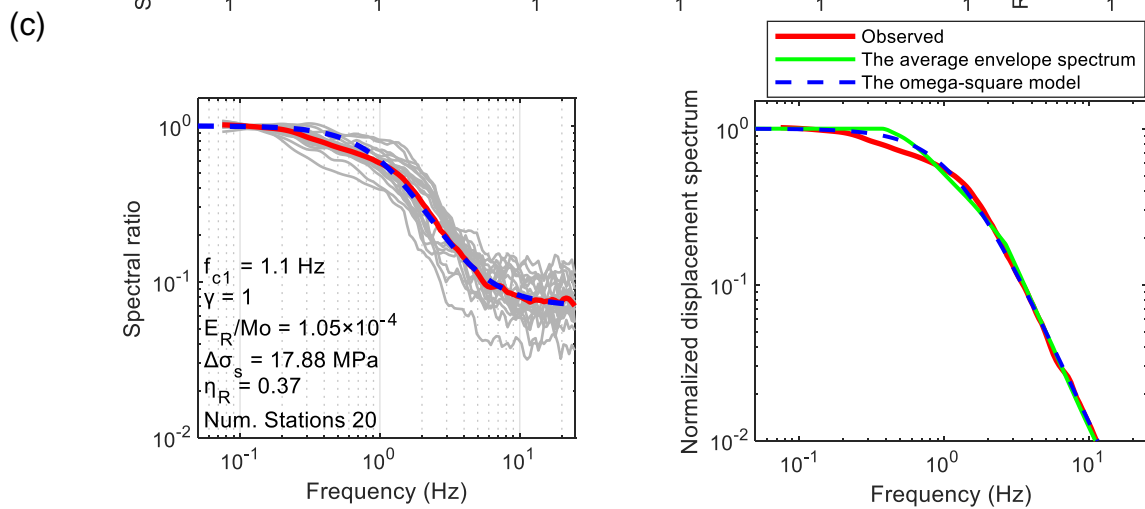
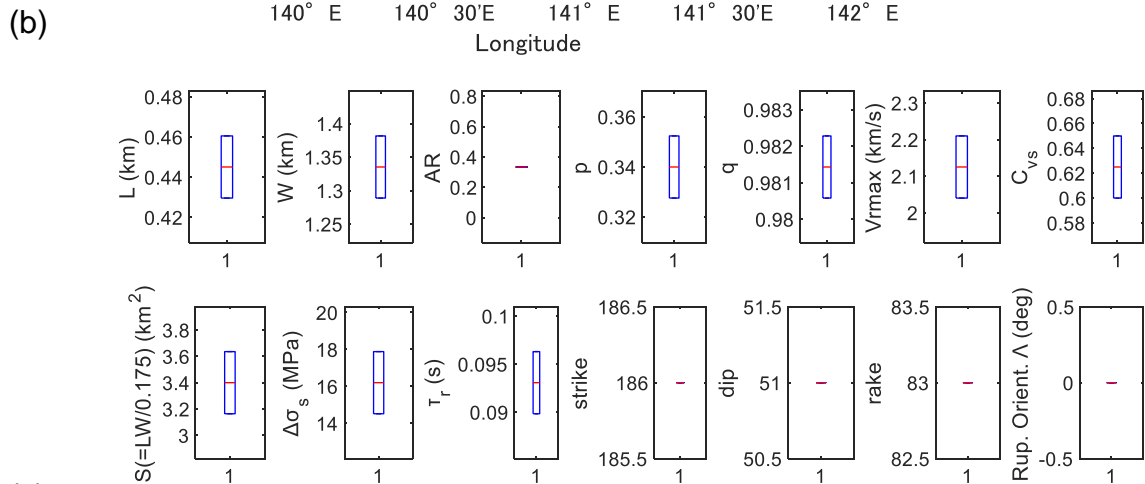
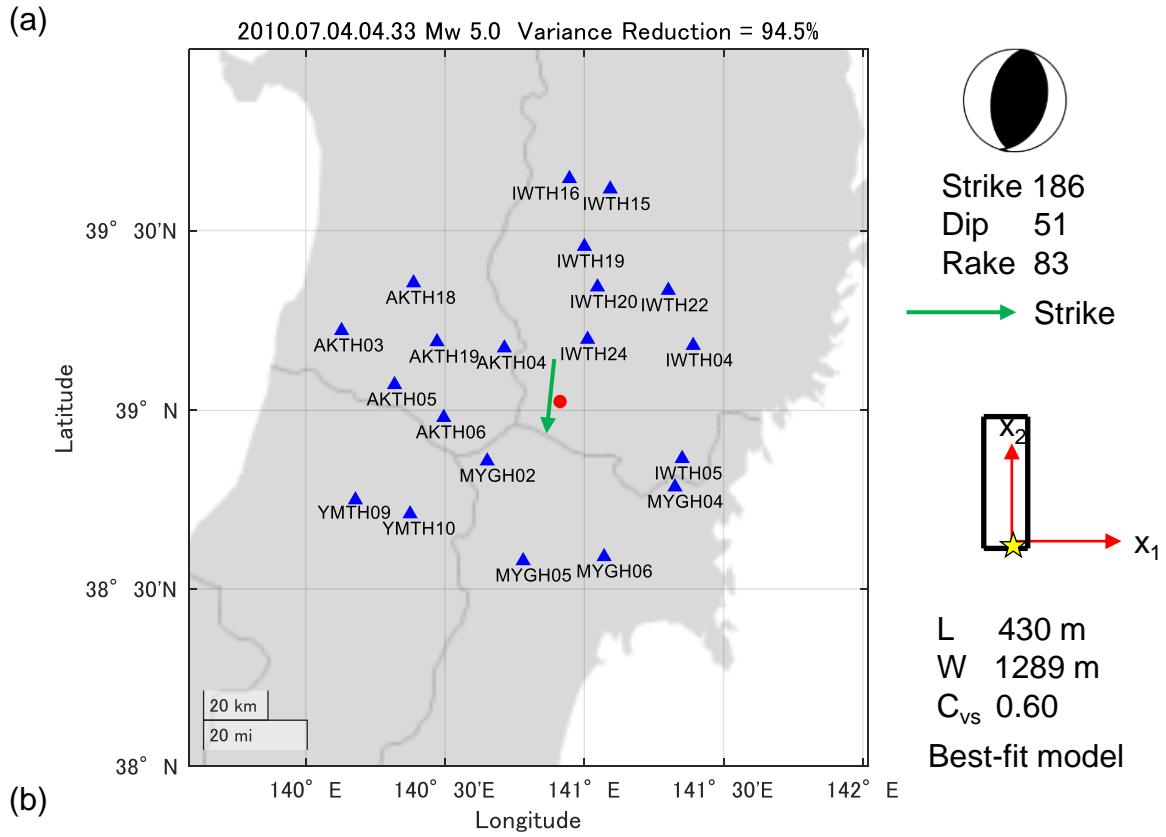


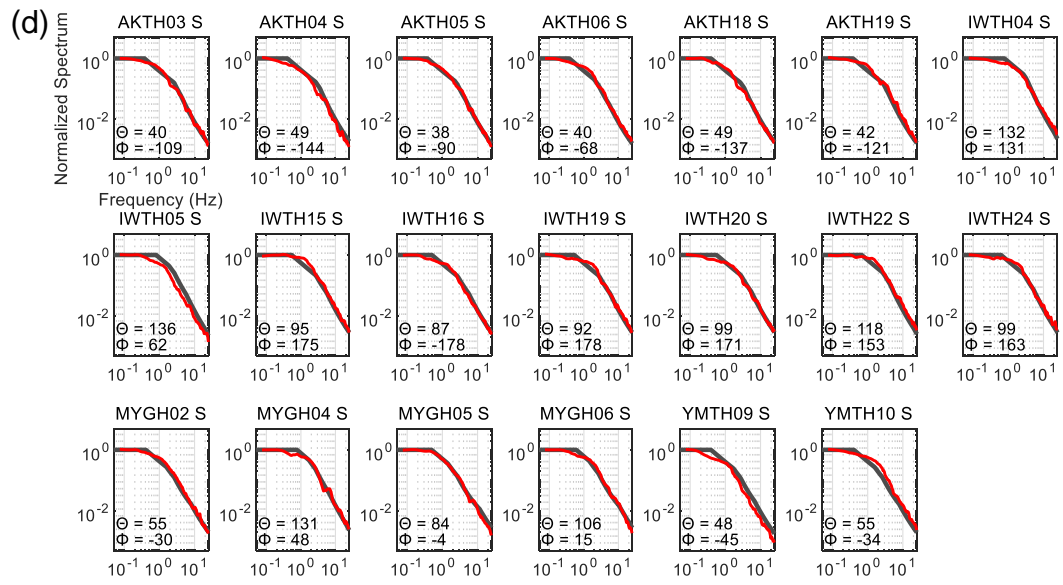


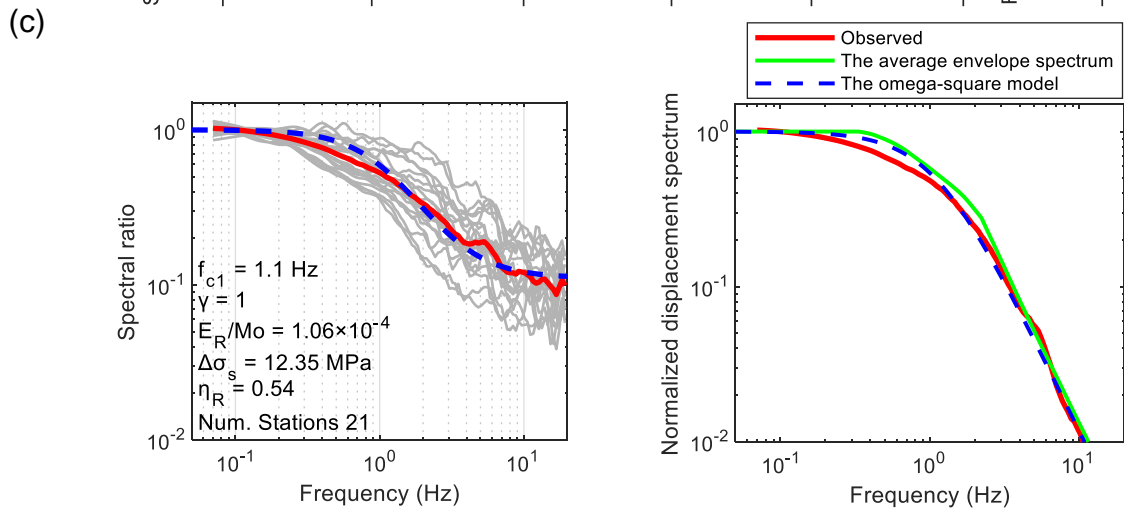
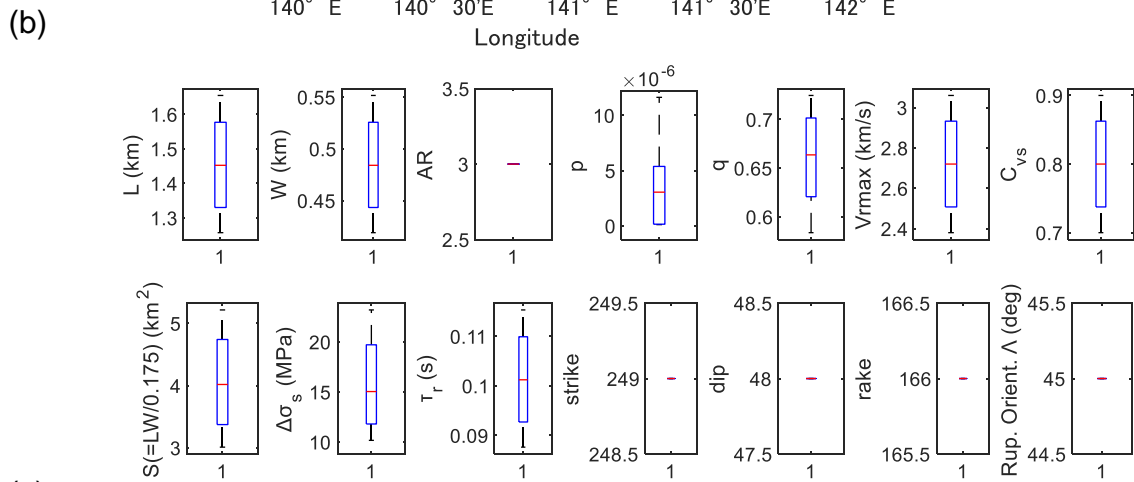
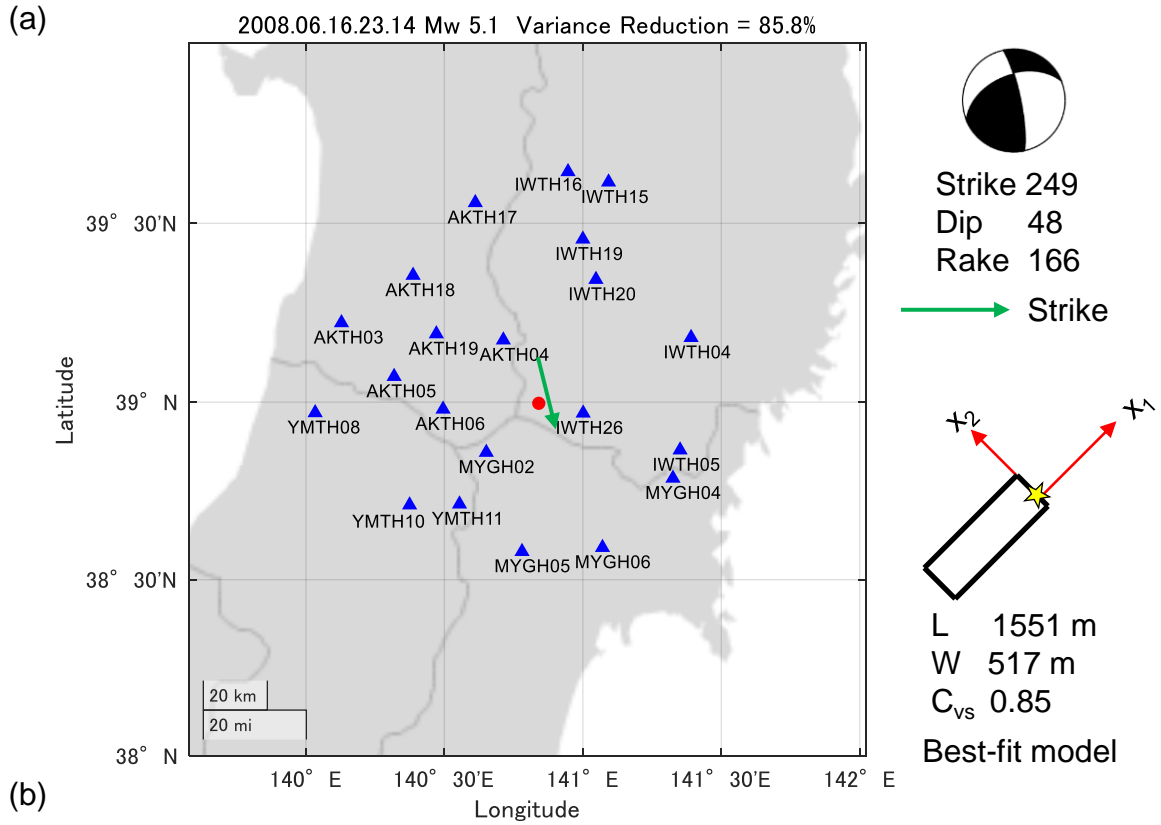




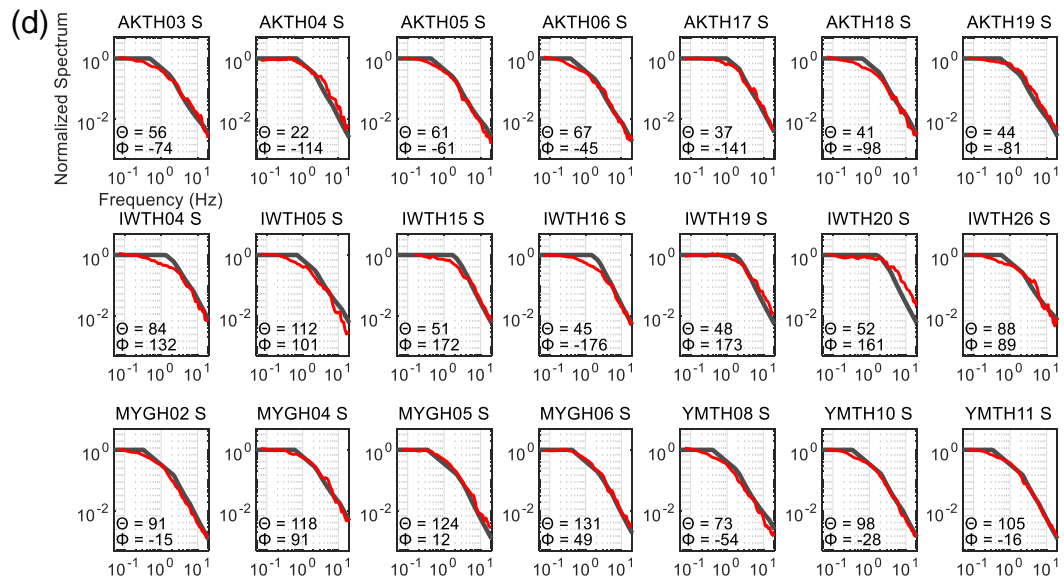


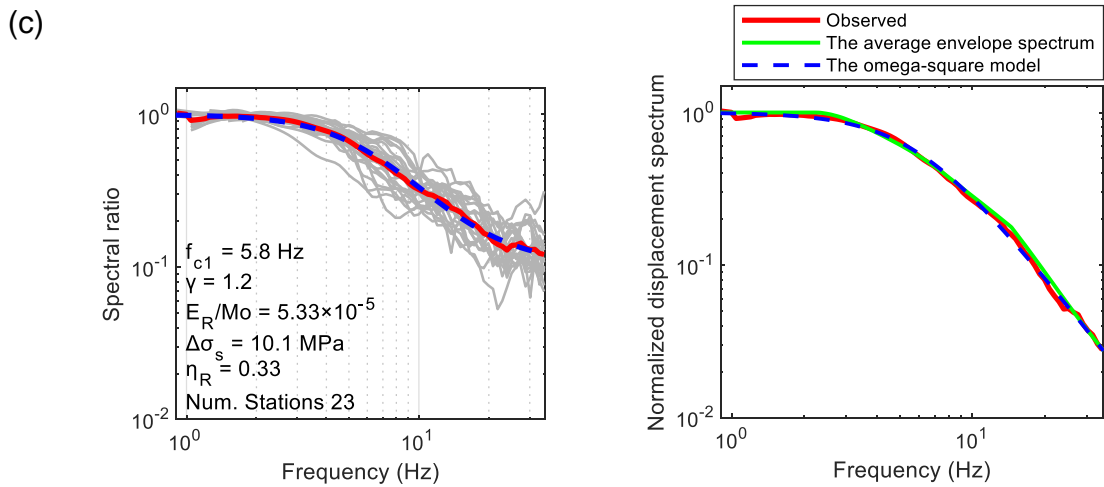
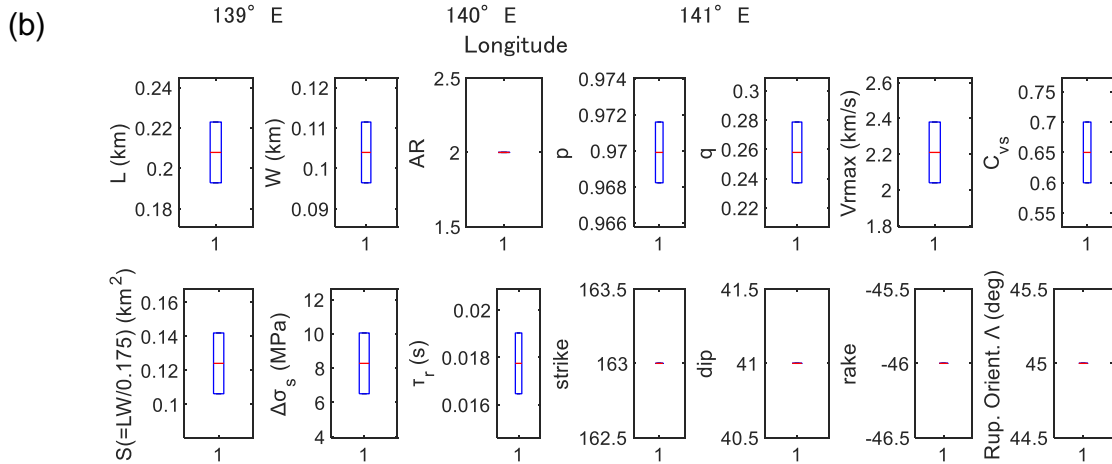
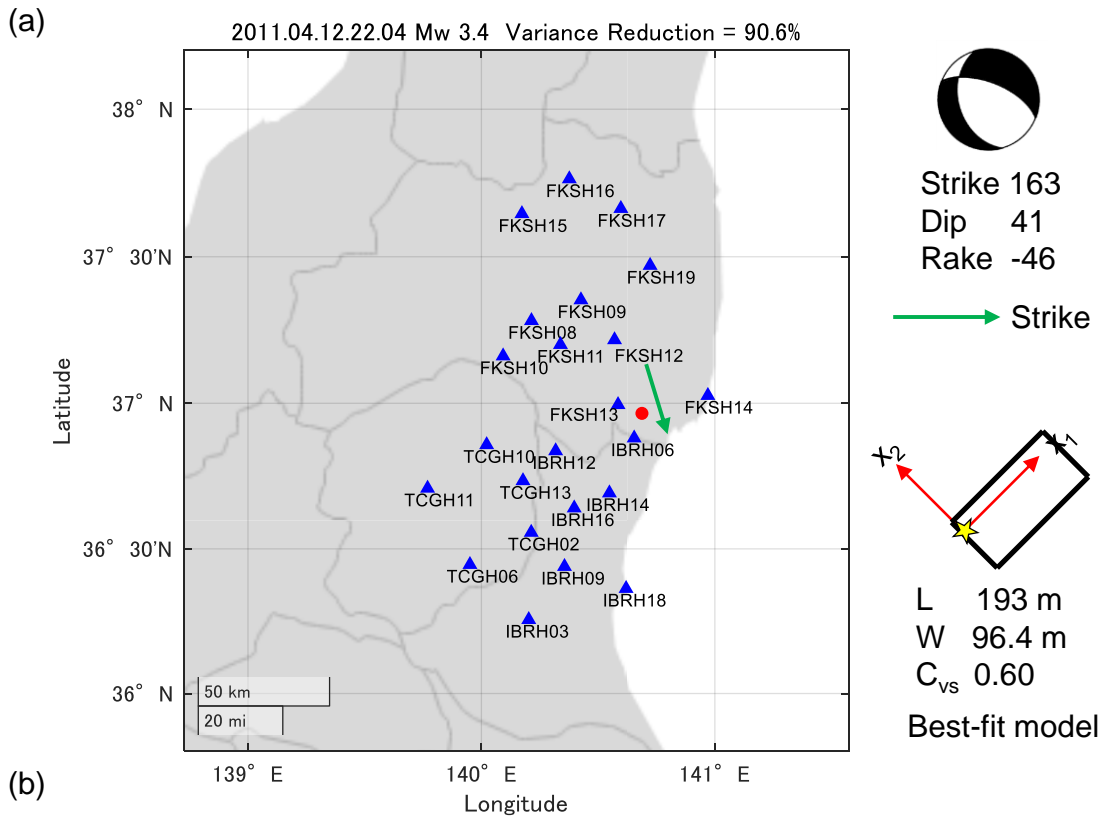


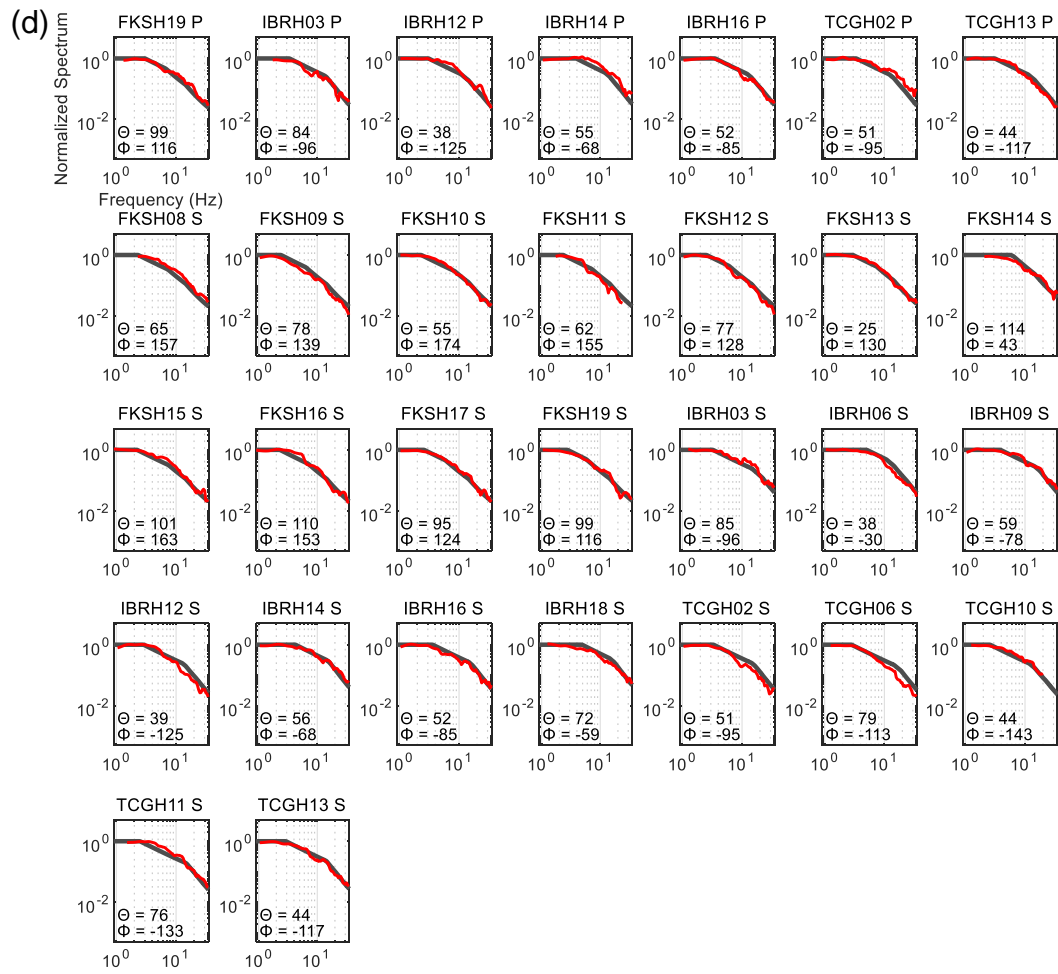


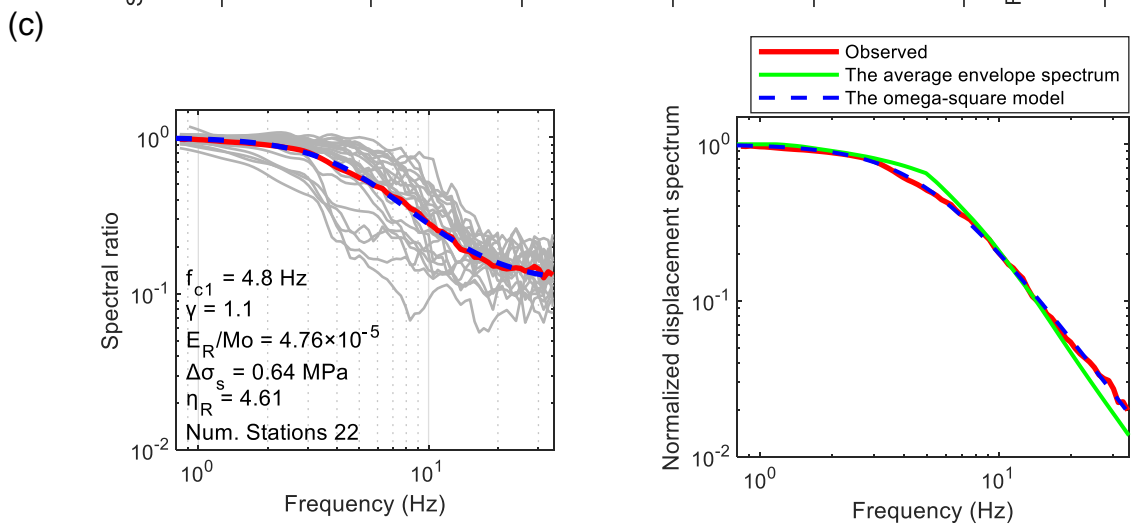
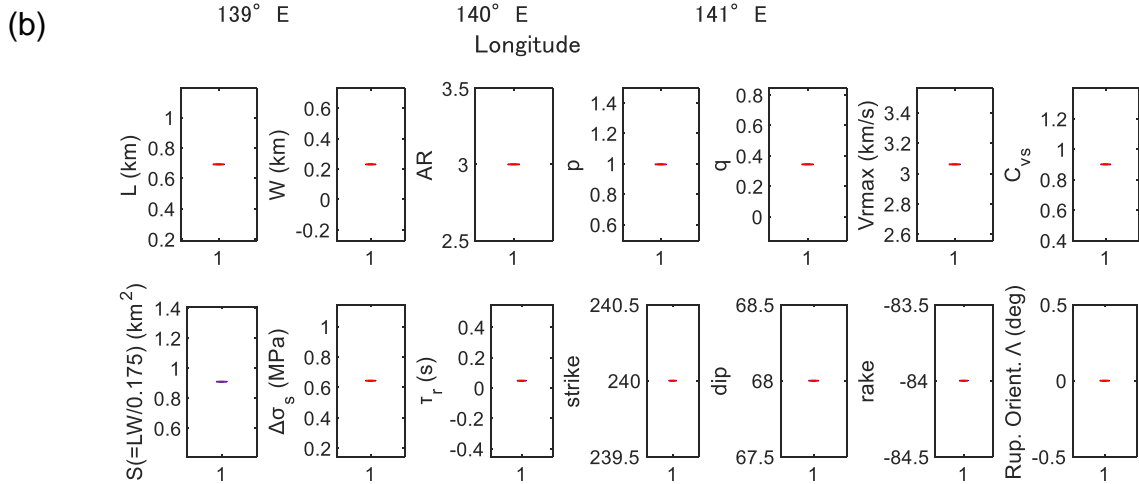
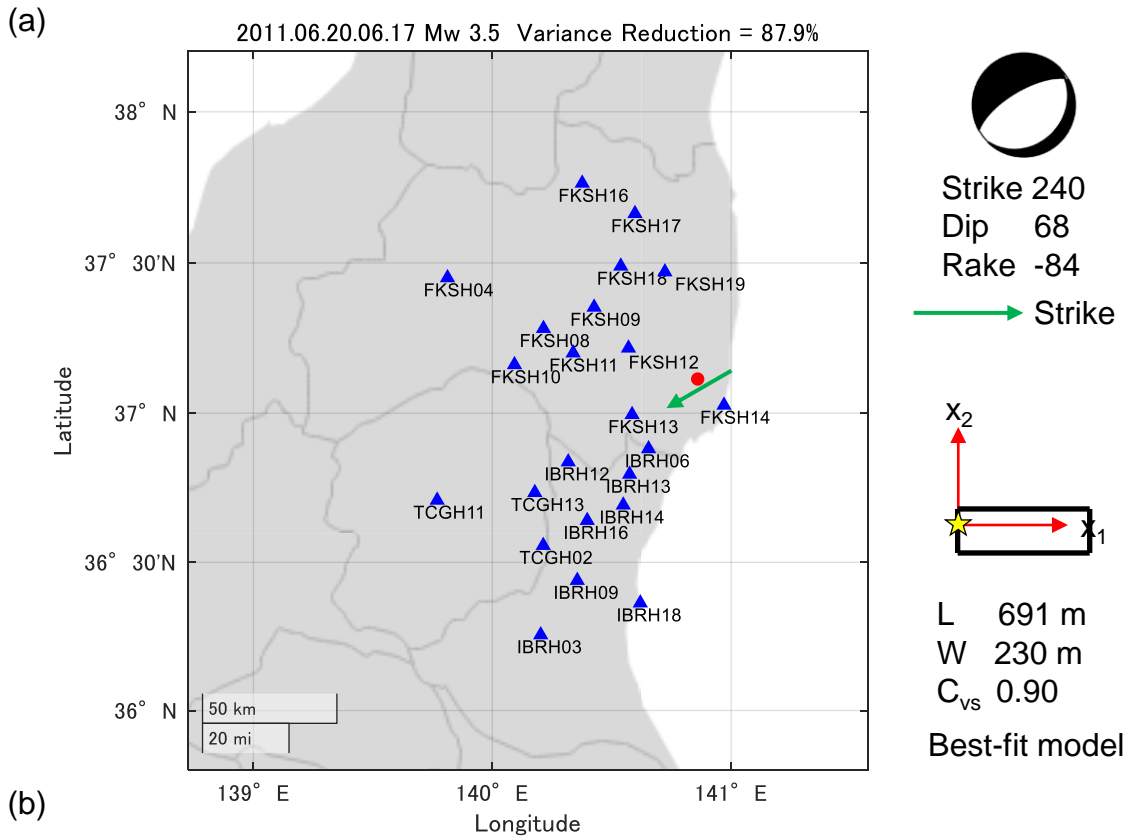


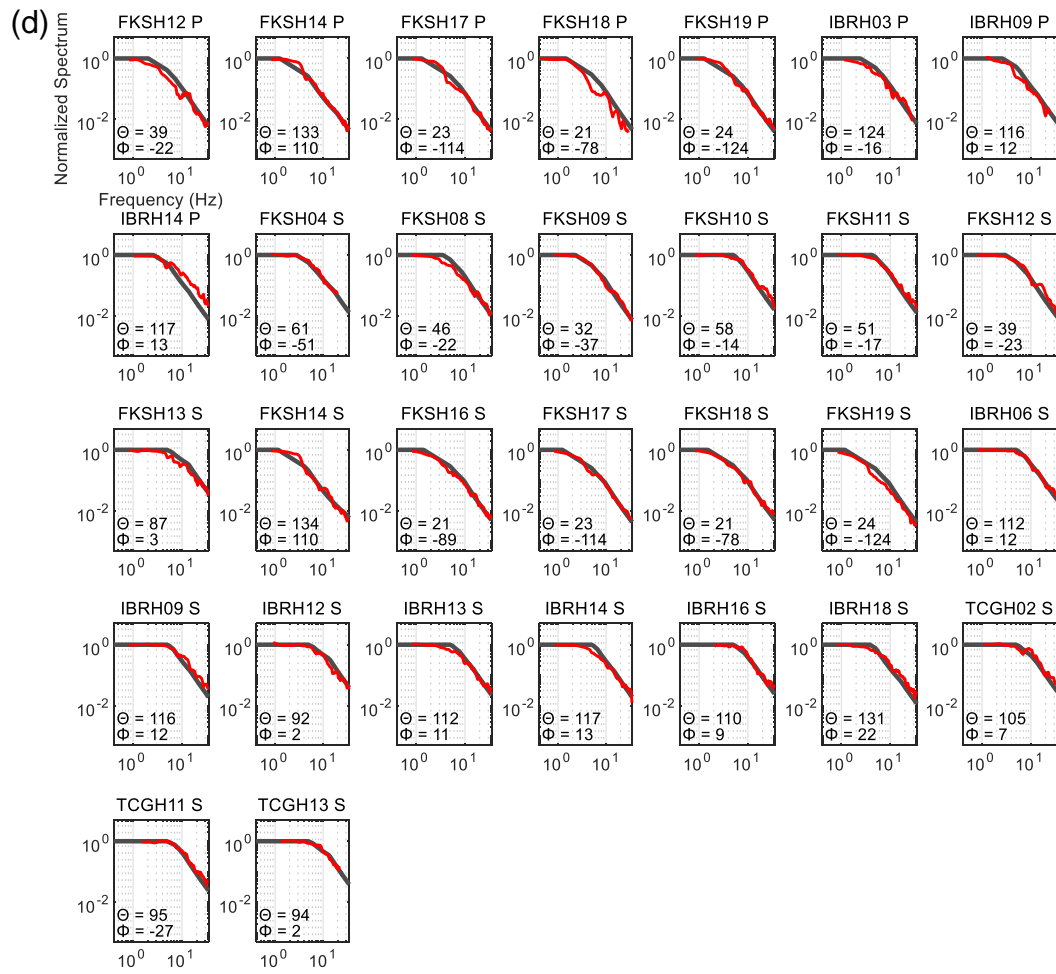


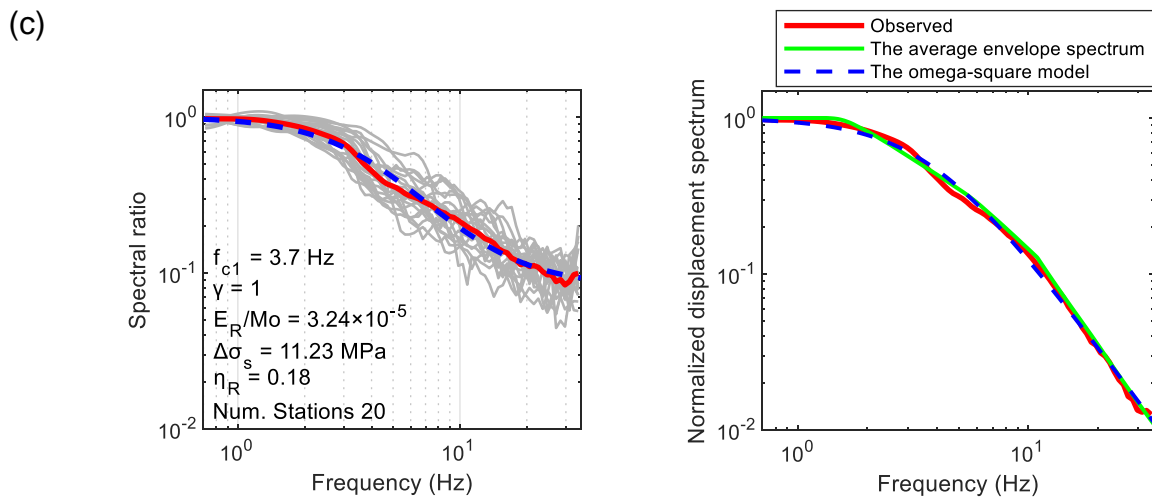
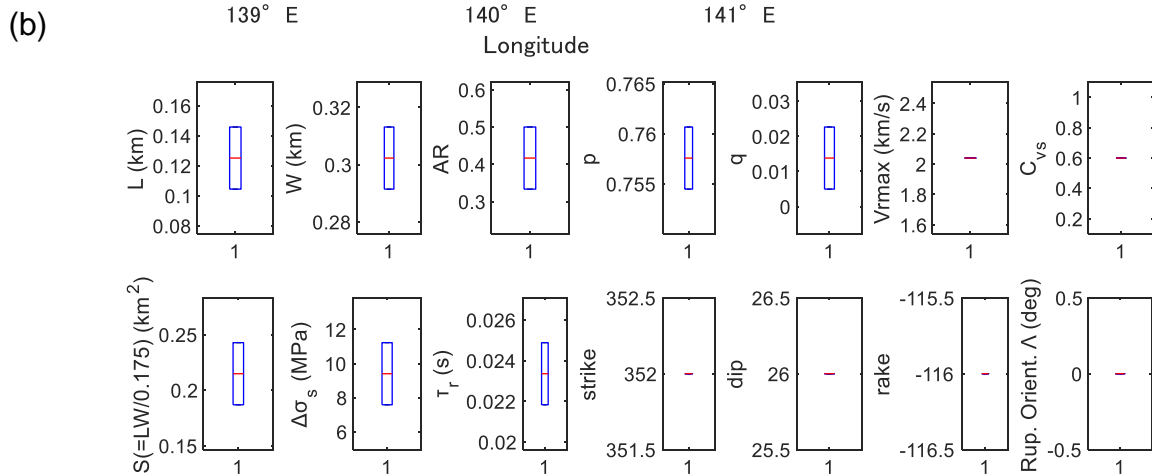
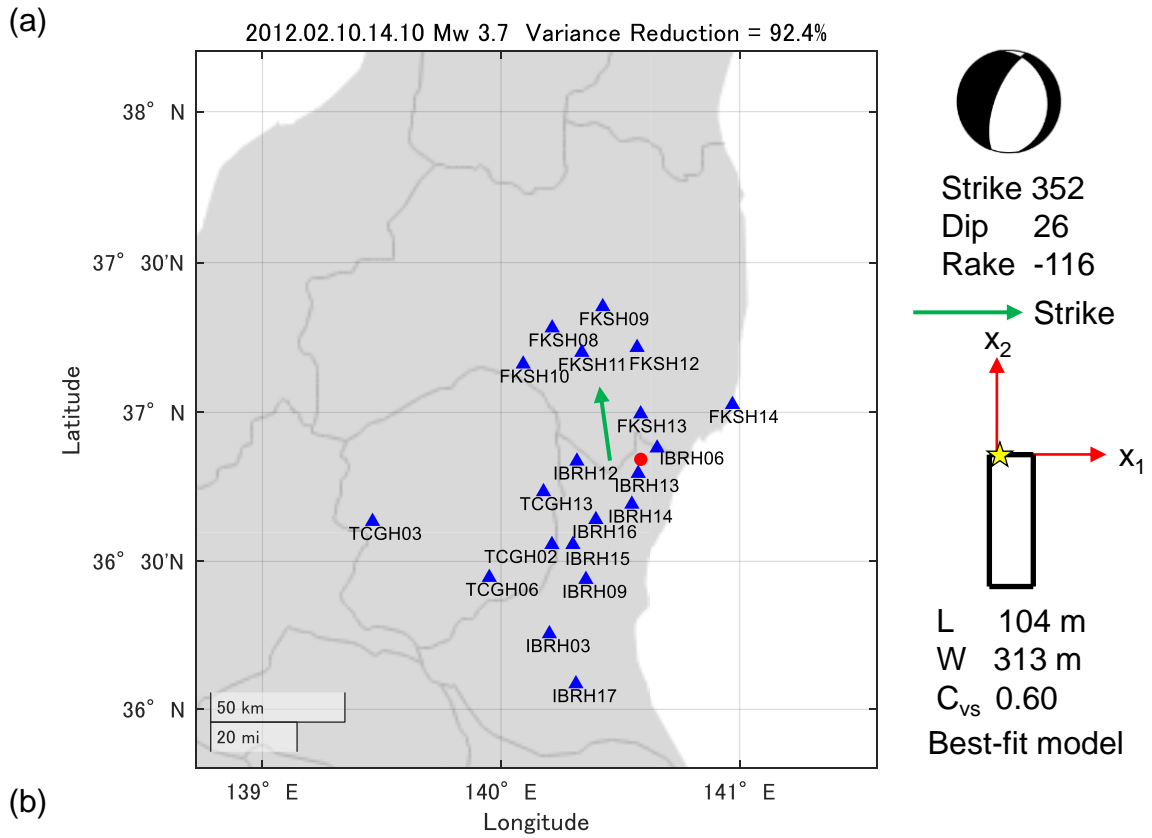


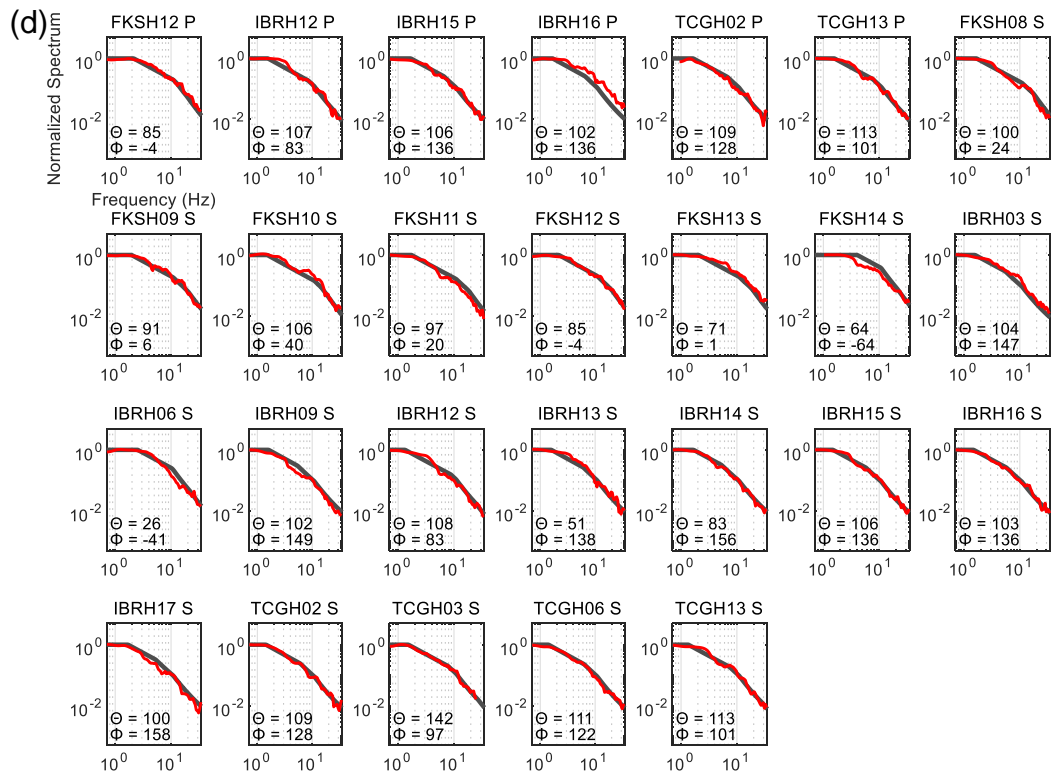


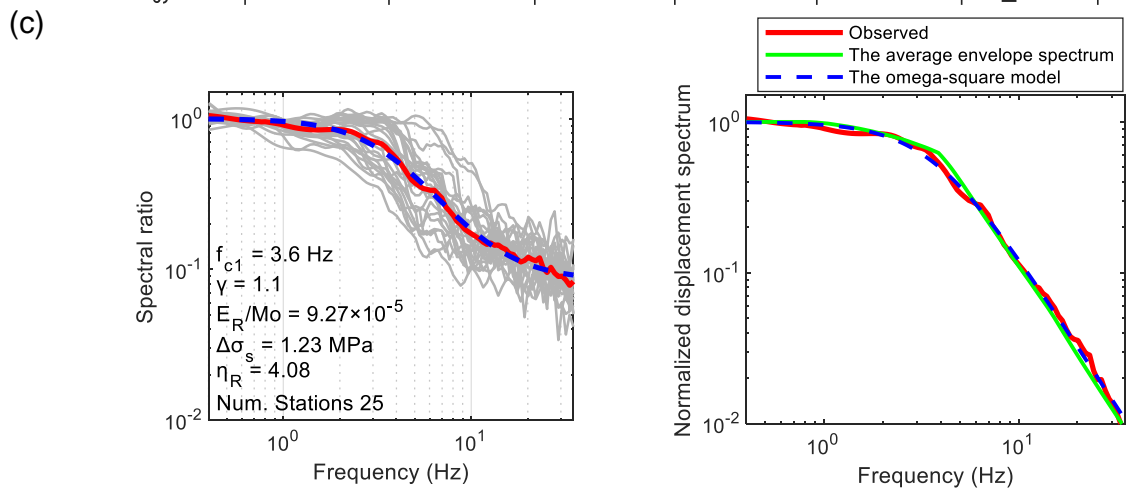
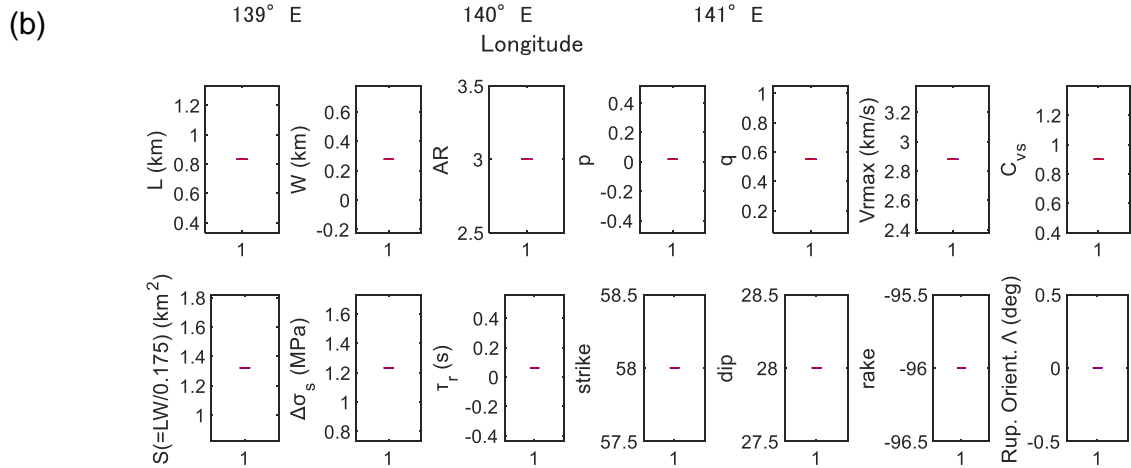
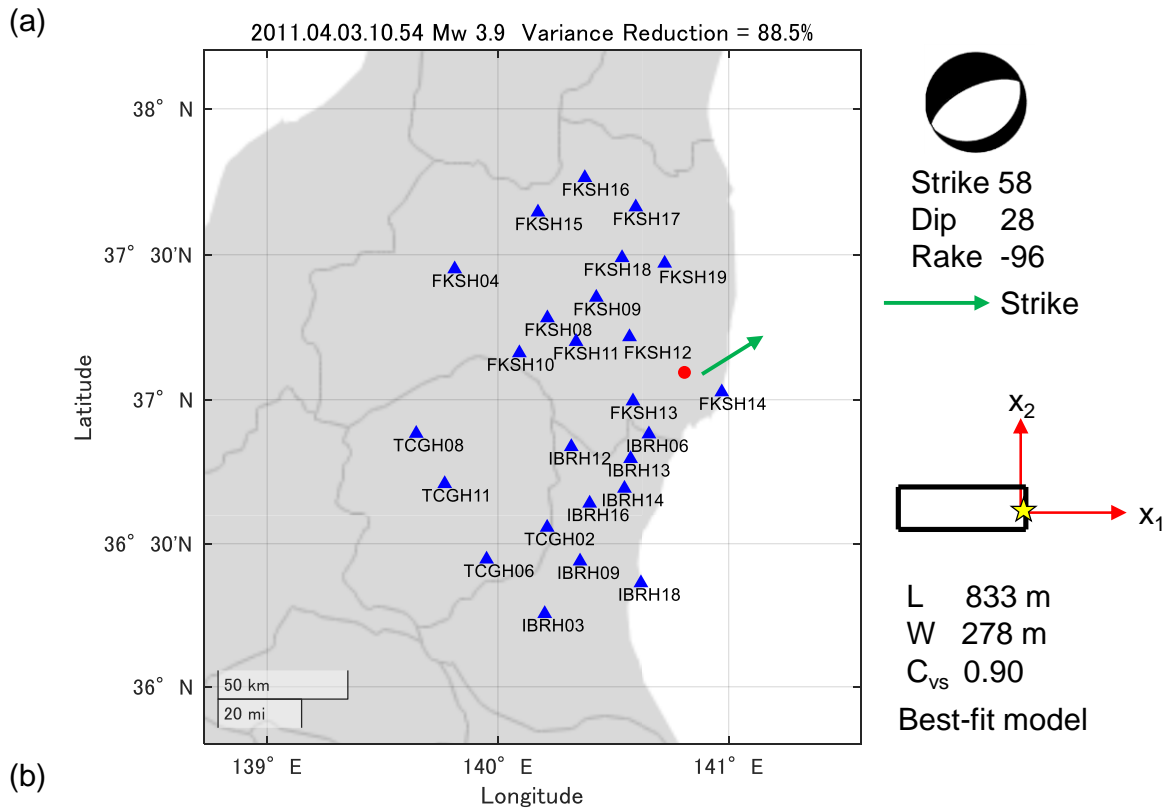




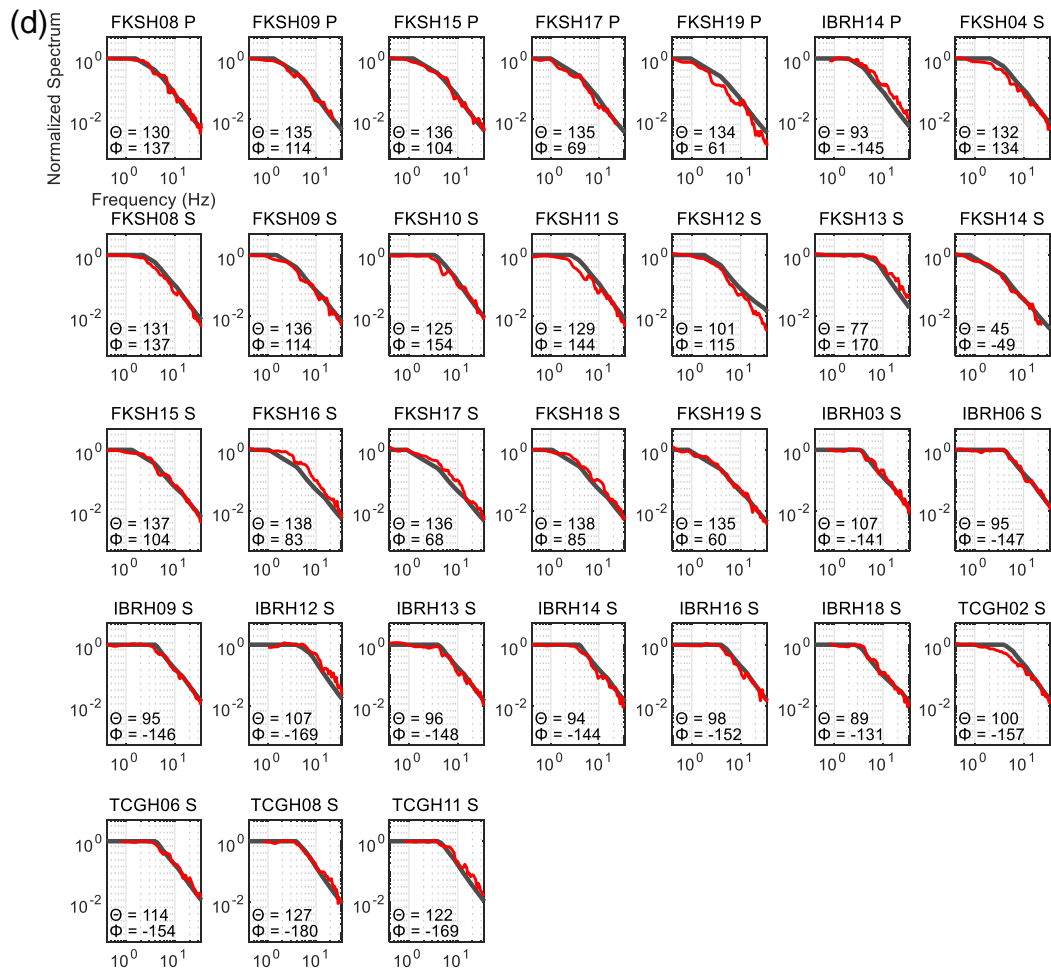


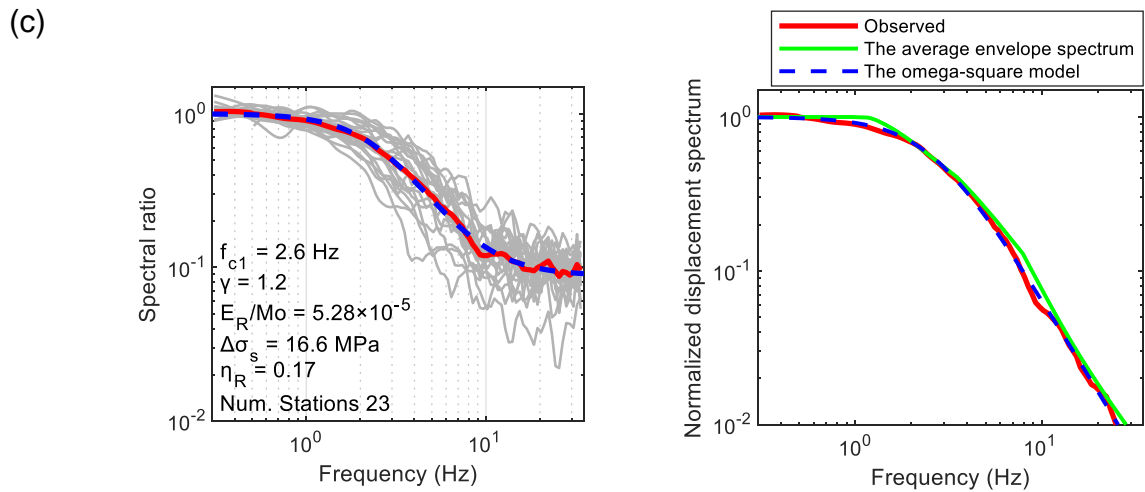
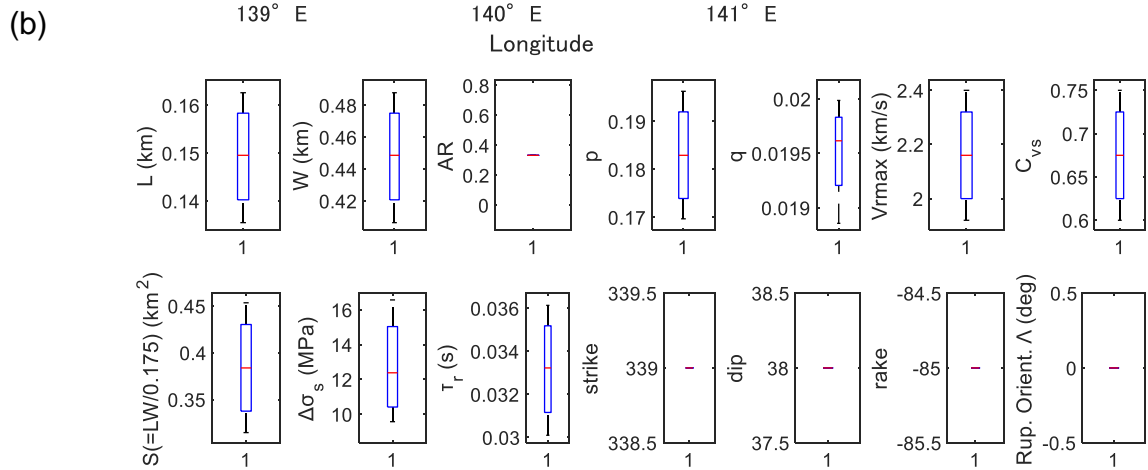
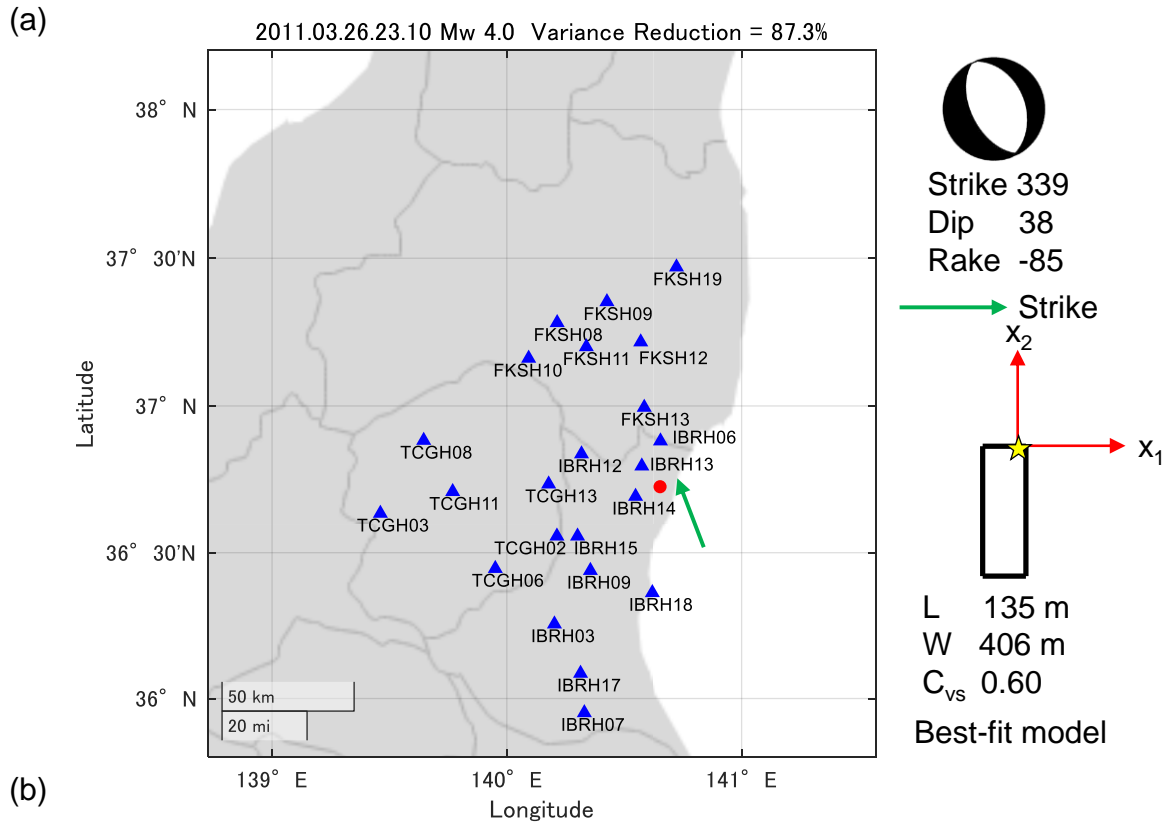


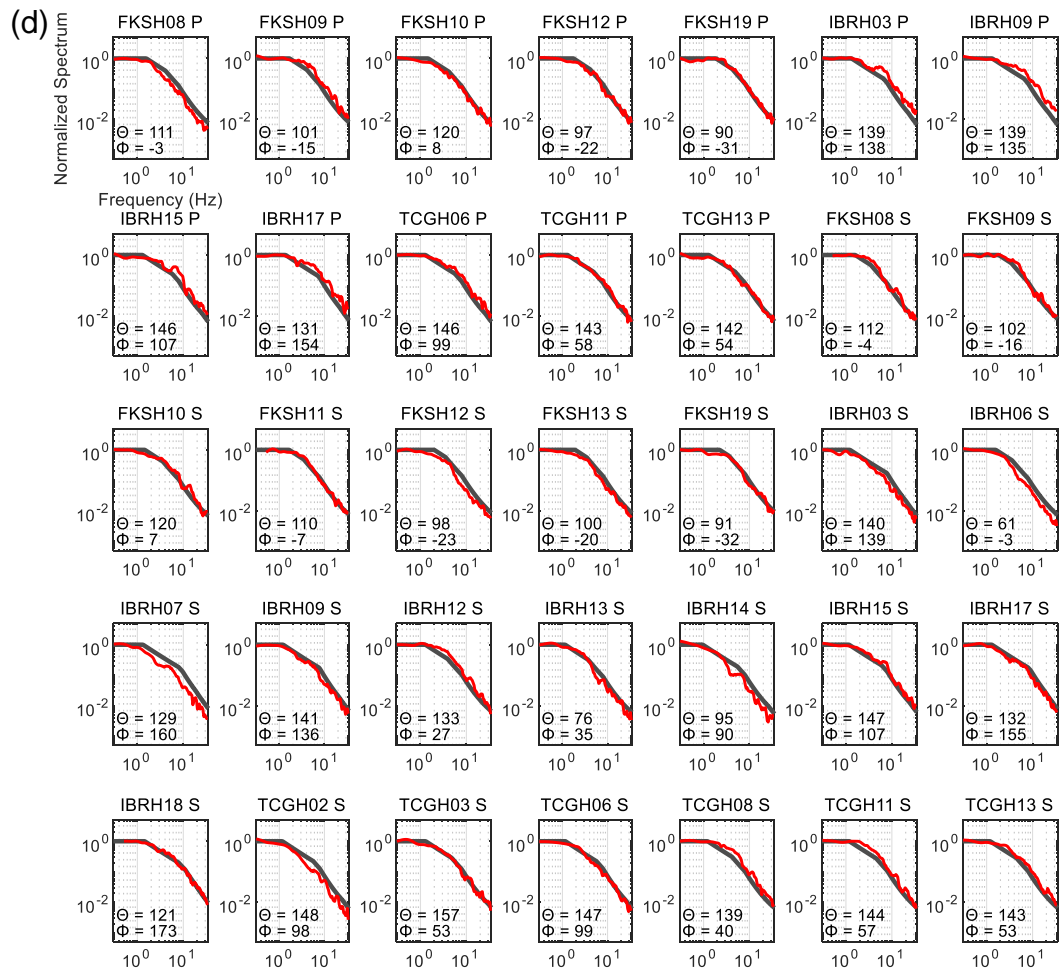




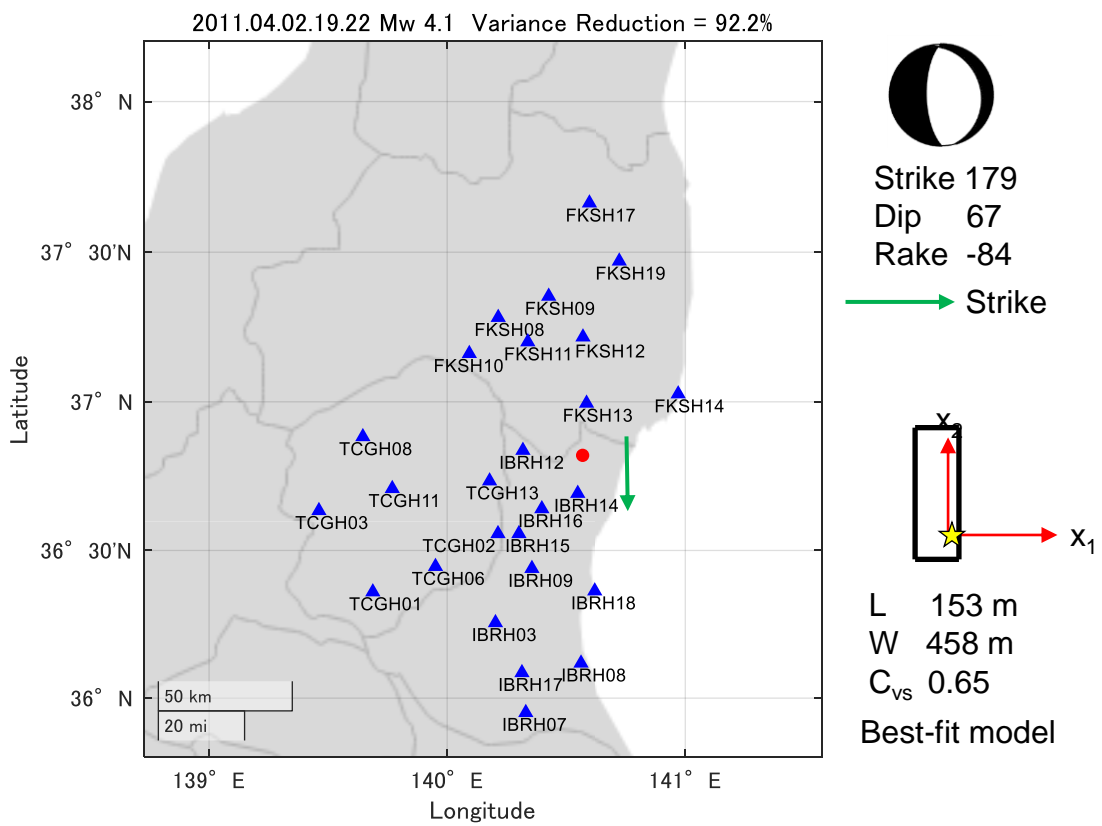




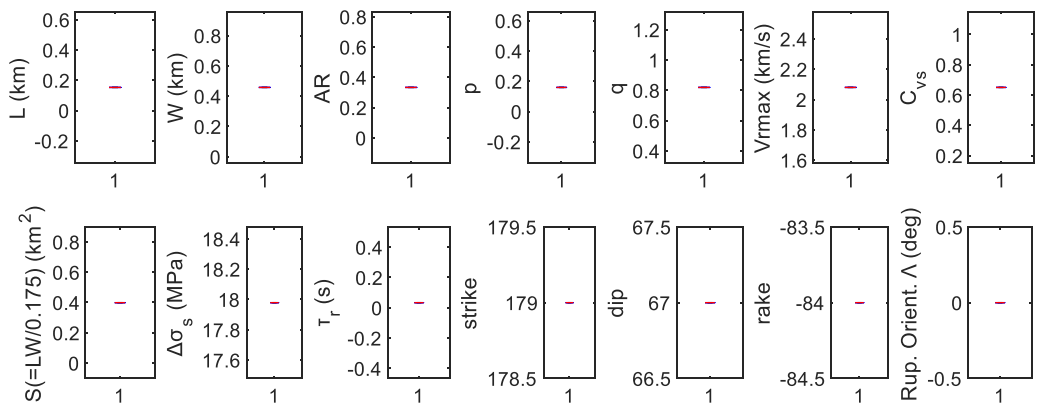




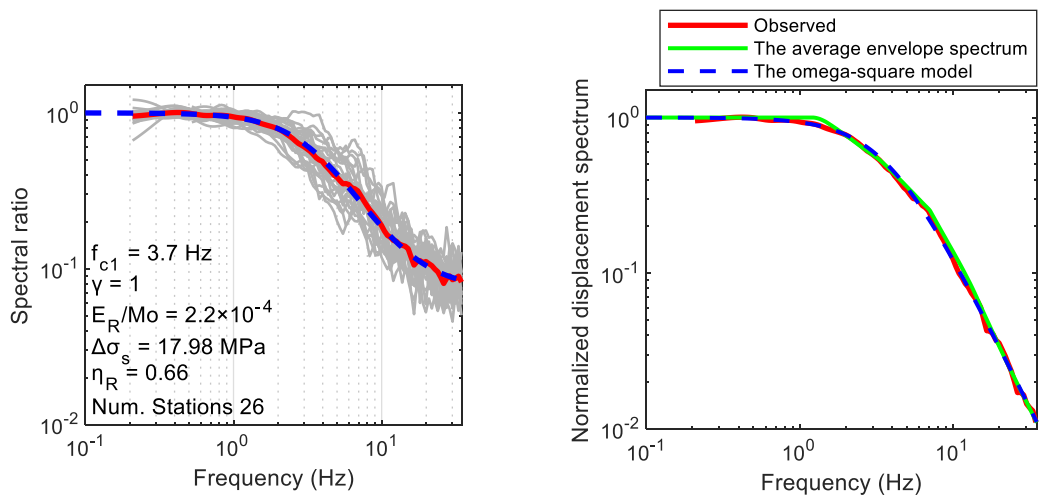
(a)

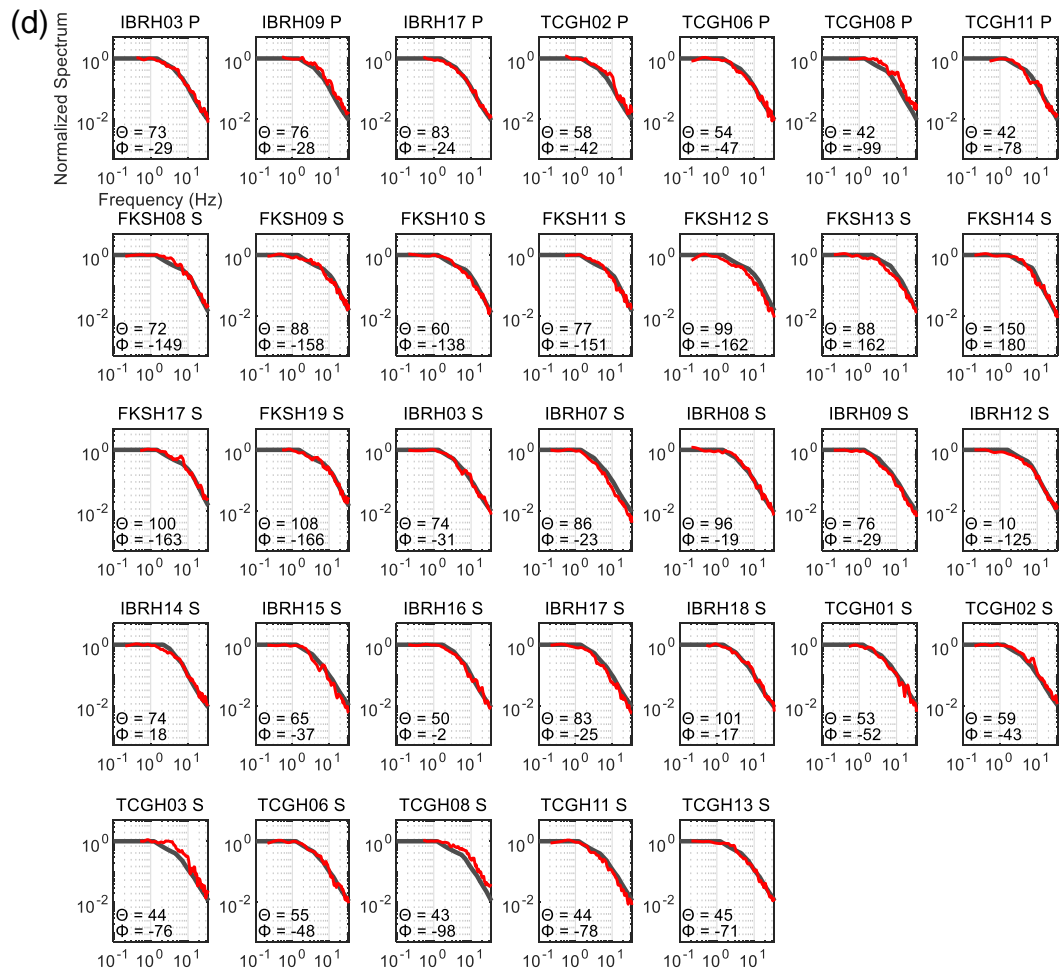


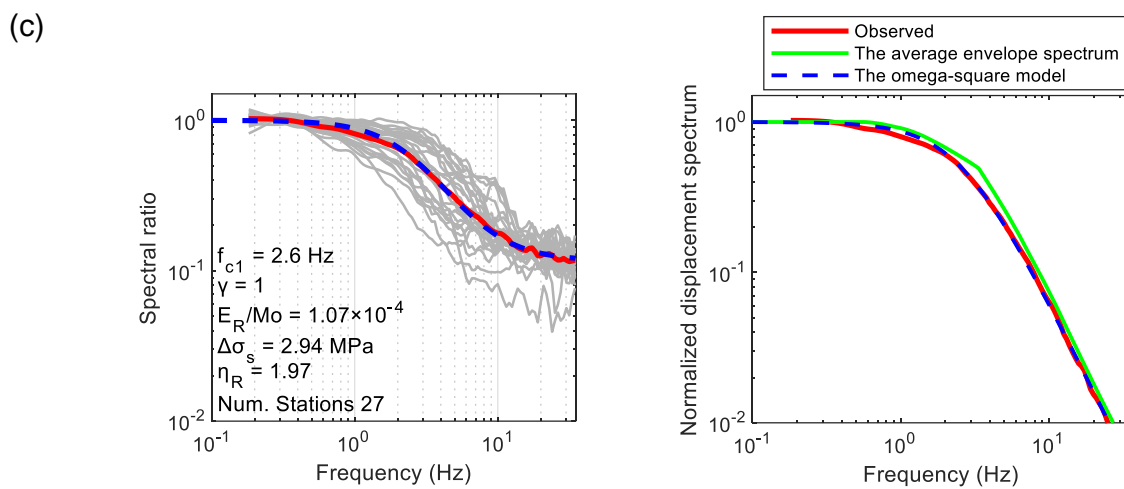
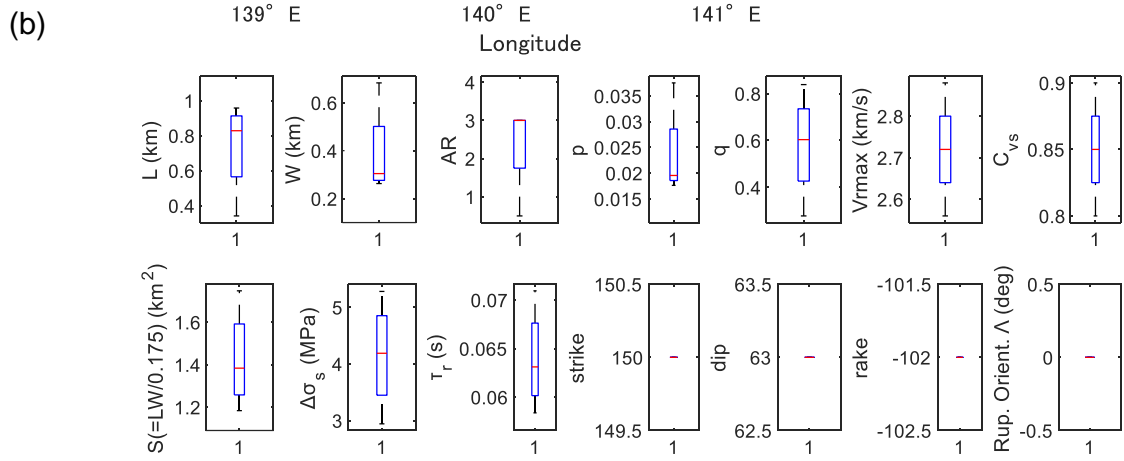
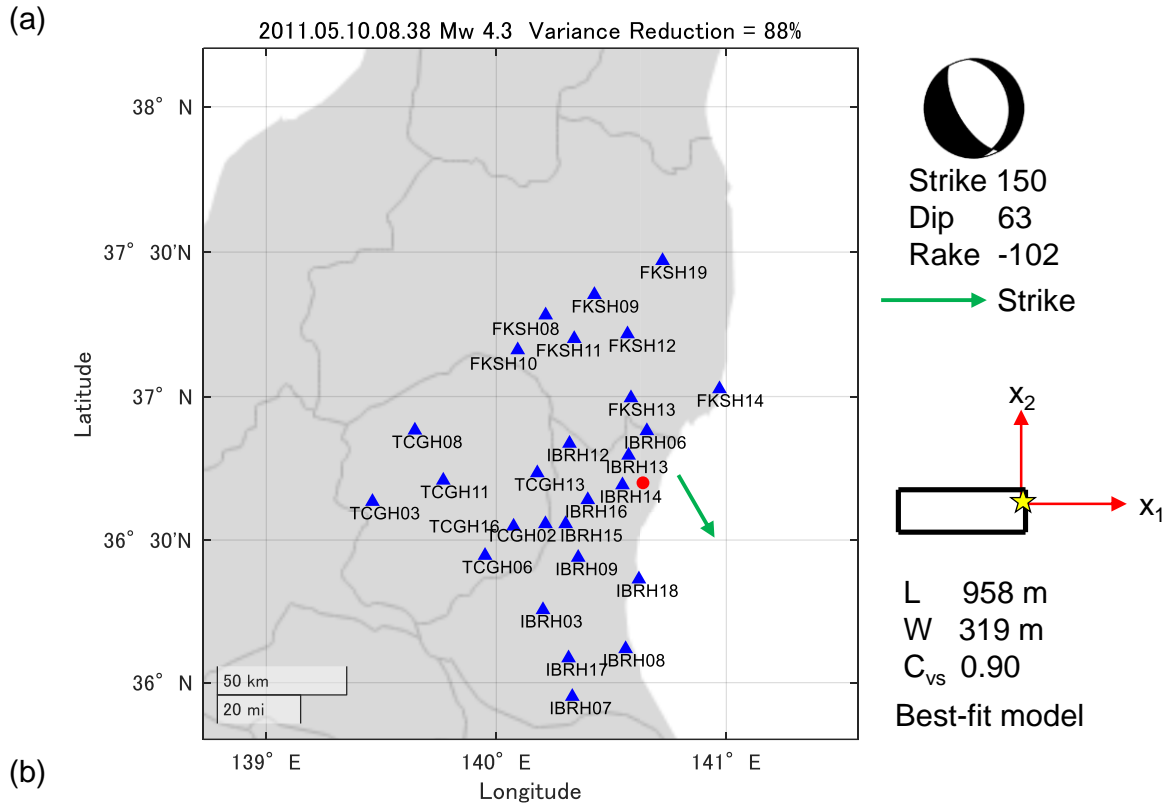
(b)

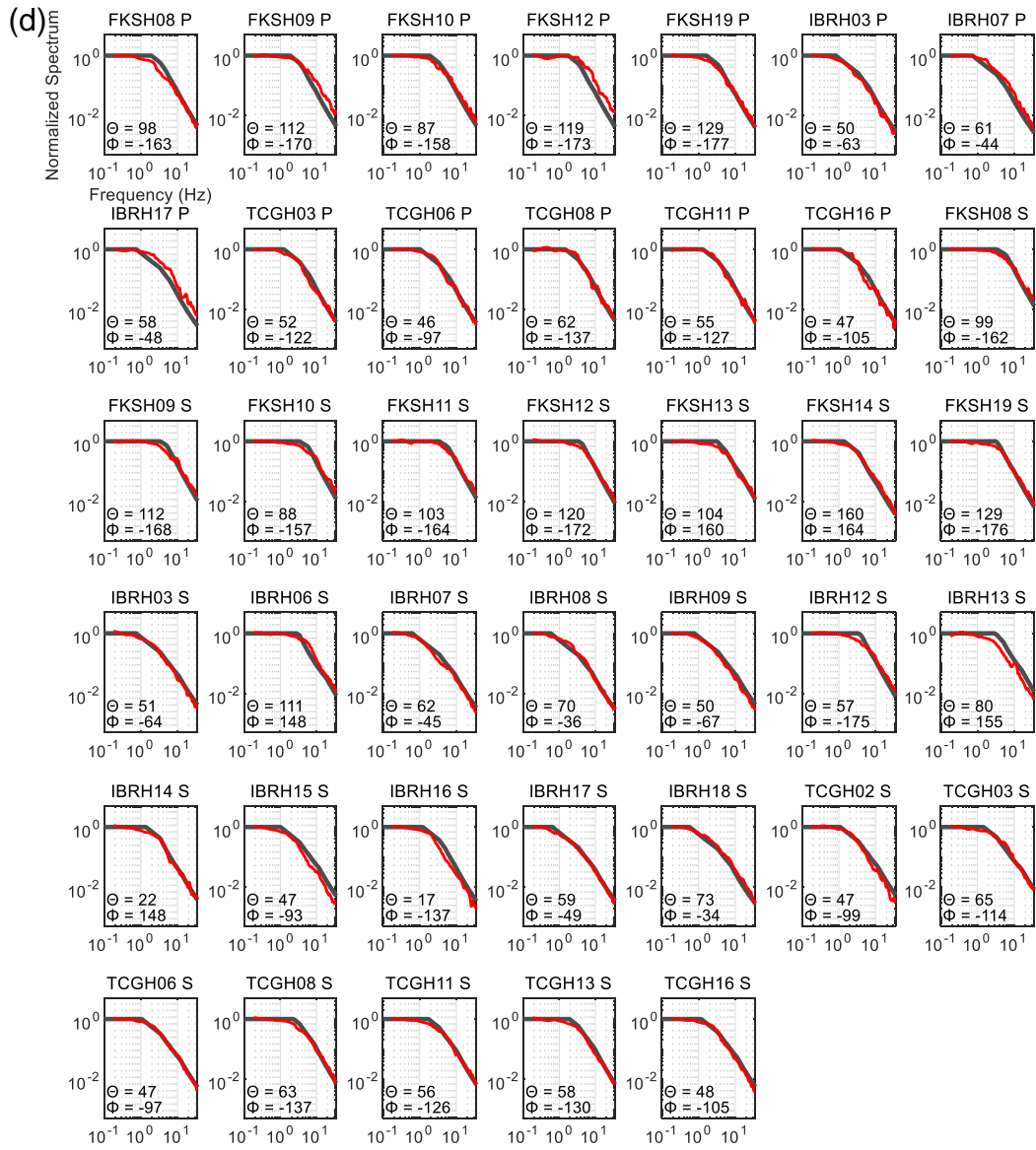


(c)

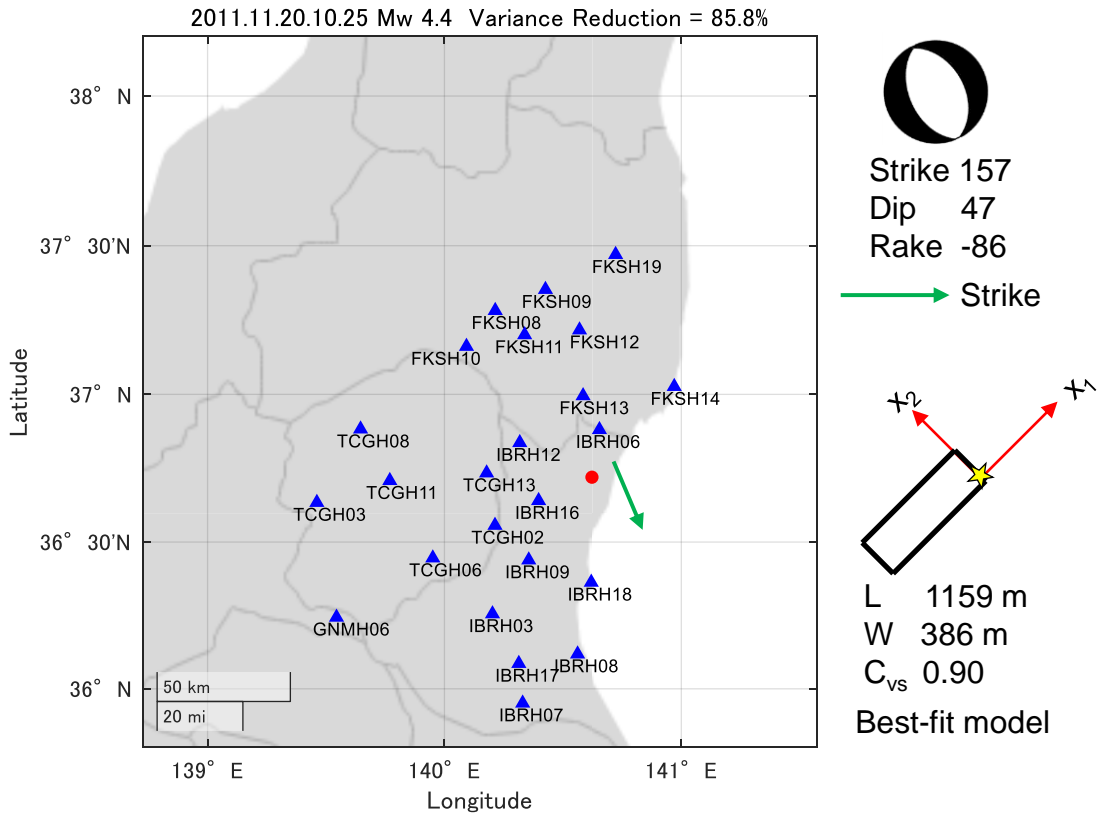




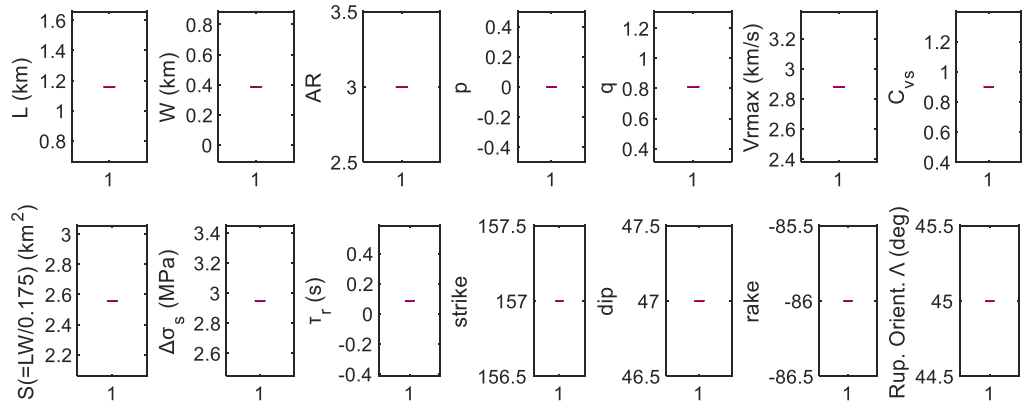




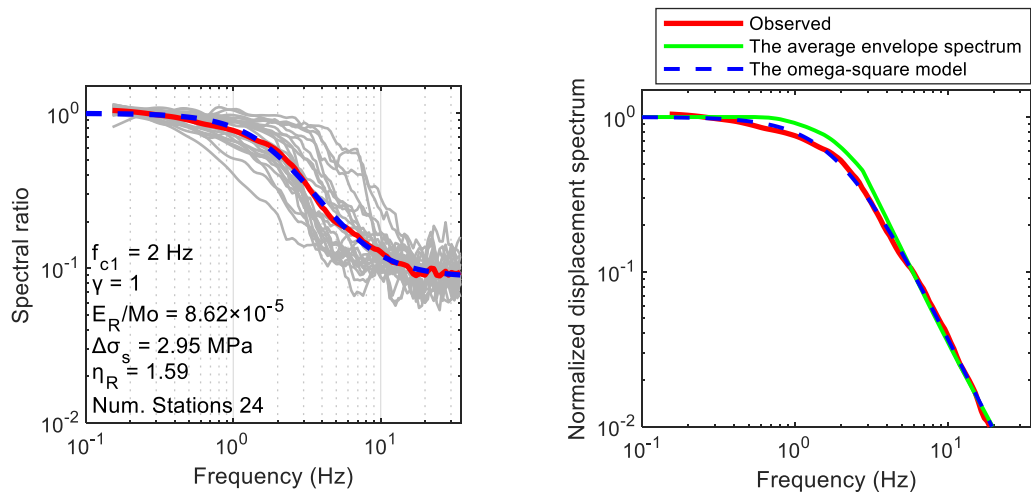
(a)



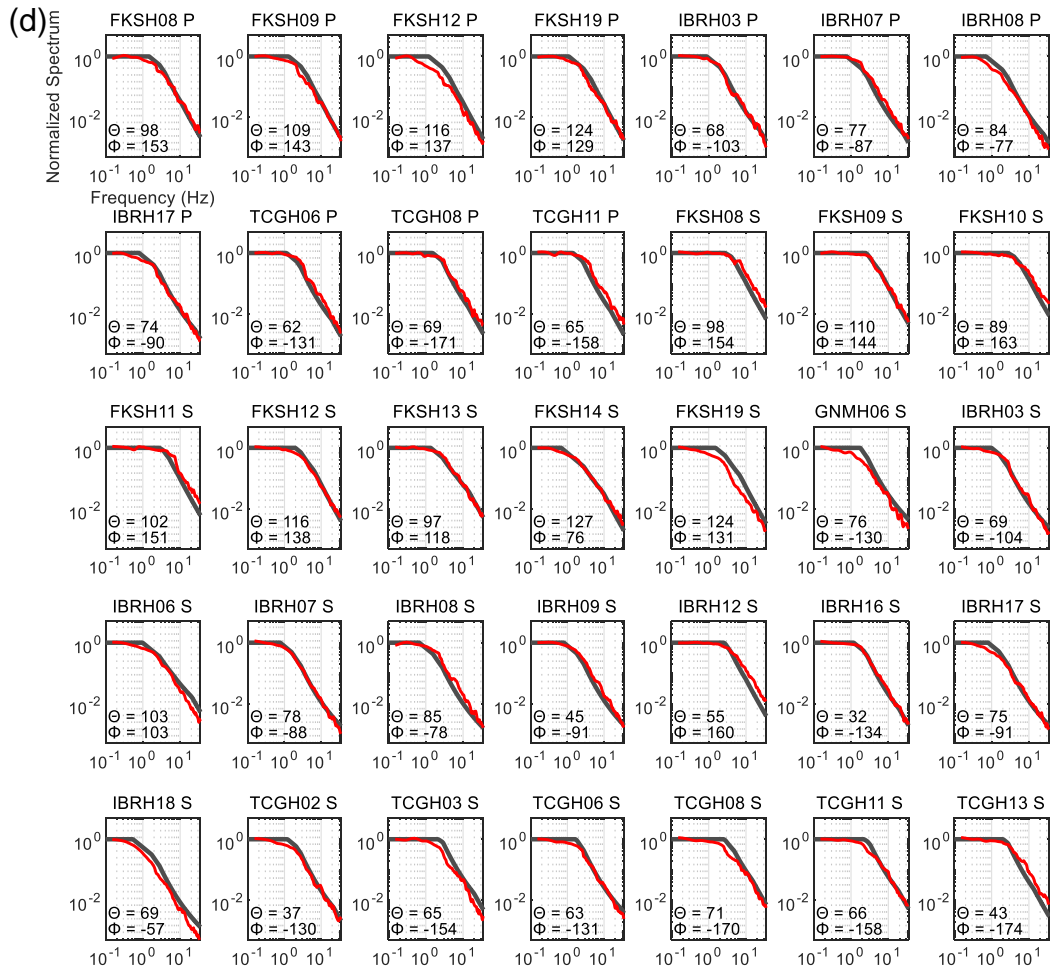
(b)



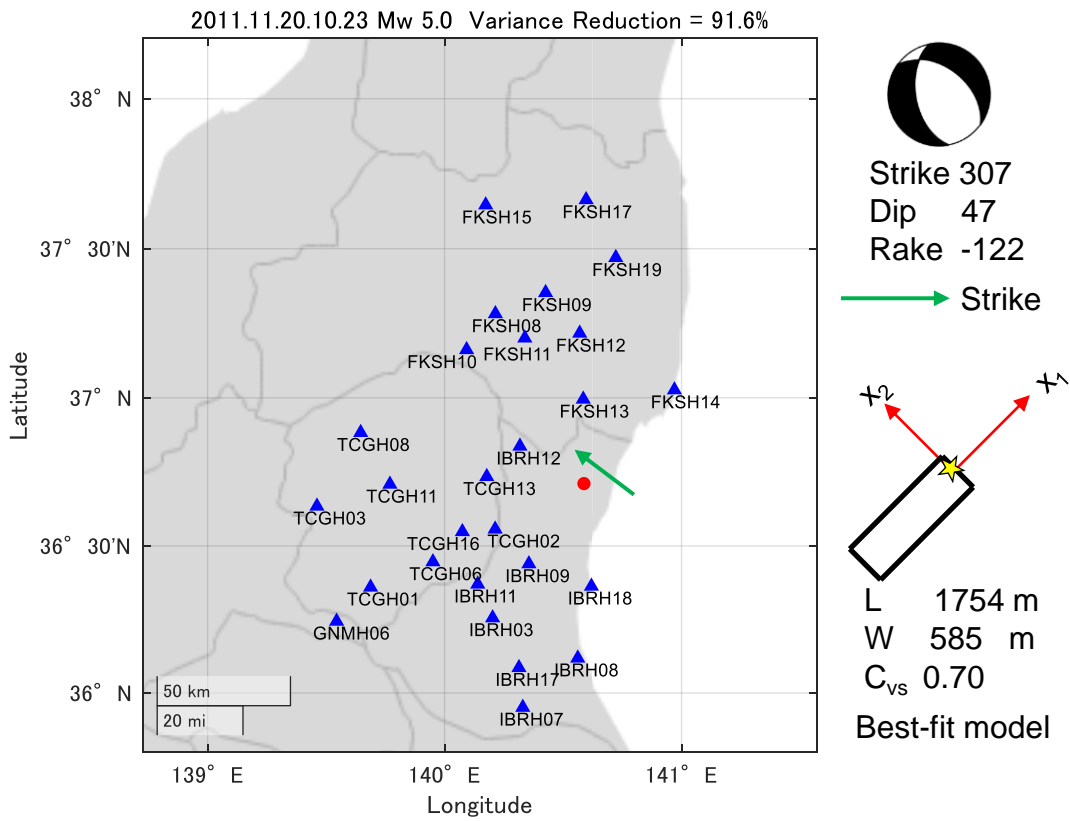
(c)



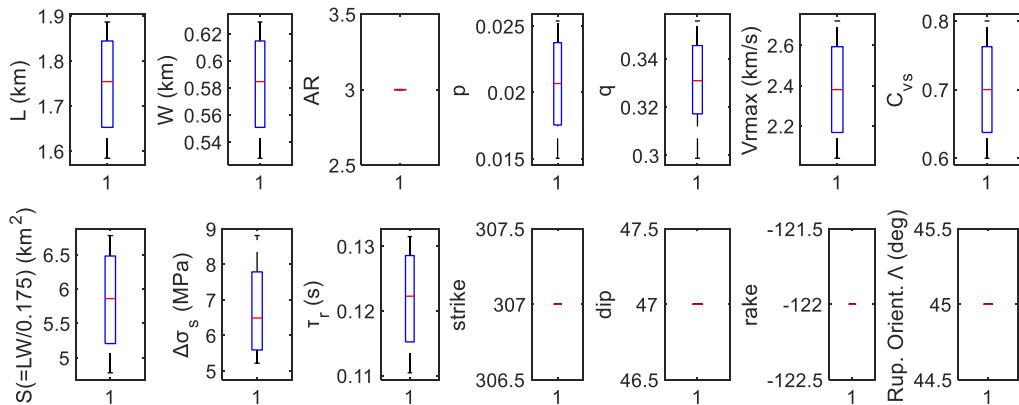




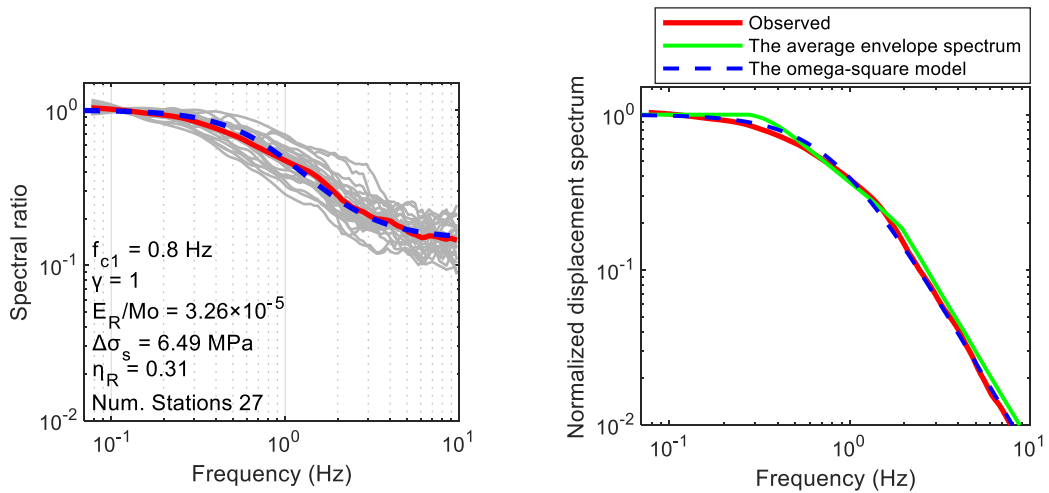
(a)

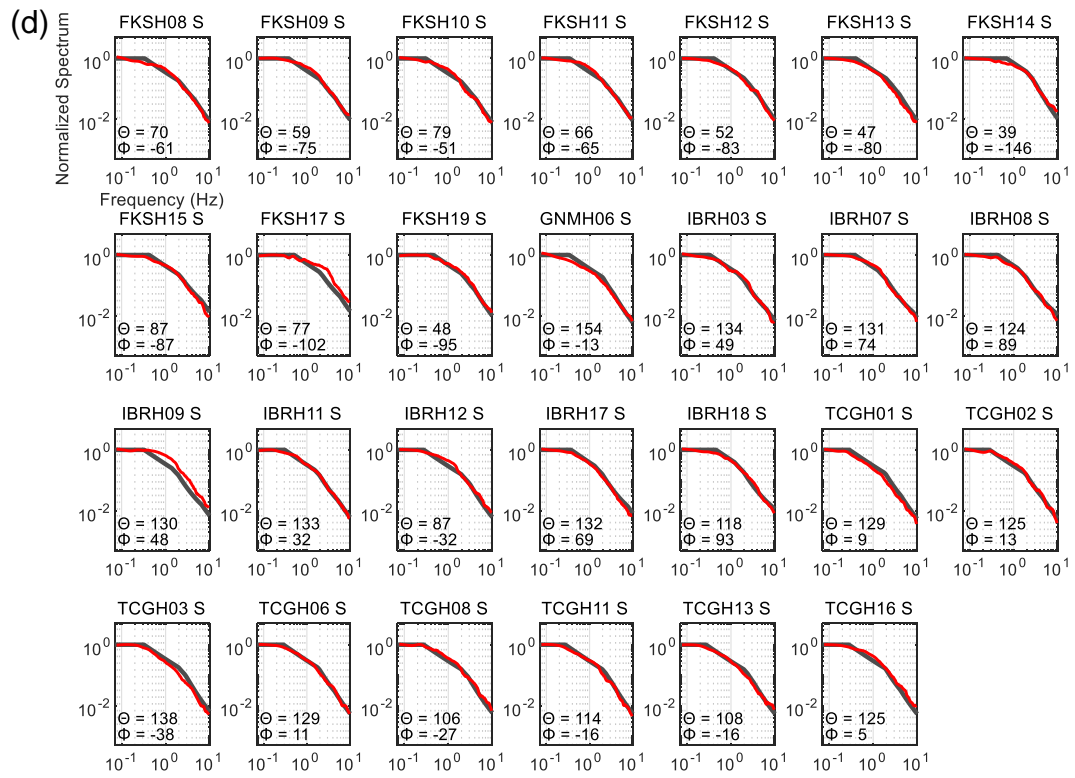


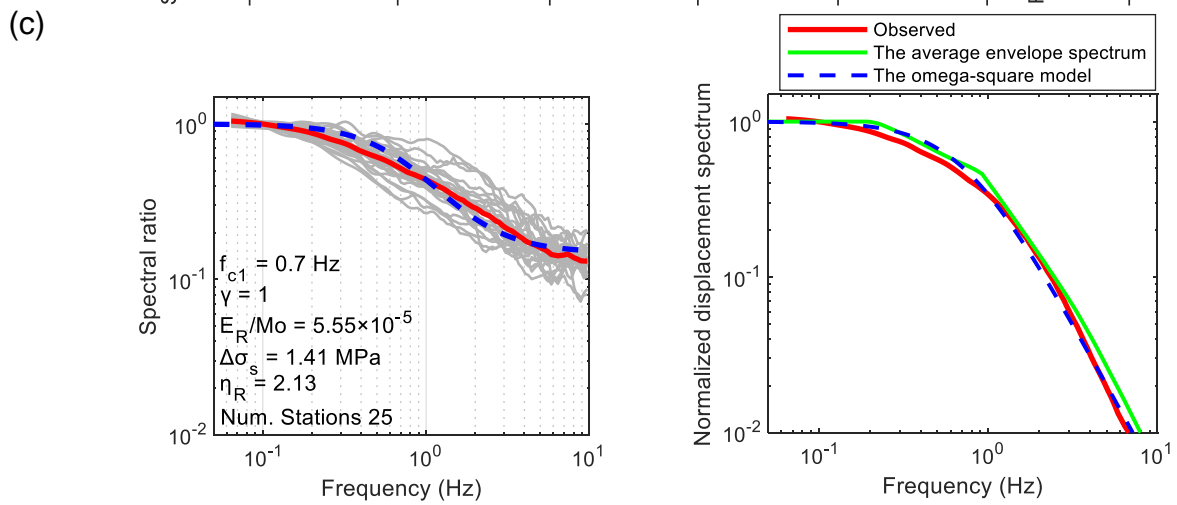
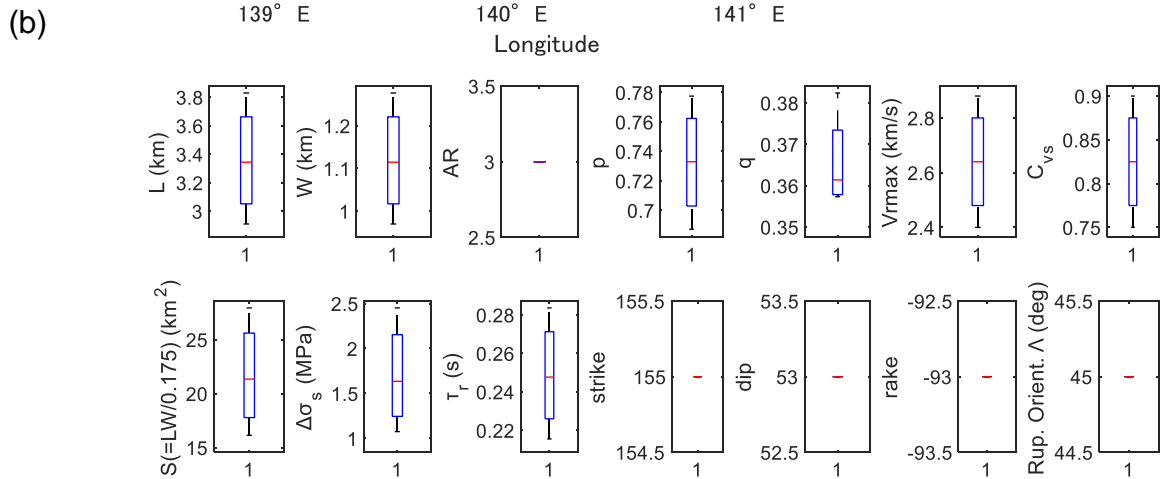
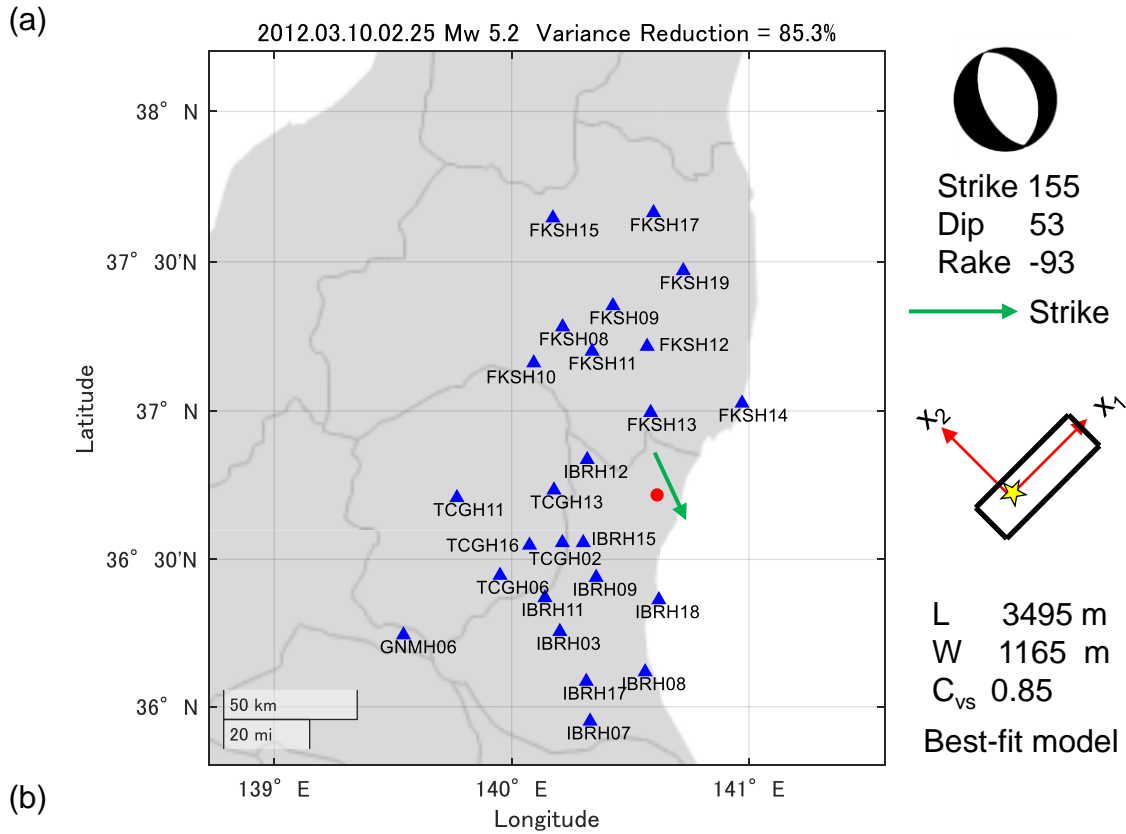
(b)

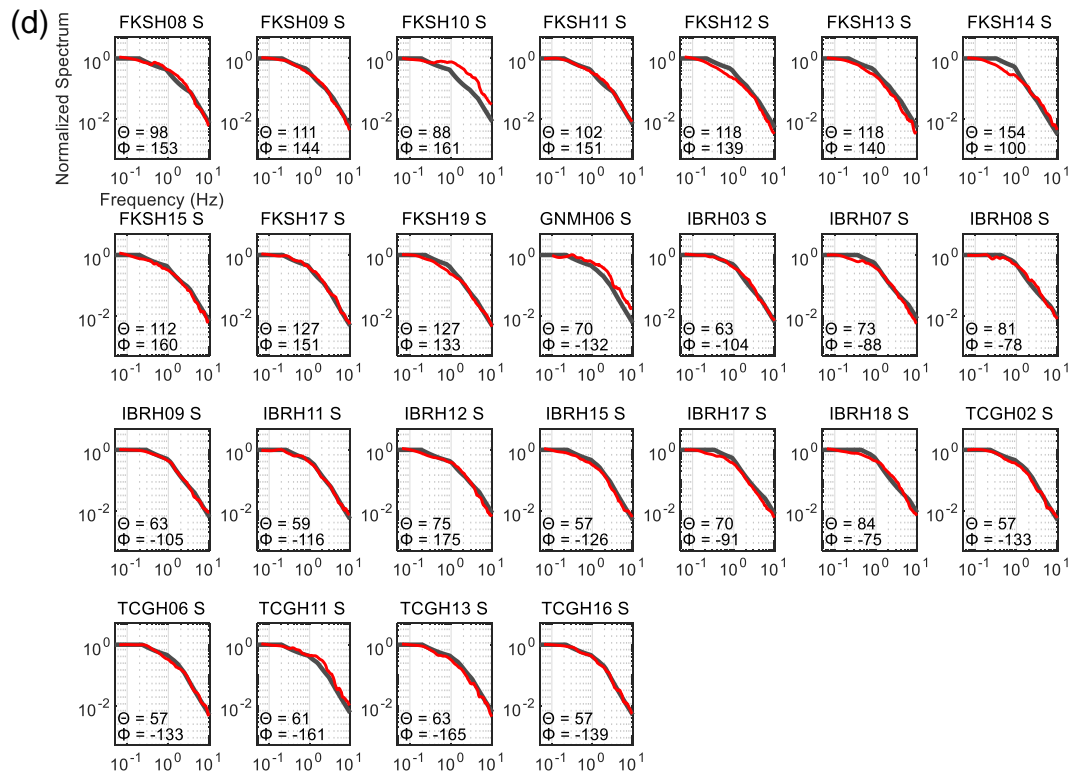


(c)

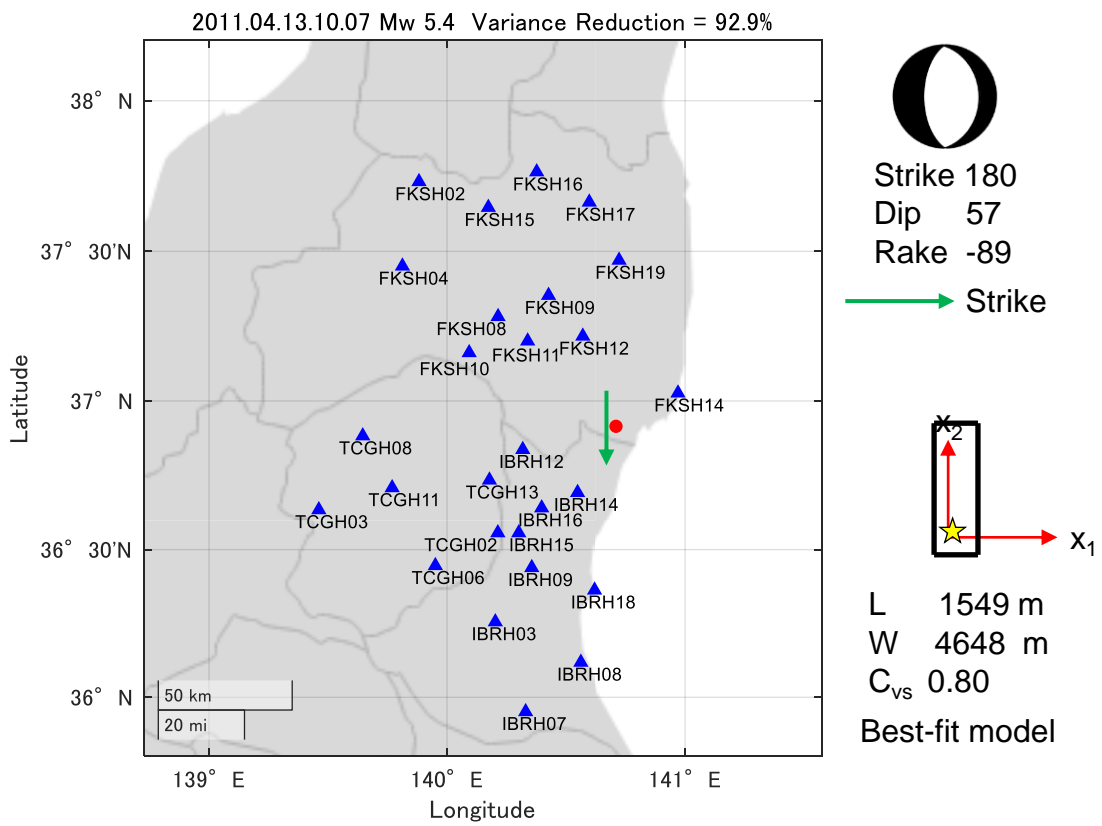




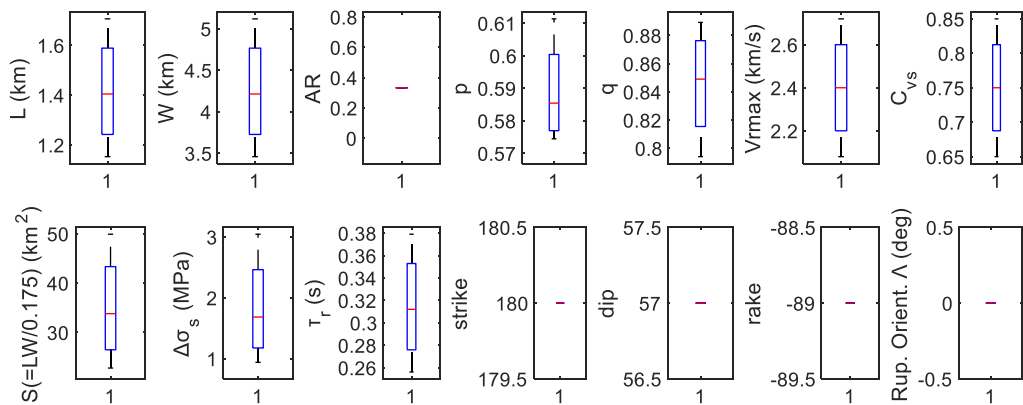




(a)



(b)



(c)

